Functional Architecture of the Medial Entorhinal Cortex

D i s s e r t a t i o n

zur Erlangung des akademischen Grades

D o c t o r r e r u m n a t u r a l i u m

(Dr. rer. nat.)

im Fach Biologie

eingereicht an der

Lebenswissenschaftlichen Fakultät

der Humboldt-Universität zu Berlin

von

M.Sc.

Saikat Ray

Präsident der Humboldt-Universität zu Berlin

Prof. Dr. Jan-Hendrik Olbertz

Dekan der Lebenswissenschaftlichen Fakultät

Prof. Dr. Richard Lucius

Gutachter/innen:

1. Prof. Dr. Michael Brecht
2. Prof. Dr. Imre Vida
3. Dr. James Poulet

Tag der mündlichen Prüfung: 22 June, 2016

Table of Contents

List of Figures

Chapter 1

Chapter 2

Chapter 3

Chapter 4

Chapter 5

Chapter 6

Chapter 7

List of Tables

Chapter 3

Chapter 4

Statutory Declaration

I declare to the best of my knowledge, that the doctoral thesis entitled, *Functional Architecture of the Medial Entorhinal Cortex* represents an original work of the author apart from the references and declared contributions under the provisions § 6 (3) of the doctoral degree regulations, dated 5 March 2015, of the faculty of Life Sciences of Humboldt-Universität zu Berlin. The work involved no collaborations with commercial doctoral degree supervisors. I affirm that I have neither applied for nor hold a corresponding doctoral degree and this work has not been submitted in full or part to another academic institution. Further, I acknowledge the doctoral degree regulations which underlie this procedure, and state that I abided by the principles of good academic practice of Humboldt-Universität zu Berlin.

2 April 2016 Saikat Ray

Abstract

The medial entorhinal cortex (MEC) is an important hub in the memory circuit in the brain and is present at the crucial juncture between the neocortex and the hippocampus. This thesis comprises of a group of studies which explores the architecture and microcircuits of the MEC. Layer 2 of the MEC is home to the largest number of pure grid cells, neurons which exhibit a hexagonal firing pattern during exploration of an open environment. The first study found that a group of pyramidal cells in layer 2 of the MEC, expressing the protein calbindin, were clustered and formed calbindin-patches in the rat brain. These calbindin-patches were physically arranged in a hexagonal grid in the MEC and received preferential cholinergic-inputs which are known to be important for grid-cell activity. A combination of identified single-cell and extracellular recordings in freely behaving rats revealed that grid cells were mostly calbindin-positive pyramidal cells. Reelin-positive stellate cells in the MEC were scattered throughout layer 2 and contributed mainly to the border cell population– neurons which fire when the animal is at the borders of an environment. To understand the importance of this grid-like layout of calbindin-patches, the next study explored the architecture of the MEC across evolution. Five mammalian species, from the smallest mammal (in the Etruscan shrew) to humans, spanning ~100 million years of evolutionary diversity and ~20,000 fold variation in brain size exhibited a periodic layout of calbindin-patches in the MEC. The sizes of these clusters was relatively invariant and the number of pyramidal neurons in them varied only ~10 fold across these species– pointing towards an evolutionarily conserved information processing role of the calbindin-patches. Next, an investigation of the developmental profile of the MEC in rats revealed that the periodic structure of the calbindin-patches and scattered layout of reelin-positive stellate cells in layer 2 was present around birth. This indicated that the architecture of the MEC, particularly the periodicity of the calbindin-patches was shaped by genetically determined processes rather than by experience. The study also revealed that calbindin-positive pyramidal cells matured later in comparison to reelin-positive stellate cells. This was established on basis of their co-localization with doublecortin, a marker for immature neurons. This dichotomy in structural maturation of pyramidal and stellate cells mirrored the difference in functional maturation profiles of grid and border cells respectively. Further, a dorsal-to-ventral maturation of layers 2 and 3 of the MEC and the adjoining parasubiculum was discovered. Functionally, grid cells in dorsal MEC have smaller spacing between the grid-nodes, while the ones in ventral MEC have progressively larger spacings. The dorso-ventral structural maturation of the MEC pointed towards a progressive functional development of spatial exploration with age. In contrast to layer 2, neurons in layer 3 of the MEC had rather homogenous intrinsic, spatiotemporal and morphological properties. Inputs from the parasubiculum, a long and narrow structure which flanks the dorsal and medial extremities of the MEC, selectively targeted the calbindin-patches in layer 2 of MEC indicating its role in shaping grid-cell function. In summary, the thesis uncovered a structure-function dichotomy of neurons in layer 2 of the MEC which is a fundamental aspect of understanding the microcircuits involved in memory formation.

Zusammenfassung

Der mediale entorhinale Kortex (MEK) ist eine wichtige Struktur für Gedächtnisleistungen und hat eine Brückenfunktion zwischen Neokortex und Hippokampus. Diese Doktorarbeit umfasst mehrere Studien zur Architektur und Verschaltung des MEK. Schicht 2 des MEK beinhaltet die größte Anzahl von Gitterzellen, welche durch ein hexagonales Aktivitätsmuster während räumlicher Exploration gekennzeichnet sind. In dieser Arbeit wird gezeigt, dass spezielle Pyramidenzellen, die das Protein Calbindin exprimieren, in einem hexagonalen Gitter im Gehirn der Ratte angeordnet sind und cholinerg innerviert werden. Es ist bekannt, dass die cholinerge Innervation wichtig für die Aktivität von Gitterzellen ist. Weiterhin ergaben extrazellulären Ableitungen und Methoden zur Identifikaktion einzelner Neurone in frei verhaltenden Ratten, dass Calbindin-positive Pyramidenzellen (Calbindin+) eine große Anzahl von Gitterzellen beinhalten. Reelin-positive Sternzellen (Reelin+) im MEK, zeigten keine anatomische Periodizität und ihre Aktivität orientierte sich an den Begrenzungen der Umgebung (Grenzzellen). Um die Bedeutung die Gitterstruktur von Calbindin Anhäufungen besser zu verstehen, untersucht eine weitere Studie die Architektur des MEK in verschiedenen Säugetieren. Die fünf untersuchten Säugetierspezies, vom kleinsten Säuger, der Etrusker Spitzmaus, bis hin zum Menschen umfassen ~100 Millionen Jahre evolutionäre Vielfalt und ~20,000 fache Variation der Gehirngröße. Alle Arten zeigten jeweils eine periodische Anhäufung der Calbindin+ Zellen. Die Größe der Anhäufungen war relativ invariant und die Anzahl an Pyramidenzellen pro Anhäufung variierte nur um den Faktor 10 zwischen den verschieden Spezies, was auf eine evolutiv konservierte Informationsverarbeitung schließen lässt. Die im Anschluss durchgeführte Studie beschäftigt sich mit der Ontogenese der Calbindin Anhäufungen in Ratten. Hier zeigte sich das die periodische Struktur der Calbindin+ Zellen, sowie die verstreute Anordnung der Reelin+ Sternzellen schon zum Zeitpunkt der Geburt erkennbar war. Dies deutet darauf hin, dass die Anordnung, besonders die der hexagonal verteilten Calbindin+ Zellen, eher durch genetisch determinierte Prozesse zu erklären ist, als dass sie auf Erfahrung beruht. Basierend auf ihrer Kolokalisation mit Doublecortin, einem Marker für unreife Neuronen, zeigte diese Studie außerdem, dass Calbindin+ Zellen strukturell später ausreifen als Reelin+ Sternzellen. Dieses Ergebnis deckt sich mit der Erkenntnis das Gitterzellen funktionell später reifen als Grenzzellen. Zusätzlich wurde herausgefunden, dass die Schichten 2 und 3 des MEK und des danebenliegenden Parasubiculum von dorsal zu ventral hin ausreifen. Die Distanz zwischen einzelnen Punkten im Raum bei denen Gitterzellen Aktionspotentiale erzeugen wird von dorsal zu ventral hin stetig größer. Dies deutet darauf hin, dass die strukturelle Reifung der Zellen in dorso-ventraler Richtung der progressive Ausweitung der räumlichen Exploration während der Entwicklung entspricht. Im Gegensatz zu Schicht 2 weisen Neurone in Schicht 3 des MEK eher homogene morphologische Eigenschaften auf. Passend dazu zeigten *in vitro* beziehungsweise *in vivo* Studien geringere Unterschiede hinsichtlich der intrinsischen und räumlich-zeitlichen elektrophsyiologischen Eigenschaften in dieser Schicht auf. Um die Projektionen in den MEK zu untersuchen fokussiert eine weitere Studie das Parasubiculum, eine längliche und schmale Struktur die den MEK dorsal und medial flankiert. Diese Untersuchung ergab, dass Verbindungen zum MEK präferiert in die Calbindin Anhäufungen in Schicht 2 projizieren. Somit ist es möglich, dass das Parasubiculum an der Bildung von Gitterzellen in Schicht 2 des MEK beteiligt ist. Zusammenfassend beschreibt diese Doktorarbeit eine Dichotomie von Struktur und Funktion in Schicht 2 des medialen entorhinalen Kortex, welche fundamental für das Verständnis von Gedächtnisbildung und deren zugrundeliegenden Mikroschaltkreisen ist.

Chapter 1

Introduction

The process of understanding the brain has gone through different approaches over the ages. From Aristotle in 4th century BC, who was wide off the mark when he believed it was an organ involved in cooling blood (Gross, 1995) to the Greek anatomist Galen in 2nd century AD, who was much closer to contemporary beliefs when he indicated it was involved in processing the senses, cognition and action (Freemon, 1994). Currently, the principal doctrine which governs neuroscience research is the neuron doctrine, pioneered on the basis of Ramon y Cajal's seminal studies at the end of the 19th century AD (Cajal, 1894), with pertinent updates (Bullock et al., 2005).

Neuronal Circuits

Neurons do not function in isolation, but rather, are connected to each other and are organized into ensembles or circuits. This forms the substrate for information processing in the brain. The parcellation of the brain into different areas by Brodmann (Brodmann, 1909) indicated that distinct brain regions specialized in processing differing kinds of information. The pathways which connect these diverse brain areas are collectively known today by the term connectome (Sporns et al., 2005), and numerous methodologies are utilized to understand these connections at different levels of granularity (Briggman et al., 2010; Wedeen et al., 2012). These pathways, together with the cells and regions they connect, form the neuronal circuits which underlie significant brain functions.

Memory Microcircuit

One of the most important functions which the brain performs, is the ability to remember things. The importance of the hippocampus and parahippocampal regions in memory arose with the curious case of HM (Scoville & Milner, 1957) which established a direct link between the hippocampal area and memory. Further, the discovery of place cells (O'Keefe & Dostrovsky, 1971) again affirmed its presence at the center of the memory microcircuit, and provided a perfect foil for interrogating the memory circuit under the ambit of spatial memory.

Entorhinal Cortex

The entorhinal cortex is located at the posterior end of the rodent cerebral cortex (Figure 1a) and forms a gateway between the neocortex and the hippocampus. It is thus uniquely positioned as a hub for translating sensory information into memories and is broadly divided into a medial and lateral subdivision (Figure 1a-c; Brodmann, 1909) across mammalian species (Rose, 1927; Naumann et al., 2016).

The lateral entorhinal cortex receives inputs from the piriform cortex, perirhinal cortex and amygdala (Kerr et al., 2007; Insausti & Amaral, 2008) and is involved in olfactory processing (Staubli et al., 1984) and object recognition (Deshmukh & Knierim, 2011). On the other hand, the medial entorhinal cortex primarily receives inputs from subicular, parahippocampal-postrhinal and retrosplenial cortices (Kerr et al., 2007; Insausti & Amaral, 2008) and is important in processing spatial information (Hafting et al., 2005).

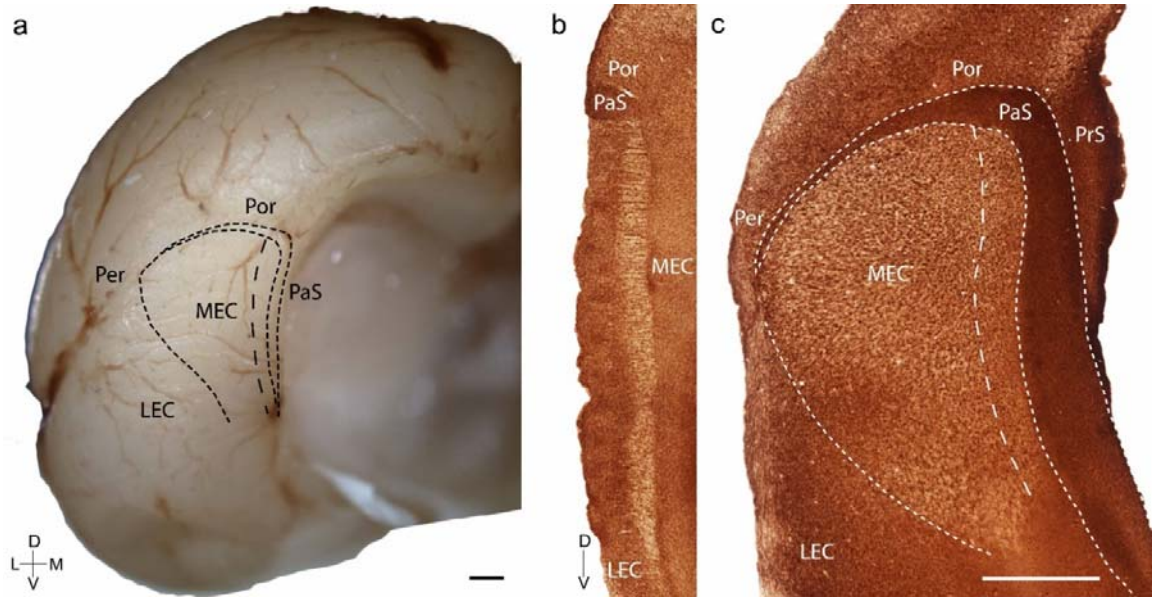

Figure 1: An overview of the rat entorhinal cortex.

(a) Posterior view of the rat left hemisphere, illustrating the location of the parahippocampal regions- Medial entorhinal cortex (MEC), lateral entorhinal cortex (LEC), parasubiculum (PaS), postrhinal cortex (Por) and perirhinal cortex (Per).
(b) A parasagittal section stained for acetylcholinesterase activity illustrating the laminar layout of the MEC. Note the microcolumnar structure in layer 3 of MEC but not LEC.
(c) A tangential section (through layer 3) stained for acetylcholinesterase activity illustrating the parahippocampal regions. Presubiculum (PrS) is visible at the medial most extent. Note the microcolumnar structure which distinguishes MEC from LEC.

Scale bars 1mm. Scale bar in (c) also applies to (b). D- Dorsal; V- Ventral; M- Medial; L- Lateral. Orientation in (a) also applies to (c). Figure adapted from Ray et al., 2014.

The entorhinal cortex is a 6 layered structure, with layers 2 and 3 providing the major inputs to the hippocampus (Steward & Scoville, 1976) and layers 5 and 6 receiving information from it (Swanson & Cowan, 1977). These connections form integral fragments of the entorhinal-hippocampal loop, which is fundamental to information processing in the hippocampal formation.

The medial entorhinal cortex (MEC) encodes spatial information (Hafting et al., 2005) and its connections with the hippocampus, where consolidated spatial information is represented in terms of a place cell (O'Keefe & Dostrovsky, 1971) form an integral aspect of the spatial memory microcircuit.

Spatial cells in the medial entorhinal cortex

The medial entorhinal cortex came into prominence early in the 21st century, with the discovery of grid cells (Figure 2a; Hafting et al, 2005) and their remarkable spatial discharge pattern. This has led to a decade of frantic work resulting in the discovery of other spatially modulated cell

types, including border cells (Figure 2b; Solstad et al., 2008) and head directional cells (Figure 2c; Sargolini et al., 2006) in the MEC in a bid to unravel the spatial memory circuit.

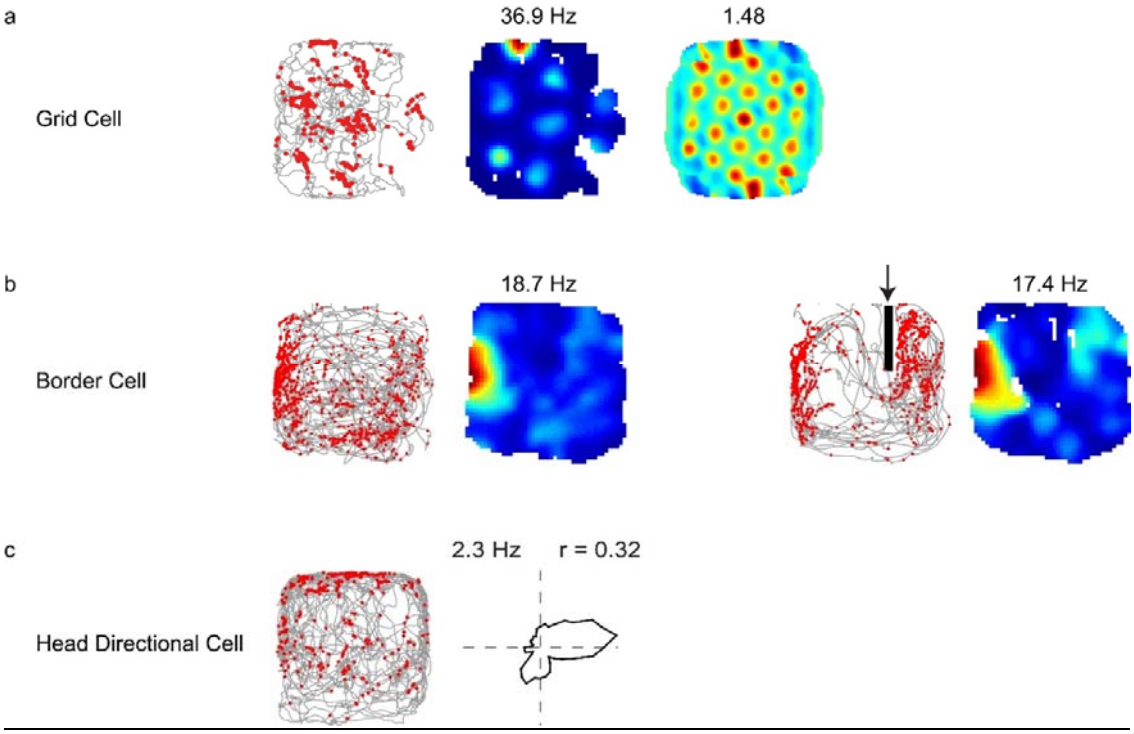

Figure 2: Spatial cell types in the medial entorhinal cortex.

(a) Trajectory of a freely exploring rat (gray) with spikes (red) from a grid cell plotted on it (left). The firing rate map (middle; number denotes peak firing rate) shows a hexagonal firing pattern of the cell, which is also illustrated in the autocorrelation of the firing rate map (right; number denotes the grid score).

(b) A border cell firing on the left boundary of the environment (left; number denotes peak firing rate) also preserves it firing characteristics on the insertion of another boundary (right, arrow; number denotes peak firing rate).

(c) A head direction cell firing when the animal is facing towards the right side of the environment as illustrated by the polar plot of head directional tuning (left; numbers denote peak firing rate and r= Rayleigh vector strength).

Figure adapted from Tang et al., 2014.

Medial entorhinal cortex microcircuit

Layer 2 of the medial entorhinal cortex contains the largest density of pure grid cells (Hafting et al., 2005; Boccara et al., 2010) and also contains other spatial cells like border cells (Solstad et al., 2008). Anatomically, it contains two classes of principal cells- pyramidal cells and stellate cells, with distinctive intrinsic conductances (Alonso & Llinás, 1989; Klink & Alonso, 1997), immunoreactivity (Varga et al, 2010; Ray et al., 2014) and projections (Lingenhöhl & Finch, 1991).

Though a repertoire of different spatial cells was discovered in MEC, it was unclear if these distinct functional cell types also corresponded to different types of neurons anatomically (Burgalossi & Brecht, 2014). This provided an opportunity to interrogate if the dichotomy in structure and function of the neurons in layer 2 of MEC map onto each other.

In this thesis, I explored the functional architecture of the MEC in a bid to understand the medial entorhinal cortex microcircuit. This was undertaken by investigating the architecture of this region across evolution and development, and establishing structure-function relationships between individual cell types.

References

Alonso, A. & Llinás, R. R. Subthreshold Na+-dependent theta-like rhythmicity in stellate cells of entorhinal cortex layer II. *Nature* **342**, 175–177 (1989).

Boccara, C.N. et al. Grid cells in pre- and parasubiculum. *Nat. Neurosci.* **13**, 987–994 (2010).

Briggman, K.L., Helmstaedter, M., Denk, W. Wiring specificity in the direction-selectivity circuit of the retina. *Nature* **471**, 183-188 (2010).

Brodmann, K. Vergleichende Lokalisationslehre der Grosshirnrinde. *Leipzig: Johann Ambrosius Barth* (1909).

Bullock, T.H. et al. The Neuron Doctrine, Redux. *Science* **310**, 791–793 (2005).

Burgalossi, A. & Brecht, M. Cellular, columnar and modular organization of spatial representations in the medial entorhinal cortex. *Curr. Opin. Neurobiol.* **24**, 47-54 (2014).

Cajal, S.R. Histology of the Nervous System of Man and Vertebrates. *Oxford University Press, Translated-1995* (1911).

Cajal, S.R. The Croonian lecture: la fine structure des centres nerveux. *Proc. R. Soc.* **55**, 444-468 (1894).

Deshmukh, S.S. & Knierim, J.J. Representation of non-spatial and spatial information in the lateral entorhinal cortex. *Front. Behav. Neurosci.* **5**, 69 (2011).

Freemon, F.R. Galen's ideas on neurological function. *J. Hist. Neurosci.* **3**, 263-271 (1994).

Gross, C.G. Aristotle on the brain. *The Neuroscientist* **1**, 245-250 (1995).

Hafting, T., Fyhn, M., Molden, S., Moser, M.B., Moser, E.I. Microstructure of a spatial map in the entorhinal cortex. *Nature* **436**, 801–806 (2005).

Insausti, R. & Amaral, D.G. Entorhinal cortex of the monkey: IV. Topographical and laminar organization of cortical afferents. *J. Comp. Neurol.* **509**, 608-641 (2008).

Kerr, K.M., Agster, K.L., Furtak, S., Burwell, R.D. Functional neuroanatomy of the parahippocampal region: the lateral and medial entorhinal areas. *Hippocampus* **17**, 697-708 (2007).

Klink, R. & Alonso, A. Muscarinic modulation of the oscillatory and repetitive firing properties of entorhinal cortex layer II neurons. *J. Neurophysiol.* **77**, 1813–1828 (1997).

Kohara, K. et al. Cell type-specific genetic and optogenetic tools reveal hippocampal CA2 circuits. *Nat. Neurosci.* **17**, 269-279 (2014).

Lingenhöhl, K. & Finch, D. M. Morphological characterization of rat entorhinal neurons in vivo: soma-dendritic structure and axonal domains. *Exp. Brain. Res.* **84**, 57–74 (1991).

Naumann, R.K. et al. Conserved size and periodicity of pyramidal patches in layer 2 of medial/caudal entorhinal cortex. J. Comp. Neurol. 524, 783-806 (2016).

O'Keefe, J. & Dostrovsky, J. The hippocampus as a spatial map. Preliminary evidence from unit activity in the freely-moving rat. *Brain Res.* **34**, 171-175 (1971).

Ray, S. et al. Grid-like arrangement and theta-modulation of a pyramidal cell microcircuit in layer 2 of medial entorhinal cortex. *Science* **343**, 891-896 (2014).

Rose, M. Der Allocortex bei Tier und Mensch I. Teil. *J. Psychol. Neurol.* **34**, 1–111 (1927).

Sargolini, F. et al. Conjunctive representation of position, direction, and velocity in entorhinal cortex. *Science* **312**, 758–762 (2006).

Scoville, W.B. & Milner, B. Loss of recent memory after bilateral hippocampal lesions. *J. Neurol. Neurosurg. Psych.* **20**, 11-21 (1957).

Solstad, T., Boccara, C.N., Kropff, E., Moser, M.B., Moser, E.I. Representation of geometric borders in the entorhinal cortex. *Science* **322**, 1865–1868 (2008).

Sporns, O., Tononi, G., Kötter, R. The human connectome: A structural description of the human brain. *PLoS Comput. Biol.* **1**, e42 (2005).

Staubli, U., Ivy, G., Lynch, G. Hippocampal denervation causes rapid forgetting of olfactory information in rats. *Proc. Natl. Acad. Sci. USA* **81,** 5885–5887 (1984).

Steward, O. & Scoville, S.A. Cells of origin of entorhinal cortical afferents to the hippocampus and fascia dentate of the rat. *J. Comp. Neurol.* **169**, 347-370 (1976).

Swanson, L.W. & Cowan, W.M. An autoradiographic study of the organization of the efferent connections of the hippocampal formation in the rat. *J. Comp. Neurol.* **172**, 49-84 (1977).

Tang, Q.et al. Pyramidal and stellate cell specificity of grid and border representations in layer 2 of medial entorhinal cortex. *Neuron* **84**, 1191–1197 (2014).

Varga, C., Lee, S. Y., Soltesz, I. Target-selective GABAergic control of entorhinal cortex output. *Nat. Neurosci.* **13**, 822–824 (2010).

Wedeen, V.J. et al. The geometric structure of the brain fiber pathways. *Science* **335**, 1628-1634 (2012).

Witter, M.P. et al. Cortico-hippocampal communication by way of parallel parahippocampal-subicular pathways. *Hippocampus* **10**, 398-410 (2000).

Chapter 2

Grid-layout and theta-modulation of layer 2 pyramidal neurons in medial entorhinal cortex.

Published as:

Ray, S. et al. (2014). Grid-layout and theta-modulation of layer 2 pyramidal neurons in medial entorhinal cortex. *Science 343:891-896*

doi: 10.1126/science.1243028

Grid-layout and Theta-modulation of Layer 2 Pyramidal Neurons in Medial Entorhinal Cortex

Saikat Ray*, Robert Naumann*, Andrea Burgalossi*,[1], Qiusong Tang*, Helene Schmidt* & Michael Brecht‡

* These authors contributed equally

‡Bernstein Center for Computational Neuroscience

Humboldt University of Berlin
Philippstr. 13 Haus 6
10115 Berlin, Germany

[1] Current Address: Werner Reichardt Centre for Integrative Neuroscience, Otfried-Müller-str. 25, 72076 Tübingen, Germany

‡To whom correspondence should be addressed: michael.brecht@bccn-berlin.de

One Sentence Summary:

We describe a grid-like microcircuit consisting of strongly theta-modulated pyramidal neurons in layer 2 medial entorhinal cortex.

Little is known about how microcircuits are organized in layer 2 of medial entorhinal cortex. We visualized principal cell microcircuits and determined cellular theta-rhythmicity in freely moving rats. Non-dentate-projecting calbindin-positive pyramidal cells bundled dendrites together and formed patches arranged in a hexagonal grid aligned to layer 1 axons, parasubiculum and cholinergic inputs. Calbindin-negative dentate-gyrus-projecting stellate cells were distributed across layer 2 but avoided centers of calbindin-positive patches. Cholinergic drive sustained theta-rhythmicity, which was two-fold stronger in pyramidal than in stellate neurons. Theta-rhythmicity was cell-type specific, but not distributed as expected from cell-intrinsic properties. Layer 2 divides into a weakly theta-locked stellate cell lattice and spatiotemporally highly organized pyramidal grid. It needs to be assessed how these two distinct principal cell networks contribute to grid cell activity.

Temporal (*1-3*) and spatial (*4*) discharge patterns in layer 2 of medial entorhinal cortex (MEC) are related through phase precession (*5*) and the correlation of gridness (hexagonal regularity) and theta-rhythmicity (*2*). Layer 2 principal neurons divide into pyramidal and stellate cells, the latter of which have been suggested to shape entorhinal theta (*6,7*) and grid activity (*8*) by their intrinsic properties. Progress in understanding entorhinal microcircuits has been limited, because most though not all (*9-11*) data stem from extracellular recordings of unidentified cells. Such recordings have characterized diverse functional cell types (*12-14*) in layer 2. Clustering of grid cells (*15*) points to spatial organization. It is not clear, however, how functionally defined cell types correspond to stellate and pyramidal cells (*7,16*), which differ in conductances, immunoreactivity, projections and inhibitory inputs (*6,17-20*). We combined juxtacellular labeling with principal cell identification (*20*) to visualize microcircuits in MEC (Fig. 1A).

Calbindin immunoreactivity (*20*) identifies a relatively homogeneous pyramidal neuron population in MEC layer 2. Parasagittal sections stained for calbindin (Fig. 1B) showed that calbindin-positive (calbindin$^+$) pyramidal cells were arranged in patches (*21*). Apical dendrites of calbindin$^+$ pyramidal cells bundled together in layer 1 to form tent-like structures over the patches (Fig. 1B). The patchy structure is well defined at the layer 1/2 border, whereas a "salt and pepper" appearance of calbindin$^+$ and calbindin$^-$ cells is observed deeper in layer 2 (Fig. S1). Patches contained 187 ± 70 cells (111 ± 42, ~60 % calbindin$^+$, 76 ± 28, ~40 % calbindin$^-$ cells; counts of 19 patches from four brains). We double-stained tangential sections for calbindin (green) and the neuronal marker NeuN (red) to visualize patches in the cortical plane. Calbindin$^+$ (green/yellow) patches covered the MEC except for a 400-500 μm wide patch-free medial stripe adjacent to the parasubiculum (Fig. 1C). Clustering was not observed in calbindin$^-$ neurons (red) (Fig. 1C). We noted a striking hexagonal organization of calbindin$^+$ patches (Fig. 1C,D) and characterized this organization by three techniques: (i) Two-dimensional spatial autocorrelation analysis (*4*), which captures spatially recurring features and revealed a hexagonal regularity (Fig. 1E). (ii) Grid scores (*12*) modified to quantify hexagonality also in elliptically distorted hexagons (*22*), distortions which result from tissue curvature and anisotropic shrinkage. Grid scores range from -2 to +2, with values > 0 indicating hexagonality. The example in Fig. 1D had a grid score of 1.18 suggesting a high degree of hexagonality. (iii) We assessed the probability of hexagonal patch arrangements given preserved local structure (*14*) by a shuffling procedure. We found that the strongest Fourier component of the sample (Fig. 1D) exceeded that of the 99th percentile of shuffled data, suggesting such hexagonality is unlikely to arise by chance.

We retrogradely labeled neurons from ipsilateral dentate gyrus (Fig. 2A) using biotinylated dextran amine (Fig. 2B) or cholera toxin B (Fig. 2C) to investigate the arrangement of layer 2 principal cells with identified projection patterns and immunoreactivity (*20*). While most retrogradely labeled neurons were stellate cells (*16,23*), a small fraction had pyramidal morphologies, but these neurons appeared larger than calbindin$^+$ pyramidal cells (Fig. 2B). Calbindin$^+$ neurons did not project to the dentate gyrus (only 1 double-labeled out of 313 neurons in Fig. 2C-E; see also *20*). Calbindin$^+$ patches were hexagonally arranged (Fig. 2C,D,F), while dentate-gyrus-projecting neurons (red) were uniformly distributed (Fig. 2E,G). Reconstructions of calbindin$^+$ and calbindin$^-$ cells labeled *in vivo* confirmed their pyramidal and stellate morphologies, respectively. Calbindin$^+$ dendrites were largely confined to patches, whereas calbindin$^-$ stellates cells had three times larger dendritic trees (7.6 vs 2.6 mm average total length, $p < 0.03$), which extended unrelated to patches (Fig. 2H,I). Differentiating layer 2

neurons by calbindin and reelin immunoreactivity confirmed patchy hexagonality of calbindin$^+$ cells and scattered distribution of reelin$^+$ cells without overlap between these neurons (*20*) (Fig. S2).

To investigate the organization of calbindin$^+$ patches across MEC, we prepared flattened whole-mount preparations. Patches had similar arrangements throughout the dorsoventral extent of MEC (Fig. S3). At the layer 1/2 border we consistently observed hexagonal arrangements in well-stained specimen. We quantified patch size and spacing in ten largely complete MEC whole-mounts. Patch density was similar throughout MEC, while patch diameter slightly increased towards ventral (Fig. S3). We estimated 69 ± 17 patches across the entire MEC (n = 10). Calbindin patches stained also positive for cytochrome-oxidase-activity *(9)*. However, the two staining patterns were not the same as calbindin patches were more sharply delineated than spots revealed by cytochrome-oxidase-activity and cytochrome-oxidase staining revealed many more patches than calbindin staining in MEC (*9*). Moreover, the staining patterns did not correspond at all in the parasubiculum.

Calbindin$^+$ patches shared a roughly 60° symmetry of their axes (Fig. 3A). One axis runs parallel to the dorsoventral axis of the parasubiculum (Fig. 3A-B). Lines fitted through the dorsoventral axis of the parasubiculum and the most medial column of calbindin$^+$ patches had the same orientation (Fig. 3B). A second consistent axis was tilted about 60° relative to the dorsoventral axis. This calbindin$^+$ patch axis curved ventrally at more lateral positions and aligned with the orientation of overlaying layer 1 myelinated axons (Fig. 3C-F). Thus, the line connecting diagonally neighboring calbindin patches (revealed by spatial autocorrelation, Fig. 3D,E) aligned with the orientation of layer 1 axons (Fig. 3F). We quantified the orientation of axonal segments by a polar plot shown in Fig. 3G and confirmed that layer 1 axons share one main orientation in MEC (*9,24,25*).

MEC function and grid cell activity (*26,27*) depends on medial septum inputs (28,29) and cholinergic transmission (30). We observed a patchy pattern of acetylcholinesterase labeling at the layer 1/2 border (Fig. 3H), which colocalized with the cores of calbindin$^+$ patches (Fig. 3H-J). Axonal terminals positive for the vesicular acetylcholine transporter (VAChT) were closely apposed to calbindin$^+$ cells and their density was twofold larger in calbindin$^+$ patches than between patches (Fig. S4). We also stained for m1 muscarinic receptors and observed a diffuse labeling without colocalization of these receptors to VAChT puncta. Moreover we analyzed the apposition and distribution of presynaptic VAChT puncta relative to dendrites of *in-vivo* filled calbindin$^+$ and calbindin$^-$ layer 2 cells by confocal microscopy. VAChT puncta were much more abundant around calbindin$^+$ than calbindin$^-$ layer 2 cells, but proximity histograms of VAChT puncta and dendrites did not indicate a direct targeting of calbindin$^+$ cell dendrites by cholinergic synapses (Fig. S4). Both the m1 receptor labeling and our dendrite- VAChT puncta colocalization analysis are in line with a volumetric action of acetylcholine in MEC (31-33).

Finally, we assessed in freely moving animals how activity of identified neurons related to the entorhinal theta-rhythm. We recorded 31 layer 2 neurons in rats trained to explore open fields, and classified them by morphology and immunoreactivity. Calbindin$^+$ neurons (n = 12) were pyramidal cells, while calbindin$^-$ neurons (n = 19) had stellate morphologies. Firing rates were not different (calbindin$^+$ = 2.1 ± 1.1 Hz; calbindin$^-$ = 2.3 ± 1.5 Hz; $p > 0.5$, Mann-Whitney test).

We found, however, that calbindin$^+$ neurons (Fig. 4A-C) showed stronger theta-rhythmicity of spiking than calbindin$^-$ cells (Fig. 4D-G; $p < 0.01$, Mann-Whitney test). Theta-rhythmicity was associated with locomotion of the animal (Fig. S5). A similar twofold difference in theta-rhythmicity between calbindin$^+$ (n=14) and calbindin$^-$ (n=20) cells was observed under urethane-ketamine anesthesia (Fig. 4H; $p = 0.0003$, Mann-Whitney test), which preserves cortico-hippocampal theta-rhythmicity (*3,34*). Pharmacological blockade of cholinergic transmission suppressed theta-rhythmicity in both calbindin$^+$ and calbindin$^-$ cells (Fig. 4I). Specifically we observed that cholinergic blockade led to a loss of the distinct peak at theta frequency in the power spectra of spike discharges (Fig. S6). Cells also differed in their phase-locking to entorhinal field potential theta: calbindin$^+$ cells were more strongly phase-locked (average Rayleigh vector length = 0.54 vs 0.22 in calbindin$^-$ cells; $p < 0.0012$, Mann-Whitney test) and fired near the trough of the theta-oscillation, whereas locking was weaker and more variable in calbindin$^-$ cells (Fig. 4J).

What is the cellular basis of theta-rhythmicity in MEC layer 2? Stellate cells have been prime candidates for theta discharges in layer 2 (*6,7*), because intrinsic conductances make them resonate at theta frequency (*35,36*). We found, however, that calbindin$^+$ pyramidal cells showed twofold stronger theta-rhythmicity and theta phase-locking than calbindin$^-$ stellate neurons. The stronger theta-rhythmicity of calbindin$^+$ pyramidal neurons, which have weaker sag-currents (*7,20*), is opposite from what had been predicted based on intrinsic properties (*8,37*). Hence, layer 2 theta-modulation is cell type specific, but not distributed as expected from cell-intrinsic resonance properties. This finding agrees with other evidence that questioned the causal relationship between intrinsic properties and theta-rhythmicity *in vivo* (*10,37,38*). The membrane properties of calbindin$^+$ neurons are not tuned to the generation of theta rhythmicity (*20*). Their strongly rhythmic discharges suggest calbindin$^+$ neurons might correspond to a subset of cells with strong membrane potential theta-oscillations (*11*), which – in the absence of cell-intrinsic mechanisms – probably arise from synaptic interactions. Cholinergic innervation and effects of cholinergic blockade suggest cholinergic drive sustains theta-rhythmicity of calbindin$^+$ cells.

We were not yet able to assess spatial modulation in a sufficient number of identified neurons to directly relate our results to grid cell function. The limited available evidence suggests grid cells are recruited from a heterogeneous neuronal population in layer 2 (*10,11,39*) possibly indicating weak structure-function relationships (*40*). Yet, we observed similarities between calbindin$^+$ neurons and grid cells: calbindin$^+$ patches receive cholinergic inputs, which are required for grid cell activity according to preliminary data (*30*); calbindin$^+$ cells have strong theta-rhythmicity, a feature which correlates with grid cell discharge (*2*); like grid cells, calbindin$^+$ cells are clustered.

We have hypothesized calbindin$^+$ neurons form a ‘grid-cell-grid’ (*41*), i.e. that their hexagonal arrangement might be an isomorphism to hexagonal grid cell activity, much like isomorphic cortical representations of body parts in tactile specialists (*42, 43*). We note, however, that hexagonality often results from spacing constraints and hence might be unrelated to grid cell activity. Determining the spatial modulation patterns of identified entorhinal neurons will help clarifying if and how the calbindin$^+$ grid is related to grid cell activity.

References and Notes

1. M. Mizuseki, A. Sirota, E. Pastalkova, G. Buzsáki, *Neuron* **64,** 267 (2009).
2. C.N. Boccara *et al., Nat. Neurosci.* **13,** 987 (2010).
3. P. Quilichini, A. Sirota, G. Buzsáki, *J. Neurosci.* **30,** 11128 (2010).
4. T. Hafting, M. Fyhn, S. Molden, M-B. Moser, E.I. Moser, *Nature* **436,** 801 (2005).
5. T. Hafting, M. Fyhn, T. Bonnevie, M-B. Moser, E.I. Moser, *Nature* **453,** 1248 (2008).
6. A. Alonso, R.R Llinás, *Nature* **342,** 175 (1989).
7. A. Alonso, R. Klink, *J. Neurophysiol.* **70,** 128 (1993).
8. M.E. Hasselmo, L.M. Giocomo, E.A. Zilli, *Hippocampus* **17,** 1252 (2007).
9. A. Burgalossi, *et al., Neuron* **70,** 773 (2011).
10. C. Schmidt-Hieber, M. Häusser, *Nat. Neurosci.* **16,** 325 (2013).
11. C. Domnisoru, A.A. Kinkhabwala, D.W. Tank, *Nature* **495,** 199 (2013).
12. F. Sargolini, et al., *Science* **312,** 758 (2006).
13. T. Solstad, C.N. Boccara, E. Kropff, M-B. Moser, E.I. Moser, *Science* **322,** 1865 (2008).
14. J. Krupic, N. Burgess, J. O'Keefe, *Science* **337,** 853 (2012).
15. H. Stensola *et al., Nature* **492,** 72 (2012).
16. P. Germroth, W.K. Schwerdtfeger, E.H. Buhl, *Neuroscience* **30,** 683 (1989).
17. K. Lingenhöhl, D.M Finch, *Exp Brain Res* **84,** 57 (1991).
18. R. Klink, A. Alonso, *J. Neurophysiol.* **77,** 1813 (1997).
19. C.B. Canto, M.P. Witter, *Hippocampus* **22,** 1277 (2012).
20. C. Varga, S.Y. Lee, I. Soltesz, *Nat. Neurosci.* **13,** 822 (2010).
21. Y. Fujimaru, T. Kosaka, *Neurosci. Res.* **24,** 329 (1996).
22. C. Barry, L.L. Ginzberg, J. O'Keefe, N. Burgess, *Proc. Natl. Acad. Sci. U.S.A.* **109,** 17687 (2012).
23. N. Tamamaki, Y. Nojyo, Y. *Hippocampus* **3,** 471 (1993).
24. T.W. Blackstad, *J. Comp. Neurol.* **105,** 417 (1956).
25. M.P. Witter, *Prog. Neurobiol.* **33,** 161 (1989).
26. C. Barry, J.G. Heys, M.E. Hasselmo, *Front Neural Circuits* **6,** 5 (2012).
27. J.G. Heys, N.W. Schultheiss, C.F. Shay, Y. Tsuno, M.E. Hasselmo, *Front Behav Neurosci* **6,** 32 (2012).
28. J. Koenig, A.N. Linder, J.K. Leutgeb, S. Leutgeb, *Science* **332,** 592 (2011).
29. M.P. Brandon *et al., Science* **332,** 595 (2011).
30. E.L. Newman, M.E. Hasselmo, Society for Neuroscience Meeting Abstract (2011).
31. M.E. Hasselmo, J. McGaughy, *Prog Brain Res.* **145**, 207 (2004).
32. L.F. Agnati *et al., Acta Physiol (Oxf)* **187**, 329 (2006).
33. L.M. Teles-Grilo Ruivo, J.R. Mellor, *Front Synaptic Neurosci.* **5**, 2 (2013).
34. T. Klausberger *et al., Nature* **421,** 844 (2003).
35. D.L.F. Garden, P.D. Dodson, C. O'Donnell, M.D. White, M.F. Nolan, *Neuron* **60,** 875 (2008).
36. L.M. Giocomo, M.E. Hasselmo, *J. Neurosci.* **28,** 9414 (2008).
37. F.R. Fernandez, J.A. White, *J. Neurosci.* **28,** 3790 (2008).
38. L.M. Giocomo et al., *Cell* **147**:1159 (2011)
39. S.J. Zhang *et al.*, *Science* **340,** 123 (2013).
40. D.C. Rowland, M.-B. Moser *Curr. Opin. Neurobiol.* **24**,22 (2014).
41. M. Brecht *et al. Phil. Trans. Royal Soc* in press (2013).
42. T.A. Woolsey, H. Van der Loos, *Brain Res.* **17,** 205 (1970).
43. K.C. Catania, R.G. Northcutt, J.H. Kaas, P.D. Beck, *Nature* **364,** 493 (1993).

44. This work was supported by Humboldt Universität zu Berlin, BCCN Berlin (German Federal Ministry of Education and Research BMBF, Förderkennzeichen 01GQ1001A), NeuroCure, the Neuro-Behavior ERC grant and the Gottfried Wilhelm Leibniz Prize of the DFG. We thank Christian Ebbesen, Moritz von Heimendahl, Rajnish Rao, Juliane Steger, John Tukker, Undine Schneeweiß, Paul Turko and Imre Vida.

Figures

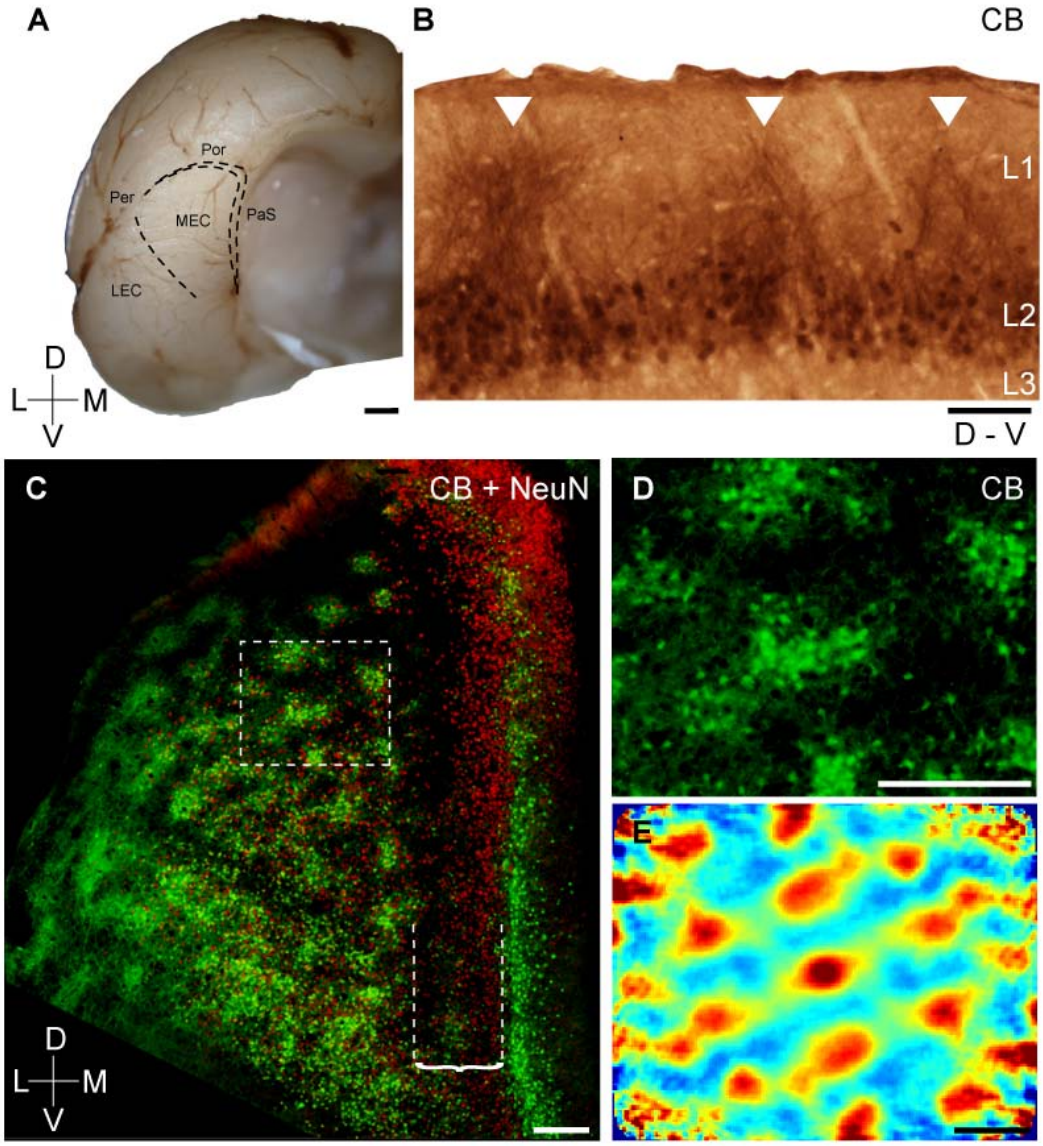

Figure 1: Grid-like arrangement of calbindin-positive pyramidal cells in the medial entorhinal cortex

A, Posterior view of a rat cortical hemisphere. Medial entorhinal cortex (MEC), lateral entorhinal cortex (LEC), parasubiculum (PaS), perirhinal cortex (Per), postrhinal cortex (Por).

B, Calbindin-immunoreactivity (brown precipitate) in a parasaggital section reveals patches with apical dendrites of calbindin$^+$ pyramidal cells forming tents (white arrows) in layer 1.

C, Tangential section showing all neurons (red, NeuN-antibody) and patches of calbindin$^+$ neurons (green). Bracket, dashed lines indicate the patch-free stripe of MEC.

D, Inset from **C**.

E, Two-dimensional spatial autocorrelation of **D** revealing a hexagonal spatial organization of calbindin$^+$ patches. Color scale: -0.5 (blue) through 0 (green) to 0.5 (red), grid score is 1.18.

Scale bars: **A** = 1 mm; **B** = 100 μm; **C**,**D**,**E** = 250 μm. D = dorsal, L = lateral, M = medial, V = ventral.

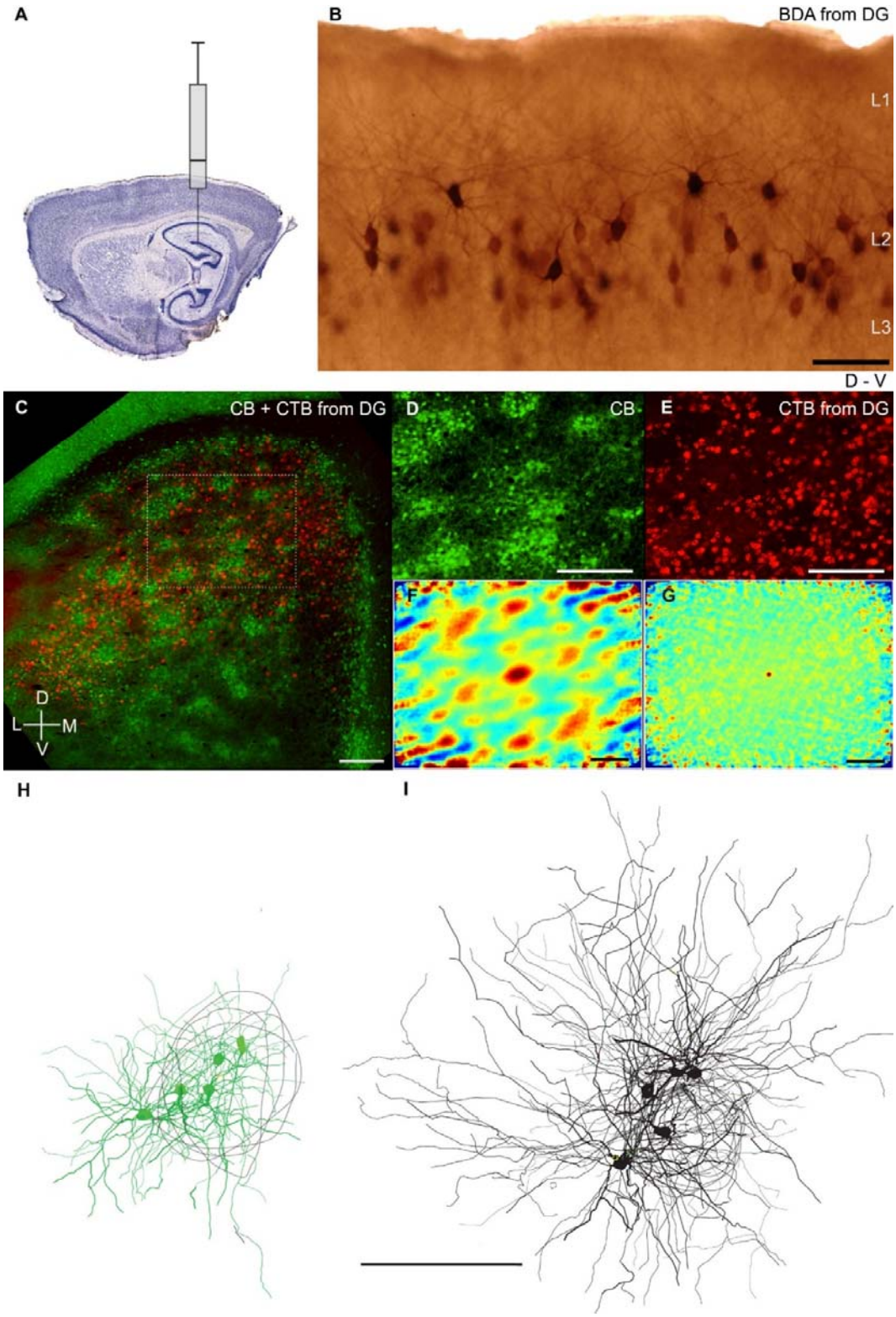

Figure 2: Calbindin positive pyramidal but not dentate-projecting stellate neurons form patches

A, Schematic of retrograde labeling from dentate gyrus.

B, Such retrograde labeling (BDA, brown) stains neurons (most with stellate morphologies) in a parasaggital MEC section.

C, Tangential MEC section showing calbindin^{+} neurons (green) and retrogradely-labeled neurons (red) following dentate-gyrus-cholera-toxin-B injection.

D,**E** insets from **C**.

F, Two-dimensional spatial autocorrelation of **D** reveals regular organization of calbindin^{+} patches; grid score is 0.32. The strongest Fourier component of the sample exceeded that of the 99th percentile of shuffled data confirming hexagonality.

G, Two-dimensional spatial autocorrelation of **E** reveals no spatial organization, grid score is -0.03.

H,**I,** Superimposed reconstructions of dendritic morphologies of 5 calbindin^{+} pyramidal (green) and 5 calbindin^{-} stellate neurons (black) in the tangential plane. Morphologies were 'patch-centered' aligned according to orientation and the center of the nearest calbindin^{+} patch (grey outlines).

Scale bars: **B** = 100 μm; **C,D,E,G,H,I** = 250 μm; D = dorsal, L = lateral, M = medial, V = ventral.

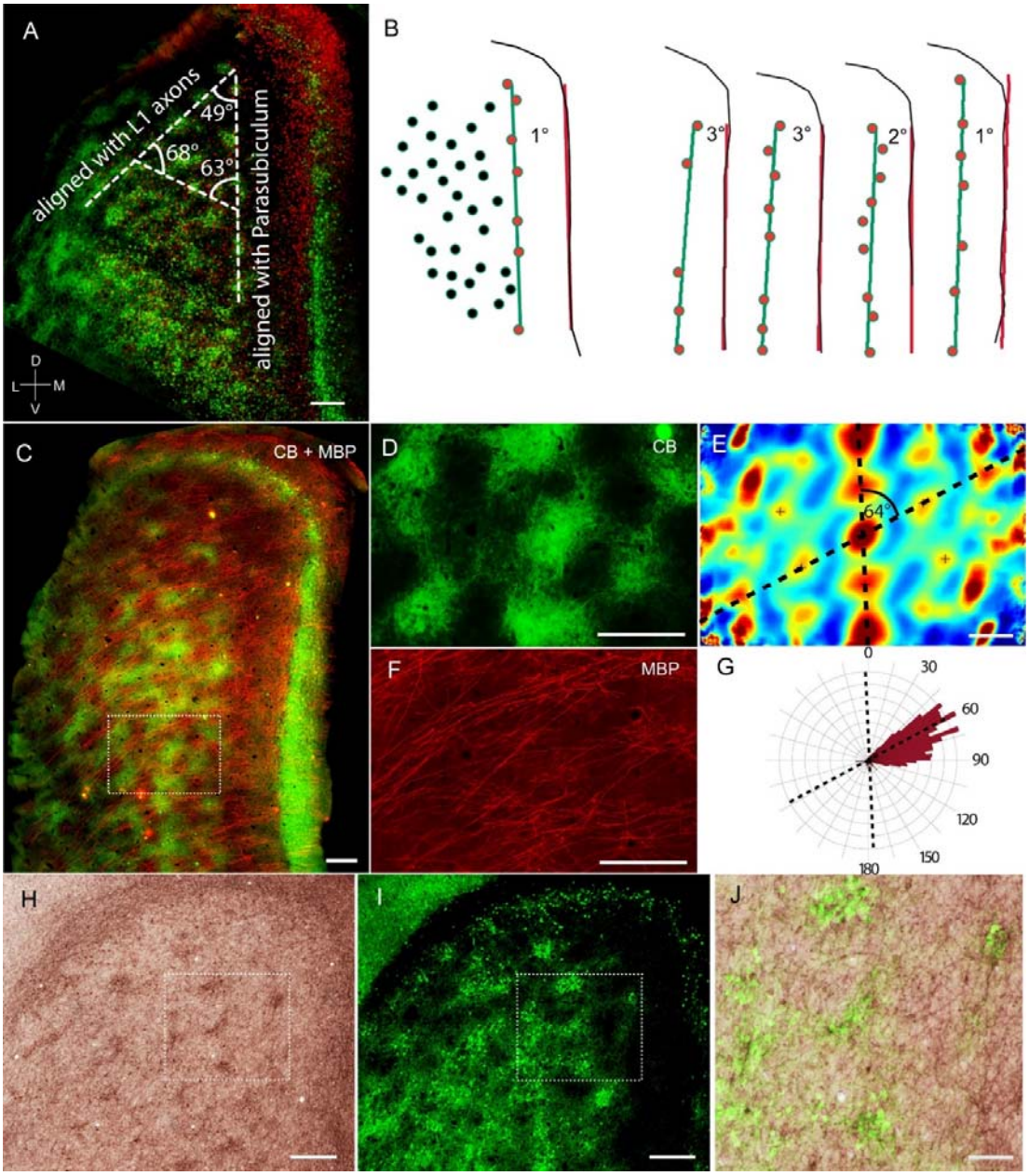

Figure 3: Alignment of the calbindin grid to parasubiculum, layer 1 axons and cholinergic markers

A, Section from Fig. 1C. Dashed white lines indicate axes of the calbindin^{+} grid (angles are indicated). Axes aligned with parasubiculum (**B**) and layer 1 axons (**C-G)**.

B, Left, schematic of calbindin patches and parasubiculum from **A**. The orange line fits the dorsoventral axis of the parasubiculum, the green line fits the most medial column of patches (red), the angle between these lines is indicated. Right, fitted lines and their relative angles for four other brains.

C, Tangential section processed for calbindin (green) and myelin basic protein (red).

D, Inset from **C**.

E, Two-dimensional spatial autocorrelation of **D**. Dashed black lines indicate grid axes.

F, inset from **C**.

G, Axonal segments in **F** were manually traced from left to right and we computed a polar plot (red) of the orientations of the axonal segments. The orientations of axonal segments aligned with one axis of the grid of calbindin patches (superimposed dashed lines from **E)**.

H, Tangential section stained for acetylcholinesterase activity.

I, Section from **H** co-stained for calbindin.

J, Overlay of **H**,**I** shows overlap between acetylcholinesterase and calbindin staining.

Scale bars: **A**,**C**,**D**,**E**,**F,H,I** = 250 μm; **J** = 100 μm. D = dorsal, L = lateral, M = medial, V = ventral.

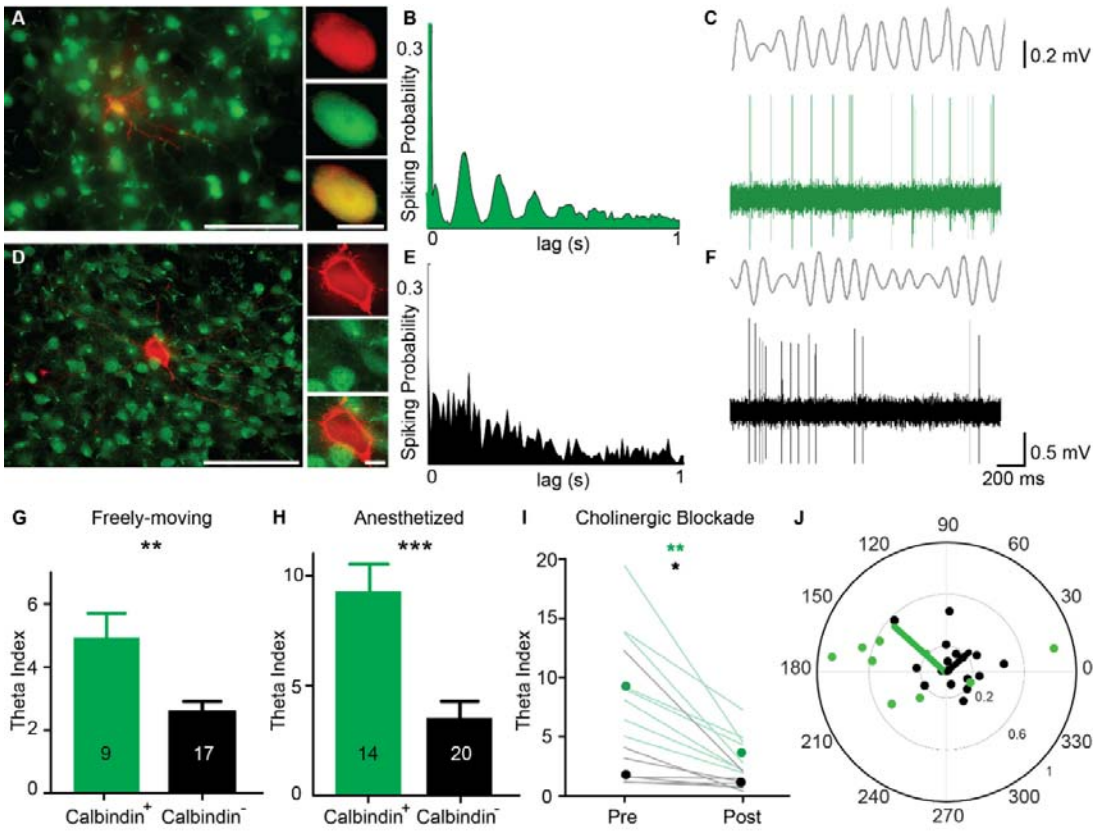

Figure 4: Theta-modulation of calbindin positive and calbindin negative cells

A, Left, micrograph (tangential section) of a calbindin$^+$ neuron recorded in a freely moving animal. Green, calbindin; red, neurobiotin. Right, soma in red, green channel and overlay.

B, Autocorrelogram of spike discharges for the calbindin$^+$ neuron shown in **A**.

C, Filtered (4-12 Hz) local field potential (top) and spiking pattern (bottom) of the neuron shown in **A**.

D-**F**, Same as **A**-**C** but for a calbindin$^-$ neuron.

G, Strength of theta-rhythmicity in calbindin$^+$ and calbindin$^-$ neurons in freely moving animals. Numbers = n of neurons. Error bars = SEM.

H, Same as **G** but for recordings under urethane-ketamine anesthesia (*34*).

I, Theta-rhythmicity in calbindin$^+$ neurons (green, n=8) and calbindin$^-$ neurons (black, n=7) under anesthesia before and after systemic cholinergic blockade with scopolamine (Wilcoxon signed rank test, P = 0.0078 for calbindin$^+$, P = 0.0156 for calbindin$^-$ cells). Dots indicate medians.

J, Polar plot of preferred theta-phase (theta-peak = 0°) and modulation strength (Rayleigh vector, 0-1, proportional to eccentricity) for calbindin$^+$ (green) and calbindin$^-$ (black), dots = single cells, lines = averages.

Scale bars: **A**,**D**, = 100 µm (left), 10 µm (right).

Supporting Online Material

1. Supplementary Figures

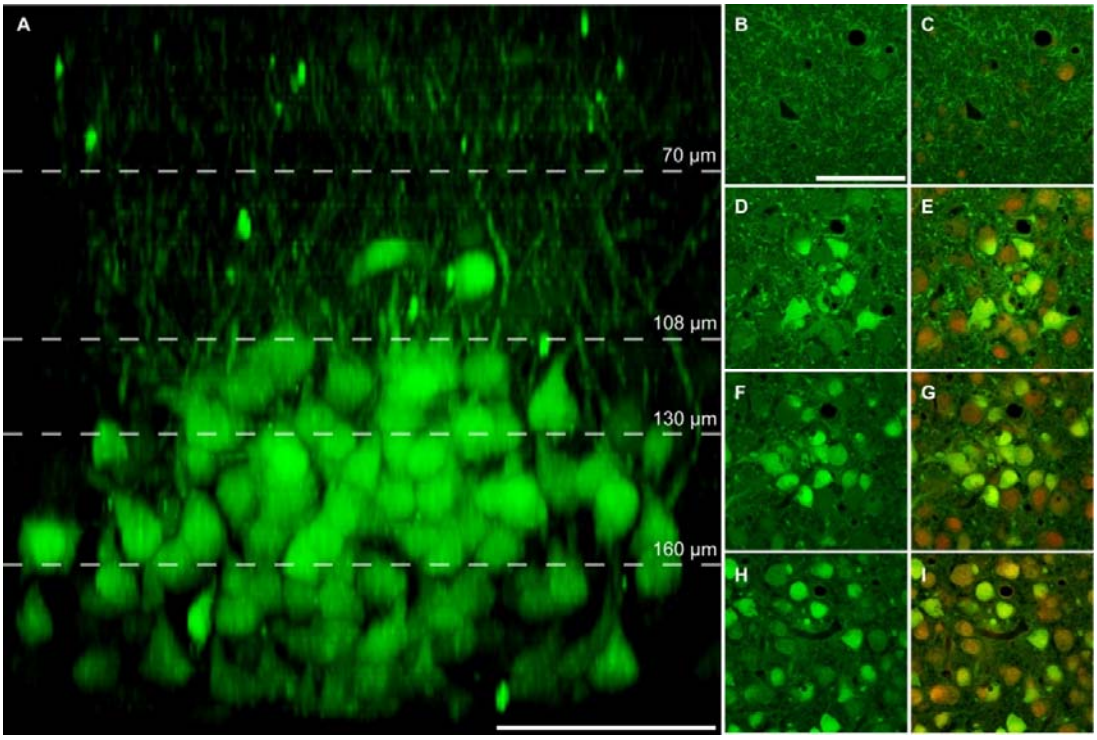

Figure S1: Cellular architecture of an individual calbindin patch

A, Side view of an optically-cleared patch of calbindin$^+$ cells. Serial optical sections spaced 2 µm apart were taken along the x-z-axis and displayed as maximum intensity projection.

B-I, Optical sections at the levels indicated in **A**, showing calbindin$^+$ cells in green (**B**, **D**, **F**, **H)** and an overlay of calbindin$^+$ cells in green and red autofluorescence showing all neurons (**C**, **E**, **G**, **I)**. Dashed lines in **A** indicate the level of the optical sections displayed in (**B-I**): 70 µm below surface (**B**, **C**), 108 µm below surface **D**, **E**, 130 µm below surface (**F**, **G**) and 160 µm below surface (**H**, **I**). Note the increase in patch diameter from the upper to middle levels. At the lower level there is no apparent modular structure of calbindin$^+$ cells.

Scale bars: **A** = 50 µm; **B** = 50 µm, applies to **B-I**.

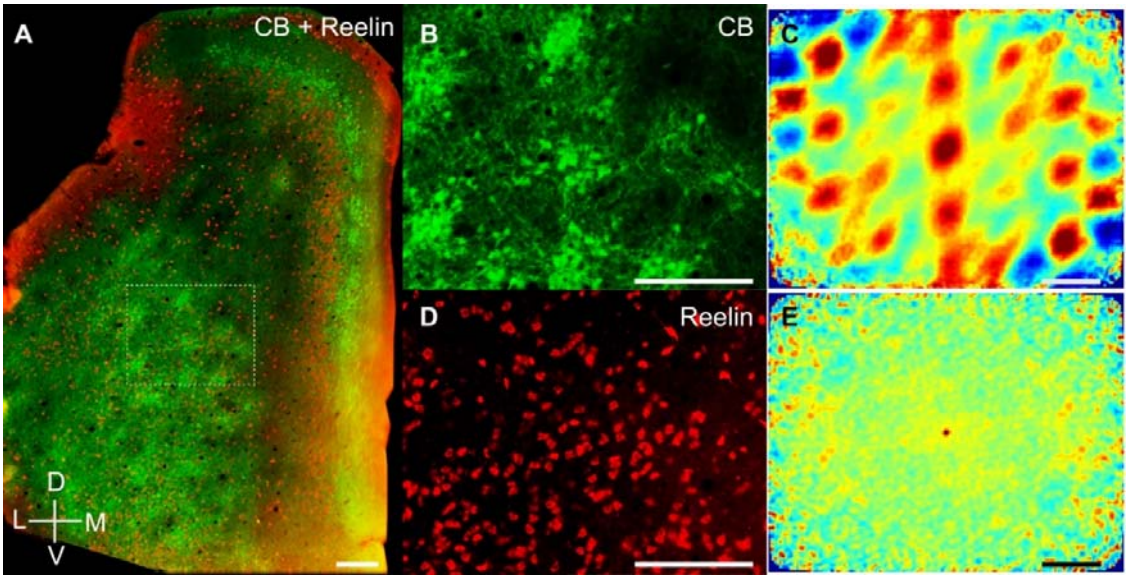

Figure S2: Calbindin-positive pyramidal neurons but not reelin-positive cells form patches

A, Tangential section of the rat MEC showing calbindin$^+$ pyramidal neurons and neuropil (green) and reelin$^+$, putative stellate, neurons (red). Calbindin$^+$ and reelin$^+$ neurons form two non-overlapping populations (2 double-labeled neurons in 168 calbindin$^+$ and 405 reelin$^+$ layer 2 neurons) (*20*).

B, Inset from **A** showing a high magnification of calbindin$^+$ patches.

C, Two-dimensional spatial autocorrelation of **B** illustrating regular spatial organization of calbindin$^+$ patches. The grid score is 0.49. The strongest Fourier component of the sample exceeded that of the 99th percentile of shuffled data, confirming hexagonality.

D, Corresponding image section from **B** showing reelin$^+$ neurons.

E, Spatial autocorrelation of **D** illustrating a lack of spatial organization of reelin$^+$ neurons. The grid score is -0.04.

Scale bars: **A-E** = 250 μm. D = dorsal, L = lateral, M = medial, V = ventral.

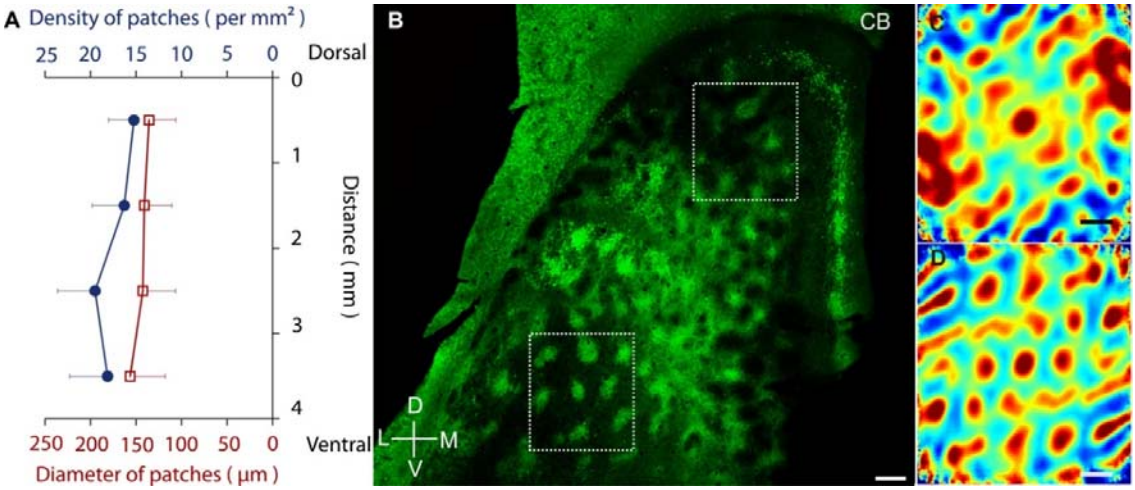

Figure S3: Layout of calbindin patches across the extent of medial entorhinal cortex

A, Measurements of mean patch diameter (red) and density (blue) across the dorsoventral extent of the MEC. Measurements refer to ten MEC whole-mounts and did not include the medial patch-free stripe of MEC (see Fig 1C). Error bars = SD.

B, Tangential section from a flattened cortical preparation processed for calbindin immunoreactivity (green) showing modularity throughout the MEC. The image was flipped around the vertical axis for comparability.

C, Two-dimensional spatial autocorrelation of the dorsal inset in **A**. The grid score is 0.32. The strongest Fourier component of samples **C**, **D** exceeded that of the 99th percentile of shuffled data confirming hexagonality.

D, Two-dimensional spatial autocorrelation of the ventral inset in **A**. The grid score is 0.79.

Scale bars: **B-D** = 250 µm. D = dorsal, L = lateral, M = medial, V = ventral.

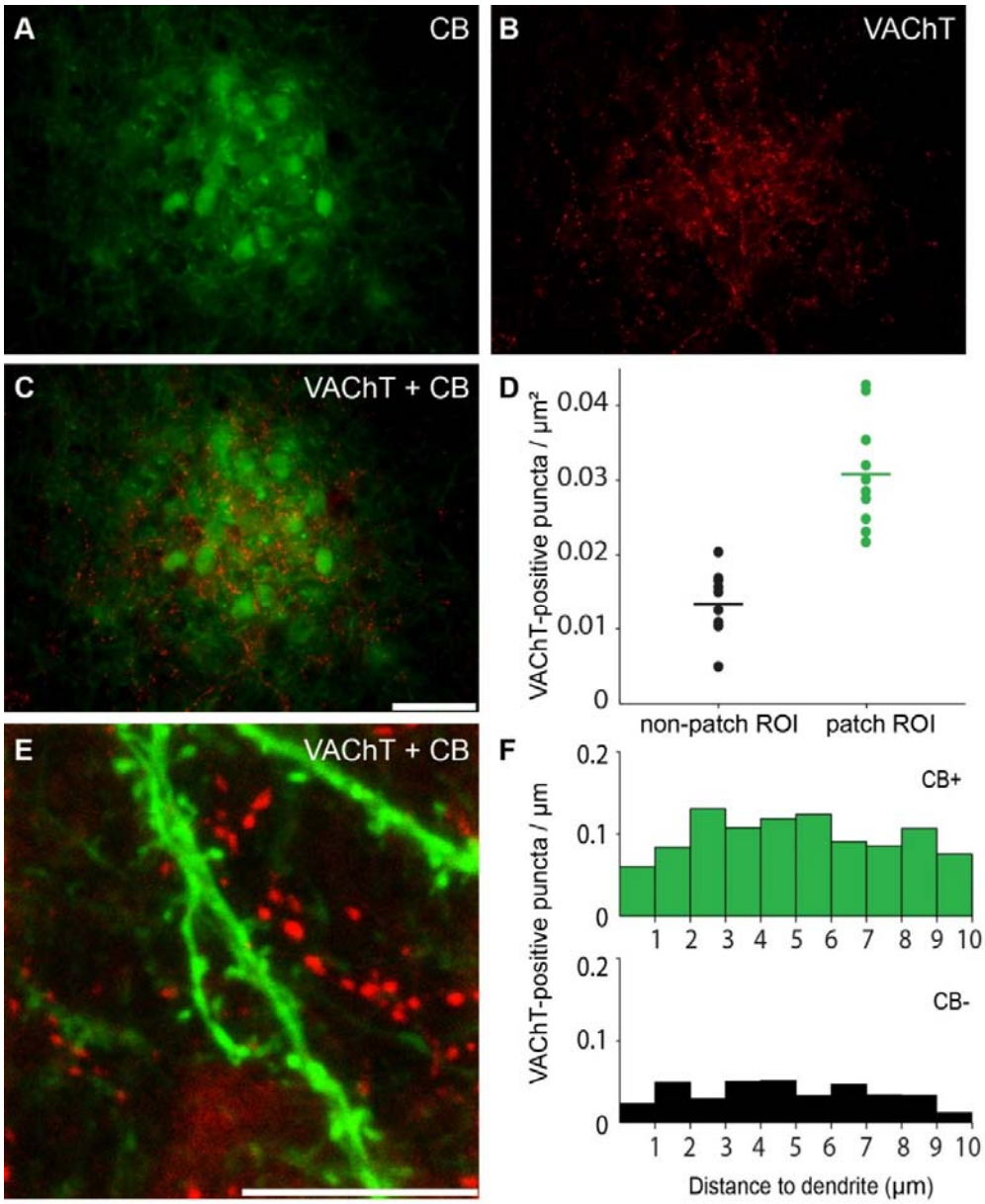

Figure S4: Vesicular acetylcholine transporter, calbindin patches and proximity of cholinergic boutons to calbindin-positive dendrites

A, Fluorescence micrograph showing one calbindin patch from a tangential section stained for calbindin (green).

B, Same section as in A stained for VAChT immunoreactivity (red). Note the higher density of VAChT-positive puncta in the calbindin-patch than in the surrounding area.

C, Overlay of **A** and **B**.

D, Density of VAChT-positive puncta in calbindin patches (green dots) and non-patch areas (black dots) at the layer 1/2 border. In five rats we selected 10 regions of interest (ROI) centered

on calbindin patches and 10 ROIs positioned equidistant between calbindin patch centers. Horizontal bars indicate mean values. All VAChT positive puncta in the ROI were counted and divided by area size to obtain puncta density.

E, Fluorescence micrograph showing an overlay of a calbindin^{+} dendrite (green) and nearby VAChT-positive puncta (red).

F, Histogram of the closest distance of VAChT-positive puncta to dendrites of calbindin^{+} (top) and calbindin^{-} (bottom) cells. We selected 35 dendritic segments of calbindin^{+} and 25 segments of calbindin^{-} dendrites and measured the distance of VAChT-positive puncta and dendrites. The histograms were normalized by dendritic length to obtain the number of VAChT-positive puncta per μm. Data refer to 10 (5 each) juxtacellularly stained calbindin^{+} and calbindin^{-} neurons.

Scale bars: **A**, **B**, **C** = 50 μm**; E** = 10 μm.

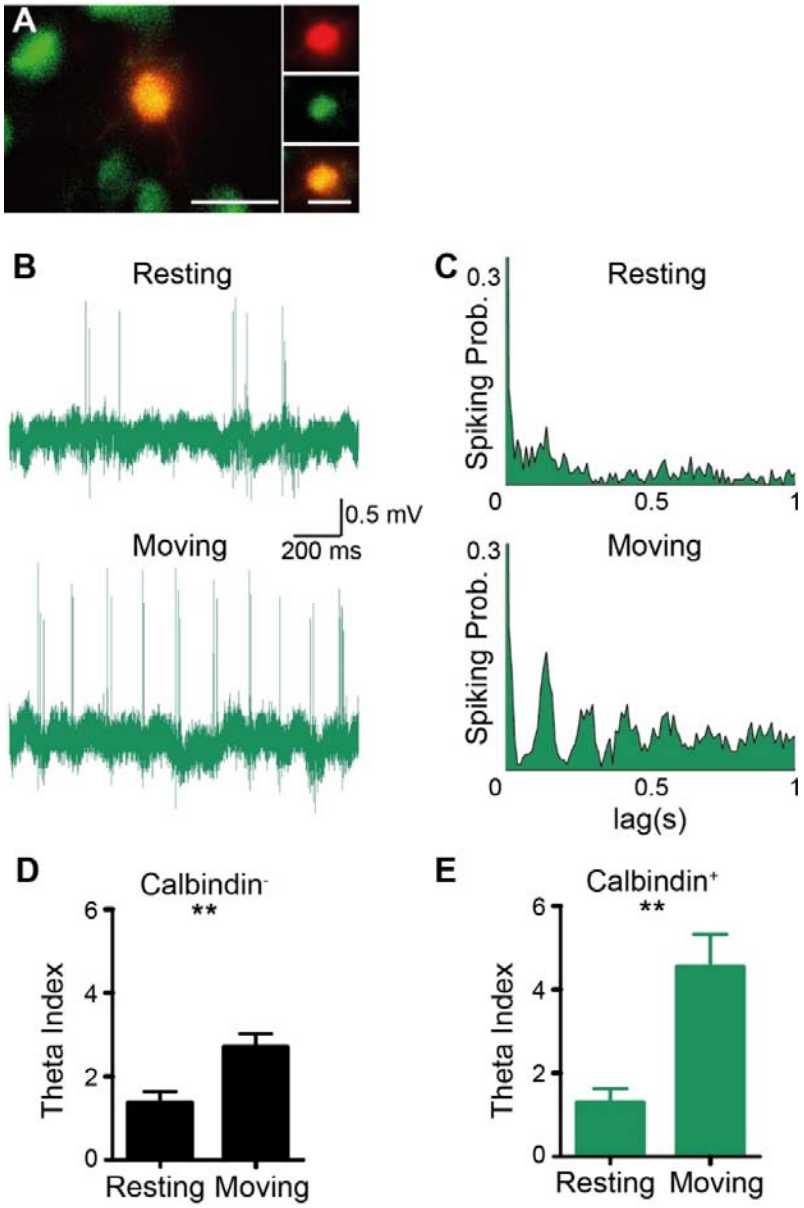

Figure S5: Movement dependency of theta-rhythmicity in calbindin-positive neurons

A, Fluorescence micrograph of a representative calbindin$^+$ layer 2 neuron recorded from a freely moving rat. Green: calbindin$^-$, red: Neurobiotin. Scale bars: 100 □m (left) and 10 □m (right).

B, Representative raw juxtacellular traces from the calbindin$^+$ neuron shown in **A** under resting (top) and moving state (bottom; speed cutoff = 2 cm/s). Note the prominent theta-rhythmicity of spiking activity during movement.

C, Spike autocorrelograms of the calbindin$^+$ neuron shown in **A** under resting (top) and moving state (bottom).

D,**E** Population average of the strength of theta-rhythmicity (theta index; see Supplementary Methods) under resting and moving state in calbindin$^-$ (**D**) and calbindin$^+$ neurons (**E**). Note

the stronger movement dependency of theta-rhythmicity for calbindin^{+} neurons. P = 0.0034 (left panel, n = 17) and 0.0036 (right panel, n = 9), Mann-Whitney test. Error bars = SEM.

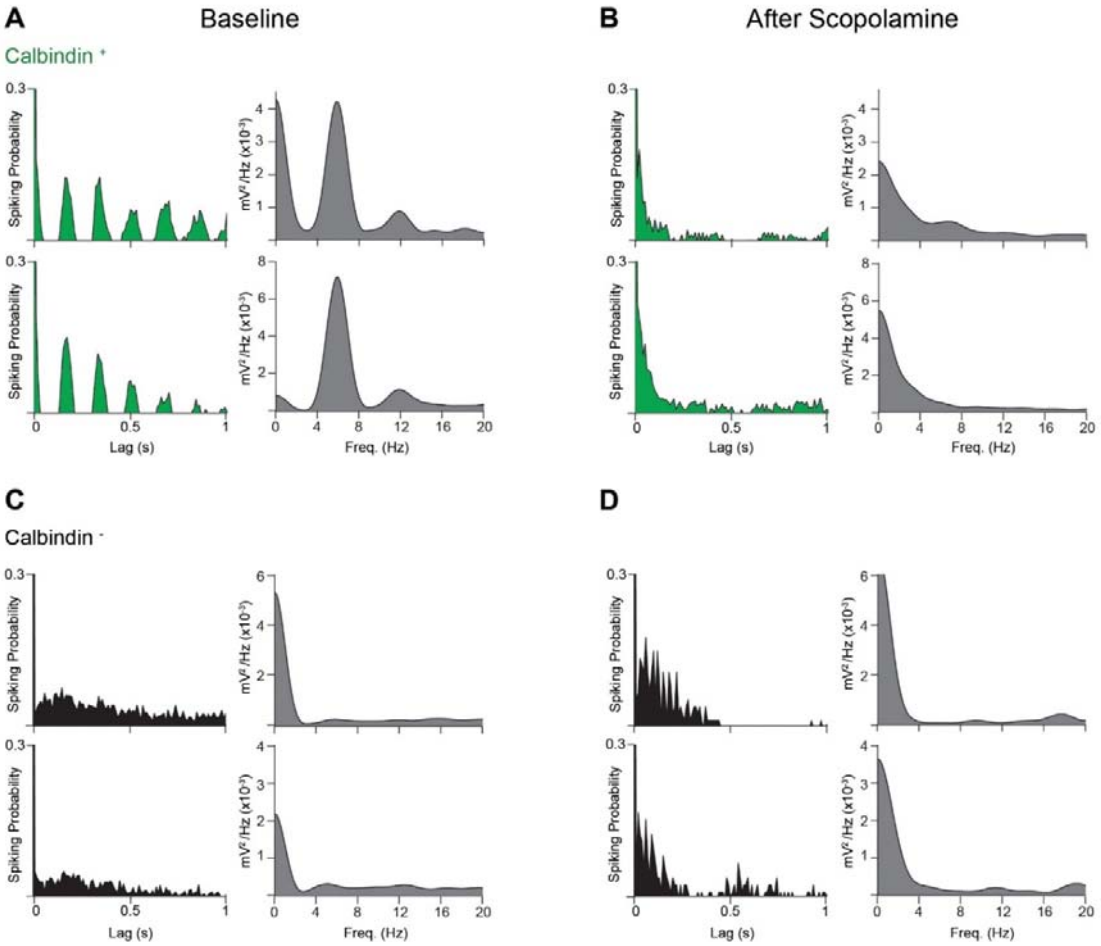

Figure S6: Effects of blockade of cholinergic transmission by scopolamine in individual neurons

Spike autocorrelograms (first and third column) and power spectra of spike discharges (second and fourth column) before (baseline) and after systemic cholinergic blockade with scopolamine.

A, B Two representative calbindin^{+} neurons, **C, D** Two representative calbindin^{-} neurons.

2. Materials and Methods

All experimental procedures were performed according to German guidelines on animal welfare.

Brain tissue preparation

For anatomy experiments, male and female Wistar rats (150-400 g) were anesthetized by isoflurane, and then euthanized by an intraperitoneal injection of 20% urethane. They were then perfused transcardially with 0.9% phosphate buffered saline solution, followed by 4% paraformaldehyde (PFA) in 0.1 M phosphate buffer (PB). After perfusion, brains were removed from the skull and postfixed in PFA overnight. They were then transferred into a 10% sucrose solution in PB and left overnight, and subsequently immersed in 30% sucrose solution for at least 24 hours for cryoprotection. The brains were embedded in Jung Tissue Freezing Medium, and subsequently mounted on the freezing microtome to obtain 20-60 µm thick sagittal sections or tangential sections (parallel to the pial surface). Tangential sections of the medial entorhinal cortex were obtained by separating posterior cortices (including the entorhinal cortex) from the remaining hemisphere by a cut parallel to the surface of the medial entorhinal cortex. The tissue was then frozen and positioned with the pial side to the block face of the microtome.

Histochemistry and immunohistochemistry

Acetylcholinesterase (AChE) activity was visualized according to previously published procedures (*45,46*). After washing brain sections in a solution containing 1 ml of 0.1 M citrate buffer (pH 6.2) and 9 ml 0.9% NaCl saline solution (CS), sections were incubated with CS containing 3 mM $CuSO_4$, 0.5 m$MK_3Fe(CN)_6$, and 1.8 mM acetylthiocholine iodide for 30 min. After rinsing in PB, reaction products were visualized by incubating the sections in PB containing 0.05% 3,3'- Diaminobenzidine (DAB) and 0.03% nickel ammonium sulfate.

Immunohistochemical stainings were performed according to standard procedures. Briefly, brain sections were pre-incubated in a blocking solution containing 0.1 M PBS, 2% Bovine Serum Albumin (BSA) and 0.5% Triton X-100 (PBS-X) for an hour at room temperature (RT). Following this, primary antibodies were diluted in a solution containing PBS-X and 1% BSA. Primary antibodies against the calcium binding proteins Calbindin (1:5000), the extracellular matrix protein Reelin (1:1000), the extrinsic membrane protein Myelin Basic Protein (1:1000), the vesicular acetylcholine transporter (1:1000), and the DNA binding neuron specific protein NeuN (1:1000) were used. Incubations with primary antibodies were allowed to proceed for at least 24 hours under mild shaking at 4°C in free-floating sections. Incubations with primary antibodies were followed by detection with secondary antibodies coupled to different fluorophores (Alexa 488 and 546). Secondary antibodies were diluted (1:500) in PBS-X and the reaction was allowed to proceed for two hours in the dark at RT. For multiple antibody labeling, antibodies raised in different host species were used. After the staining procedure, sections were mounted on gelatin coated glass slides with Mowiol or Vectashield mounting medium.

In a subset of experiments, primary antibodies were visualized by DAB staining. For this purpose, endogenous peroxidases were first blocked by incubating brain tissue sections in methanol containing 0.3% hydrogen peroxide in the dark at RT for 30 min. The subsequent

immunohistochemical procedures were performed as described above, with the exception that detection of primary antibodies was performed by biotinylated secondary antibodies and the ABC detection kit. Immunoreactivity was visualized using DAB staining.

For whole-mount immunohistochemistry (as in Fig. S1) we used a variant of the protocol in (*47,48*). Thick tangential sections (~ 300 μm) containing layer 2 of the MEC were first post-fixed in Dent's fixative overnight at 4°C and then incubated in Dent's bleach overnight at 4°C. They were then dehydrated twice in 100% methanol for 30 min each and then rehydrated for 90 min each in 50% and 15% methanol in PBS at RT. Subsequently, sections were incubated with 10 μg/ml proteinase K for 5 min at RT. Sections were then rinsed three times for ten minutes in PBS at RT and subsequently incubated in PBS-X containing 2% BSA overnight. Primary antibodies were diluted in PBS-X containing 5% DMSO, 1% BSA and incubated for 96 hours at 4°C. After this incubation, whole-mounts were washed in PBS-X three times for 2–3 h each and then incubated overnight in secondary antibodies diluted in PBS-X and 5% DMSO at 4°C. Sections were then washed three times in PBS-X for 2–3 h each and incubated in PBS-X overnight to ensure efficient removal of unbound antibodies. The sections were dehydrated in series of 50%, 80%, and 100% methanol in PBS at RT for 90 min each. Finally, the sections were transferred for at least 2 days into a clearing solution consisting of two parts of benzyl benzoate and one part of benzyl alcohol at RT, until they became transparent.

For histological analysis of juxtacellularly-labeled neurons, neurobiotin was visualized with streptavidin conjugated to Alexa 546 (1:1000). Subsequently, immunohistochemistry for Calbindin was performed as described above and visualized with Alexa Fluor 488. After fluorescence images were acquired, the neurobiotin staining was converted into a dark DAB reaction product, performed as previously described (*34*). This has advantages of being more sensitive than most fluorescent dyes, is permanent and not sensitive to photobleaching (*49*). In general we found similar results for calbindin immunohistochemistry as previous authors (*20,50*), who showed that the large majority (~90% in *50*) of calbindin$^+$ cells are glutamatergic neurons.

Retrograde Neuronal Labeling

Retrograde tracer solutions containing either Biotynilated-Dextrane Amine (BDA) (10% w/v; 3.000 MW) or Cholera Toxin Subunit B, Alexa Fluor 488 Conjugate (CTB) (0.8 % in PB) were injected in juvenile rats (~150 gr) under ketamine/xylazine anesthesia. Briefly, a small craniotomy was opened above the dentate gyrus at intermediate positions along the septo-temporal axis. Animals were placed in a stereotaxic apparatus, and prior to injection, the granule cell layer was localized by electrophysiological recordings, based on characteristic signatures of the local field potential and neuronal spiking activity. Glass electrodes with a tip diameter of 10-20 μm, filled with CTB or BDA solution, were then lowered unilaterally into the target region. Tracers were either pressure-injected (CTB; 10 injections using positive pressure of 20 p.s.i., 10-15 s injection duration) or iontophoretically-injected (BDA; 7s on/off current pulses of 1-5 mA for 15 min). After the injections, the pipettes were left in place for several minutes and slowly retracted. The craniotomies were closed by application of silicone and dental cement. The animals survived for 3-7 days before being transcardially perfused. The results from back-labeling agreed with previous authors (*16,23,51*), who also found that the large majority of retrogradely-labeled neurons from the dentate gyrus had stellate morphologies.

Image acquisition

A microscope equipped with a motorized stage and a z-encoder, was used for bright field microscopy. Images were captured using a MBF CX9000 camera using Neurolucida or StereoInvestigator. Confocal and epifluorescence microscopes with camera were used to image the immunofluorescent sections. Alexa fluorophores were excited using the appropriate filters (Alexa 488 – L5, Alexa 546 – N3, Alexa 633 – Y5). Fluorescent images were acquired in monochrome, and colour maps were applied to the images post acquisition. Whole-mount stainings were imaged using a microscope. Fluorescence images were acquired with a 25x (1.05 NA) water-immersion objective. A femtosecond laser was used to excite fluorophores at 850 nm. Post hoc linear brightness and contrast adjustment were applied uniformly to the image under analysis.

Cell Counts and Patch Sizes

In the analysis for determining cell numbers and patch sizes, patches in consecutive sections were matched by overlaying them in Adobe Photoshop, and only the ones which could be reliably followed in all the sections under consideration were taken up for further analysis. Image stacks were first converted into .tiff files for different channels and focal planes using ImageJ. These files were then merged back together into a single file using the Neurolucida image stack module. In these patches all cells positive for Calbindin and NeuN were counted manually.

Quantification of patch sizes was done with the Neurolucida software by using the mean of maximum and minimum Feret diameter, defined as the maximum and minimum diameter of the patch, respectively. To correct for overestimation of neurons due to double counting in two adjacent sections, we estimated the number of cells in a section assuming uniform cell density and uniform spherical cell shape in the section and applied a correction factor of $s / (s+d)$ where, s is the section thickness and d is the diameter of a cell, to correct for the cells which would be counted again in an adjacent section.

Quantification of axonal orientation and cholinergic boutons

To quantify the orientation of axonal fibers in layer 1, axon segments from myelin-stained sections were traced using Neurolucida software. The polar histogram in Fig. 3G was constructed with angular bins of 3°, and the total length of axons in each angular direction was summed up.

Using Stereoinvestigator software we quantified the density of VAChT-positive puncta in calbindin patch and non-patch areas at the layer 1/2 border in tangential sections from five rats. In total, we selected 10 regions of interest (ROI) centered on calbindin patches and 10 ROIs positioned equidistant between calbindin patch centers. All VAChT positive puncta in the ROI were counted manually and divided by area size to obtain puncta density.

To assess the colocalization of VAChT puncta and calbindin$^+$ and calbindin$^-$ dendrites, we labeled neurons *in vivo* juxtacellularly and identified the cells based on their calbindin immunoreactivity. We calculated the proximity histograms of the closest distance between VAChT puncta and dendrite segments (35 calbindin$^+$ and 25 calbindin$^-$ segments), at 50 µm and 100 µm from the soma (5 calbindin$^+$ and 5 calbindin$^-$ cells from 4 brains). The histograms were normalized by dendritic length to obtain the number of VAChT-positive puncta per µm.

The proximity analysis between VAChT puncta and dendritic segments was done in two ways: 1. We measured the closest distance of VAChT puncta to the dendrite shaft. 2. We measured the distance of the VAChT-positive puncta to the closest spine. Both results give rise to the same conclusion. Here, we show the results of analysis 1 only.

Analysis of Spatial Periodicity

To determine the spatial periodicity of calbindin^{+} patches, we determined spatial autocorrelations and spatial Fourier spectrograms. The spatial autocorrelogram was based on Pearson's product moment correlation coefficient (as in *12*):

$$r(\tau_x, \tau_y) = \frac{\mathrm{n}\sum f(x,y) f(x-\tau_x, y-\tau_y) - \sum f(x,y) \sum f(x-\tau_x, y-\tau_y)}{\sqrt{n\sum f(x,y)^2 - (\sum f(x,y))^2}\sqrt{n\sum f(x-\tau_x, y-\tau_y)^2 - (\sum f(x-\tau_x, y-\tau_y))^2}}$$

where, $r(\tau_x, \tau_y)$ is the autocorrelation between pixels or bins with spatial offset τ_x and τ_y. f is the image without smoothing or the firing rate map after smoothing, n is the number of overlapping pixels or bins. Autocorrelations were not estimated for lags of τ_x and τ_y, where n<20. Grid scores were calculated as previously described (*52*) by taking a circular sample of the autocorrelogram, centered on, but excluding the central peak. The Pearson correlation of this circle with its rotation for 60 degrees and 120 degrees was obtained (on peak rotations) and also for rotations of 30 degrees, 90 degrees and 150 degrees (off peak rotations). Gridness was defined as in (*13*) as the minimum difference between the on-peak rotations and off-peak rotations. To determine the grid scores, gridness was evaluated for multiple circular samples surrounding the center of the autocorrelogram with circle radii increasing in unitary steps from a minimum of 10 pixels more than the width of the radius of the central peak to the shortest edge of the autocorrelogram. The radius of the central peak was defined as the distance from the central peak to its nearest local minima in the spatial autocorrelogram. The grid score was defined as the best score from these successive samples (*13*).

Grid scores reflect both the hexagonality in a spatial field and also the regularity of the hexagon. To disentangle the effect of regularity from this index, and consider only hexagonality, we transformed the elliptically distorted hexagon into a regular hexagon (*22*) and computed the grid scores. A linear affine transformation was applied to the elliptically distorted hexagon, to stretch it along its minor axis, till it lay on a circle, with the diameter equal to the major axis of the elliptical hexagon. The grid scores were computed on this transformed regular hexagon.

The spatial Fourier spectrogram was calculated by implementing a two dimensional discrete Fourier transform and determining its power (*14*):

$$F(x,y) = \frac{1}{\sqrt{MN}} \sum_{n=0}^{N-1} \sum_{m=0}^{M-1} f(m,n) e^{-2\pi i \left(\frac{mx}{M} + \frac{ny}{N}\right)}$$

$$P(x,y) = \sqrt{{F_r}^2(x,y) + {F_i}^2(x,y)}$$

where, *F* is the spatial Fourier transform of *f*, which is a binary image representing the sample with regions of interest (patches) marked as white blocks, with the remaining area as black and zero padded to 2048x2048. M and N are the width and height of the image before zero-padding. Normalization by $\sqrt{MN}$ enables comparison of Fourier power in differently sized samples. P is the power of the Fourier transform with F_r and F_i being the real and imaginary parts of the Fourier transform.

To determine the probability that the patches present in the selected area would be arranged hexagonally, we employed a shuffling procedure and compared the maximum Fourier power of the block pattern representing the original image, to the 99th percentile of the power of a shuffled one with the same blocks (representing the patches) being randomly distributed in the same area without overlapping. This shuffling was performed on all samples on a sample-by-sample basis until the 99th percentile of the maximum power Fourier component converged to a constant.

Electrophysiology methods

Basic procedures for obtaining juxtacellular recordings in freely moving animals were essentially performed as previously described (*9,53*), but with two significant changes in our procedures: (1) different from the approach taken previously, we worked exclusively with animals extensively familiarized with the test arenas and trained to forage for chocolate pellets during the recording (see below); (2) We did not use our previous wake-up protocol, where single neurons were labeled in initially anesthetized animals, which were woken-up by injection of antagonist, and the activity of the neurons subsequently monitored in freely-moving animals. Instead, neurons were analyzed in drug-free animals. These changes were implemented to have the same experimental conditions as in previous studies (i.e. ref *4*). Juxtacellular recordings in freely moving animals were obtained in male Wistar and Long-Evans rats (150-250 g) which were maintained on a 12-h light / 12-h dark schedule and tested in the dark phase. Pipettes (4-6 MΩ) were filled with extracellular (Ringer) solution containing (in mM) NaCl 135, KCl 5.4, HEPES 5, $CaCl_2$ 1.8, and $MgCl_2$ 1 (pH 7.2) as well as neurobiotin (1-2%). Rats were habituated to the behavioral arena and trained for 3-7 days (2-6 sessions per day, of 15-20 min duration each) to collect randomly scattered chocolate crumbs in the behavioral arena (80x80 cm or 1x1m square box with a white cue card on the wall). Training was performed both before and after implantation (see below), or only after implantation (3-5 days). Animals were then implanted according to previously published procedures (*9,53)* with a basic head-implant, which included a metal post for head-fixation and placement of a miniaturized preamplifier, a plastic ring and a protection cap (*53*). For targeting the dorsalmost region of medial entorhinal cortex, a plastic ring was glued on the skull surface 0.2-0.8 mm anterior to the transverse sinus and 4.5-5 mm lateral to the midline. Animals were allowed to recover from the surgery, after which they were habituated to head-fixation for 3-5 days, as

previously described (*54*), and trained to chase chocolate pellets in the open field arena. On the day of recording, the implants were completed under isoflurane anesthesia (1-3%) by implanting an additional metal post, which served to anchor the miniaturized micromanipulator (*55*). Animals were put back in their cages, and allowed to recover from the isoflurane anesthesia. 3-4 hours to 1 day later, rats were then head-fixed and the miniaturized micromanipulator and preamplifier secured to the metal posts. After the recording glass electrode was advanced into the brain, a thick agarose solution (4-5% in Ringer) was applied into the recording chamber for sealing the craniotomy. Animals were then released from the fixation frame and gently transferred to the behavioral arena. To minimize discomfort from the head implant, we sometimes supplied local anesthesia in the neck region. Searching for neurons began when animals were already freely behaving and running in the arena. At the end of the recording, juxtacellular labeling was attempted according to standard procedures (*56*). After labeling, the animal was injected with an overdose of ketamine or urethane and perfused transcardially with 4% paraformaldehyde solution, typically within 10-30 min after labeling.

Juxtacellular recordings in anesthetized animals (Fig. 4H-I) were performed under ketamine/urethane anesthesia, essentially as previously described (*34*). The ketamine/urethane mix is the anesthetic of choice for studying temporal dynamics of spiking activity, and it has long been used to study many aspects of hippocampal and entorhinal physiology (*3,34*). In a subset of recordings (n=15, Fig. 4I), scopolamine was injected systemically (0.4-1 mg/ml, i.p.) (*57*). After a pre-injection baseline recording of ~5 min, scopolamine was injected and the effect on the recorded cell's activity monitored for further 15-20 min.

The juxtacellular signals were amplified by the ELC-03XS amplifier and sampled at 20 kHz by a data-acquisition interface under the control of PatchMaster 2.20 software. The animal's location was automatically tracked at 25 Hz by a videotracking system.

Data analysis

The position of the rat was defined as the midpoint between two head-mounted LEDs. A running speed threshold (2 cm/s) was applied for isolating periods of rest from active movement. Theta-rhythmicity of spiking discharge was determined by first calculating the spike train's autocorrelation determined from the Fast Fourier Transform–based power spectrum of the spike-train autocorrelation functions of the cells, binned at 10 ms. To measure modulation strength in the theta band (4-12 Hz), a theta-index was computed (*2*), defined as the average power within 1 Hz of the maximum of the autocorrelation function in the 4-12 Hz, and divided by the average power in the 3-125 Hz range. Only cells with firing rate > 0.5 Hz were included in the theta analysis (17 out of 19 calbindin$^-$ cells and 9 out of 12 calbindin$^+$ cells) since low firing rates impede detection of firing rhythmicity (58). Statistical significance was assessed by two-tailed Mann-Whitney nonparametric test with 95% confidence intervals.

For spike-theta phase analysis, juxtacellular signals were band-pass filtered at 4-12 Hz, and a Hilbert transform was used to determine the instantaneous theta phase of the filtered theta wave (peaks = 0, 360° and troughs = 180°). Then, each spike was assigned to the theta-phase of the Hilbert transform at the time of that spike. Only spikes during running (speed cutoff = 2 cm/s) were included in the analysis. To estimate the modulation strength, the Rayleigh average vector of spikes' theta phases was calculated for each cell and then averaged across each neuronal subpopulation (calbindin$^-$ and calbindin$^+$ neurons). Spike distributions within the theta cycle were computed for each cell by using bins of 18°.

Methods references.

45. N. Ichinohe *et al., Cereb. Cortex* **18**, 1125 (2008).

46. S. Tsuji, *Folia Histochem. Cytobiol*. **36**, 67 (1998).

47. R.V. Sillitoe, R. Hawkes, *J. Histochem. Cytochem*. **50**, 235 (2002).

48. N. Jährling, K. Becker, E.R. Kramer, H-U. Dodt, *Medical Laser Application*. **23**, 209 (2008).

49. M. Marx, R.H. Günter, W. Hucko, G. Radnikow, D. Feldmeyer, *Nat. Protoc*. **7**, 394 (2012).

50. R.F. Langston *et al., Science* **328**, 1576 (2010).

51. D.A. Peterson *et al., Journal of Neuroscience* **16**, 886 (1996).

52. S.P. Schwartz, P.D. Coleman, *Experimental neurology* **74**, 305 (1981).

53. L. Herfst *et al., J Neurophysiol*. **108**, 697 (2012).

54. A.R. Houweling, G. Doron, B.C. Voigt, L.J. Herfst, M. Brecht, *J. Neurophysiol*. **103**, 1696 (2010).

55. A.K. Lee, I.D. Manns, B. Sakmann, M. Brecht, *Neuron* **51**, 399 (2006).

56. D.A. Pinault, *J. Neurosci. Methods* **65**, 113 (1996).

57. Y. Tsuno, N.W. Schultheiss, M.E. Hasselmo, *J Physiol*. **15**, 2611 (2013).

58. C. Barry, D. Bush, J. O'Keefe, N. Burgess, *Nature* **488**, 103 (2012).

Chapter 3

Pyramidal and stellate cell specificity of grid and border representations in layer 2 of medial entorhinal cortex.

Published as:

Tang, Q. et al. (2014). Pyramidal and stellate cell specificity of grid and border representations in layer 2 of medial entorhinal cortex. *Neuron 84:1191-1197*

doi: 10.1016/j.neuron.2014.11.009

Pyramidal and Stellate Cell-specificity of Grid and Border Representations in Layer 2 of Medial Entorhinal Cortex

Qiusong Tang[1,*], Andrea Burgalossi[1,2,*,‡], Christian Laut Ebbesen[1,3,*], Saikat Ray[1], Robert Naumann[1,4], Helene Schmidt[1], Dominik Spicher[1] & Michael Brecht[1,‡]

[1]Bernstein Center for Computational Neuroscience, Humboldt University of Berlin, Philippstr. 13 Haus 6, 10115 Berlin, Germany

[2] Current Address: Werner Reichardt Centre for Integrative Neuroscience, Otfried-Müller-str. 25, 72076 Tübingen, Germany

[3]Berlin School of Mind and Brain, Humboldt University of Berlin, Unter den Linden 6, 10099 Berlin, Germany

[4]Current Address: Max-Planck-Institute for Brain Research, Max-von-Laue-Str. 4, 60438 Frankfurt am Main, Germany

[*] These authors contribute equally

[‡]To whom correspondence should be addressed: andrea.burgalossi@bccn-berlin.de or michael.brecht@bccn-berlin.de

Submitted to: *Neuron*

Running Title: *Layer 2 Grid and Border Cells*

Keywords: Entorhinal cortex, Calbindin, Grid cell, Border cell, Juxtacellular, Freely-moving

Highlights:

1. Recordings can be putatively assigned to stellates and pyramids by spike-locking to theta
2. Grid cells in entorhinal layer 2 corresponded largely to putative pyramidal cells
3. Border responses in layer 2 corresponded largely to putative stellate cells

Summary

In medial entorhinal cortex, layer 2 principal cells divide into pyramidal neurons (mostly calbindin-positive) and dentate-gyrus-projecting stellate cells (mostly calbindin-negative). We juxtacellularly labeled layer 2 neurons in freely-moving animals, but small sample size prevented establishing unequivocal structure-function-relationships. We show, however, that spike-locking to theta oscillations allows assigning unidentified extracellular recordings to pyramidal and stellate cells with ~83 and ~89% specificity, respectively. In pooled anatomically-identified and theta-locking-assigned recordings, non-spatial discharges dominated and weakly hexagonal spatial discharges and head-direction selectivity were observed in both cell types. Clear grid-discharges were rare and mostly classified as pyramids (19%, 19/99 putative pyramids vs 3%, 3/94 putative stellates). Most border cells were classified as stellate (11%, 10/94 putative stellates vs 1%, 1/99 putative pyramids). Our data suggest weakly theta-locked stellate border cells provide spatial input to dentate-gyrus, whereas strongly theta-locked grid discharges occur mainly in hexagonally-arranged pyramidal cell patches and do not feed into dentate-gyrus.

Introduction

The medial entorhinal cortex is critically involved in spatial navigation and memory. Among other functionally-specialized cell types (Sargolini et al., 2006; Solstad et al., 2008; Savelli et al., 2008), it contains grid cells (Hafting et al., 2005), spatially modulated neurons which show periodic, hexagonally arranged spatial firing fields. Given the striking regularity and invariance of the grid representation, these cells are thought to be part of the brain's coordinate system supporting spatial navigation (see Moser and Moser, 2013 for review).

Pure grid cells are primarily found in layer 2 (Boccara et al., 2010), which differs from other cortical laminae in its unique cell biology. Here the two types of principal cells, stellate and pyramidal neurons have been described (Alonso and Klink, 1993; Germroth et al., 1989). Specifically, stellate and pyramidal neurons differ in conductances and projection patterns (Alonso and Llinás, 1989; Lingenhöhl and Finch, 1991; Klink and Alonso, 1997; Canto and Witter, 2012). Recent work indicates that stellate and pyramidal neurons can be reliably differentiated by calbindin immunoreactivity (Ray et al. 2014; Kitamura et al., 2014) and that these cells also differ in their inhibitory inputs (Varga et al., 2010). Calbindin-positive (calbindin^{+}) cells, which are clustered and arranged in a hexagonal grid (Ray et al., 2014), have been recently shown to project to the CA1 (Kitamura et al., 2014), while calbindin-negative (calbindin^{-}) neurons are homogeneously distributed and project primarily to the dentate-gyrus (Varga et al., 2010; Ray et al., 2014). Few studies have so far explored structure-function relationships in entorhinal circuits (Schmidt-Hieber and Häusser, 2013; Domnisoru et al., 2013; Zhang et al., 2013; see Rowland and Moser, 2014 and Burgalossi and Brecht, 2014 for reviews). Thus, the functional implications of the remarkable cellular diversity of layer 2 have remained largely unresolved.

Resolving how differential spatial firing relates to principal cell types will clarify the cellular mechanisms of grid discharges and spatial input patterns to distinct subfields of the hippocampus. In the present work we aim at resolving layer 2 circuits by taking advantage of improved methodologies for identifying individual neurons recorded in freely moving animals. By cell identification and theta-locking-based classification of unidentified recordings, we provide evidence that grid and border responses are preferentially contributed by pyramidal and stellate cells, respectively.

Results

To explore the cellular basis of grid cell activity in medial entorhinal cortex, we juxtacellularly recorded and labeled neurons in layer 2 (which contains the largest percentage of pure grid cells; Boccara et al., 2010) in awake rats trained to explore 2D environments (Tang et al., 2014). Clear grid cell discharges were rare. The clearest grid-like firing pattern in our sample of 31 identified cells (17 of which met the criteria for spatial analysis; see Methods) was observed in the calbindin$^+$ cell shown in Figure 1A. This neuron had pyramidal morphology, with simple dendritic arborization and a single large apical dendrite targeting a calbindin$^+$ patch (Figure 1B; see also Ray et al., 2014). During exploratory behavior, calbindin$^+$ neurons fired with strong theta-rhythmicity and phase-locked near the trough of the local field potential theta-rhythm (Figure 1C; Ray et al., 2014). Spatial autocorrelation analysis of the firing pattern in the 2D environment revealed a hexagonal periodicity of firing fields (grid score = 1.07; Figure 1D), indicative of grid cell activity (Hafting et al., 2005). Because of its relatively low firing rate (~ 0.5 Hz) this cell was not included in the grid cell sample (see Methods). Most other identified calbindin$^+$ neurons had no clear spatial firing patterns.

The clearest border discharge in our sample of identified cells was observed in the calbindin$^-$ cell shown in Figure 1E. This cell was a stellate neuron, which did not have a single apical dendrite, but instead extended multiple and widely diverging ascending dendrites; this dendritic tree spanned a vast field, which encompassed multiple calbindin$^+$ patches (Figure 1F; see also Ray et al., 2014). On average, spikes from calbindin$^-$ neurons were weakly modulated by the local theta-rhythm (Figure 1G). In 3 out of 11 calbindin$^-$ cells from recordings with sufficient spatial coverage, we observed clear border firing patterns as in Figure 1H. While we did not observe grid cells, non-spatial firing patterns also dominated in calbindin$^-$ neurons.

While the small size of the dataset of identified neurons prevented us from establishing firm structure-function relationships, four preliminary observations can be drawn: (i) grid cells are less abundant in layer 2 than previously assumed (Sargolini et al., 2006; Boccara et al., 2010; but see Mizuseki et al., 2009; Gupta et al., 2012; Bjerknes et al., 2014) and there is no one-to-one relationship between spatial discharge characteristics and cell type; (ii) calbindin$^+$ neurons probably include grid cells; (iii) the absence of grid cells in the 22 identified calbindin$^-$ stellate neurons suggests that grid cells are rare in this cell population; (iv) calbindin$^-$ neurons include border cells.

Currently available evidence points to a correspondence between cytochemical (calbindin$^+$ vs calbindin$^-$) and morphological (pyramidal vs stellate) classification of principal neurons in layer 2 (Varga et al., 2010; Kitamura et al., 2014). To further explore these relationships, we determined the percentage of calbindin$^+$ cells in layer 2 and compared these data with related measurements in the literature (Figure S1A). In agreement with previous studies (Peterson et al., 1996; Kumar and Buckmaster, 2006; Varga et al., 2010), we found that layer 2 neurons consist of about 34% calbindin$^+$ and ~53% calbindin$^-$ (and reelin$^+$) principal cells, and ~13% interneurons (Figure S1B). We note that while Ray et al. 2014 found about 30% of calbindin$^+$ cells, most of which were shown to have pyramidal morphology (see also Varga et al. 2010, Kitamura et al. 2014), Gatome et al. 2010 found a slightly lower fraction of putative pyramidal cells. Calbindin$^+$ and calbindin$^-$ cells showed large quantitative differences in their morphology but without a clear bimodality in individual morphological parameters (Figure S1C,D). Calbindin$^+$ cells had significantly (on average ~2.5 fold) smaller dendritic trees (Figure S1E). Dendritic trees also differed in shape between cell types. Calbindin$^+$ cells had a single long

(always apical) dendrite, which accounted on average for 63% of the total dendritic length (Figure S1E) and which was polarized towards the center of pyramidal cell patches as shown previously (Ray et al., 2014). Calbindin expression matched well but not perfectly with pyramidal cell morphology (Figure S1C,D). Calbindin$^-$ cells featured similar length dendrites with the longest dendrite contributing on average for 33% of the total dendritic length (Figure S1E). These results are in line with published data and indicate that calbindin$^+$ and calbindin$^-$ cells largely correspond to pyramidal and stellate neurons, respectively. However, the lack of clear morphological bimodality in layer 2 (see also Canto and Witter, 2012) implies that the correspondence pyramidal/calbindin$^+$ and stellate/calbindin$^-$ might not be perfect. Interestingly, the spine density in calbindin$^+$ cells decreased as a function of distance from the soma, whereas the reverse was true for calbindin$^-$ cells (Figure S1F). These morphological differences, together with clustering of calbindin$^+$ cells in patches and the polarization of their apical dendrites towards the center of calbindin$^+$ patches (Ray et al., 2014) likely result in a local and overlapping sampling of inputs in neighboring calbindin$^+$ cells, whereas neighboring calbindin$^-$ stellate cells sample large and non-overlapping input territories.

Calbindin$^-$ stellate and calbindin$^+$ pyramidal cells differ strongly in their temporal discharge properties (Figure 1C,G; Ray et al., 2014). We therefore wondered, if temporal discharge properties could be used to classify layer 2 cells as putative pyramidal or stellate neurons. We used a support vector machine to classify neurons based on both the spike-phase and strength of phase-locking to local field potential theta oscillations, which indeed clearly segregated calbindin$^+$ and calbindin$^-$ cells with a large distance to the separating hyperplane (Figure 2A; see Supplemental Information). To further improve the purity of assigned cells, we added a guard zone around the hyperplane separating the Gaussian kernels classifying calbindin$^+$ (light green background) and calbindin$^-$ (grey background) cells (omitting the guard zone and classifying all cells did not qualitatively affect the results; data not shown). We tested our classifier by a bootstrapping approach (Figure S2A,B) and found that a large fraction of calbindin$^+$ and calbindin$^-$ cells could be correctly assigned (Figure S2C). More importantly, the specificity of classification procedure – reflected in the purity of the resulting cell samples – was excellent, i.e. ~89% for putative calbindin$^-$ cells and ~83% for putative calbindin$^+$ cells (Figure S2D), and even higher values for combination of identified and putatively assigned cells (Figure S2E). We further evaluated the robustness of the classifier by testing it on a larger dataset of identified layer 2 neurons (Ray et al., 2014) recorded under urethane/ketamine anesthesia (Klausberger et al., 2003). We consider this a challenging test of the classifier, as theta-phase and strength of locking might differ between the awake and anesthetized state. Similarly to the awake situation however, the large majority of neurons recorded under anesthesia were also correctly classified (92% of calbindin$^+$, 65% of calbindin$^-$ cells, $p < 0.001$, bootstrap; Figure 2B bottom), suggesting that our classification criteria work robustly and can effectively generalize across very different recording conditions (Figure 2B). Encouraged by these results, we classified the larger dataset of our hitherto unidentified layer 2 juxtacellular and tetrode recordings (classified + identified n = 193 cells).

To assess the relationship between cell identity and spatial firing properties, we pooled the non-identified recordings, assigned to putative calbindin$^+$ and calbindin$^-$ cells, with the recordings from histologically identified neurons. The pooled datasets included n = 99 calbindin$^+$ and n = 94 calbindin$^-$ cells, respectively. In our first assessment of spatial discharge patterns, we attempted to classify grid and border-cells solely using scores (grid score > 0.3; border score > 0.5, Solstad et al., 2008). According to visual inspection of individual rate maps, however, these criteria were not sufficiently stringent and returned a majority of weakly to non-

modulated neurons, i.e. possibly a majority of false positive grid and border cells. To resolve this issue, we adopted the cell classification approach of Bjerknes et al., (2014), in which spatial discharge properties were only quantified in those cells, which carried significant amounts of spatial information (as assessed by a spike shuffling procedure, see Skaggs et al., 1993 and Supplemental Methods). This approach identified grid- and border-responses, which in a majority of cases were convincing according to visual inspection. Consistent with previous studies (Hafting et al., 2005; Sargolini et al., 2006; Boccara et al., 2010; Burgalossi et al., 2011; Domnisoru et al., 2013), a fraction of layer 2 neurons (33%; n = 63 cells) were significantly spatially-modulated. Weak hexagonal symmetry of spatial firing patterns was observed in both the calbindin$^+$ and calbindin$^-$ dataset, in line with previous observations (Burgalossi et al., 2011; Domnisoru et al., 2013; Schmidt-Hieber and Häusser, 2013). However, grid scores in the calbindin$^+$ population were significantly higher than those in the calbindin$^-$ population (p = 0.000046, Mann-Whitney U-test; Figure 2D,E), consistent with observations from the identified dataset (Figure 1). On the other hand, in line with observations from the identified dataset (Figure 1), calbindin$^-$ cells had significantly higher border scores than calbindin$^+$ cells (Figure 2G; p = 0.0012, Mann-Whitney U-test). Border discharges in calbindin$^-$ cells are shown in Figure 2F, which also includes an example where border firing was confirmed by a border test (Solstad et al., 2008; Lever et al., 2009). Thus, according to the grid and border scores shown in Figure 2D,G putative pyramidal and stellate cells have significantly different, but overlapping spatial properties.

Figure 2H gives an overview of the spatial response properties of our pooled calbindin$^+$ and calbindin$^-$ datasets, respectively (see also Figures S3 and S4). The majority of both calbindin$^+$ and calbindin$^-$ neurons showed no significant spatial selectivity. Grid patterns were significantly more common in the calbindin$^+$ population, where 19% (19/99) of the cells passed our grid cell criteria, compared to only 3% (3/94) in the calbindin$^-$ population (p = 0.00046, Fisher's exact test). A higher fraction of calbindin$^-$ cells passed the border cell criterion (11% calbindin$^-$, 10/94 cells; vs 1% calbindin$^+$, 1/99 cells) and this difference was statistically significant (p = 0.0042, Fisher's exact test). These data confirm and extend the conclusion from our recordings of identified cells and indicate that grid cells are preferentially recruited from the calbindin$^+$ population, while border responses preferentially occur in calbindin$^-$ cells.

Unlike many studies based on tetrode recordings (Sargolini et al., 2006; Boccara et al., 2010; but see Zhang et al., 2013) a substantial fraction of cells showed head-direction selectivity both in identified and theta-assigned calbindin$^+$ and calbindin$^-$ cells (Figure S5). Head-direction selectivity was more common in calbindin$^+$ (19%, 19 out of 99 cells) than in calbindin$^-$ cells (12%, 11 out 94 cells), but this difference was not significant, (p = 0.17, Fisher's exact test) and both classes contained pure as well as conjunctive responses (Sargolini et al., 2006).

The grid- and border-cells recorded here showed systematic differences in spike-locking to local field potential theta oscillations (Figure 3A). Spikes from most grid cells were strongly entrained by the theta-rhythm, with strong phase-locking (Figure 3B) and a phase-preference near the theta-trough (Figure 3C; p = 0.000000027, Rayleigh's test for nonuniformity). The modulation of spiking activity of border cells by the theta-rhythm was significantly weaker than in grid cells (Figure 3B; p = 0.0013, Mann-Whitney U-test) and showed on average only a weak non-significant phase-preference for the theta-peak (Figure 3C; p = 0.21, Rayleigh's test for nonuniformity), which differed significantly from the phase-preference of grid cells (Figure 3B and 3C; p = 0.0000088, Parametric Watson-Williams multi-sample test). Thus, in

layer 2 grid and border signals mirrored the temporal differences between calbindin$^+$ pyramidal and calbindin$^-$ stellate cells reported earlier (Ray et al., 2014).

Discussion

Relating functionally defined discharge patterns to principal cell diversity is an unresolved issue in cortical physiology. In layer 2 of medial entorhinal cortex, most studies suggested that spatially-modulated responses are common, and that grid firing patterns are contributed by both stellate and pyramidal neurons (Burgalossi et al., 2011; Schmidt-Hieber and Häusser, 2013; Domnisoru et al., 2013; Zhang et al., 2013). In line with such evidence, we observed a consistent fraction of spatially-modulated neurons in layer 2, and weakly hexagonal firing patterns in both stellate and pyramidal neurons. At the same time however, most grid patterns that met our grid score and spatial information criteria (see Supplemental Methods) were classified as putative calbindin$^+$ pyramidal cells (see Figures S3 and S4). Border responses on the other hand were predominantly observed in the calbindin$^-$ stellate population. Our data indicate a strong interdependence between cell type and spatial discharge pattern in layer 2, where a calbindin$^+$ cell is about 6 times more likely to be a grid cell and 10 times less likely to be a border cell than a calbindin$^-$ neuron. Our confidence in classification is based on the striking differences of calbindin$^+$ and calbindin$^-$ cells in their temporal discharge properties (Ray et al., 2014), the assessment of classification quality by our boot-strapping approach, and the robustness of classification across widely differing recording conditions. It is important however to note that our conclusions rest on the validity and accuracy of our classification procedure.

A key finding from our work is that layer 2 principal cells can be classified with high accuracy by their distinct temporal discharge properties. Such classification can be extended to a large number of unidentified layer 2 recordings from other laboratories, provided that the required histology and local field potential data have been collected. To this end we provide our classification training data set (Supplementary Table 1) and a custom written MATLAB function (Supplementary Note 1: CbClassify.m). Such *post-hoc* assignment of principal cell types to recordings – i.e. supplying identity to formerly blind extracellular recordings – could be instrumental for understanding principal cell diversity and cortical microcircuitry.

Calbindin$^+$ pyramidal cells might be predetermined for grid cell function as they receive cholinergic inputs, are strongly theta-modulated, and arranged in a hexagonal grid (Ray et al., 2014). We suggested an ‘isomorphic mapping hypothesis’, according to which an anatomical grid of pyramidal cells (Ray et al., 2014) generates grid cell activity (Brecht et al., 2014) and is an embodiment of the brain’s representation of space in hexagonal grids. Representing grid discharge by a ‘cortical grid’ might offer similar advantages as isomorphic representations of body parts, as barrel fields (Woolsey and van der Loos, 1970) or nose stripes (Catania et al., 1993) in somatosensory cortices of tactile specialists. Notably, the local similarity of grid cell discharges is high, as neighboring grid cells share the same grid orientation, scaling and are phase-coupled even across distinct environments (Hafting et al., 2005; Fyhn et al., 2007). We speculate that calbindin$^+$ pyramidal neuron clustering and apical dendrite bundling in patches (Ray et al., 2014) might impose this local similarity of grid discharges. A surprising implication

of our data is that the spatial input to the dentate-gyrus is provided mainly by stellate border cells, whereas pyramidal grid cells do not feed into this pathway (Kitamura et al., 2014; Ray et al. 2014). Border responses arise in stellate neurons, with long and widely diverging dendritic trees, i.e. such discharge patterns may result from a relatively global sampling of incoming inputs in medial entorhinal cortex and help generate place cell activity (Bjerknes et al., 2014; Bush et al., 2014). Recognizing the functional dichotomy of pyramidal and stellate cells in layer 2 will help elucidating how spatial discharge patterns arise in cortical microcircuits.

Methods summary

All experimental procedures were performed according to the German guidelines on animal welfare under the supervision of local ethics committees. Juxtacellular recordings and tetrode recordings in freely moving animals were obtained in male Wistar and Long-Evans rats (150-250 g), which were habituated to the behavioral arena and trained for 3-7 days. Experimental procedures were performed as previously described (Burgalossi et al., 2011; Herfst et al., 2012) with the exception that methodological developments allowed us to identify neurons in drug-free animals (Tang et al., 2014; see Supplemental Information). Some of the data have been published in a previous report (Ray et al., 2014). Recordings in anesthetized animals were performed under urethane/ketamine/xylazine (Klausberger et al., 2003). Juxtacellularly labeled neurons were visualized with streptavidin-conjugated to Alexa 546 (1:1000). A Hilbert transform was used for assigning instantaneous theta phase of each spike based on theta in the local field potential in the spike-theta phase analysis. The spatial periodicity of recorded neurons was assessed by spatial autocorrelations. Grid scores were calculated as previously described (Barry et al., 2012) by taking a circular sample of the spatial autocorrelogram, centered on, but excluding the central peak. To determine the modulation of a cell firing along a border, we determined border scores as previously described or performed border tests (Solstad et al., 2008; Lever et al., 2009). Head-direction tuning was measured as the excentricity of the circular distribution of firing rates. Classification based on strength of locking to theta phase, S, and preferred theta phase angle, φ, was done by building a support vector machine, trained on the vectors $(\cos(\varphi)\cdot S, \sin(\varphi)\cdot S)$ using a Gaussian radial basis function kernel. Classification of non-identified cells into putative calbindin$^+$ and calbindin$^-$ cells was performed by applying a conservative classification threshold, where we did not classify cells close to the separating hyperplane. Detailed experimental and analytical procedures are provided in the Supplemental Information.

References

Alonso, A., and Klink, R. (1993). Differential electroresponsiveness of stellate and pyramidal-like cells of medial entorhinal cortex layer II. J. Neurophysiol. *70*, 128–143.

Alonso, A., and Llinás, R.R. (1989). Subthreshold Na+-dependent theta-like rhythmicity in stellate cells of entorhinal cortex layer II. Nature *342*, 175–177.

Barry, C., Ginzberg, L.L., O'Keefe, J., and Burgess, N. (2012). Grid cell firing patterns signal environmental novelty by expansion. Proc. Natl. Acad. Sci. U S A. *109*, 17687-92.

Bjerknes, T.L., Moser, E.I., and Moser, M.-B. (2014). Representation of Geometric Borders in the Developing Rat. Neuron *82*, 71–78.

Boccara, C.N., Sargolini, F., Thoresen, V.H., Solstad, T., Witter, M.P., Moser, E.I., and Moser, M.-B. (2010). Grid cells in pre- and parasubiculum. Nat. Neurosci. *13*, 987-94.

Brecht, M., Ray, S., Burgalossi, A., Tang, Q., Schmidt, H., and Naumann, R. (2014). An isomorphic mapping hypothesis of the grid representation. Phil. Trans. R. Soc. B *369*, 20120521.

Burgalossi, A., and Brecht, M. (2014). Cellular, columnar and modular organization of spatial representations in medial entorhinal cortex. Curr. Opin. Neurobiol. *24*, 47-54.

Burgalossi, A., Herfst, L., von Heimendahl, M., Förste, H., Haskic, K., Schmidt, M., and Brecht, M. (2011). Microcircuits of functionally identified neurons in the rat medial entorhinal cortex. Neuron *70*, 773–786.

Bush, D., Barry, C., and Burgess, N. (2014). What do grid cells contribute to place cell firing? Trends. Neurosci. *37*,136-45.

Canto, C.B., and Witter, M.P. (2012). Cellular properties of principal neurons in the rat entorhinal cortex. II. The medial entorhinal cortex. Hippocampus *22*, 1277–1299.

Catania, K.C., Northcutt, R.G., Kaas, J.H., and Beck, P.D. (1993). Nose stars and brain stripes. Nature *364*, 493.

Domnisoru, C., Kinkhabwala, A.A., and Tank, D.W. (2013). Membrane potential dynamics of grid cells. Nature *495*, 199–204.

Fyhn, M., Hafting, T., Treves, A., Moser, M.-B., and Moser, E.I. (2007). Hippocampal remapping and grid realignment in entorhinal cortex. Nature 446, 190-4.

Gatome, C.W., Slomianka, L., Lipp, H.P., and Amrein, I (2010). Number estimates of neuronal phenotypes in layer II of the medial entorhinal cortex of rat and mouse. Neuroscience 170, 156-65.

Germroth, P., Schwerdtfeger, W.K., and Buhl, E.H. (1989). Morphology of identified entorhinal neurons projecting to the hippocampus. A light microscopical study combining retrograde tracing and intracellular injection. Neuroscience *30*, 683–691.

Gupta, K., Keller, L.A., and Hasselmo, M.E. (2012). Reduced spiking in entorhinal cortex during the delay period of a cued spatial response task. Learn. Mem. 2012 *19*, 219-30.

Hafting, T., Fyhn, M., Molden, S., Moser, M.-B., and Moser, E.I. (2005). Microstructure of a spatial map in the entorhinal cortex. Nature *436*, 801–806.

Herfst, L., Burgalossi, A., Haskic, K., Tukker, J.J., Schmidt, M., and Brecht, M. (2012). Friction-based stabilization of juxtacellular recordings in freely moving rats. J. Neurophysiol. *108*, 697-707.

Kitamura, T., Pignatelli, M., Suh, J., Kohara, K., Yoshiki, A., Abe, K., and Tonegawa, S. (2014). Island cells control temporal association memory. Science *343*, 896-901.

Klausberger, T., Magill, P.J., Márton, L.F., Roberts, J.D., Cobden, P.M., Buzsáki, G., and Somogyi, P. (2003). Brain-state- and cell-type-specific firing of hippocampal interneurons in vivo. Nature *421*, 844-8.

Klink, R., and Alonso, A. (1997). Muscarinic modulation of the oscillatory and repetitive firing properties of entorhinal cortex layer II neurons. J. Neurophysiol. *77*, 1813–1828.

Kumar, S.S., and Buckmaster, P.S. (2006). Hyperexcitability, interneurons, and loss of GABAergic synapses in entorhinal cortex in a model of temporal lobe epilepsy. J. Neurosci. *26*:4613–4623.

Lever, C., Burton, S., Jeewajee, A., O'Keefe, J., and Burgess, N. (2009). Boundary vector cells in the subiculum of the hippocampal formation. J. Neurosci. *29*, 9771-7.

Lingenhöhl, K., and Finch, D.M. (1991). Morphological characterization of rat entorhinal neurons in vivo: soma-dendritic structure and axonal domains. Exp. Brain. Res. 84, 57–74

Moser, E.I., and Moser, M.-B. (2013). Grid cells and neural coding in high-end cortices. Neuron 80, 765-74.

Peterson, D.A., Lucidi-Phillipi, C.A., Murphy, D.P., Ray, J., and Gage, F.H. (1996). Fibroblast growth factor-2 protects entorhinal layer II glutamatergic neurons from axotomy-induced death. J. Neurosci. 16:886–898.

Ray, S., Naumann, R., Burgalossi, A., Tang, Q., Schmidt, H., and Brecht, M. (2014). Grid-layout and theta-modulation of layer 2 pyramidal neurons in medial entorhinal cortex. Science 343, 891-6.

Rowland, D.C., and Moser, M.-B. (2014). From cortical modules to memories. Curr. Opin. Neurobiol. 24, 22-27.

Sargolini, F., Fyhn, M., Hafting, T., McNaughton, B.L., Witter, M.P., Moser, M.-B., and Moser, E.I. (2006). Conjunctive representation of position, direction, and velocity in entorhinal cortex. Science 312, 758–762.

Savelli, F., Yoganarasimha, D., and Knierim, J.J. (2008). Influence of boundary removal on the spatial representations of the medial entorhinal cortex. Hippocampus 18, 1270-82.

Schmidt-Hieber, C., and Häusser, M. (2013). Cellular mechanisms of spatial navigation in the medial entorhinal cortex. Nat. Neurosci. *16*, 325–331.

Skaggs, W.E., McNaughton, B.L., Gothard, K.M., and Markus, E.J. (1993). An information-theoretic approach to deciphering the hippocampal code. In Advances in Neural Processing Systems, Volume 5, S.J. Hanson, J.D. Cowan, and C.L. Giles, eds. (San Mateo: Morgan Kaufmann), pp. 1030–1037.

Solstad, T., Boccara, C.N., Kropff, E., Moser, M.-B., and Moser, E.I. (2008). Representation of geometric borders in the entorhinal cortex. Science *322*, 1865–1868.

Tang, Q., Brecht, M., and Burgalossi, A. (2014). Juxtacellular recording and morphological identification of single neurons in freely moving rats. Nat. Protoc. *9*, 2369-2381.

Varga, C., Lee, S.Y., and Soltesz, I. (2010). Target-selective GABAergic control of entorhinal cortex output. Nat. Neurosci. *13*, 822–824.

Woolsey, T.A., and van der Loos, H. (1970). The structural organization of layer IV in the somatosensory region (SI) of mouse cerebral cortex. The description of a cortical field composed of discrete cytoarchitectonic units. Brain Res. *17*, 205–242.

Zhang, S.-J., Ye, J., Miao, C., Tsao, A., Cerniauskas, I., Ledergerber, D., Moser, M.-B., and Moser, E.I. (2013). Optogenetic dissection of entorhinal-hippocampal functional connectivity. Science *340*, 1232627.

Acknowledgements

This work was supported by Humboldt-Universität zu Berlin, BCCN Berlin (German Federal Ministry of Education and Research BMBF, Förderkennzeichen 01GQ1001A), NeuroCure, the Neuro-Behavior ERC grant and the Gottfried Wilhelm Leibniz Prize of the DFG. We thank Moritz von Heimendahl for programming, and Andreea Neukirchner, Juliane Steger, John Tukker and Undine Schneeweiß. We are thankful to Francesca Sargolini, May-Britt and Edvard Moser and the other authors (Sargolini et al., 2006), who generously provided access to grid cell data, which were helpful in assembling an earlier version of this manuscript.

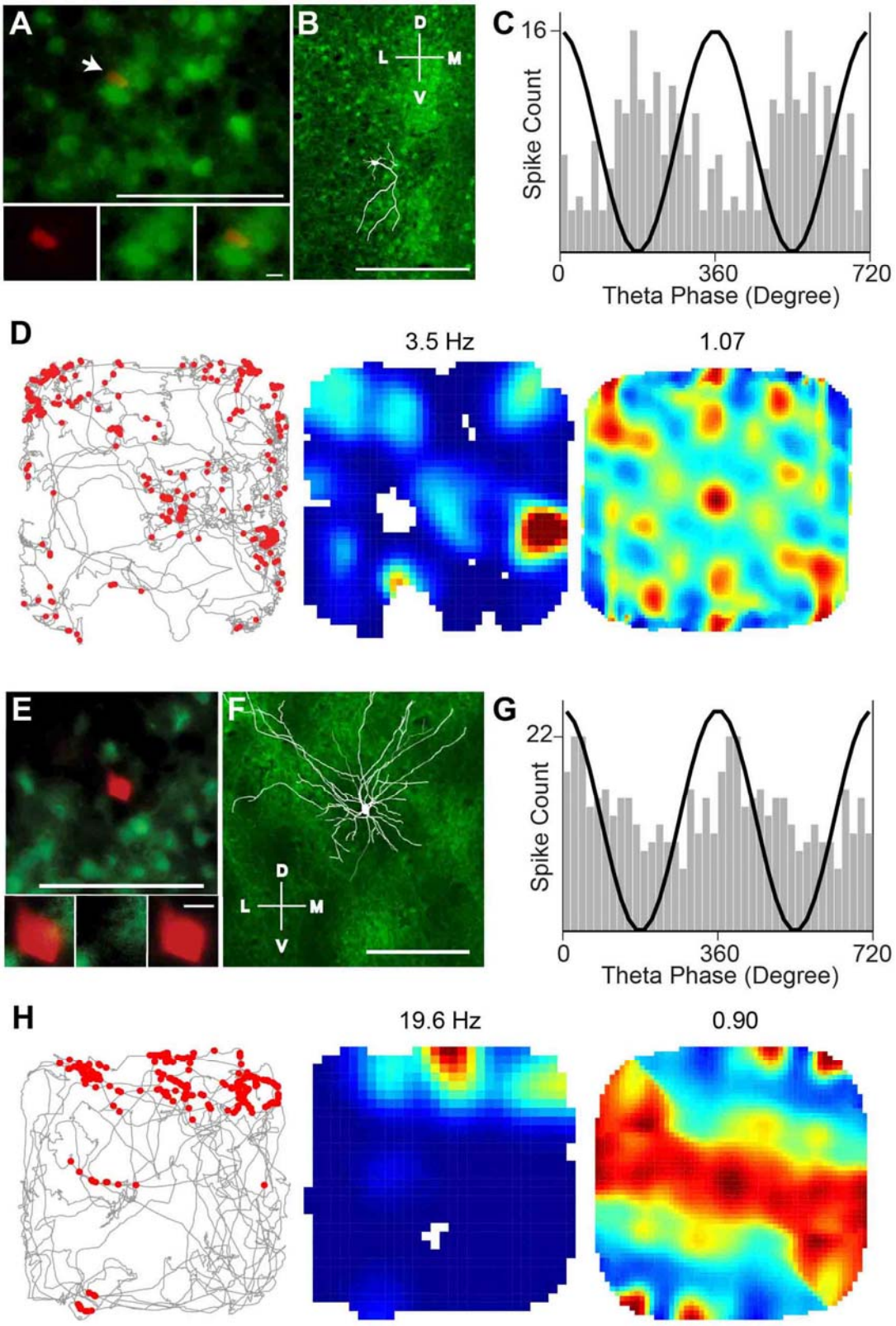
A
B
D
L
M
V
C
16
Spike Count
0
360
720
Theta Phase (Degree)
D
3.5 Hz
1.07
E
F
D
L
M
V
G
22
Spike Count
0
360
720
Theta Phase (Degree)
H
19.6 Hz
0.90

Figure 1. Grid-like firing properties in a calbindin-positive pyramidal neuron and border-responses in a calbindin-negative stellate neuron.

(A) Top, micrograph (tangential section) of a calbindin$^+$ neuron recorded in a rat exploring a 2D environment (1 x 1 m). Green, calbindin; red, neurobiotin. Bottom panels, soma in red, green channel and overlay. Scale bars, 100 μm (top), 10 μm (bottom).

(B) Micrograph of a tangential layer 2 section with calbindin immunoreactivity (green) and superimposed reconstruction of the pyramidal neuron (white). The cell was poorly stained, basal dendrites were minor and a prominent apical dendrite extended towards the center of a calbindin patch ventral from the neuron. Scale bar, 250 μm.

(C) Theta-phase histogram of spikes for the neuron shown in (A). For convenience, two repeated cycles are shown. The black sinusoid is a schematic local field potential theta wave for reference.

(D) Spike-trajectory plot, rate map and two-dimensional spatial autocorrelation of the rate-map revealing the hexagonal grid cell periodicity. Spike-trajectory plot: red dots indicate spike locations, grey lines indicate the rat trajectory. Rate map: red indicates maximal firing rate, value noted above. Spatial autocorrelation: color scale -1 (blue) through 0 (green) to 1 (red). For this cell, the grid score is 1.07.

(E) Left, micrograph (tangential section) of a calbindin$^-$ neuron recorded in a rat exploring a 2D environment (70 x 70 cm). Green, calbindin; red, neurobiotin. Right panels, soma in red, green channel and overlay. Scale bars, 100 μm (left), 10 μm (right).

(F) Micrograph of the tangential layer 2 section with calbindin immunoreactivity (green) and superimposed reconstruction of the stellate neuron (white). The cell was well stained and the huge dendritic field encompassed several calbindin patches. Scale bar, 250 μm.

(G) Theta-phase histogram of spikes for the neuron shown in (A). For convenience, two repeated cycles are shown. The black sinusoid is a schematic local field potential theta wave for reference.

(H) Spike-trajectory plot, rate map and two-dimensional spatial autocorrelation of the rate-map revealing the elongated firing field. Spike-trajectory plot: red dots indicate spike locations, grey lines indicate the rat trajectory. Rate map: red indicates maximal firing rate, value noted above. Spatial autocorrelation: color scale -0.5 (blue) through 0 (green) to 0.5 (red). For this cell, the border score is 0.90.

D = dorsal, L = lateral, M = medial, V = ventral.

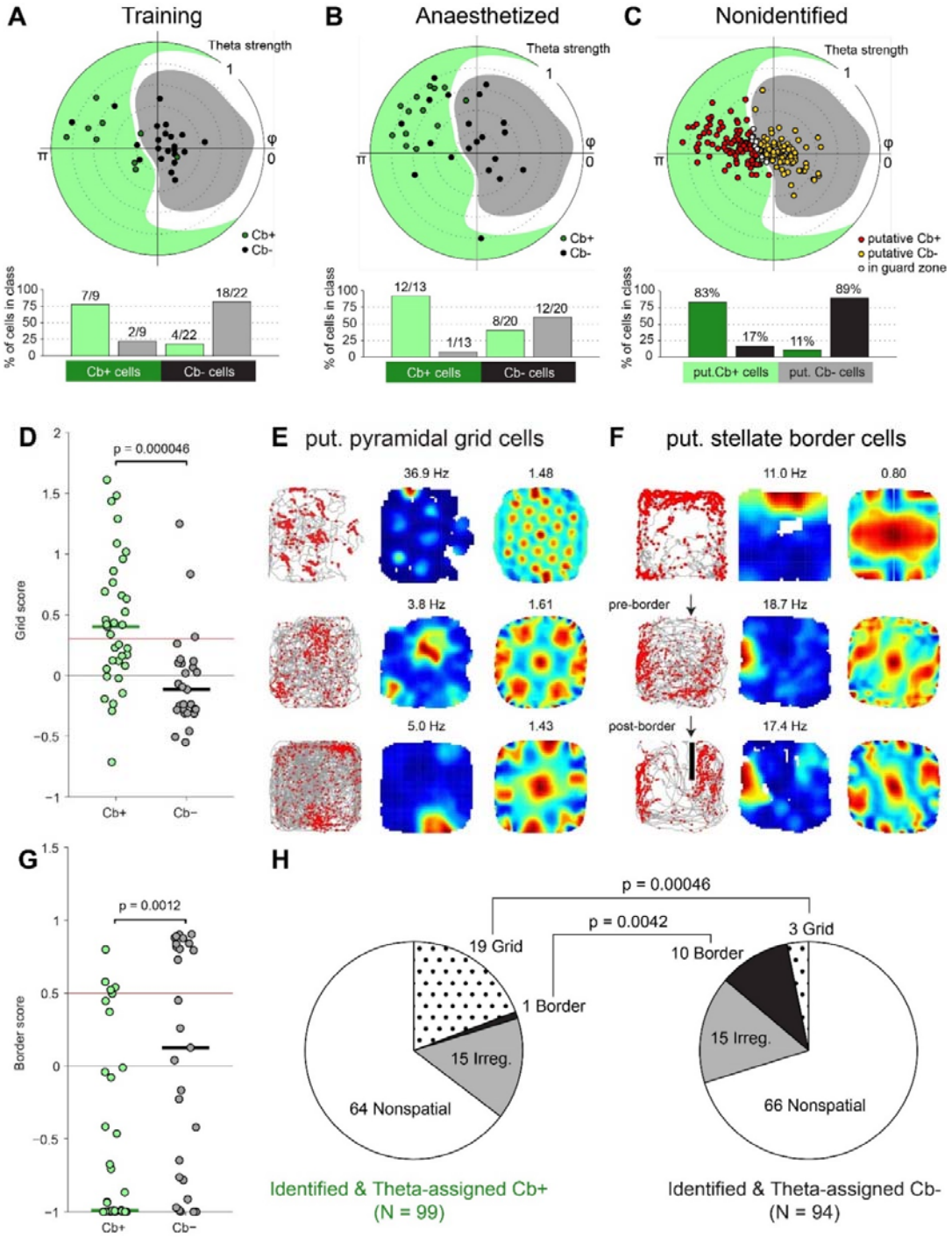

Figure 2. Cell classification and grid and border responses in pooled identified and theta-assigned cells.

(A) Top, classification training set: Polar plot of theta strength (value indicated by the upper right number) and preferred theta phase angle, φ, for calbindin$^+$ cells (green dots) and calbindin$^-$ cells (black dots) identified in freely moving rats. Background color fill shows classification boundary based on φ and theta strength: Cells in the pale green area and grey area will be classified as calbindin$^+$ and calbindin$^-$ cells respectively. Bottom, fraction of cells in classification categories.

(B) Top, polar plot of theta strength and of preferred theta phase angle, φ, for calbindin$^+$ cells (green dots) and calbindin$^-$ cells (black dots) identified in anaesthetized rats, overlaid on classification boundary. Bottom, fraction of cells in classification categories.

(C) Top, polar plot of theta strength and preferred theta phase angle, φ, for non-identified cells. Putative calbindin$^+$ cells (red dots) and putative calbindin$^-$ cells (yellow dots) are shown overlaid on the classification boundary, together with unclassified cells (white dots). Bottom, estimate of the purity of the theta-assigned cell categories. The sample of putative calbindin$^-$ cells are estimated to be 89% pure, and the sample of putative calbindin$^+$ cells are estimated to be 83% pure (see Figure S2)

(D) Comparison of grid scores between (identified and putative) calbindin$^+$ and calbindin$^-$ neurons; the dotted line indicates the threshold for grid cell; vertical lines indicate medians (p = 0.000046, Mann-Whitney U-test).

(E) Representative grid firing pattern observed in calbindin$^+$ neurons (spike-trajectory plot, rate-map and spatial autocorrelation. Maximum firing rate and grid score indicated above plots.).

(F) Border firing patterns in calbindin$^-$ neurons. Conventions as in (E). Arrows indicate insertion of additional border.

(G) Comparison of border scores between (identified and putative) calbindin$^+$ and calbindin$^-$ neurons; the dotted line indicates the threshold for border cells; vertical lines indicate medians (p = 0.0012; Mann-Whitney U-test).

(H) Distribution of spatial discharge types in calbindin$^+$ (left) and calbindin$^-$ (right) neurons, was found to be significantly different in numbers of grid cells and border cells (p = 0.00046 and 0.0042, Pearson's Chi-squared test).

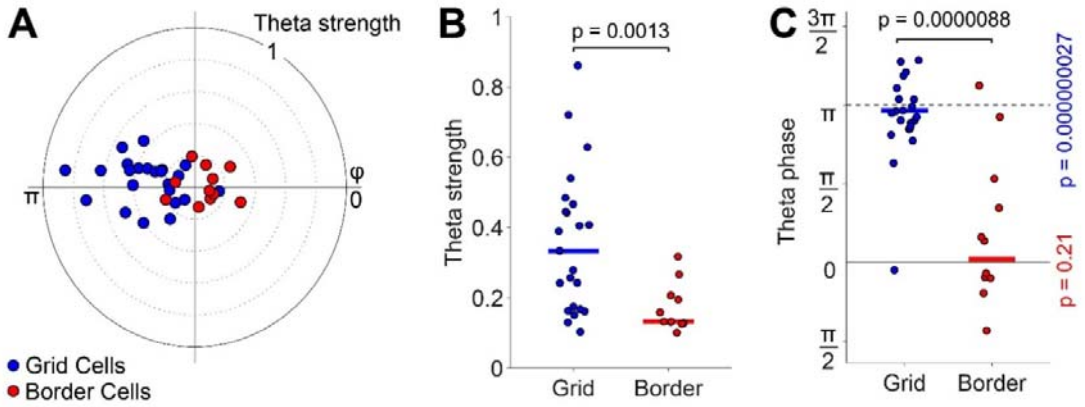

Figure 3. Temporal spiking properties of grid cells and border cells.

(A) Polar plot of theta strength as a function of preferred theta phase angle, φ, for grid cells (blue dots), border cells (red dots).

(B) Theta strength of recorded grid cells (blue dots) and border cells (red dots) is significantly different. Blue and red lines indicate medians (p = 0.0013, Mann-Whitney U-test).

(C) Preferred theta phase for grid cells (blue dots) and border cells (red dots). Blue and red lines indicate circular means (p = 0.0000088, Parametric Watson-Williams multi-sample test). Grid cells show a significant tendency to fire near the trough (p = 0.000000027, Rayleigh's test for nonuniformity). Border cells show a tendency to fire near the peak of theta rhythm, but the phase-locking to theta peak did not reach significance in our data set (p = 0.21, Rayleigh's test for nonuniformity).

SUPPLEMENTARY DATA

Pyramidal and Stellate Cell-specificity of Grid and Border Representations in Layer 2 Medial Entorhinal Cortex

Qiusong Tang, Andrea Burgalossi, Christian Ebbesen, Saikat Ray, Robert Naumann, Helene Schmidt, Dominik Spicher, & Michael Brecht

Inventory list of supplementary data

	Title	Related to
Figure S1	Anatomical characterization of calbindin-positive pyramidal and calbindin-negative stellate cells in layer 2 of medial entorhinal cortex	Figure 1
Figure S2	Firing properties of those identified and theta-assigned calbindin-positive neurons, which carry significant spatial information	Figure 2 & 3
Figure S3	Firing properties of those identified and theta-assigned calbindin-negative neurons, which carry significant spatial information	Figure 2 & 3
Figure S4	Head-direction tuning and theta-assigned calbindin-positive and calbindin-negative neurons	Figure 2
Table S1	Theta modulation (phase, strength and theta index) of juxtacellularly identified calbindin$^{+/-}$ cells from layer 2 of medial entorhinal cortex	Figure 3
Note S1	Custom-written Matlab script to classify non-identified cells into putative calbindin$^{+/-}$ by phase/strength of phase/index	Figure 3

SUPPLEMENTARY FIGURES

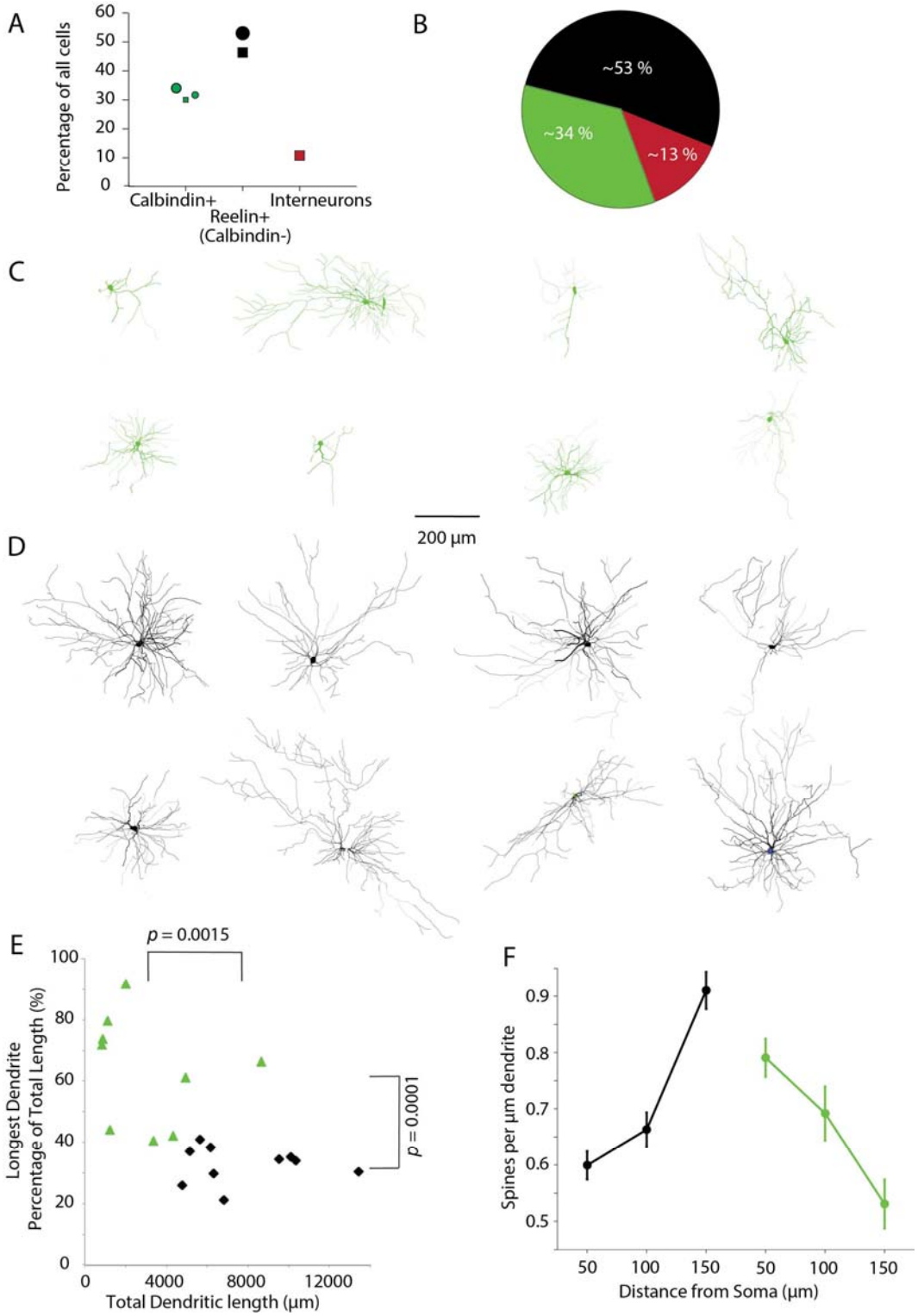

Figure S1 Anatomical characterization calbindin-positive pyramidal and calbindin-negative stellate cells in layer 2 of medial entorhinal cortex.

(A) Percentage of all neurons classified as calbindin+, reelin+ (calbindin-) and interneurons in layer 2 of the medial entorhinal cortex of a rat. Absolute reelin+ numbers have been extrapolated from calbindin+ and reelin+ counts. Circular markers indicate measurement made in this study. Square markers indicate measurements made by other studies (Peterson et al., 1996; Kumar and Buckmaster, 2006; Varga et al., 2010).

(B) Distribution of calbindin+ neurons (green), reelin+ neurons (black) and interneurons (red) in layer 2 of the medial entorhinal cortex of a rat. Numbers indicate averages of measurements indicated in panel A.

(C) Identified calbindin+ cells have pyramidal morphologies. All cells come from tangential sections and are hence shown in 'views from the top'.

(D) Identified calbindin- cells have stellate morphologies. All cells come from tangential sections and are hence shown in 'views from the top'.

(E) Identified and reconstructed calbindin+ cells and calbindin- cells show significant (*t*-test) size and shape differences.

(F) Spine distribution differs in calbindin+ cells and calbindin- cells; data refer to ten cells each, for which we counted spine densities in multiple ~30 µm dendrite segments at the distances from the soma specified in the plot. Slopes of spine density differed significantly between calbindin+ cells and calbindin- cells ($p = 0.0023$, *t*-test). Error bars indicate SEM.

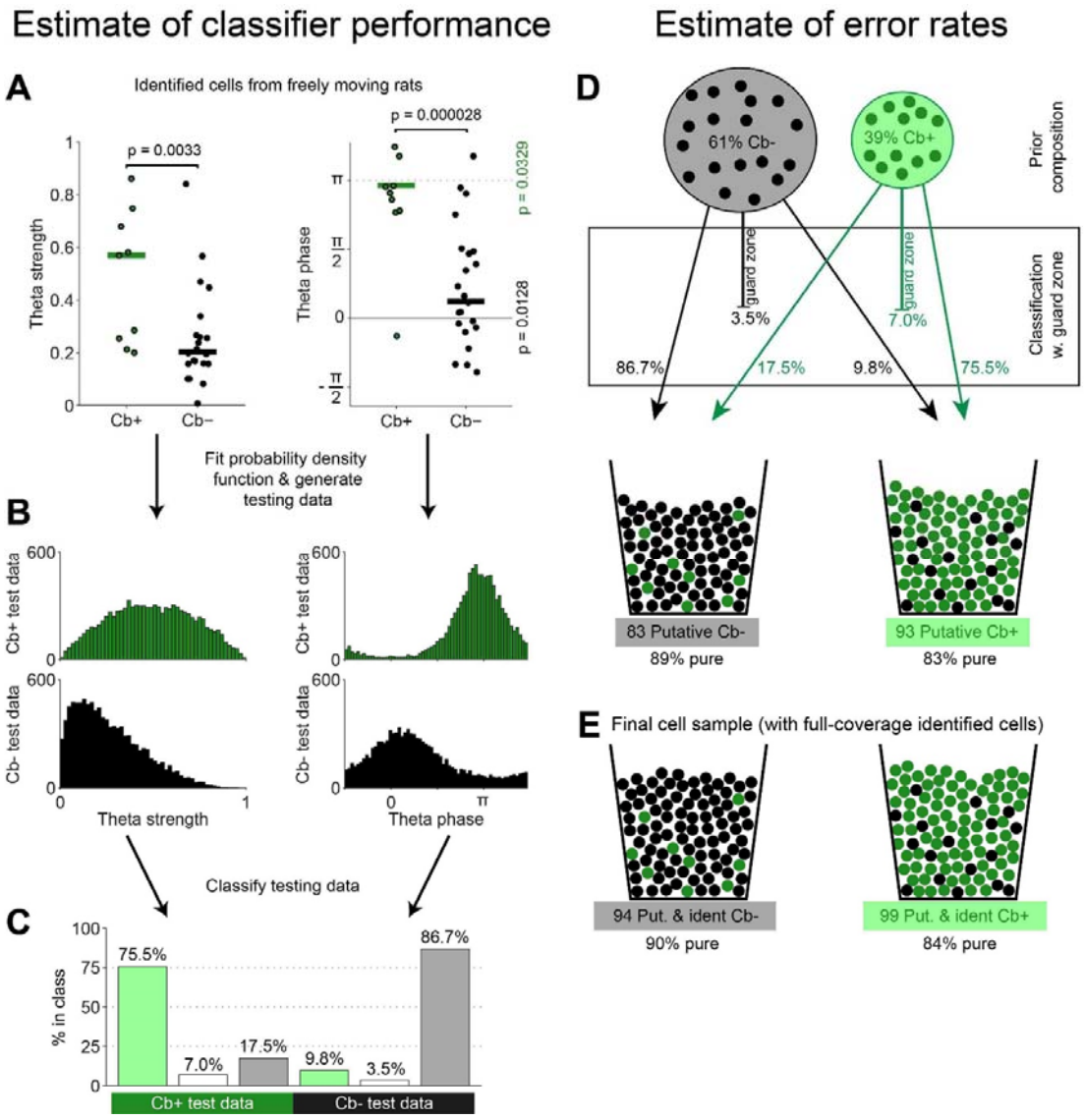

Figure S2 Testing of the classifier and error estimates.

(A) Theta strength and preferred theta phase of identified calbindin+ cells (green dots) and calbindin- cells (black dots) is significantly different. Green and black lines indicate medians of theta strength (p = 0.0033, Mann-Whitney U-test). Green and black lines indicate circular means of preferred theta phase (p = 0.000028, Parametric Watson-Williams multi-sample test). Calbindin+ cells show a significant tendency to fire near the trough (p = 0.013, Rayleigh's test for nonuniformity) and calbindin- cells show a tendency to fire near the peak of theta rhythm (p = 0.033, Rayleigh's test for nonuniformity).

(B) Distribution of testing data for estimation of classifier performance. Testing data is generated by fitting the appropriate probability density functions (beta distributions and circular Gaussian distributions, respectively) to the distributions of theta strength and preferred theta phase of identified calbindin+ and calbindin- cells (N = 10.000 for both cell types).

(C) Result of classification of testing data shows that both calbindin+ cells and calbindin- cells are classified with high accuracy and low false classification rates (75.5% correct and 17.5%

incorrect for calbindin+ cells, 86.7% correct and 9.8% incorrect for calbindin- cells). This shows that the classification boundary is robust and not just overfitting the small training set of identified cells.

(D) Estimation of the purity (positive predictive value) of the classifier based on the estimate of 34% calbindin+, 53% reelin+ (calbindin-) and 13% interneurons in L2 of rat MEC (Figure S1A,B). The sample of 93 putative calbindin+ cells is estimated to be 83% pure, and the sample of 83 putative calbindin- cells is estimated to be 89% pure.

(E) After addition of identified, full-coverage cells (11 calbindin- and 6 calbindin+), we estimate the purity of our final cell sample to be 84% for calbindin+ cell and 90% for calbindin- cells.

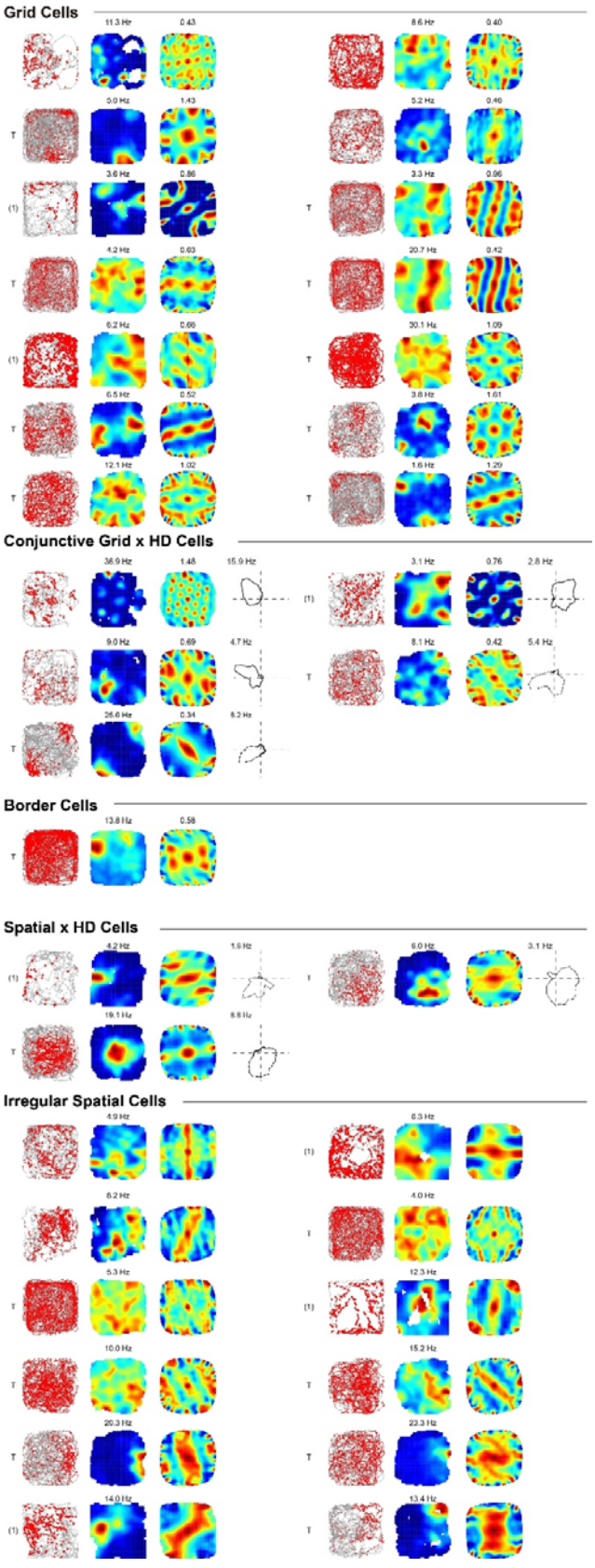
Grid Cells
Conjunctive Grid x HD Cells
Border Cells
Spatial x HD Cells
Irregular Spatial Cells

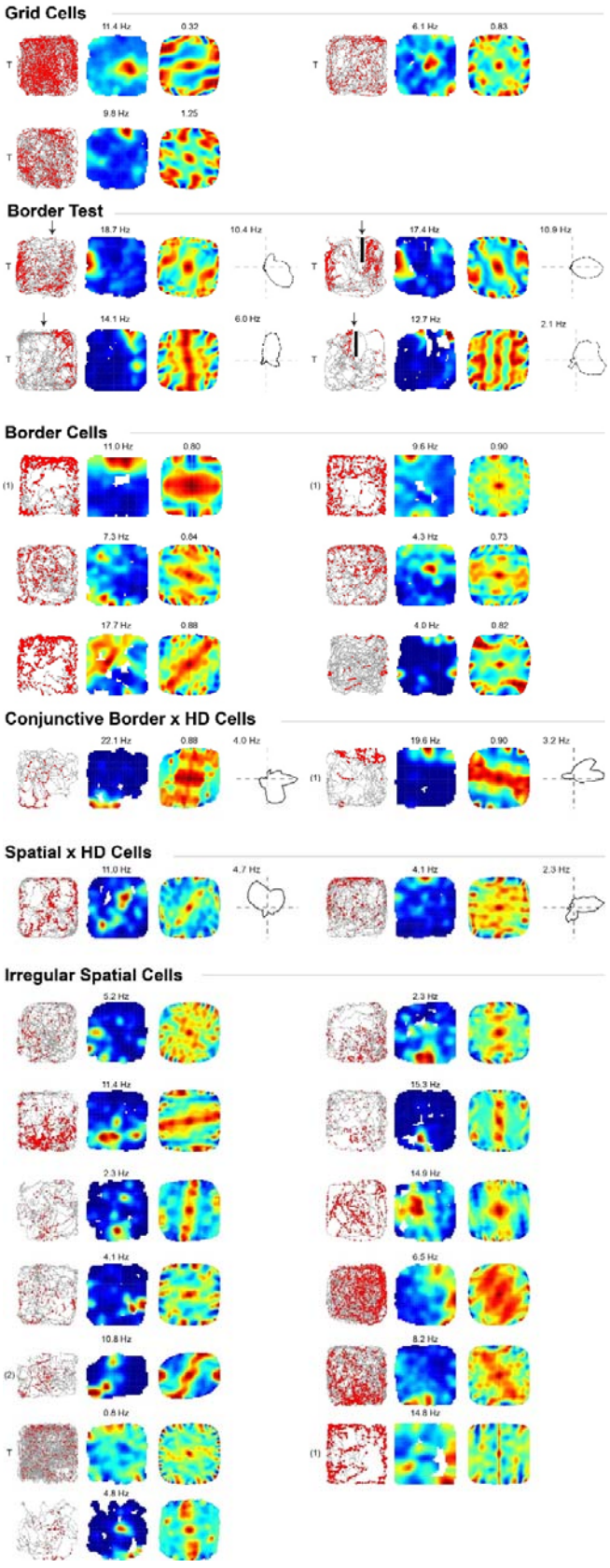
Grid Cells
11.4 Hz
0.32
6.1 Hz
0.83
9.8 Hz
1.25
Border Test
18.7 Hz
10.4 Hz
17.4 Hz
10.9 Hz
14.1 Hz
6.0 Hz
12.7 Hz
2.1 Hz
Border Cells
11.0 Hz
0.80
9.6 Hz
0.90
7.3 Hz
0.64
4.3 Hz
0.73
17.7 Hz
0.88
4.0 Hz
0.82
Conjunctive Border x HD Cells
22.1 Hz
0.88
4.0 Hz
19.6 Hz
0.90
3.2 Hz
Spatial x HD Cells
11.0 Hz
4.7 Hz
4.1 Hz
2.3 Hz
Irregular Spatial Cells
5.2 Hz
2.3 Hz
11.4 Hz
15.3 Hz
2.3 Hz
14.9 Hz
4.1 Hz
6.5 Hz
10.8 Hz
8.2 Hz
0.8 Hz
14.8 Hz
4.8 Hz

Figure S3. Firing properties of those identified and theta-assigned calbindin-positive and calbindin-negative neurons, which carry significant spatial information.

(A) Calbindin-positive neurons. Cells are ordered according to spatial firing properties. From left to right we show spike-trajectory plot, rate map, two-dimensional spatial autocorrelation and angular tuning (which is shown only for head-direction selective cells. Note that pure head direction cells that do not carry positional information are not included in this Figure). Numbers above the rate map indicate maximum firing rate. Numbers above the spatial autocorrelation indicate grid or border scores with respect to their properties. (T) indicates cells recorded with tetrodes; all other cells are from juxtacellular recordings. (1) indicates cells recorded in 0.7 x 0.7 m arena, all other recordings are from 1 x 1 m arena.

(B) Calbindin-negative neurons. Cells are ordered according to spatial firing properties. From left to right we show spike-trajectory plot, rate map, two-dimensional spatial autocorrelation and angular tuning (which is shown only for head-direction selective cells. Note that pure head direction cells that do not carry positional information are not included in this Figure). Numbers above the rate map indicate maximum firing rate. Numbers above the spatial autocorrelation indicate grid or border scores with respect to their properties. (T) indicates cells recorded with tetrodes; all other cells are from juxtacellular recordings. (1) indicates cells recorded in 0.7 x 0.7 m arena, (2) one cell recorded in a 0.6 x 0.8 m arena; all other recordings are from 1 x 1 m arena.

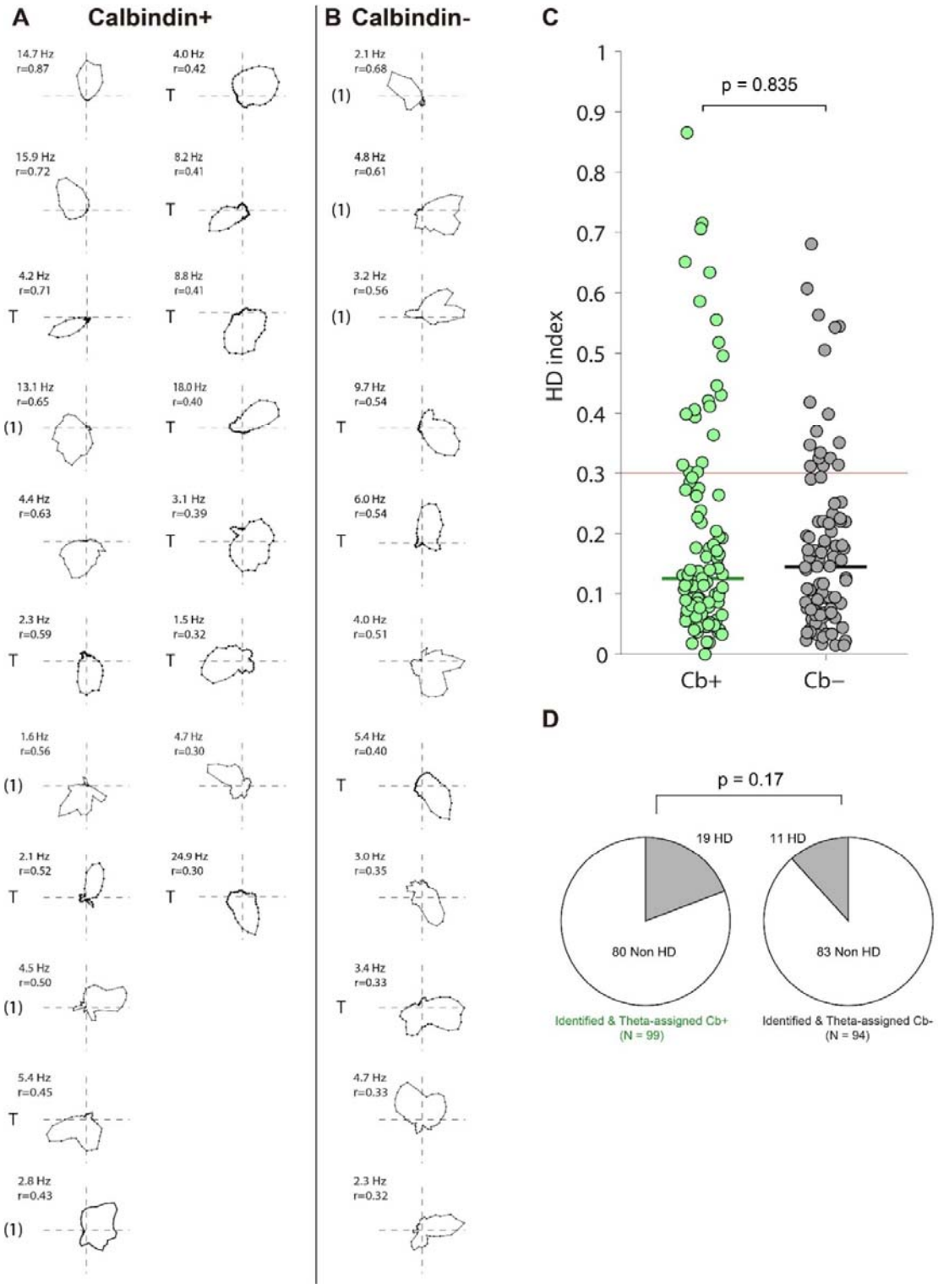

Figure S4. Head-direction tuning of those identified and theta-assigned calbindin-positive and calbindin-negative neurons.

(A) Polar plots of the head-direction tuning in identified and theta-assigned calbindin-positive neurons, which carry significant directional information. Cells are ranked according to Rayleigh vector lengths. (T) indicates cells recorded with tetrodes; all other cells are from juxtacellular recordings. (1) indicates cells recorded in 0.7 x 0.7 m arena, all other recordings are from 1 x 1 m arena.

(B) Polar plots of the head-direction tuning in identified and theta-assigned calbindin-negative neurons, which carry significant directional information. Cells are ranked according to Rayleigh vector lengths.

(C) Comparison of HD index (Rayleigh vector length) between (identified and putative) calbindin$^+$ and calbindin$^-$ neurons; the dotted line indicates the threshold for head-direction cell; vertical lines indicate medians (p = 0.835, Mann-Whitney U-test).

(D) Numbers of head-direction cells in (identified and putative) calbindin$^+$ (A) and calbindin$^-$ (B) neurons were not different (p = 0.17, Fisher's exact test).

SUPPLEMENTARY TABLE 1

TYPE	PHASE	STRENGTH	
0	1,2318	0,238	Calbindin-
0	2,8419	0,84031	Calbindin-
0	1,5892	0,21271	Calbindin-
0	1,5243	0,46896	Calbindin-
0	0,14037	0,44728	Calbindin-
0	2,3605	0,56663	Calbindin-
0	-0,0628	0,1579	Calbindin-
0	0,3543	0,0073	Calbindin-
0	-1,0621	0,3383	Calbindin-
0	-0,2142	0,1004	Calbindin-
0	1,0873	0,15808	Calbindin-
0	-0,11996	0,25522	Calbindin-
0	1,4714	0,0817	Calbindin-
0	-0,31369	0,16922	Calbindin-
0	2,9724	0,1946	Calbindin-
0	-1,2278	0,1007	Calbindin-
0	-1,0479	0,25896	Calbindin-
0	0,50391	0,26567	Calbindin-
0	-0,69228	0,20623	Calbindin-
0	0,72691	0,16779	Calbindin-
0	0,12994	0,15958	Calbindin-
0	-2,5888	0,1987	Calbindin-
1	-2,3775	0,28433	Calbindin+
1	2,7056	0,56983	Calbindin+
1	-0,40718	0,19952	Calbindin+
1	-2,5879	0,2532	Calbindin+
1	3,0164	0,86095	Calbindin+
1	2,4491	0,7484	Calbindin+
1	2,9923	0,58077	Calbindin+
1	2,856	0,67846	Calbindin+
1	2,4112	0,21168	Calbindin+

Table S1. Classification training dataset of putative calbindin$_{+}$ cells or calbindin$_{-}$ cells. Cells were recorded and identified juxtacellularly in freely-moving animals. Phase value is the preferred firing phase in radians, in relation to theta rhythm. Strength is the average Rayleigh vector length of the phase locking to theta (0 to 1). Type = 1 means calbindin$_{+}$, Type = 0 means calbindin$_{-}$.

SUPPLEMENTARY NOTE 1

MATLAB File Help: CbClassify View code for CbClassify Default Topics

CbClassify

```
Function to classify unitentified cell as putative Cb+ and Cb-.
Classification can use Phase and Strength or Phase and Index.

Output of function is CellClass and Distance. CellClass = 1 means Cb+,
CellClass = 0 means Cb-. Distance is the signed distance to the
classification boundary.
HOW TO USE - Example:
Cell has Phase = 2.6, Strength = 0.45 and Index = 6.4.
To classify using Phase and Strength, call:
  [CellClass,Distance] = CbClassify(2.6,0.45,'Strength')
To classify using Phase and Index, call:
  [CellClass,Distance] = CbClassify(2.6,6.4,'Index')

Function can also run on many cells, if they are passed as column vectors
of e.g. Phases and Strengths. Example:
  [CellClass,Distance] = CbClassify([-3.0;2.7;0.3],[0.5;0.6;0.1],'Strength')

After classification, the training set of identified Cb+ and Cb- cells
are plotted as green and black dots, respectively. The classified cell
is plotted as a red dot.
Pale green and grey background color indicates the classification
boundary.

Training set of identified Cb+ and Cb- cells are also available as an
excel sheet.

----------------------------------------

This is a supplementary file to:
Qiusong Tang, Andrea Burgalossi, Saikat Ray, Robert Naumann, Dominik
Spicher, Christian Ebbesen & Michael Brecht: Pyramidal Grid Cells in
Layer 2 of Medial Entorhinal Cortex (2014)

Copyright 2014 by the authors.

Affiliation:
  Bernstein Center for Computational Neuroscience
  Humboldt University of Berlin
  Philippstr. 13 Haus 6
  10115 Berlin, Germany

To whom correspondence should be addressed:
andrea.burgalossi@bccn-berlin.de or michael.brecht@bccn-berlin.de

You can redistribute it and/or modify it under the terms of the GNU
General Public License as published by the Free Software Foundation.

For the GNU General Public License, see <http://www.gnu.org/licenses/>.
```

```
function [CellClass,Distance] = CbClassify(Pha,Str,StrOrIdx)
% Function to classify unitentified cell as putative Cb+ and Cb-.
% Classification can use Phase and Strength or Phase and Index.
%
% Output of function is CellClass and Distance. CellClass = 1 means Cb+,
% CellClass = 0 means Cb-. Distance is the signed distance to the
% classification boundary.
% HOW TO USE - Example:
% Cell has Phase = 2.6, Strength = 0.45 and Index = 6.4.
% To classify using Phase and Strength, call:
%   [CellClass,Distance] = CbClassify(2.6,0.45,'Strength')
% To classify using Phase and Index, call:
%   [CellClass,Distance] = CbClassify(2.6,6.4,'Index')
%
% Function can also run on many cells, if they are passed as column vectors
% of e.g. Phases and Strengths. Example:
%   [CellClass,Distance] = CbClassify([-3.0;2.7;0.3],[0.5;0.6;0.1],'Strength')
%
% After classification, the training set of identified Cb+ and Cb- cells
% are plotted as green and black dots, respectively. The classified cell
% is plotted as a red dot.
% Pale green and grey background color indicates the classification
% boundary.
%
% Training set of identified Cb+ and Cb- cells are also available as an
% excel sheet.
%
% ----------------------------------------
%
% This is a supplementary file to:
% Qiusong Tang, Andrea Burgalossi, Saikat Ray, Robert Naumann, Dominik
% Spicher, Christian Ebbesen & Michael Brecht: Pyramidal Grid Cells in
% Layer 2 of Medial Entorhinal Cortex (2014)
%
% Copyright 2014 by the authors.
%
% Affiliation:
%   Bernstein Center for Computational Neuroscience
%   Humboldt University of Berlin
%   Philippstr. 13 Haus 6
%   10115 Berlin, Germany
%
% To whom correspondence should be addressed:
% andrea.burgalossi@bccn-berlin.de or michael.brecht@bccn-berlin.de
%
% You can redistribute it and/or modify it under the terms of the GNU
% General Public License as published by the Free Software Foundation.
%
% For the GNU General Public License, see <http://www.gnu.org/licenses/>.

% Load the training set, also available as an excel sheet.
isCbPlus = [0;0;0;0;0;0;0;0;0;0;0;0;0;0;0;0;1;1;1;1;1;1;1;1;1;1;1;];
trainPhases = [2.36050000000000;0.401000000000000;1.52430000000000;1.58920000000000;↙
2.84240000000000;1.08870000000000;-0.120000000000000;1.47330000000000;↙
-2.58880000000000;0.777700000000000;0.726900000000000;0.503900000000000;↙
```

```
-0.692300000000000;-0.315400000000000;3.00600000000000;-1.22480000000000;↙
-1.04790000000000;2.41140000000000;2.85620000000000;2.99230000000000;2.45830000000000;↙
3.00940000000000;-2.58790000000000;-2.61430000000000;-0.407200000000000;↙
2.70560000000000;-2.37310000000000;];
trainStrength = [0.566600000000000;0.225500000000000;0.469000000000000;↙
0.212700000000000;0.0404000000000000;0.158100000000000;0.255200000000000;↙
0.0818000000000000;0.198700000000000;0.0187000000000000;0.167800000000000;↙
0.265700000000000;0.206200000000000;0.169000000000000;0.233600000000000;↙
0.100900000000000;0.259000000000000;0.211900000000000;0.678500000000000;↙
0.580800000000000;0.751900000000000;0.892000000000000;0.253200000000000;↙
0.490300000000000;0.199500000000000;0.569800000000000;0.287100000000000;];
trainIndex = [3.06030000000000;1.37570000000000;4.08910000000000;3.01480000000000;↙
3.90410000000000;3.47700000000000;1.32150000000000;2.57130000000000;2.66360000000000;↙
0.932400000000000;2.56060000000000;2.81200000000000;1.22700000000000;1.89870000000000;↙
3.18580000000000;1.02960000000000;2.04650000000000;2.65730000000000;9.42810000000000;↙
6.00010000000000;3.19010000000000;5.24920000000000;2.85560000000000;2.88980000000000;↙
4.46720000000000;7.90350000000000;1.43540000000000;];


if strcmp(StrOrIdx,'Strength')
% Calculate the training set for the classifier using phase and theta strength
TrainingSet = [cos(trainPhases).*trainStrength, sin(trainPhases).*trainStrength];
% Train the classifier
svmStruct = svmtrain(TrainingSet,isCbPlus,'kernel_function','rbf');

elseif strcmp(StrOrIdx,'Index')
% Calculate the training set for the classifier usind phase and theta index
TrainingSet = [cos(trainPhases).*trainIndex, sin(trainPhases).*trainIndex];
% Train the classifier
svmStruct = svmtrain(TrainingSet,isCbPlus,'kernel_function','rbf');

end

% Calculate the features of the cell to be classified
Cell = [cos(Pha).*Str sin(Pha).*Str];

% Classify the cell
CellClass = svmclassify(svmStruct, Cell);

% Calculate the distance to the classification boundary
    SampleScaleShift = bsxfun(@plus,Cell,svmStruct.ScaleData.shift);
    CellScaled = bsxfun(@times,SampleScaleShift,svmStruct.ScaleData.scaleFactor);
    sv = svmStruct.SupportVectors;
    alphaHat = svmStruct.Alpha;
    bias = svmStruct.Bias;
    kfun = svmStruct.KernelFunction;
    kfunargs = svmStruct.KernelFunctionArgs;
    Distance = kfun(sv,CellScaled,kfunargs{:})'*alphaHat(:) + bias;


% Colors for plotting
Black = [0 0 0];
DarkGrey = [0.6602 0.6602 0.6602];
PaleGreen = [0.5938 0.9833 0.5938];
ForestGreen = [0.1328 0.5430 0.1328];
```

```
Red = [1 0 0];
%figure
figure();
    set(gcf,'PaperUnits','centimeters')
    xSize = 15; ySize = 15;
    xLeft = (21-xSize)/2; yTop = (30-ySize)/2;
    set(gcf,'PaperPosition',[xLeft yTop xSize ySize])
    X = 100;Y = 100;
    set(gcf,'Position',[X Y xSize*50 ySize*50]);
    set(gca,'TickDir','out')
hold on;

if strcmp(StrOrIdx,'Strength')
%% now plot it, usind strength

% make a big matrix to plot the area
rangesMax = [1.1 1.1];
rangesMin = [-1.1 -1.1];
xRange = linspace(rangesMin(1),rangesMax(1),1000);
yRange = linspace(rangesMin(2),rangesMax(2),1000);
[xx,yy] = meshgrid(xRange,yRange);
gridSamples = [xx(:),yy(:)];

% classify the big matrix
gridLabels = svmclassify(svmStruct, gridSamples);
xDisp = reshape(xx,1000,1000);
yDisp = reshape(yy,1000,1000);
labelDisp = reshape(gridLabels,1000,1000);

% plot the matrix using labelDisp as colormap
[ch,ch]=contourf(xDisp,yDisp,labelDisp);
     set(ch,'edgecolor','none');
set(gcf, 'ColorMap', [DarkGrey;PaleGreen])

plot([rangesMin(1) rangesMax(1)],[0 0],'-k')
plot([0 0],[rangesMin(1) rangesMax(1)],'-k')


th = 0:0.005:2*pi;
for i=[0.2 0.4 0.6 0.8]
plot(i*cos(th),i*sin(th),':k')
end
plot(cos(th),sin(th),'k')

h=scatter(TrainingSet(isCbPlus==0,1),TrainingSet(isCbPlus==0,2),90);
set(h,'MarkerEdgeColor',Black,...
              'MarkerFaceColor',Black,...
              'LineWidth',1)

          h=scatter(TrainingSet(isCbPlus==1,1),TrainingSet(isCbPlus==1,2),90);
set(h,'MarkerEdgeColor',Black,...
              'MarkerFaceColor',ForestGreen,...
              'LineWidth',1)

          h=scatter(Cell(:,1),Cell(:,2),90);
```

```
set(h,'MarkerEdgeColor',Black,...
              'MarkerFaceColor',Red,...
              'LineWidth',1)

xlabel('$\cos(\phi) \times S$','Interpreter','LaTex','FontSize',20)
ylabel('$\sin(\phi) \times S$','Interpreter','LaTex','FontSize',20)

xlim([rangesMin(1) rangesMax(1)])
ylim([rangesMin(1) rangesMax(1)])


% Display the result
if CellClass == 0
    title(['Cell is putative Cb-, d = ' num2str↙
(Distance)],'Interpreter','LaTex','FontSize',20)

elseif CellClass == 1
    title(['Cell is putative Cb+, d = ' num2str↙
(Distance)],'Interpreter','LaTex','FontSize',20)

end


elseif strcmp(StrOrIdx,'Index')
% find the max index, we need to plot

% make a big matrix to plot the area
rangesMax = [19 19];
rangesMin = [-19 -19];
xRange = linspace(rangesMin(1),rangesMax(1),1000);
yRange = linspace(rangesMin(2),rangesMax(2),1000);
[xx,yy] = meshgrid(xRange,yRange);
gridSamples = [xx(:),yy(:)];

% classify the big matrix
gridLabels = svmclassify(svmStruct, gridSamples);
xDisp = reshape(xx,1000,1000);
yDisp = reshape(yy,1000,1000);
labelDisp = reshape(gridLabels,1000,1000);

% plot the matrix using labelDisp as colormap
[ch,ch]=contourf(xDisp,yDisp,labelDisp);
     set(ch,'edgecolor','none');
set(gcf, 'ColorMap', [DarkGrey;PaleGreen])

plot([rangesMin(1) rangesMax(1)],[0 0],'-k')
plot([0 0],[rangesMin(1) rangesMax(1)],'-k')

th = 0:0.005:2*pi;
for i=[3 6 9 12 15]
plot(i*cos(th),i*sin(th),':k')
end
plot(18*cos(th),18*sin(th),'k')

h=scatter(TrainingSet(isCbPlus==0,1),TrainingSet(isCbPlus==0,2),90);
```

```
set(h,'MarkerEdgeColor',Black,...
              'MarkerFaceColor',Black,...
              'LineWidth',1)

          h=scatter(TrainingSet(isCbPlus==1,1),TrainingSet(isCbPlus==1,2),90);
set(h,'MarkerEdgeColor',Black,...
              'MarkerFaceColor',ForestGreen,...
              'LineWidth',1)

          h=scatter(Cell(:,1),Cell(:,2),90);
set(h,'MarkerEdgeColor',Black,...
              'MarkerFaceColor',Red,...
              'LineWidth',1)

xlabel('$\cos(\phi) \times I$','Interpreter','LaTex','FontSize',20)
ylabel('$\sin(\phi) \times I$','Interpreter','LaTex','FontSize',20)


xlim([rangesMin(1) rangesMax(1)])
ylim([rangesMin(1) rangesMax(1)])


 % Display the result
if CellClass == 0
    title(['Cell is putative Cb-, d = ' num2str↙
(Distance)],'Interpreter','LaTex','FontSize',20)

elseif CellClass == 1
    title(['Cell is putative Cb+, d = ' num2str↙
(Distance)],'Interpreter','LaTex','FontSize',20)

end

end


end
```

Supplemental Experimental Procedures

All experimental procedures were performed according to German guidelines on animal welfare.

Freely-moving juxtacellular recordings

Experimental procedures for obtaining juxtacellular recordings in freely moving animals were performed similar to earlier publications (Ray et al., 2014; Tang et al., 2014). Briefly, recordings were made from male Wistar and Long-Evans rats (150-350 g) maintained in a 12-h light / dark phase and were recorded in the dark phase. Glass pipettes with resistance 4-6 MΩ were filled with extracellular (Ringer) solution containing (in mM) NaCl 135, KCl 5.4, HEPES 5, $CaCl_2$ 1.8, and $MgCl_2$ 1 (pH = 7.2) and Neurobiotin (1-2%). Animal implantations were performed as previously described (Burgalossi et al., 2011; Herfst et al., 2012, Tang et al., 2014), with a basic head-implant including a metal post for head-fixation and placement of a miniaturized preamplifier, a plastic ring and a protection cap (Herfst et al., 2012). In order to target the dorsalmost region of medial entorhinal cortex, a plastic ring was glued on the skull surface 0.2- 0.8 mm anterior to the transverse sinus and 4.5-5 mm lateral to the midline. After implantation, rats were allowed to recover from the surgery and were habituated to head-fixation for 3-5 days, as previously described (Houweling et al., 2008, Tang et al., 2014). Rats were trained in the experimental arena for 3-7 days (multiple sessions per day, 15-20 min duration each). Within the recording arena (70 x 70 cm or 1 x 1 m square black box, with a white cue card on the wall; 1 cell was recorded in a square arena, 60 cm x 80 cm), rats were trained to chase for chocolate or sugar pellets. Training was performed both before and after implantation (see below), or after implantation only. On the day of recording, under isoflurane anesthesia (1-3%), implants were completed, and an additional metal post was cemented, which served to anchor the miniaturized micromanipulator (Kleindiek Nanotechnik GmbH; Lee et al., 2006; Tang et al., 2014). 3-4 hours to 1 day later after recovery from anesthesia, rats were head-fixed, full implants were assembled, and the miniaturized micromanipulator and preamplifier were secured to the metal posts. The glass recording pipette was advanced into the brain; a thick agarose solution (4-5% in Ringer) was applied into the recording chamber for sealing the craniotomy and stabilization. Animals were then released and gently transferred into the behavioral arena. To minimize discomfort from the head implant, we sometimes supplied local anesthesia in the neck region. Juxtacellular recordings were established while animals were running in the arena. Juxtacellular labeling was attempted at the end of the recording session according to standard procedures (Pinault et al., 1996). A number of recordings (non-identified recordings; see data analysis) putatively in layer 2 (n = 61) were either lost before the labeling could be attempted, or the recorded neurons could not be unequivocally identified. After the experiment, the animals were euthanized with an overdose of ketamine or urethane and perfused transcardially with 0.1 M PB followed by 4% paraformaldehyde solution, shortly after the labeling protocol. Juxtacellular recordings in anesthetized animals (Ray et al., 2014) were performed under ketamine/urethane anesthesia according to established procedures (Klausberger et al., 2003, Quilichini et al., 2010). The juxtacellular signals were amplified by the ELC-03XS amplifier and sampled at 20 kHz by a data-acquisition interface under the control of PatchMaster 2.20 software. The animal's location and head-direction was automatically tracked at 25 Hz by the Neuralynx video tracking system and two head-mounted LEDs.

Tetrode recordings

Tetrode recordings (n = 126 layer 2 single units) were obtained as previously described in detail (von Heimendahl et al., 2012). Tetrodes were turned from 12.5 μm diameter nichrome wire (California Fine Wire Company) and goldplated to ~250 kOhm impedance. Spiking activity and local field potential were recorded at 32 kHz (Neuralynx; Digital Lynx). Local field potential for theta phase assignment was recoded from the same tetrode as single units, relative to one tetrode left in superficial cortex. All recordings were done in a 1x1m box with behavioral training tasks same as juxtacellular procedures. The animal's location and head-direction was automatically tracked at 25 Hz by video tracking and head-mounted LEDs, as described above. After recordings, tetrode tracks were lesioned and the animal was trancardially perfused. The brain was sectioned tangentially and recording sites assigned by histology. Spikes were pre-clustered using KlustaKwik (K.D. Harris, Rutgers University) and manually using MClust (A.D. Redish, University of Minnesota). Cluster quality was assessed by spike shape, ISI-histogram, L-ratio and isolation distance, as previously described (von Heimendahl et al., 2012). Putative interneurons were identified based on firing rate, spike shape and ISI-histogram and were excluded from classification.

Neurobiotin labeling and calbindin immunohistochemistry

For histological analysis of juxtacellularly-labeled neurons, Neurobiotin was visualized with streptavidin conjugated to Alexa 546 (1:1000). Subsequently, immunohistochemistry for Calbindin was performed as previously described (Ray et al., 2014) and visualized with Alexa Fluor 488. After fluorescence images were acquired, the Neurobiotin staining was converted into a dark DAB reaction product. Neuronal morphologies were reconstructed by computer-assisted manual reconstructions (Neurolucida).

Spine density measurement

To assess the spine density of calbindin^{+} and calbindin^{-} dendrites, we labeled neurons in vivo juxtacellularly and identified the cells based on their calbindin immunoreactivity. We counted spines of fluorescent and DAB converted cells (10 calbindin^{+} and 10 calbindin^{-} neurons) at 50 μm, 100 μm and 150 μm from the soma. The spine counts were normalized by dendritic length to obtain the number of spines per μm.

Estimate of the fraction of unintentionally included non-layer 2 cells

Targeting recordings to layer 2 was achieved by mapping (1) the depth at which a pronounced increase in spiking activity and multi-unit synchrony during running was observed (Domnisoru et al., 2013) and (2) the L2/L1 border, which was always easy to identify as a reference point due to the drop in spiking activity and the more prominent local field potential gamma oscillations during theta epochs observed in L1 (Quilichini et al., 2010). We estimated the fraction of non-layer 2 principal cells included in our sample and expect that this mistaken fraction is in the < 10% range and probably consists mainly of parasubicular cells.

This estimate was computed as follows:

(1) We included 126 unidentified cells from tetrodes, and according to histology this sample does not contain off-target cells, as all recording sites could be reliably assigned to medial entorhinal cortex layer 2.

(2) The laminar mistakes in our assignment of juxtacellular recordings seem to be small, i.e. in 31 recording attempts where we aimed at layer 2, we never recovered layer 6, layer 5 and layer 4 cells, but indeed recovered cells in the expected target. In only 2 additional cases we recovered cells in layer 3, where we expected to find layer 2 cells. Hence we expect a 6% laminar error rate.

(3) Dorsoventral / mediolateral mistakes. We never recovered unintentionally postrhinal, retrospenial or lateral entorhinal cells in our medial entorhinal cortex recording attempts. However, in 9 experiments where we aimed at targeting layer 2, 9 parasubicular cells were recovered instead. Thus, there are probably also parasubicular cells in the unidentified cells sample and this error might appear to be substantial (22% error rate). However, in 36 of the 61included unidentified cells we could exclude such mistakes, because we identified the respective tracks in the correct target location. In 25 included unidentified juxtacellular recordings we could not rule out such mistakes, because tracks were not found, because of poor histology or proximity of tracks to the parasubiculum.

From these numbers we expect about 4 laminar mistakes (unintentionally recorded layer 3 cells) in the 61 included juxtacellular recordings. We expect about 6 dorsoventral / mediolateral mistakes (unintentionally recorded parasubicular cells) in the 25 included juxtacellular recordings, where we could not exclude such mistakes.

This leads to the following overall numbers: 16% unidentified recordings are expected to be non layer 2 cells. This corresponds to a 5% rate of mistakes in our overall sample (identified and unidentified cells).

Analysis of theta locking

For all cells, we calculated the locking to theta phase based on spiking discharge in relation to theta rhythm in the local field potential. The local field potential was zero-phase band-pass filtered (4-12 Hz) and a Hilbert transform was used to determine the instantaneous phase of the theta wave. The strength of locking to theta phase, S, and the preferred phase angle, φ, was defined as the modulus and argument of the Rayleigh average vector of the theta phase at all spike times. Only spikes during running (speed cutoff = 1 cm/s for juxtacellular signals, 5 cm/s for tetrode recordings) were included in the analysis. Only cells with firing rate ≥ 0.5 Hz were included in the analysis (Barry et al., 2012b). Both the analysis procedures and the juxtacellular data set largely correspond to our recent publication (Ray et al., 2014), whereby a more stringent band-pass filtering was applied in a subset of cells.

Analysis of Spatial Modulation

The position of the rat was defined as the midpoint between two head-mounted LEDs. A running speed threshold (2 cm/s) was applied for isolating periods of rest from active movement. Color-coded firing maps were plotted. For these, space was discretized into pixels of 2.5 cm x 2.5 cm, for which the occupancy z of a given pixel x was calculated as

$$z(x) = \sum_t w(|x - x_t|)\Delta t$$

where x_t is the position of the rat at time t, Δt the inter-frame interval, and w a Gaussian smoothing kernel with σ = 5cm.
Then, the firing rate r was calculated as

$$r(x) = \frac{\sum_i w(|x - x_i|)}{z}$$

where x_i is the position of the rat when spike i was fired. The firing rate of pixels, whose occupancy z was less than 20 ms, was considered unreliable and not shown.
To determine the spatial periodicity of juxtacellularly recorded neurons, we determined spatial autocorrelations. The spatial autocorrelogram was based on Pearson's product moment correlation coefficient:

$$r(\tau_x, \tau_y) = \frac{n\sum f(x,y)f(x-\tau_x, y-\tau_y) - \sum f(x,y)\sum f(x-\tau_x, y-\tau_y)}{\sqrt{n\sum f(x,y)^2 - (\sum f(x,y))^2}\sqrt{n\sum f(x-\tau_x, y-\tau_y)^2 - (\sum f(x-\tau_x, y-\tau_y))^2}}$$

where, $r(\tau_x, \tau_y)$the autocorrelation between pixels or bins with spatial offset τ_x and τ_y. f is the image without smoothing or the firing rate map after smoothing, n is the number of overlapping pixels or bins. Autocorrelations were not estimated for lags of τ_x and τ_y, where n < 20. For spatial and head-directional analysis, both a spatial (> 50% spatial coverage) and a firing rate inclusion criterion (> 0.5 Hz) were applied. Spatial coverage was defined as the fraction of visited pixels (bins) in the arena to the total pixels.

Analysis of Spatial Information

For all neurons, we calculated the spatial information rate, I, from the spike train and rat trajectory:

$$l = \frac{1}{T}\int r(x)\log_2\frac{r(x)}{\bar{r}}o(x)dx$$

where r(x) and o(x) are the firing rate and occupancy as a function of a given pixel x in the rate map. $\bar{r}$ is the overall mean firing rate of the cell and T is the total duration of a recording session (Skaggs et al., 1993). A cell was determined to have a significant amount of spatial information, if the observed spatial information rate exceeded the 95th percentile of a distribution of values of I obtained by circular shuffling. Shuffling was performed by a circular time-shift of the recorded spike train relative to the rat trajectory by a random time $t' \in]0, T[$ for 1000 permutations (von Heimendahl et al., 2012; Bjerknes et al., 2014).

Analysis of Gridness

Grid scores were calculated as previously described (Barry et al., 2012) by taking a circular sample of the autocorrelogram, centered on, but excluding the central peak. The Pearson correlation of this circle with its rotation for 60 degrees and 120 degrees was obtained (on peak rotations) and also for rotations of 30 degrees, 90 degrees and 150 degrees (off peak rotations). Gridness was defined as the minimum difference between the on-peak rotations and off-peak rotations. To determine the grid scores, gridness was evaluated for multiple circular samples surrounding the center of the autocorrelogram with circle radii increasing in unitary steps from a minimum of 10 pixels more than the width of the radius of the central peak to the shortest edge of the autocorrelogram. The radius of the central peak was defined as the distance from the central peak to its nearest local minima in the spatial autocorrelogram. The radius of the inner circle was increased in unitary steps from the radius of the central peak to 10 pixels less than the optimal outer radius. The grid score was defined as the best score from these successive samples. Grid scores reflect both the hexagonality in a spatial field and also the regularity of the hexagon. To disentangle the effect of regularity from this index, and consider only hexagonality, we transformed the elliptically distorted hexagon into a regular hexagon and computed the grid scores (Barry et al., 2012). A linear affine transformation was applied to the elliptically distorted hexagon, to stretch it along its minor axis, until it lay on a circle, with the diameter equal to the major axis of the elliptical hexagon. The grid scores were computed on this transformed regular hexagon (Barry et al., 2012).

Analysis of Border Cells

To determine the modulation of a cell firing along a border, we determined border scores (Solstad et al., 2008). Border fields were identified from a collection of neighboring pixels having a firing rate higher than 0.3 times the maximum firing rate and covering an area of at least 100 cm (Sargolini et al., 2006). The coverage (Cm) along a wall was defined as the maximum length of a putative border field parallel to a boundary, divided by the length of the boundary. The mean firing distance (Dm) of a field was defined as the sum of the square of its distance from the boundary, weighted by the firing rate (Solstad et al., 2008). The distance from a boundary was defined as the exponential of the square of the distance in pixels from the closest boundary, normalized by half the length of the boundary. Border scores were defined as the maximum difference between Cm and Dm, divided by their sum, and ranged from -1 to +1.

Analysis of Head Direction

Head-direction tuning was measured as the excentricity of the circular distribution of firing rates. For this, firing rate was binned as a function of head-direction (N = 36). A cell was said to have a significant head-direction tuning, if the length of the average vector exceeded the 95th percentile of a distribution of average vector lengths calculated from shuffled data and had a Rayleigh vector length > 0.3. Data was shuffled by applying a random circular time-shift to the recorded spike train for 1000 permutations.

Classification of non-identified cells into putative cell types

For classification based on strength of locking to theta phase, S, and preferred theta phase angle, φ, we built a support vector machine using the built-in functions of the MATLAB Statistics Toolbox (The MathWorks Inc., Natick, MA, USA) using pairs of φ and S obtained from juxtacellular recording of identified cells. Because the phase angle is a circular variable, we trained the classifier on a space of the vectors (cos(φ)·S,sin(φ)·S), scaled to zero mean and unit variance using a gaussian radial basis kernel function with a scaling factor, sigma, of 1. To avoid cross-contamination of the two clusters, we employed a guard zone and excluded cells with a distance to the classification hyperplane < 0.1 from classification (white dots in Figure 2C). Classifier robustness was evaluated using a bootstrapping approach. To test if the putative calbindin$^+$/calbindin$^-$ border suggested by the classifier based on our limited set of identified cells would also correctly classify a large number of non-identified cells, we fitted the appropriate probability density functions to the theta strength and phase angle of identified cells (beta distributions and circular Gaussian distributions, respectively) and generated 10.000 calbindin$^+$ and 10.000 calbindin$^-$ testing cells drawn from these distributions (Figure S2A and S2B). Testing cells were classified and found to be classified 75.5% correctly for calbindin$^+$ cells and 86.7 % correctly for calbindin$^-$ cells (Figure S2C), suggesting that our classifier generally performs well and is not just overfitting our small dataset of identified cells from freely-moving rats. Assuming the prior distribution of ~34% calbindin$^+$ neurons , ~53% reelin$^+$ (calbindin$^-$) neurons and ~13% interneurons in layer 2 of the medial entorhinal cortex of a rat (Figure S1A and S1B), we estimate the purity (positive predictive value) of putative calbindin$^+$ and putative calbindin$^-$ cells assigned by our classifier to be 83% and 89%, respectively (Figure S2D). This gives us the final cell sample purity of our putative and identified dataset of 84% and 90% for calbindin$^+$ and calbindin- cells, respectively.

Classification of cells into functional categories

Cells were classified as head-direction cells, grid cells, conjunctive cells, border cells and nonspatially modulated cells based on their grid score, border score, spatial information and significance of head-directionality according to the following criteria:

Head direction cells: Rayleigh vector length > 0.3 & significant head-direction tuning (Boccara et al., 2010)

Grid cells: Grid score > 0.3 & significant spatial information.

Border cells: Border score > 0.5 & significant spatial information (Solstad et al., 2008), or those who passed border test (Lever et al., 2009).

Spatially irregular cells: significant spatial information (Bjerknes et al., 2014).

Non-spatially modulated cell: no significant spatial information.

In agreement with previous work (Solstad et al., 2008), few cells (n = 6) passed both the border cell and the grid cell threshold. These six cells were assigned to be grid cells by visual inspection.

SUPPLEMENTARY REFERENCES

Barry, C., Bush, D., O'Keefe, J., and Burgess, N. (2012). Models of grid cells and theta oscillations. Nature *488,* 103.

Houweling, A.R., Doron, G., Voigt, B.C., Herfst, L.J., and Brecht, M. (2010). Nanostimulation: manipulation of single neuron activity by juxtacellular current injection. J. Neurophysiol. *103,* 1696-704.

Lee, A.K., Manns, I.D., Sakmann, B., and Brecht, M. (2006). Whole-cell recordings in freely moving rats. Neuron *51,* 399-407.

Pinault, D. (1996). A novel single-cell staining procedure performed in vivo under electrophysiological control: morpho-functional features of juxtacellularly labeled thalamic cells and other central neurons with biocytin or Neurobiotin. J. Neurosci. Methods *65,* 113-136.

Quilichini, P., Sirota, A., and Buzsáki, G. (2010). Intrinsic circuit organization and theta-gamma oscillation dynamics in the entorhinal cortex of the rat. J. Neurosci. *18,* 11128-42.

Chapter 4

Conserved size and periodicity of layer 2 pyramidal patches in medial/caudal entorhinal cortex.

Published as:

Naumann, R. et al. (2016). Conserved size and periodicity of layer 2 pyramidal patches in medial/caudal entorhinal cortex. *J. Comp. Neurol. 524:783-806*

doi: 10.1002/cne.23865

Conserved Size & Periodicity of Pyramidal Patches in Layer 2 of Medial/ Caudal Entorhinal Cortex

Robert K. Naumann[‡*#], Saikat Ray[‡*], Stefan Prokop[1], Liora Las[2], Frank L. Heppner[1] & Michael Brecht[‡]

* These authors contributed equally

[‡]Bernstein Center for Computational Neuroscience

Humboldt University of Berlin
Philippstr. 13 Haus 6
10115 Berlin, Germany

[1]Institut für Neuropathologie
Charité - Universitätsmedizin Berlin, Campus Charité Mitte
Charitéplatz 1 | Virchowweg 15
10117 Berlin, Germany

[2]Department of Neurobiology, Weizmann Institute of Science,

Rehovot 76100, Israel.

[#]Current Address: Max-Planck-Institute for Brain Research, Max-von-Laue-Str. 4, 60438 Frankfurt am Main, Germany

Abbreviated title: Comparative entorhinal pyramidal patches

Associate editor: Kathleen S. Rockland

Key words: Calbindin-positive pyramidal neuron patches, grid-like arrangement of patches in layer 2, conserved patch size and cell number per patch, variable patch number and cholinergic innervation pattern

Corresponding author: Michael Brecht

Email: michael.brecht@bccn-berlin.de

Acknowledgements:

This work was supported by the Deutsche Zentrum für Neurodegenerative Erkrankungen (DZNE), the Humboldt Universität zu Berlin, the Bernstein Center for Computational Neuroscience Berlin, the German Federal Ministry of Education and Research (BMBF, Förderkennzeichen 01GQ1001A), NeuroCure, European Research Council grant and the Gottfried Wilhelm Leibniz prize of the DFG.

Abstract

To understand the structural basis of grid cell activity, we compare medial entorhinal cortex architecture in layer 2 across five mammalian species (Etruscan shrews, mice, rats, Egyptian fruit bats and humans), bridging ~100 million years of evolutionary diversity. Principal neurons in layer 2 are divided into two distinct cell types, pyramidal and stellate, based on morphology, immunoreactivity and functional properties. We confirm the existence of patches of calbindin-positive pyramidal cells across these species, arranged periodically according to analyses techniques like spatial autocorrelation, grid scores, and modifiable areal unit analysis. In rodents, which show sustained theta oscillations in entorhinal cortex, cholinergic innervation targeted calbindin patches. In bats and humans, which only show intermittent entorhinal theta activity, cholinergic innervation avoided calbindin patches. The organization of calbindin-negative and calbindin-positive cells showed marked differences in entorhinal subregions of the human brain. Layer 2 of the rodent medial and the human caudal entorhinal cortex were structurally similar in that in both species patches of calbindin-positive pyramidal cells were superimposed on scattered stellate cells. The number of calbindin-positive neurons in a patch increased from ~80 in Etruscan shrews to ~800 in humans, only a ~10-fold over a 20000-fold difference in brain size. The relatively constant size of calbindin patches differs from cortical modules such as barrels, which scale with brain size. Thus, selective pressure appears to conserve the distribution of stellate and pyramidal cells, periodic arrangement of calbindin patches, and relatively constant neuron number in calbindin patches in medial/caudal entorhinal cortex.

Introduction

The entorhinal cortex is uniquely positioned as a gateway between the neocortex and the hippocampus, and the discovery of grid cells and their remarkable discharge pattern (Hafting et al., 2005) established it as a key structure for spatial representation in mammals. In rats, grid cells are most abundant in layer 2 of the medial entorhinal cortex (Boccara et al., 2010). However, grid cells were not only recorded in rats but also in the entorhinal cortex of a range of mammalian species including mice (Fyhn et al., 2008), bats (Yartsev et al., 2011), monkeys (Killian et al., 2012), and humans (Doeller et al., 2010; Jacobs et al., 2013; reviewed in Las and Ulanovsky, 2014). To understand the structural basis of cellular activity in the entorhinal cortex, we thus compare the organization in layer 2 of five mammalian species (Etruscan shrews, mice, rats, Egyptian fruit bats and humans), which come from 4 mammalian orders covering almost 100 million years of divergent evolutionary history and span a ~ 20000 fold range of brain sizes.

The simplest areal partitioning scheme of the human entorhinal region consists of two subdivisions, a lateral and a medial entorhinal area (Brodmann, 1909). These areas have been identified even in the smallest mammals (Rose, 1927a), and hence we follow this scheme. Studies in the human entorhinal cortex have suggested a multitude of parcellation schemes with up to 23 subfields (Rose, 1927b; Sgonina, 1938; Braak, 1972; Krimer et al., 1997; Hanke and Yilmazer-Hanke, 1997), however a subdivision into 8 fields adapted from studies on macaque monkeys (Amaral et al., 1987) is now most commonly used (Beall and Lewis, 1992; Insausti et al., 1995; Insausti and Amaral 2011). It is likely that the medial entorhinal cortex of rodents corresponds to the dorso-caudal part of the entorhinal cortex in primates since both are close to the parasubiculum and presubiculum (Bakst and Amaral, 1984) or medio-caudal on the basis of their projections to the dentate gyrus (Insausti, 1993). Consequently, the rodent lateral entorhinal cortex may correspond to the ventro-rostral primate entorhinal cortex.

Anatomical modules in the supragranular layers of the cerebral cortex were described in a wide range of species and cortical areas (Manger et al., 1998; Ding and Rockland, 2001; Ichinohe et al., 2003; Ichinohe, 2012). Such modules are characterized by their complex and variable anatomical structure (Rockland and Ichinohe, 2004; Rockland, 2010) and their relation to various neurotransmitter systems (Gaspar et al., 1990; Akil & Lewis, 1994; van Kleef et al., 2012). In the entorhinal cortex, this complexity is exemplified even within a single cortical region containing different types of modules (Beall and Lewis, 1992). Recent studies in rodents identified functional modules of grid cells with different spacing between their firing fields along the dorso-ventral axis of entorhinal cortex (Barry et al., 2007; Brun et al., 2008; Stensola et al. 2012) and also provided evidence for anatomical modularity of entorhinal circuits (Burgalossi et al., 2011; Ray et al., 2014; Heys et al., 2014). Yet, relating functional and anatomical modularity has been difficult in the entorhinal cortex in particular (Burgalossi and Brecht, 2014) and throughout cortex in general (Horton and Adams, 2005; da Costa and Martin, 2010).

The human temporal lobe shows a distinct surface structure comprising myelinated fibers and cellular islands in the entorhinal cortex and presubiculum (Klingler, 1948). Islands can be visualized by Nissl staining, histochemistry or immunoreactivity (Braak, 1972; Solodkin and van Hoesen, 1996; Mikkonen et al, 1997; van Hoesen et al, 2000). In primates, most cellular islands consist mainly of stellate cells (Braak et al., 1976), which stain positively for neurofilament protein, cytochrome oxidase, and are surrounded by parvalbumin positive neuropil (Beall and Lewis, 1992; Hevner and Wong-Riley, 1992).

Another set of modules, formed by a class of small pyramidal cells located in between and deep to the islands, is stained by an antibody against calbindin (Beall and Lewis, 1992; Suzuki and Porteros, 2002). Calbindin positive cells in superficial cortical layers show pyramidal morphology (Hayes and Lewis, 1992) and are typically not GABAergic (Kubota et al., 1994; Kitamura et al., 2014). In the rodent entorhinal cortex ~ 88 % of calbindin-positive cells are glutamatergic (Peterson et al., 1996) and form discrete cell clusters (Fujimaru and Kosaka, 1996; Ray et al., 2014).

In layer 2 of the medial entorhinal cortex, stellate cells have markedly different electrophysiological properties from pyramidal cells (Alonso and Llinás, 1989; Alonso and Klink, 1993). Reelin-positive cells project to the dentate gyrus and show electrophysiological parameters of stellate cells (Varga et al., 2010), whereas calbindin positive cells project to CA1 (Kitamura et al., 2014) and have electrophysiological properties described previously for pyramidal cells (Klink and Alonso, 1997). Calbindin-positive pyramidal cells show strong theta modulation and are arranged in a hexagonal grid of patches that receives cholinergic innervation (Ray et al., 2014). Grid cells occur in discrete spatial patterns (Barry et al., 2007; Stensola et al., 2012; Heys et al., 2014). Thus, based on clustering, rhythmicity, cholinergic modulation (Ray et al., 2014) and spatial discharge properties (Tang et al., 2014), we proposed that calbindin positive pyramidal cells play an important role in generating grid cell activity. Another line of work implicated the same neuron clusters as key regulators of temporal association memory (Kitamura et al., 2014).

Here we compare the laminar structure, the spatial arrangement of patches in the tangential plane, the cholinergic innervation and the patch size and numbers of calbindin-positive pyramidal cells in medial/ caudal entorhinal cortex across five mammalian species.

Materials and Methods

All experimental procedures were performed according to German and Israeli guidelines on animal welfare.

Animals

Male and female young adult wistar rats (N = 22), C57BL/6JOlaHsd inbred mice (N = 16), Etruscan shrews (N = 13), and Egyptian fruit bats (N = 10) were used in the study. All experimental procedures were performed according to the German guidelines on animal welfare under the supervision of local ethics committees.

Human brain tissue

Brain autopsies (N = 6) were performed following written consent for pathological examination according to the law of the city of Berlin, Germany. Brain tissues were obtained from males and females varying within the age of 56-67 years and having post mortem processing intervals between 24-96 hours. Brain tissue was then fixed in 4% formaldehyde, derived from paraformaldehyde, in 0.1 M phosphate buffer (PFA) for 1-4 days. Following routine diagnostic neuropathological examination, parts of the medial entorhinal cortex were obtained by separating the entorhinal cortex from the remaining hemisphere by a cut parallel to the surface of the medial entorhinal cortex and, thereafter, used for sectioning and conventional as well as immunohistochemical stainings. This procedure was approved by the Charité ethics commission (EA1/320/13).

Tissue Preparation

Etruscan shrews, mice and rats were anaesthetized by isoflurane, and then euthanized by an intraperitoneal injection of 20% urethane, while bats were euthanized by an overdose of pentobarbital. Animals were then perfused transcardially with first 0.9% phosphate buffered saline solution, followed by PFA. After perfusion, brains were removed from the skull and postfixed in PFA overnight. Brains were then transferred to 10% sucrose solution for one night and subsequently immersed in 30% sucrose solution for at least one night for cryoprotection. The brains were embedded in Jung Tissue Freezing Medium (Leica Microsystems Nussloch, Germany), and subsequently mounted on the freezing microtome (Leica 2035 Biocut) to obtain coronal, sagittal sections or tangential sections parallel to the pia. We used 20 µm thick sections for tangential sections of shrew cortex, 30 µm thick sections for coronal sections of shrew cortex and tangential sections of mouse cortex, 60 µm thick sections for human cortex and 40 µm thick sections in all other cases.

Tangential sections of the medial entorhinal cortex were obtained by separating the entorhinal cortex from the remaining hemisphere by a cut parallel to the surface of the medial entorhinal cortex. For subsequent sectioning the surface of the entorhinal cortex was attached to the block face of the microtome, which means the most superficial sections were cut last. We found this reliably generates sections parallel to the surface of the entorhinal cortex.

Histochemistry

Acetylcholinesterase activity

Acetylcholinesterase (AChE) was stained following the method of Ichinohe et al. (2008) and Tsuji (1998). After washing in a mixture containing 1 ml of 0.1 M citrate buffer (pH 6.2) and 9 ml 0.9% saline (CS), sections were incubated with CS containing 3 mM $CuSO_4$, 0.5 mM $K_3Fe(CN)_6$, and 1.8 mM acetylthiocholine iodide for 30 min. After rinsing in 0.1 M phosphate buffer (PB), sections were intensified in PB containing 0.05% 3,3'- Diaminobenzidine (DAB) and 0.03% nickel ammonium sulfate.

Myelin

For myelin staining we used the gold-chloride protocol (Schmued, 1990). Briefly, free-floating cryostat sections were incubated for 2-4 hours in a 0.1 % solution of gold chloride in 0.02 M phosphate buffer, pH 7.4, and 0.9 % sodium chloride. After staining, sections were rinsed for 5 min in 0.9 % sodium chloride, fixed for 5 min in a 2.5 % solution of sodium thiosulfate, and rinsed again for 30 min before mounting with Mowiol.

Cytochrome oxidase

Cytochrome oxidase activity was visualized according to the protocol of Wong-Riley (1979).

Synaptic Zinc

After perfusion with 0.1% sodium sulfide in 0.1 M PB, brain sections were rinsed with 0.1 M PB, followed by 0.01 M PB. For the visualization of synaptic zinc, sections were developed as described by Danscher & Stoltenberg (2006). In brief, sections were exposed to a solution containing gum arabic, citrate buffer, hydroquinone and silver lactate for 60–120 minutes, in the dark at room temperature. Development of reaction products was checked under a microscope and terminated by rinsing the sections in 0.01 M PB and, subsequently in 0.1 M PB.

NADPH Diaphorase

NADPH diaphorase activity was visualized according to the protocol of Paxinos et al. (2009). Sections were washed in 0.1 M PB and then incubated in 0.1 M PB containing 1.35 mM ß-NADPH (Sigma, N1630), 305 µM nitroblue tetrazolium (Sigma, N6876), 1 mM MgCl2, and 0.5% Triton X-100. The incubation was done at 37 °C for 30 min and terminated by washing in PB.

Immunohistochemistry

Tangential, horizontal and sagittal sections were immunostained with the antibodies listed in Table 1. For multiple antibody labeling, antibodies raised in different host species were combined. In each series of sections the primary antibody was omitted in one section to control

for secondary antibody specificity. This always led to complete absence of staining. In one human brain, we compared antigen retrieval to no pretreatment in adjacent tissue slabs. We used the antigen retrieval method indicated by Evers and Uylings (1997) for anti-calbindin antibodies. However, we did not detect a qualitative improvement in staining, possibly due to the short fixation time of the human brain tissue we used. Overall we found staining quality to be more variable in human brain tissue than in perfusion fixed animals, possibly due to the long and variable post-mortem interval. For immunofluorescence, the sections were pre-incubated in a blocking solution containing 0.1 M PBS, 2% Bovine Serum Albumin (BSA) and 0.5% Triton X-100 (PBS-X) for an hour. Following this, the primary antibody was diluted as described in Table 1 with PBS-X and 1% BSA and incubated overnight at 4°C. Subsequently, secondary antibodies conjugated to different fluorophores (Invitrogen, Carlsbad, CA; 488 nm, 546 nm excitation wavelength) and reactive to different species were diluted (1:500) with PBS-X to incubate the sections for two hours, in the dark, at room temperature. After the staining procedure, sections were mounted on gelatin coated glass slides and cover-slipped with Fluoromount (0100-01, Southern Biotech, Birmingham AL, USA) mounting medium.

SMI-32

The SMI-32 mouse monoclonal IgG1 antibody was prepared against the nonphosphorylated epitope of neurofilament H isolated from homogenized hypothalami from Fischer 344 rats. SMI-32 has been shown to visualize two bands (200 and 180 kDa), which merge into a single neurofilament H line on two-dimensional blots and is expressed in neuronal cell bodies, dendrites, and some thick axons in both the central and the peripheral nervous systems (Sternberger and Sternberger, 1983). SMI-32 immunreactivity has previously been shown to label stellate cells, multipolar neurons, and modified pyramidal neurons in layer 2 of human entorhinal cortex (Beall and Lewis, 1992). These studies demonstrate that this antibody generally produces strong labeling in medium-sized to large pyramidal neurons located in layers 3 and 5 as well as demarcating the six cortical layers of the ferret visual cortex (Homman-Ludiye et al., 2010).

Calbindin

The mouse monoclonal anti-calbindin (CB) antibody was raised using hybridization of mouse myeloma cells with spleen cells from mice immunized with the CB D-28k that was purified from the chicken gut (Celio M.R. et al., 1990). This monoclonal antibody is not known to cross-react with other known calcium binding-proteins and specifically stains the 45Ca-binding spot of CB D-28k (MW 28,000, IEP 4.8) of different mammals in a two-dimensional gel (manufacturer's technical information). The rabbit polyclonal anti-CB antiserum was raised against recombinant rat calbindin D-28k (Airaksinen et al., 1997). It cross-reacts with calbindin D-28k from many mammalian species. In immunoblots it recognizes a single band of approximately 27-28 kDa (manufacturer's technical information).

NeuN

One series of coronal sections was stained for neuronal nuclei with mouse anti-neuronal nuclei I (NeuN) antibody. This purified monoclonal (Clone A60) antibody (Chemicon, Catalog Nr. MAB377) which we used at a dilution of 1:1,000 was raised against purified cell nuclei from mouse brain. A previous lot of this antibody recognized 2-3 bands in the 46-48 kDa range and

possibly another band at approximately 66 kDa (manufacturer's technical information). Staining of sections through the cerebral cortex produced a pattern of neuronal nuclei as expected from previous descriptions (Lind et al., 2005).

Cell Counts and Patch Sizes

In the analysis for determining cell numbers and patch sizes, patches in consecutive sections were matched by overlaying them in Adobe Photoshop, and only the ones, which could be reliably followed in all the sections under consideration, were taken up for further analysis. Image stacks were first converted into .tiff files for different channels and focal planes using ImageJ. These files were then merged back together into a single file using the Neurolucida image stack module. In these patches all cells positive for Calbindin were counted manually. In the rat brains, also cells positive for NeuN were counted.

Quantification of patch sizes was done with the Neurolucida software by using the mean of maximum and minimum Feret diameter, defined as the maximum and minimum diameter of the patch, respectively. To correct for overestimation of neurons due to potential double counting in adjacent sections, we estimated the number of cells in a section assuming uniform cell density and uniform spherical cell shape in the section and applied a correction factor of $s / (s+d)$ where, s is the section thickness and d is the diameter of a cell, to correct for the cells which would be counted again in an adjacent section (Abercrombie, 1946).

Analysis of Spatial Periodicity

To determine the spatial periodicity of calbindin-positive patches, we calculated spatial autocorrelations and spatial Fourier spectrograms. The spatial autocorrelogram was based on Pearson's product moment correlation coefficient (as in Sargolini et al., 2006):

$$r(\tau_x, \tau_y) = \frac{n\sum f(x,y) f(x-\tau_x, y-\tau_y) - \sum f(x,y) \sum f(x-\tau_x, y-\tau_y)}{\sqrt{n\sum f(x,y)^2 - (\sum f(x,y))^2}\sqrt{n\sum f(x-\tau_x, y-\tau_y)^2 - (\sum f(x-\tau_x, y-\tau_y))^2}}$$

where, $r(\tau_x, \tau_y)$ is the autocorrelation between pixels or bins with spatial offset τ_x and τ_y. f is the image without smoothing and n is the number of overlapping pixels. Autocorrelations were not estimated for lags of τ_x and τ_y, where n<20. Grid scores were calculated as previously described (Sargolini et al., 2006) by taking a circular sample of the spatial autocorrelation map, centered on, but excluding the central peak. Autocorrelograms were obtained by calculating the Pearson correlation coefficient of this circle with its rotation by every degree for up to 180 degrees. On peak rotations were defined as the Pearson correlation values for rotations of 60 degrees and 120 degrees and off peak rotations as the Pearson correlation coefficient values for rotations of 30 degrees, 90 degrees and 150 degrees. Gridness was defined as the minimum difference between the on-peak rotations and off-peak rotations. To determine the grid scores, gridness was evaluated for multiple circular samples surrounding the center of the spatial

autocorrelation map with circle radii increasing in unitary steps from a minimum of 10 pixels more than the width of the radius of the central peak to the shortest edge of the spatial autocorrelation map. The grid score was defined as the best score from these successive samples (Langston et al, 2010). The radius of the central peak was defined as the distance from the central peak to its nearest local minima in the spatial autocorrelogram.

Grid scores reflect both the hexagonality in a spatial field and also the regularity of the hexagon. To disentangle the effect of regularity of the hexagon from this index, and consider only hexagonality, we transformed the elliptically distorted hexagon into a regular hexagon (Barry et al., 2012) and computed the grid scores. A linear affine transformation was applied to the elliptically distorted hexagon, to stretch it along its minor axis, till it lay on a circle, with the diameter equal to the major axis of the elliptical hexagon. The grid scores were computed on this transformed regular hexagon.

To assess if the grid pattern was rectangular, as opposed to hexagonal, analogous 90-degree-grid-scores (hereafter named "cartesian scores") were evaluated analogous to grid scores but with on peak rotation at 90 degrees, and off peak rotations at 45 degrees and 135 degrees. No elliptical modifications were made to this score, and to ensure compatibility, comparisons were always made between Cartesian scores and unmodified grid scores.

Further, to determine the generality of the spatial structure, we performed a modifiable areal unit problem (MAUP) analysis (Gehlke and Biehl, 1934; Openshaw, 1983) to determine the spatial characteristics of the grid in an unbiased manner. The two critical issues when performing a spatial analysis are (i) scaling issue and (ii) zoning issue. The scaling issue refers to how looking at a problem over different scales, can lead to different results. This issue is present because we boil down spatial features to a single number, namely the grid-score. To counteract this problem, we analysed a subset of the data at multiple scales, i.e. systematically choosing different window sizes. We utilized two scales for each of the three species with large entorhinal cortices (rat, bat, human) which were obtained by dividing the entire medial/caudal entorhinal cortex into square grids with the smallest side being divided in to three and six parts respectively for the two scales. The zoning issue refers to selection of the boundaries of the window, which can lead to a selection bias in the analysis. To cope with this issue, we performed a sliding window analysis with 50% overlap in successive samples, and calculating the spatial autocorrelation, grid scores and cartesian scores for each sample. To ensure comparability, grid scores without elliptical modifications were used for comparison with cartesian scores.

We performed shuffling procedure on the block pattern of the original image. The blocks representing the patches were shuffled in original space, and no overlap or abutting of the patches was allowed during the shuffling. This resulted in the original number of patches being randomly distributed in the same area without overlapping. We evaluated the 95th percentile of the grid scores from the shuffled data. However, since shuffled images often led to spatial autocorrelations without clear peaks, it wasn't always possible to obtain elliptically modified grid scores to compare with our data. This however means that the grid scores and cartesian scores attained from the spatial autocorrelation analysis are only indicative of the particular

geometry exhibited and not proof of it. However, to counteract the issue of whether a particular pattern present, regardless of its particular geometry, was only a chance occurrence, we performed a spatial fourier analysis, which can be performed independent of this issue.

The spatial Fourier spectrogram was calculated by implementing a two dimensional discrete Fourier transform and determining its power (Krupic et al., 2012):

$$F(x,y) = \frac{1}{\sqrt{MN}} \sum_{n=0}^{N-1} \sum_{m=0}^{M-1} f(m,n) e^{-2\pi i \left(\frac{mx}{M} + \frac{ny}{N}\right)}$$

$$P(x,y) = \sqrt{{F_r}^2(x,y) + {F_i}^2(x,y)}$$

where, *F* is the spatial Fourier transform of *f*, which is a binary image representing the sample with regions of interest (patches) marked as white blocks, with the remaining area as black and zero padded to 2048x2048. M and N are the width and height of the image before zero-padding. Normalization by $\sqrt{MN}$ enables comparison of Fourier power in differently sized samples. P is the power of the Fourier transform with F_r and F_i being the real and imaginary parts of the Fourier transform. To determine the probability that the spatial structure of the patches present in the selected area was not a chance effect, we employed a shuffling procedure. This shuffling was performed on all samples on a sample-by-sample basis until the 99th percentile of the maximum power Fourier component converged to a constant. This indicated, that the spatial structure present in the sample analyzed, regardless of the particular geometry of the structure, was highly unlikely to arise out of chance.

Light and fluorescence microscopy

An Olympus BX51 microscope (Olympus, Shinjuku Tokyo, Japan) was used to view the images using bright field microscopy. The microscope was equipped with a motorized stage (LUDL Electronics, Hawthorne NY, USA) and a z-encoder (Heidenhain, Shaumburg IL, USA). Images were captured using a MBF CX9000 (Optronics, Goleta CA, USA) camera using Neurolucida or StereoInvestigator (MBF Bioscience, Williston VT, USA).

A Leica DM5500B epifluorescence microscope with a Leica DFC345 FX camera (Leica Microsystems, Mannheim, Germany) was used to image the immunofluorescent sections. Alexa fluorophores were excited using the appropriate filters (Alexa 488 – L5, Alexa 546 – N3). The fluorescent images were acquired in monochrome and colour maps were applied to the images post acquisition. Post hoc linear brightness and contrast adjustment were applied uniformly to the image under analysis.

Estimate of the neuron number in a human layer 4 finger module

We chose to compare the estimated number of neurons in the human area 3b finger representation to neuron number layer 4 barrels of Etruscan shrews, mice and rats. This comparison is motivated by: (i) finger related modules have been described in primate area 3b

(Jain et al., 1998; Catania and Henry 2006), (ii) finger related barrels are observed in rodents and finger barrels have a similar size in rats as whisker barrels (Waters et al. 1995). We obtained an estimate of the number of layer 4 neurons in a human area 3b finger representation. We computed a number of ~1150000 neurons in a single finger module of layer 4 neurons in the human area 3b finger representation, by the formula:

$$n = \frac{\mathrm{N} * \phi * \lambda * \alpha * \theta}{\mathrm{r} * \mathrm{s}}$$

where, n is the number of neurons in a single finger module in layer 4 in the human area 3b finger representation, and N = 20 billion refers to the total number of cortical neurons (Koch 1999; Pakkenberg et al. 1997). $\phi = 0.023$ refers to the fraction of the total human cortical sheet occupied by areas 3a and 3b, based on functional imaging data (Orban et al., 2004), and $\lambda = 0.67$ refers to the approximate fraction of this area corresponding to area 3b. $\alpha = 0.16$ denotes that ~16% of this area corresponds to the finger representation based on the Penfield maps (Penfield and Rasmussen 1950) and $\theta = 0.23$ refers to the fraction of neurons in this finger cortical column present in layer 4, derived from rat data, where layer 4 contributes 23% of neurons in a column (Meyer et al. 2010). This value was normalized by r = 2, to obtain the value for a single hemisphere and s = 5 to obtain the value for a single finger.

Results

Phylogeny and location of entorhinal cortex in five mammalian species

In our comparative analysis of entorhinal architecture we identified the entorhinal cortex based on previous publications for bats (Schneider, 1966; Yartsev et al., 2011), rodents (Blackstad, 1956; van Groen, 2001; Kjonigsen et al., 2011; Boccara et al., 2015), and humans (Sgonina, 1938; Insausti et al., 1995;) and our own work on the Etruscan shrew (Naumann et al., 2012). The remarkably different sizes of the brains under study and their divergence in the phylogenetic tree is illustrated in Figure 1A. The position of entorhinal cortex and its medial (caudal in humans) and lateral (rostral in humans) subdivisions is indicated in Figure 1B.

Laminar architecture of calbindin-positive cells in entorhinal cortex

Calbindin-immunoreactivity identifies a variety of cells in medial entorhinal cortex. As noted in the introduction, the majority of these cells are layer 2 pyramidal neurons and this neuronal population is what we focus on in the present article. Figure 2 shows cortical lamination in sections perpendicular to the pial plane stained for calbindin, namely parasagittal sections from a mouse (*Mus musculus*), rat (*Rattus norvegicus*), bat (*Rousettus aegyptiacus*) and coronal sections from shrew (*Suncus etruscus*) and human (*Homo sapiens*) medial entorhinal cortex. Calbindin-positive cells in the entorhinal cortex form periodic clusters (Fig. 2 A,C,E,G,I). Higher-magnification views show that these patches contain both calbindin-positive cells and calbindin-positive neuropil and are most easily detected in layer 2 (Fig. 2 B,D,F,H). Calbindin positive cells within patches also show differences in laminar distribution across species. The medial part of the entorhinal cortex in the Etruscan shrew is very thin (~ 200 μm), comparable in thickness to single layers in other species, such as layer 3 in rodents. We were able to identify layer 1 and a thin cell free layer (lamina dissecans) separating superficial and deep entorhinal layers (Fig. 2 A). However, despite the small size of the region, calbindin-positive cells form a small number of clearly separated clusters in layer 2/3. In rodents, calbindin-positive cells form clusters only in layer 2 (Fig. 2 C-F), whereas in shrews (Fig. 2 A,B), bats (Fig. 2 G,H), and humans (Fig. 2I) they appear to extend through layer 2 and 3. In addition to the calbindin-positive pyramidal neurons which are clustered in patches we observed two other calbindin-positive cell populations: (i) a scattered population of cells with intense calbindin-immunoreactivity and non-pyramidal morphologies, perhaps corresponding to a specific interneuron-subpopulation (DeFelipe, 1997), (ii) a population of weakly calbindin-immunoreactive neurons outside of patches, which are likely to be calbindin-positive pyramidal neurons. These neurons were differently distributed in the species investigated. In mice, very few weakly calbindin-positive neurons were found outside of patches, whereas in shrews and rats there was a larger number of such cells outside of patches in the same cortical layer.

Architecture of calbindin-positive cells in tangential cortical sections

Next we focused on the cross-species comparison of entorhinal organization in the tangential cortical plane. To this end we stained tangential sections from Etruscan shrew (Fig. 3A), mouse (Fig. 3B), rat (Fig. 3C), bat (Fig. 3D) and human (Fig. 3E) medial/ caudal entorhinal cortex for calbindin immunoreactivity. All species display a modular arrangement of calbindin-positive cells or neuropil (Fig. 3). Bundling of calbindin-positive dendrites superficial to the patches

were prominent in the rat entorhinal cortex (Fig. 2E,F, Ray et al., 2014), but this was not obvious in sections perpendicular to the surface in other species. Despite this, we found that calbindin-positive neuropil contributes to patch architecture in tangential sections and in the shrew we could detect calbindin-positive neuropil above the calbindin-positive cells in tangential sections (Fig. 3A).

When comparing the size of individual calbindin patches across species, we observed that individual modules were remarkably similar in size (Fig. 3, Table 4), whereas the size of the entorhinal cortex increases significantly in larger species. The average diameter of an entorhinal calbindin patch is 104 ± 25 μm in the Etruscan shrew, 94 ± 37 μm in the mouse, 145 ± 41 μm in the rat, 250 ± 77 μm in the bat and 532 ± 197 μm in humans. In contrast, entorhinal cortex volume increases from 0.73 mm^3 (area ~2.81mm^2) in the shrew, to 19 mm^3 in rats (Wree et al., 1992) and to ~1678 mm^3 (517.90 mm^2) in humans (Insausti et al., 1998; Velayudhan et al., 2013), an approximately 2300 fold increase (184 fold areal increase). The number of patches also shows an increase, with 14 ± 2 in shrews, 22 ± 7 in mice, 69 ± 17 in rats, 100 ± 1 in bats to 115 ± 16 in humans (Table 4).

Periodicity of calbindin patch pattern in entorhinal cortex

Another species-invariant feature of the organization of calbindin patches was their spatially periodic grid-like arrangement. In specimen of medial entorhinal cortex stained for calbindin, one observes periodic arrangements of calbindin patches in the superficial layers. We analyzed the spatial periodicity of calbindin-positive patches with a variety of techniques. As shown in Figure 4 we applied two-dimensional spatial autocorrelation analysis to calbindin stained tangential sections (Fig. 4A,C,E,G,I) of medial/ caudal entorhinal cortex. Two-dimensional spatial autocorrelation captures spatially recurring features and revealed a periodic arrangement of calbindin patches in all species (Fig. 4B,D,F,H,J). However, the particular geometry of the layout is difficult to ascertain due to confounding factors like distortions of the surface when flattening the brain, uneven shrinkage in tissue processing, and incomplete capture of a particular pattern in any single histological section.

Quantification of the periodicity of calbindin patches

To quantify the nature of the periodicity in the samples, we calculated grid scores (Sargolini et al., 2006) to determine hexagonality - and cartesian scores to determine rectangularity. The grid scores were also modified to quantify hexagonality in elliptically distorted hexagons (Barry et al., 2012; see methods for details). Grid and cartesian scores vary from -2 to +2 with values > 0 indicative of hexagonality and rectangularity respectively. However, it should be noted, that these values only provide an indication of the nature of periodicity and do not provide proof of the absolute geometry without further statistical testing. We observed periodic arrangements in all species and determined grid scores or cartesian scores as indicated for individual images in the figure legend (Fig. 4). In addition, we prepared further sets of tangential sections and computed the following average grid scores (Table 6): shrews (0.73 ± 0.21, N=2), mice (0.55 ± 0.09, N=3), rats (0.84 ± 0.23, N=9), bats (0.81 ± 0.04, N=3) and humans (1.18 ± 0.10, N=3). To assess the probability of a chance occurrence of the arrangement of the patches, we employed a shuffling procedure (Krupic et al., 2012; Ray et al. 2014). We found that the strongest fourier component in each of the samples exceeded that of the 99th percentile of the shuffled data, given preserved local structure, suggesting that such spatial arrangement, regardless of the particular geometry of the arrangement, is unlikely to arise by

chance. The number of samples for each individual species was in general not high enough to statistically determine if the periodicity present was hexagonal or rectangular. However, in rats, where a sufficiently large number of samples were present, the grid score was significantly higher than the cartesian score ($p=0.0416$, one tailed t-test; Shapiro-Wilk normality test), indicating that in rats the grid-like layout is rather hexagonal than rectangular. To ensure compatibility we used grid scores without elliptical modifications to compare to cartesian scores.

Further, to assess the generality of the grid layout across the medial/caudal entorhinal surface, we introduced a 'Modifiable Areal Unit Analysis**,** MAUP' analysis (Gehlke and Biehl, 1934; Openshaw, 1983). A critical issue while performing a spatial analysis corresponds to selecting the size of the region under observation, since analysis at different scales can lead to different outcomes. This issue is known as the scaling problem (Openshaw, 1983). To resolve this issue, we performed our analysis at two different scales, obtained by dividing the smallest side of the whole entorhinal patch pattern into three and six parts. Another critical issue pertaining to spatial analysis corresponds to selecting the boundaries of the region under analysis (as opposed to size described by the scaling problem). This issue is known as the zoning problem (Schuurman et al., 2007), and to cope with this problem we performed a sliding window analysis, with 50% overlap between the successive windows, at each of the two scales. We performed these analyses on micrographs of the whole medial/caudal entorhinal cortices from species with large entorhinal cortices (human, bat and rat), and compared grid scores with cartesian scores. To ensure compatibility we used grid scores without elliptical modifications to compare to cartesian scores. We counted the number of regions having positive grid scores and cartesian scores and classified them as hexagonal or rectangular grid-like regions respectively. In case a region exhibited both positive grid and cartesian scores, then the region was classified as hexagonal grid-like, if the grid score exceeded the cartesian score and rectangular grid-like, if the cartesian score exceeded the grid score. We observed that in most cases (5 out of 6, Table 5), more samples exhibited greater positive grid scores than cartesian scores. This indicated the underlying periodicity was more hexagonal than rectangular. However, the difference between hexagonal and rectangular regions was minor and cannot be used to make conclusions about the particular geometry of the periodicity till a larger number of samples are analyzed to increase the power of the analysis.

Periodicity of modular structures in the cortex and colliculus of mammals

Modular structures are a prominent feature of many cortical areas (Kaas, 2012) but also other regions of the mammalian (Roney et al., 1979) and non-mammalian brain (Leise, 1990). In the cerebral cortex, modules are commonly defined as a set of structural features that repeats in a relatively regular fashion in a plane parallel to the surface (Manger et al., 1998). Modules are not necessarily circular in shape but can also take the form of bands or stripes and may be arranged in different patterns. We suggest that spatial autocorrelation analysis can complement manual analysis of patch patterns and apply it to tangential sections of other modular cortical structures from rats, monkeys and humans in Figure 5. We obtained images of monkey primary and secondary visual cortex stained for cytochrome oxidase (Fig. 5A, 5C) from Dr. Lawrence C. Sincich and Dr. Jonathan C. Horton (Sincich and Horton, 2002). Autocorrelation analysis of these patterns (Fig. 5B, 5D) show similar grid scores and cartesian scores. Figure 5E shows the NADPH diaphorase staining in the superior colliculus of the rat (Wallace, 1986) and 5G shows the cytochrome oxidase staining pattern in the rat barrel cortex (Woolsey and van der Loos, 1970). Autocorrelation analysis of these patterns (Fig. 5F, 5H) shows regular patterns with higher cartesian scores than grid scores. Figure 5I shows myelin staining in patches of the

presubiculum of the human brain (Sgonina, 1938) and 5K shows the zinc staining pattern in the rat visual cortex (Ichinohe et al. 2003). Autocorrelation analysis of these patterns (Fig. 5J, 5L) shows patterns more similar to hexagonal patterns of the entorhinal cortex with higher grid scores than cartesian scores. In summary we find that periodic structures are not unique to the entorhinal cortex; yet the pattern in the entorhinal cortex appears well preserved across different species in contrast to other structures, like the cytochrome oxidase patterns of monkey visual cortex and rat barrel cortex.

Acetylcholinesterase staining in relation to calbindin patches

In rodents acetylcholine has diverse effects on medial entorhinal cortex (for review see Hasselmo, 2006). Ray et al. (2014) have described a preferential cholinergic innervation of calbindin patches in rats. In mice we observed a similar preferential cholinergic innervation of calbindin patches as shown in a tangential section of mouse entorhinal cortex stained for both acetylcholinesterase activity (Fig. 6A) and calbindin (Fig. 6B), revealing a close match of the two staining patterns, which was confirmed in overlays (not shown). Equivalent observations were made in the rat (Fig. 6C-D). In both species we observe a medial stripe free of calbindin patches (Fujimaru and Kosaka, 1996) which has homogeneous acetylcholinesterase activity similar to the staining pattern in between the calbindin patches. The parasubiculum has high acetylcholinesterase activity and surrounds the dorsal medial entorhinal cortex. A striking species difference in cholinergic innervation is evident, however, when one compares rat and mouse to the bat and human entorhinal cortices. In bats, a section stained for acetylcholinesterase shows clusters of increased activity in the dorsal part but little staining in the ventral part (Fig. 7A). The reverse is true for calbindin staining (Fig. 7B). Thus, in contrast to the nearly complete overlap in rats, cholinergic and calbindin patches form two largely non-overlapping sets of modules in bats. Finally, in human caudal entorhinal cortex we observed anti-correlated cholinergic and calbindin staining patterns (Fig. 7C-D).

Calbindin patches in the human entorhinal cortex

Modularity of the human entorhinal cortex has been intensely investigated (for review see Insausti and Amaral, 2011). Since human entorhinal cortex shows a high degree of regional diversity (Sgonina, 1938; Rose, 1927b) and most of this work has focused on so called stellate cell islands, we add an overview (Figure 8), which shows to which entorhinal subregion our conclusions on the arrangement of calbindin patches apply and how these compare to stellate cell islands. Fig. 8A shows a ventral view of a human cortical hemisphere; the white box indicates the position of tangential section whole-mount preparation of flattened entorhinal cortex shown in Fig. 8B. We identified putative stellate cell islands by neurofilament-immunoreactivity (Fig. 8B, red) and calbindin patches by calbindin-immunoreactivity (Fig. 8B, green). In caudal human entorhinal cortex (Fig. 8C) we observed hexagonally (Fig. 8C-D) arranged calbindin patches, which were superimposed to a spatially scattered population of putative stellate cells (Fig. 8E,F). This arrangement is remarkably similar to the cellular organization of rat medial entorhinal cortex (Ray et al., 2014). Consistent with previous observations (Mikkonen et al., 1997) we observed little calbindin-immunoreactivity (Fig. 8G-H) around stellate cell islands in more rostral parts of entorhinal cortex (Fig. 8I). Such islands of stellate cells in the rostral parts of human entorhinal cortex are perhaps the most distinct modular structures in human cortex and they have a regular but somewhat less periodic organization (Fig. 8J) than calbindin patches in caudal entorhinal cortex (Fig. 8D).

Extent of calbindin patches in entorhinal cortex

In rats, we have observed calbindin patches quite ventrally (4mm from the dorsal border, Ray et al., 2014). However, the modular architecture of more ventral regions is difficult to assess in tangential sections due to (i) strong local tissue curvature in the rat ventral entorhinal cortex, (ii) variable definitions of ventral areas in the literature (Haug, 1976; Paxinos & Watson, 1998). Coronal sections stained for calbindin in an atlas of the parahippocampal region (Kjonigsen et al., 2011) suggest that the most ventral (anterior) parts of the medial entorhinal cortex do not contain patches but more homogeneous calbindin staining. Thus, the borders of the medial entorhinal cortex as defined by Kjonigsen et al. (2011) do not coincide with the occurrence of patches. While assessing patch patterns is difficult in coronal sections as shown by Kjonigsen et al. (2011), our tangential sections do not allow conclusions about patch patterns in the ventral entorhinal cortex. In bats, the dorsal end of the entorhinal region has a wide, calbindin free region, putatively corresponding to the parasubiculum (Fig. 2G, 3D). Similar to rodents (Fig. 6), this region has high cholinergic innervation (Fig. 7A).

In humans, we outlined the caudal calbindin patch region and thus marked the caudal border of the entorhinal cortex (Fig. 8B). In the rostral and medial regions the section is too fractured to delineate the borders. However, we think that all or nearly all parts present in the section belong to the entorhinal cortex.

Allometry of calbindin patches

Our species sample, with the Etruscan shrew's brain and the human brain, contained the smallest and one of the largest mammalian brains. Thus, this sample provides an ideal opportunity to analyze how calbindin patches scale with brain size. To approach this question quantitatively we counted the number of calbindin-positive cells per patch in all species (Table 2). For an allometric analysis we relate this number to brain weight (Table 3). We find that the number of calbindin-positive cells per patch increased from about 80 calbindin-positive cells per patch in Etruscan shrews to about 800 neurons in humans (Table 3 and Figure 9). Thus, the number of a calbindin-positive cells increases only 10-fold from shrews to humans while in contrast brain size increases 20000-fold. The relatively minor changes in size of calbindin-positive cells per patch is also apparent, when one compares it to the scaling of layer 4 barrels (in Etruscan shrews, mice and rats) or the finger representation in humans. We chose to plot the estimated number of neurons in the human area 3b finger representation together with barrels in Figure 9 because: (i) finger related modules have been described in primate area 3b (Jain et al., Kaas 1998; Catania and Henry 2006), (ii) finger related barrels are observed in rodents and the 3 barrels per finger have a similar size in rats as a large whisker barrel (Waters et al. 1995; Riddle al. 1992). From Figure 9 it appears that somatosensory module neuron number scales isometrically with brain size, whereas calbindin-positive cell number scales allometrically and stays relatively constant in evolution.

We identified two factors that seem to contribute to the relatively constant calbindin-positive cell number per patch across species. First, it appears that the total number of entorhinal neurons does not scale isometrically with brain size (Table 3). Second, we found that the increase of entorhinal cortex across species was associated with an increasing number of calbindin patches (Table 4). Also the density of patches decreases with increasing entorhinal cortex size (Table 4).

Discussion

We confirm the existence of calbindin-positive patches in layer 2 of entorhinal cortex in five mammalian species. While we observe in all species a periodic modular arrangement of calbindin-positive patches, we detected major species differences in the cholinergic innervation of these patches. The architecture of calbindin-positive patches in the entorhinal cortex also showed clear species differences, particularly in terms of lamination, but the organization of calbindin patches was remarkably constant in specific subregions. Anatomical similarity is not sufficient to define homology; however, our findings support earlier conclusions about the correspondence of entorhinal subregions (Insausti, 1993). The number of neurons in a calbindin patch increased only ~10-fold over a 20000-fold difference in brain size between Etruscan shrew and human (~2300 fold difference in volume of entorhinal cortex). In rats, but also in other species we observed substantial animal to animal variability in the number of calbindin patches, which strongly argues against 'identical' calbindin patch maps in individual rats in contrast to modular structures such as the barrel cortex, which are very similar in every animal.

Entorhinal modules: comparison with neocortical modules and evolutionary perspective

Our results confirm and extend a range of studies, which described calbindin-positive modules in the mammalian entorhinal cortex. Fujimaru and Kosaka (1996) described patches of calbindin-positive neurons in the mouse dorsal medial entorhinal cortex. Calbindin positive cell clusters were also described in monkeys (Suzuki and Porteros, 2002) and humans (Beall and Lewis, 1992). In primates, these calbindin cell clusters are most prominent at the caudal pole of entorhinal cortex, which may correspond to medial entorhinal cortex of rodents (Bakst and Amaral, 1984).

Evidence for columnar organization in superficial layers of the cerebral cortex was obtained from a wide range of cortical areas in a variety of species (Manger et al., 1998; Ichinohe et al., 2003; Rockland and Ichinohe, 2004). Interestingly, commonly studied modules in the neocortex such as barrels and orientation columns are present only in a limited number of species (Kaschube et al., 2010; Keil et al., 2012; Molnar, 2013). In the case of ocular dominance columns, even individuals of the same species show a large variability in the expression of the columnar pattern (Adams & Horton, 2003). Based on our observations in the entorhinal cortex of five species, we speculate that parahippocampal modules may be more conserved across species than neocortical modules. However, while parahippocampal modules are present in a wide range of species, they have been less extensively studied than neocortical modules (Ikeda et al., 1989; Hevner and Wong-Riley., 1992; Ding and Rockland, 2001; Ichinohe, 2012). For example, the human entorhinal cortex appears to consist of homogeneous modules varying only in size when using cytochrome oxidase or pigment staining (Hevner and Wong-Riley., 1992; Braak & Braak 1995) but can be shown to contain different types of modules when using markers such as calbindin (Fig. 9) or markers for different neuromodulatory systems (Gaspar et al., 1990; Akil & Lewis, 1994).

Our analysis in five mammalian species shows that the periodic arrangement of patches in layer 2 is present in species that are separated for millions of years in evolution and that differ in size by several orders of magnitude. This indicates a conserved mechanism for generating

entorhinal architecture; but anatomical study of further mammalian species such as marsupials is necessary. Of particular interest would be investigating similar brain regions in other amniotes. Interestingly, in adult lizards (Dávila et al., 1999) and during development of the hippocampal region in chickens, modular structures enriched in calbindin (and acetylcholinesterase in chickens) emerge (Kovjanic and Redies, 2003; Suárez et al., 2006); however, the exact correspondence of mammalian and bird hippocampal regions is currently a topic of ongoing research (Herold et al., 2014; Abellán et al., 2014).

Quantification of periodicity in neocortical modules has been challenging, though observations of hexagonality in apical dendritic columns (Gabbott, 2003; Peters and Kara, 1987) have been reported. Our analysis of patch patterns reveals their periodicity across species, however, what the particular geometry of that periodicity might be is less clear. In the rat, we demonstrate that the layout is rather hexagonal than rectangular, and an analysis of a larger number of samples from each species would be required to ascertain the nature of periodicity across species.

Calbindin patches as putative functional modules

Grid cells form functional modules (Stensola et al., 2012), are anatomically clustered in the medial entorhinal cortex (Heys et al., 2014), and may be found within the calbindin-positive cell population in rats (Tang et al., 2014). The similarity of the hexagonal patch arrangement in layer 2 in rats to the hexagonal discharge pattern of grid cells inspired a hypothesis (Brecht et al., 2014), according to which specific local connectivity of pyramidal cells might be important for generating grid cell activity. The comparative analysis of calbindin patches presented here does not provide direct proof for this concept. However, our findings are consistent with two important elements of this theory: (i) the data suggest that the regular arrangement is functionally relevant as it is evolutionary conserved; (ii) the relatively inelastic scaling of a calbindin patch size is consistent with the theory that an individual calbindin patch is a structurally preserved functional unit. It would be interesting to explore the relation of anatomical and functional modules as described by Stensola et al., 2012. We wonder whether the relatively conserved patch size indicates that scaling of brain size does not change the number of spatial phases and orientations which need to be represented by an animal.

However, the functional relevance of most cortical modules is poorly understood (Horton and Adams, 2005), and they have been described as a mere by-product of cortical development. Resolving these questions will require as a first step knowledge about the connectivity within and between modules such as calbindin patches. However, only few studies have investigated projection patterns of individual pyramidal cells in the entorhinal cortex area (Lorente de No, 1933, Klink and Alonso, 1997). Studies in the superior colliculus have indicated structure-function relationships (Mana and Chevalier, 2001), and future studies will be needed to address whether clustered intrinsic connections similar to those described in other regions of cortex (Rockland and Lund, 1983; Gilbert and Wiesel, 1983; Lund et al., 1993) are present in the entorhinal cortex and how they relate to functional (Barry et al., 2007; Brun et al., 2008; Stensola et al. 2012) and anatomical modules (Burgalossi and Brecht 2014).

Cholinergic innervation differs across mammalian species

Acetylcholinesterase shows a modular staining pattern at the layer 1/2 border of rodent medial entorhinal cortex (Mathisen and Blackstad, 1964; Slomianka and Geneser, 1991). In primates,

increased acetylcholinesterase activity has been described as either coinciding with stellate cell clusters (Solodkin and Van Hoesen, 1996) or with pyramidal cell clusters in between the stellate cells (Bakst and Amaral, 1984), depending on the subregion of entorhinal cortex studied (Bakst and Amaral, 1984). While the distribution of acetylcholinesterase is similar in mice and rats, in Egyptian fruit bats, there is little overlap between acetylcholinesterase modules and calbindin patches (Fig. 7A-B). Interestingly, the most dorsal aspect of the bat entorhinal cortex (Yartsev et al., 2011) contains very few calbindin-positive cells, a feature often ascribed to the neighbouring parasubiculum in rodents. Further studies will need to investigate whether this type of entorhinal architecture is special to bats or more widespread among mammals. Similarly, it is not known whether the alignment of the patches to layer 1 axons and the parasubiculum described in rats (Ray et al., 2014) applies to all species.

Grid cells in rodents show increased theta-rhythmicity compared to other cells in entorhinal cortex (Hafting et al., 2005). Blocking septal inputs to the entorhinal cortex has been shown to abolish grid cell activity (Koenig et al., 2011; Brandon et al., 2011) and it was suggested that in particular the cholinergic septal input to the entorhinal cortex is essential for grid cell firing (Newman et al., 2013). We found that calbindin-positive cells in rats show increased theta-rhythmicity and appear to receive more cholinergic input compared to calbindin-negative cells (Ray et al., 2014), and that grid cells preferentially correspond to this calbindin-positive pyramidal cell population (Tang et al., 2014). In Egyptian fruit bats, grid cells do not oscillate in the theta frequency range (Yartsev et al., 2011). If cholinergic inputs are important for theta-rhythmicity, it will be interesting to investigate if there is a link between the lack of theta oscillations in grid cells in bats and the low amount of overlap between cholinergic inputs and calbindin patches reported here. The preferential cholinergic input to calbindin patches in rodents, and the lack thereof in bats and humans suggests a link between cholinergic inputs and theta modulation of grid cells (Yartsev et al., 2011).

Relation of rodent medial and primate caudal entorhinal cortex

In caudal human entorhinal cortex we observed regularly arranged calbindin patches, which were superimposed to a spatially scattered population of putative stellate cells. This arrangement is remarkably similar to the cellular organization of the rat medial entorhinal cortex (Ray et al., 2014). This finding supports earlier conclusions (Bakst and Amaral, 1984) that the medial entorhinal cortex of rodents corresponds to the dorso-caudal part of the entorhinal cortex in primates, since both are close to the parasubiculum and presubiculum. Lateral entorhinal cortex is located more rostral and medial entorhinal cortex more caudal in the rat. Larger brains have a greatly enlarged neocortex so that the entorhinal cortex is now on the medial side of the brain, but the topography of medial entorhinal cortex at the caudal end and lateral entorhinal cortex at the rostral end is likely to be conserved (Insausti, 1993).

Quantitative analysis of neuron number in calbindin patches and stellate cell islands in entorhinal cortex

Over the last thirty years converging evidence from physiology, anatomy and cell biology indicates that principal cells in layer 2 of entorhinal cortex divide into at least two very distinct types of principal cells: calbindin-positive pyramidal cells and stellate cells. As described previously for the rat (Ray et al., 2014) and also shown in Figure 8B,C for the human, medial/

caudal entorhinal cortex contains calbindin-positive pyramidal cell patches and scattered stellate cells (Fig. 8E). These modules are different from the stellate cell islands (Fig. 8B,I) in rostral entorhinal cortex that have been extensively characterized in the human brain. In total, there are on average 121 entorhinal stellate islands in the left - and 111 modules in the right hemisphere of the human brain (Simic et al., 2005). Simic et al., 2005 also estimated the subset of entorhinal cortex layer 2 cells contained in cellular clusters to be $4.68*10^5$ in the left and $4.05*10^5$ in the right hemisphere. From these data one can calculate that there may be close to 4000 neurons in one entorhinal stellate cell island. This number is quite different from our count of ~ 800 calbindin-positive neurons per calbindin patch. In the mouse, Fujimaru and Kosaka (1996) estimated that there are about 600 calbindin-positive neurons in the dorsal half of medial entorhinal cortex; ~75 % of these were in layer 2. If we assume that there are 5-6 calbindin patches in the dorsal half of mouse medial entorhinal cortex (Fig. 3B), our estimates of calbindin-positive cell number per patch are in agreement with the data of Fujimaru and Kosaka (1996). Peterson et al. (1996) provided the most extensive cell type specific quantification of rat entorhinal cortex layer 2 neurons. They estimated that ~ 32 % of all layer 2 neurons are calbindin-positive and of those ~ 88 % were glutamatergic. We find a similar fraction of calbindin-positive neurons (Ray et al., 2014). However, given the total number of calbindin-positive neurons estimated by Peterson et al. (1996) and our count of patch numbers one would predict a ~3-fold higher number of calbindin-positive neurons per patch in rats. This may be due to intrinsic variability in patch number or differences in the definition of areal borders. In addition, while in the mouse most calbindin-positive neurons in layer 2 are within patches, in the rat deep layer 2 tangential sections show an almost uniform distribution of calbindin-positive cells. Neuron density varies up to 5-fold across the neocortical sheet (Collins et al., 2010) and up to 3-fold even in well-defined modules such as barrels (Meyer et al., 2013). Our counts indicate up to 2-fold differences in the number of calbindin-positive cells per patch, indicating a similar or lower variability of cell numbers within a species.

Constant size of calbindin patches and allometry of entorhinal cortex

In contrast to the variability of patches observed within species, our analysis suggests that calbindin patches are relatively 'inelastic' in evolution and maintain a relatively constant size in mammals. When comparing mammals of different brain sizes, the allocortex takes up a large part of total brain volume in small mammals and a progressively smaller part in larger brained mammals (Stephan, 1983). This is mainly due to the enormous enlargement of the neocortex. When size differences are calculated independent of increased neocortical volume, it becomes - clear that the entorhinal cortex, as well as the hippocampus and septum are progressively enlarged in larger brained species (Stephan, 1983). The opposite is true for the olfaction related parts of the allocortex; therefore in small mammals the olfactory bulb is larger than the entorhinal cortex, whereas in primates this relation is reversed (Rose S., 1927). The calbindin patches only show a 10-fold increase in cell numbers, when the brain shows ~20000-fold increase in volume (~2300 fold increase in entorhinal cortex volume). Patches also only show ~5-fold increase in diameter across these species, which is much smaller than ~13-fold increase in size expected if the scaling of the patches is linear to the increase in entorhinal volume (~2300-fold increase) or area (~180-fold increase). Earlier studies have also observed the relative inelasticity in the size of certain modules, like insula patches (Manger et al., 1998) and visual cortex patches (Lund et al., 1993; Luhmann et al., 1986; Rockland et al., 1982). It would be interesting to investigate if the relatively constancy of module size across evolution is linked with its functionality.

In summary, we describe modular structures in the entorhinal cortex, which are largely invariant in size, arrangement and neuron numbers across five mammalian species, which span ~ 100 million years of evolutionary divergence and ~20000 fold difference in brain size.

Other acknowledgments.

We thank Carolin Mende for contributions to the Figures, Susanne Grübel, Undine Schneeweiß, and Juliane Steger for outstanding technical assistance and Dr. Nachum Ulanovsky for generously providing bat brains and comments on the manuscript. We thank Dr. Lawrence C. Sincich and Dr. Jonathan C. Horton for kindly providing images of macaque primary and secondary visual cortex.

Conflict of interest statement.

The authors declare that they have no conflict of interest.

Role of authors.

All authors had full access to all the data in the study and take responsibility for the integrity of the data and the accuracy of the data analysis. Study concept and design: RN, SR, MB. Acquisition of data: RN, SR, LL, MB. Analysis and interpretation of data: RN, SR, MB. Drafting of the manuscript: RN, SR, MB. Critical revision of the manuscript for important intellectual content: RN, SR, SP, LL, FLH, MB. Statistical analysis: RN, SR, MB. Obtained funding: FLH, MB. Administrative, technical, and material support: SP, LL, FLH, MB. Study supervision: MB.

Literature Cited

Abellán A, Desfilis E, Medina L. 2014. Combinatorial expression of Lef1, Lhx2, Lhx5, Lhx9, Lmo3, Lmo4, and Prox1 helps to identify comparable subdivisions in the developing hippocampal formation of mouse and chicken. Front neuroanat 8:59.

Abercrombie M. 1946. Estimation of nuclear population from microtome sections. Anat Rec 942:239-247.

Adams DL, Horton JC. 2003. Capricious expression of cortical columns in the primate brain. Nat Neuro 6:113-114.

Airaksinen MS, Eilers J, Garaschuk O, Thoenen H, Konnerth, A, Meyer M. 1997. Ataxia and altered dendritic calcium signaling in mice carrying a targeted null mutation of the calbindin D28k gene. Proc Natl Acad Sciences USA 94:1488-1493.

Akil M, Lewis DA. 1994. The distribution of tyrosine hydroxylase-immunoreactive fibers in the human entorhinal cortex. Neuroscience, 60:857-874.

Alonso A, Klink R. 1993. Differential electroresponsiveness of stellate and pyramidal-like cells of medial entorhinal cortex layer II. J Neurophysiol 70:128-143.

Alonso A, Llinás RR. 1989. Subthreshold Na+-dependent theta-like rhythmicity in stellate cells of entorhinal cortex layer II. Nature 342:175-177.

Amaral DG, Insausti R, Cowan WM. 1987. The entorhinal cortex of the monkey: I. Cytoarchitectonic organization. J Comp Neurol 264:326-355.

Bakst I, Amaral DG. 1984. The distribution of acetylcholinesterase in the hippocampal formation of the monkey. J Comp Neurol 225:344-371.

Barry C, Hayman R, Burgess N, Jeffery KJ. 2007. Experience-dependent rescaling of entorhinal grids. Nat Neuro 10:682-684.

Barry C, Ginzberg LL, O'Keefe J, Burgess N. 2012. Grid cell firing patterns signal environmental novelty by expansion. Proc Natl Acad Sciences USA 109:17687-17692.

Beall MJ, Lewis DA. 1992. Heterogeneity of layer II neurons in human entorhinal cortex. J Comp Neurol 321:241-266.

Blackstad TW. 1956. Commissural connections of the hippocampal region in the rat, with special reference to their mode of termination. J Comp Neurol 105:417-537.

Blinkov SM, Glezer II. 1968. The Human Brain in Figures and Tables. A Quantitative Handbook, New York: Plenum Press.

Boccara CN, Kjonigsen LJ, Hammer IM, Bjaalie JG, Leergaard TB, Witter MP. 2015. A three-plane architectonic atlas of the rat hippocampal region. Hippocampus. Advance online publication. Boccara CN, Sargolini F, Thoresen VH, Solstad T, Witter MP, Moser EI, Moser MB. 2010. Grid cells in pre-and parasubiculum. Nat Neuro 13:987-994.

Braak H. 1972. Zur Pigmentarchitektonik der Großhirnrinde des Menschen. I. Regio entorhinalis. Z Zellforsch Mikrosk Anat 127:407-438.

Braak H, Braak E, Strenge H. 1976. Gehören die Inselneurone der Regio entorhinalis zur Klasse der Pyramiden oder der Sternzellen. Z Mikrosk Anat Forsch 90:1017-1031.

Braak H, Braak E. 1995. Staging of Alzheimer's disease-related neurofibrillary changes. Neurobiology of aging 16:271-278.

Brandon MP, Bogaard AR, Libby CP, Connerney MA, Gupta K, Hasselmo ME. 2011. Reduction of theta rhythm dissociates grid cell spatial periodicity from directional tuning. Science 332:595-599.

Brecht M, Ray S, Burgalossi A, Tang Q, Schmidt H, Naumann R. 2014. An isomorphic mapping hypothesis of the grid representation. Proc R Soc Lond B Biol Sci 369:20120521.

Brodmann K. 1909. Vergleichende Lokalisationslehre der Grosshirnrinde: in ihren Prinzipien dargestellt auf Grund des Zellenbaues. Ja Barth.

Brun VH, Solstad T, Kjelstrup KB, Fyhn M, Witter MP, Moser EI, Moser MB. 2008. Progressive increase in grid scale from dorsal to ventral medial entorhinal cortex. Hippocampus 18:1200-1212.

Burgalossi A, Brecht M. 2014. Cellular, columnar and modular organization of spatial representations in medial entorhinal cortex. Curr Opin Neurobiol 24:47-54.

Burgalossi A, Herfst L, von Heimendahl M, Förste H, Haskic K, Schmidt M, Brecht M. 2011. Microcircuits of functionally identified neurons in the rat medial entorhinal cortex. Neuron 70:773–786.

Catania KC, Henry EC. 2006. Touching on somatosensory specializations in mammals. Curr Opin Neurobiol 16:467-73.

Celio MR, Baier W, Schärer L, Gregersen HJ, De Viragh PA, Norman AW. 1990. Monoclonal antibodies directed against the calcium binding protein Calbindin D-28k. Cell Calcium 11:599-602.

Collins CE, Airey DC, Young NA, Leitch DB, Kaas JH. 2010. Neuron densities vary across and within cortical areas in primates. Proc Natl Acad Sciences USA 107:15927-15932.

da Costa NM, Martin KA. 2010. Whose cortical column would that be? Front Neuroanat 4:16.

Danscher G, Stoltenberg M. 2006. Silver enhancement of quantum dots resulting from (1) metabolism of toxic metals in animals and humans, (2) in vivo, in vitro and immersion created zinc-sulphur/zinc-selenium nanocrystals, (3) metal ions liberated from metal implants and particles. Prog Histochem Cytochem. 41:57-139.

Davila JC, Padial J, Andreu MJ, Guirado, S. 1999. Calbindin-D28k in cortical regions of the lizard Psammodromus algirus. J Comp Neurol 405:61-74.

DeFelipe J. 1997. Types of neurons, synaptic connections and chemical characteristics of cells immunoreactive for calbindin-D28K, parvalbumin and calretinin in the neocortex. J Chem Neuroanat 14:1-19.

Ding SL, Rockland KS. 2001. Modular organization of the monkey presubiculum. Exp Brain Res 139:255-265.

Doeller CF, Barry C, Burgess N. 2010. Evidence for grid cells in a human memory network. Nature 463:657-661.

Donaldson HH, Hatai S. 1931. On the weight of the parts of the brain and on the percentage of water in them according to brain weight and to age, in albino and wild Norway rats. J Comp Neurol 53:263–307.

Evers P, Uylings HBM. 1997. An optimal antigen retrieval method suitable for different antibodies on human brain tissue stored for several years in formaldehyde fixative. J Neurosci Methods 72:197-207.

Fujimaru Y, Kosaka T. 1996. The distribution of two calcium binding proteins, calbindin D-28K and parvalbumin, in the entorhinal cortex of the adult mouse. Neurosci Res 24:329-43.

Fyhn M, Hafting T, Witter MP, Moser EI, Moser MB. 2008. Grid cells in mice. Hippocampus 18:1230-1238.

Gabbott PLA. 2003. Radial organisation of neurons and dendrites in human cortical areas 25, 32, and 32'. Brain Res 992:298–304

Gaspar P, Berger B, Febvret A. 1990. Neurotensin innervation of the human cerebral cortex: lack of colocalization with catecholamines. Brain Res 530:181-195.

Gehlke CE, Biehl K. 1934. Certain effects of grouping upon the size of the correlation coefficient in census tract material. J Am Statist Ass 29:169–170.

Gilbert CD, Wiesel TN. 1983. Clustered intrinsic connections in cat visual cortex. J Neurosci 3:1116-1133.

Hafting T, Fyhn M, Molden S, Moser MB, Moser EI. 2005. Microstructure of a spatial map in the entorhinal cortex. Nature 436:801-6.

Hallström BM, Kullberg M, Nilsson MA, Janke A. 2007. Phylogenomic data analyses provide evidence that Xenarthra and Afrotheria are sister groups. Mol Biol Evol 249:2059-2068.

Hanke J, Yilmazer-Hanke DM. 1997. Pigmentarchitectonic subfields of the entorhinal region as revealed in tangential sections. J Hirnforsch 38:427-432.

Hasselmo ME. 2006. The role of acetylcholine in learning and memory. Curr Opin Neurobiol 16:710–715.

Hayes TL, Lewis DA. 1992. Nonphosphorylated neurofilament protein and calbindin immunoreactivity in layer III pyramidal neurons of human neocortex. Cereb cortex 21:56-67.

Herold C, Bingman VP, Ströckens F, Letzner S, Sauvage M, Palomero-Gallagher N, Zilles K, Güntürkün O. 2014. Distribution of neurotransmitter receptors and zinc in the pigeon (Columba livia) hippocampal formation: a basis for further comparison with the mammalian hippocampus. J Comp Neurol 522:2553-2575.

Hevner RF, Wong-Riley MT. 1992. Entorhinal cortex of the human, monkey, and rat: metabolic map as revealed by cytochrome oxidase. J Comp Neurol 326: 451-69.

Heys JG, Rangarajan KV, Dombeck DA. 2014. The functional micro-organization of grid cells revealed by cellular-resolution imaging. Neuron 84:1079-1090

Homman-Ludiye J, Manger PR, Bourne JA. 2010. Immunohistochemical parcellation of the ferret Mustela putorius visual cortex reveals substantial homology with the cat Felis catus. J Comp Neurol 518:4439-62.

Horton JC, Adams DL. 2005. The cortical column: a structure without a function. Proc R Soc Lond B Biol Sci 360:837-862.

Ichinohe N, Fujiyama F, Kaneko T, Rockland KS. 2003. Honeycomb-like mosaic at the border of layers 1 and 2 in the cerebral cortex. J Neurosci 23:1372-1382.

Ichinohe N, Knight A, Ogawa M, Ohshima T, Mikoshiba K, Yoshihara Y, Rockland, KS. 2008. Unusual Patch–Matrix Organization in the Retrosplenial Cortex of the reeler Mouse and Shaking Rat Kawasaki. Cereb Cortex 185:1125-1138.

Ichinohe N. 2012. Small-Scale Module of the Rat Granular Retrosplenial Cortex: An Example of the Minicolumn-Like Structure of the Cerebral Cortex. Front Neuroanat 5:69.

Ikeda J, Mori K, Oka S, Watanabe Y. 1989. A columnar arrangement of dendritic processes of entorhinal cortex neurons revealed by a monoclonal antibody. Brain Res 5051:176-179.

Insausti R. 1993. Comparative anatomy of the entorhinal cortex and hippocampus in mammals. Hippocampus 3(S1):19-26.

Insausti R, Amaral DG. 2011. Hippocampal formation. In The human nervous system, Paxinos G, Mai JK. Eds. Elsevier. 871-914.

Insausti R, Juottonen K, Soininen H, Insausti AM, Partanen K, Vainio P, Laakso MP, Pitkanen A. 1998. MR volumetric analysis of the human entorhinal, perirhinal, and temporopolar cortices. Am J Neuroradiol 19:659–671.

Insausti R, Tunon T, Sobreviela T, Insausti AM, Gonzalo LM. 1995. The human entorhinal cortex: a cytoarchitectonic analysis. J Comp Neurol 355:171-198.

Irizarry MC, Soriano F, McNamara M, Page KJ, Schenk D, Games D, Hyman BT. 1997. Aß deposition is associated with neuropil changes, but not with overt neuronal loss in the human amyloid precursor protein V717F PDAPP transgenic mouse. J Neurosci 17:7053–7059.

Jacobs J, Weidemann CT, Miller JF, Solway A, Burke JF, Wei XX, ...

Kahana MJ. 2013. Direct recordings of grid-like neuronal activity in human spatial navigation. Nat Neuroscience 16:1188-1190.

Jacobs LL, Downs WR. 1994. The evolution of murine rodents in Asia. In: Tomida Y, Li CK, Setoguchi T. Eds., Rodent and Lagomorph Families of Asian Origins and Diversification. National Science Museum Monographs, Tokyo, 8:149-156.

Jacobs LL, Flynn LJ. 2005. Of mice… again: the Siwalik rodent record, murine distribution, and molecular clocks. Interpreting the Past: Essays on Human, Primate, and Mammal Evolution in Honor of David Pilbeam, 63-80.

Jain N, Catania KC, Kaas JH. 1998. A histologically visible representation of the fingers and palm in primate area 3b and its immutability following long-term deafferentations. Cereb Cortex 8:227-236.

Janečka JE, Miller W, Pringle TH, Wiens F, Zitzmann A, Helgen KM, Springer MS, Murphy WJ. 2007. Molecular and genomic data identify the closest living relative of primates. Science 318:792-794.

Kaas JH. 2012. Evolution of columns, modules, and domains in the neocortex of primates. Proc Natl Acad Sciences USA 109(Supplement 1):10655-10660.

Kaschube M, Schnabel M, Löwel S, Coppola DM, White LE, Wolf F. 2010. Universality in the evolution of orientation columns in the visual cortex. Science 330:1113-1116.

Keil W, Kaschube M, Schnabel M, Kisvarday ZF, Löwel S, Coppola DM, ... Wolf F. 2012. Response to Comment on "Universality in the Evolution of Orientation Columns in the Visual Cortex ". Science 336:413-413.

Killian NJ, Jutras MJ, Buffalo EA. 2012. A map of visual space in the primate entorhinal cortex. Nature 491:761-764.

Kitamura T, Pignatelli M, Suh J, Kohara K, Yoshiki A, Abe K, Tonegawa S 2014. Island Cells Control Temporal Association Memory. Science 343:896-901.

Kjonigsen LJ, Leergaard TB, Witter MP, Bjaalie JG. 2011. Digital atlas of anatomical subdivisions and boundaries of the rat hippocampal region. Front Neuroinform. 5:2.

Klingler J. 1948. Die makroskopische Anatomie der Ammonsformation: Denkschriften der schweizerischen naturforschenden Gesellschaft, Band LXVIII. Abh. l , Gebrüder Fretz Ag., Zürich.

Klink R, Alonso A. 1997. Morphological characteristics of layer II projection neurons in the rat medial entorhinal cortex. Hippocampus 7:571-583.

Koch C. 1999. Biophysics of Computation. Information Processing in Single Neurons, New York: Oxford Univ. Press.

Koenig J, Linder AN, Leutgeb JK, Leutgeb S. 2011. The spatial periodicity of grid cells is not sustained during reduced theta oscillations. Science 332:592-595.

Kovjanic D, Redies C. 2003. Small-scale pattern formation in a cortical area of the embryonic chicken telencephalon. J Comp Neurol 456:95-104.

Krimer LS, Hyde TM, Herman MM, Saunders RC. 1997. The entorhinal cortex: an examination of cyto-and myeloarchitectonic organization in humans. Cereb Cortex 78:722-731.

Krupic J, Burgess N, O'Keefe J. 2012. Neural representations of location composed of spatially periodic bands. Science 337:853-857.

Kubota Y, Hattori R, Yui Y. 1994. Three distinct subpopulations of GABAergic neurons in rat frontal agranular cortex. Brain Res 649:159-173.

Langston RF, Ainge JA, Couey JJ, Canto CB, Bjerknes TL, Witter MP, Moser EI, Moser, MB. 2010. Development of the spatial representation system in the rat. Science 328:1576–1580.

Las L, Ulanovsky N. 2014. Hippocampal neurophysiology across species. In: Derdikman D, Knierim JJ. Eds. Space, Time and Memory in the Hippocampal Formation, Springer Verlag 431-464.

Lee KJ, Woolsey TA 1975. A proportional relationship between peripheral innervation density and cortical neuron number in the somatosensory system of the mouse. Brain Res 99:349-53.

Leise EM. 1990. Modular construction of nervous systems: a basic principle of design for invertebrates and vertebrates. Brain Res Brain Res Rev. 15:1-23.

Lind D, Franken S, Kappler J, Jankowski J, Schilling K. 2005. Characterization of the neuronal marker NeuN as a multiply phosphorylated antigen with discrete subcellular localization. J Neurosci Res 79: 295–302.

Lorente de No R. 1933. Studies on the structure of the cerebral cortex. I. The area entorhinalis, J Psychol Neurol 45:381-438.

Luhmann HJ, Martinez-Millin L, Singer W. 1986. Development of intrinsic connections in cat striate cortex. Exp Brain Res 63:443-448.

Lund JS, Yoshioka T, Levitt JB. 1993. Comparison of intrinsic connectivity in different areas of macaque monkey cerebral cortex. Cereb Cortex 3:148-162.

Mana S, Chevalier G. 2001. The fine organization of nigro-collicular channels with additional observations of their relationships with acetylcholinesterase in the rat. Neuroscience 106:357–374.

Manger P, Sum M, Szymanski M, Ridgway S, Krubitzer L. 1998. Modular subdivisions of dolphin insular cortex: does evolutionary history repeat itself? J Cogn Neurosci 10:153-166.

Mathisen JS, Blackstad TW. 1964. Cholinesterase in the hippocampal region. Acta Anat (Basel) 56:216-253.

Meyer HS, Wimmer VC, Oberlaender M, de Kock CP, Sakmann B, Helmstaedter M. 2010. Number and laminar distribution of neurons in a thalamocortical projection column of rat vibrissal cortex. Cereb Cortex 20:2277-86.

Meyer HS, Egger R, Guest JM, Foerster R, Reissl S, Oberlaender M. 2013. Cellular organization of cortical barrel columns is whisker-specific. Proc Natl Acad Sciences USA 110:19113-19118.

Mikkonen M, Soininen H, Pitkänen A. 1997. Distribution of parvalbumin-, calretinin-, and calbindin-D28k–immunoreactive neurons and fibers in the human entorhinal cortex. J Comp Neurol 388:64-88.

Molnár Z. 2013. Cortical Columns. In: Neural Circuit Development and Function in the Heathy and Diseased Brain. Rubinstein J. and Rakic P. Eds. Academic Press, 109-129.

Naumann RK, Anjum F, Roth-Alpermann C, Brecht M. 2012. Cytoarchitecture, areas, and neuron numbers of the Etruscan shrew cortex. J Comp Neurol 520:2512-30.

Newman EL, Gillet SN, Climer JR, Hasselmo ME. 2013. Cholinergic Blockade Reduces Theta-Gamma Phase Amplitude Coupling and Speed Modulation of Theta Frequency Consistent with Behavioral Effects on Encoding. J Neurosci 33:19635-19646.

Oberlaender M, de Kock CP, Bruno RM, Ramirez A, Meyer HS, Dercksen VJ, Helmstaedter M, Sakmann B. 2012. Cell type-specific three-dimensional structure of thalamocortical circuits in a column of rat vibrissal cortex. Cereb Cortex 22:2375-91.

Openshaw, S. 1983. The modifiable areal unit problem. Norwick: Geo Books.

Orban GA, Van Essen D, Vanduffel W. 2004. Comparative mapping of higher visual areas in monkeys and humans. Trends Cogn Sci 8:315-324.

Pakkenberg B, Gundersen HJG. 1997. Neocortical neuron number in humans: effect of sex and age. J Comp Neurol 384:312-320.

Paxinos G, Watson C, Carrive P, Kirkcaldie MTK, Ashwell K. 2009. Chemoarchitectonic atlas of the rat brain. Elsevier, USA.

Penfield W, Rasmussen TL. 1950. The cerebral cortex of man: a clinical study of localization of function. New York: Macmillan.

Peters A, and Kara DA. 1987. The neuronal composition of area 17 of rat visual cortex. IV.The organization of pyramidal cells. J. Comp. Neurol.260: 573–590.

Peterson DA, Lucidi-Phillipi CA, Murphy DP, Ray J, Gage FH. 1996. Fibroblast growth factor-2 protects entorhinal layer II glutamatergic neurons from axotomy-induced death. J Neurosci 163:886-898.

Rapp PR, Deroche PS, Mao Y, Burwell RD. 2002. Neuron number in the parahippocampal region is preserved in aged rats with spatial learning deficits. Cereb Cortex 12:1171–1179.

Ray S, Naumann R, Burgalossi A, Tang Q, Schmidt H, Brecht M. 2014. Grid-like arrangement and theta-modulation of a pyramidal cell microcircuit in layer 2 of medial entorhinal cortex. Science 343:891-896.

Riddle D, Richards A, Zsuppan F, Purves D. 1992. Growth of the rat somatic sensory cortex and its constituent parts during postnatal development. J Neurosci 12:3509–3524.

Rockland KS, Lund JS, Humphrey AL. 1982. Anatomical banding of intrinsic connections in striate cortex of tree shrews. J Comp Neurol 209:41-58.

Rockland KS, Lund JS. 1983. Intrinsic laminar lattice connections in primate visual cortex. J Comp Neurol 216:303-318.

Rockland KS, Ichinohe N. 2004. Some thoughts on cortical minicolumns. Exp Brain Res 158:265-277.

Rockland KS. 2010. Five points on columns. Front Neuroanat 4:22.

Roney KJ, Scheibel AB, Shaw GL. 1979. Dendritic bundles: survey of anatomical experiments and physiological theories. Brain Res. 180:225-71

Rose M. 1927a. Der Allocortex bei Tier und Mensch I. Teil. J Psychol Neurol 34:1-111.

Rose M. 1927b. Die sog. Riechrinde beim Menschen und beim Affen. II. Teil des „Allocortex bei Tier und Mensch". J Psychol Neurol 34:261-401

Rose S. 1927. Vergleichende Messungen im Allocortex bei Tier und Mensch. J. Psychol. Neurol 34:250–255

Sargolini F, Fyhn M, Hafting T, McNaughton BL, Witter MP, Moser MB, Moser EI. 2006. Conjunctive representation of position, direction, and velocity in entorhinal cortex. Science 312:758-762.

Schmued LC. 1990. A rapid, sensitive histochemical stain for myelin in frozen brain sections. J. Histochem. Cytochem. 38:717-720.

Schneider R. 1966. Das Gehirn von Rousettus aegypticus E. Geoffroy 1810, Megachiroptera, Chiroptera, Mammalia: ein mit Hilfe mehrerer Schnittserien erstellter Atlas. Abhandlungen der Senckenbergischen Naturforschenden Gesellschaft no. 513, Frankfurt am Main.

Schuurman N, Bell N, Dunn JR, Oliver L. 2007. Deprivation indices, population health and geography: an evaluation of the spatial effectiveness of indices at multiple scales. J Urban Health, 84:591–603.

Sgonina K. 1938. Zur vergleichenden Anatomie der Entorhinal- und Präsubikularregion. J Psychol Neurol 48:56-163.

Simic G, Bexheti S, Kelovic Z, Kos M, Grbic K, Hof PR, Kostovic I. 2005. Hemispheric asymmetry, modular variability and age-related changes in the human entorhinal cortex. Neuroscience 130:911-925.

Sincich LC, Horton JC. 2002. Pale cytochrome oxidase stripes in V2 receive the richest projection from macaque striate cortex. J Comp Neurol 447:18-33.

Slomianka L, Geneser FA. 1991. Distribution of acetylcholinesterase in the hippocampal region of the mouse: I. Entorhinal area, parasubiculum, retrosplenial area, and presubiculum. J Comp Neurol 303:339-354.

Solodkin A, Van Hoesen GW. 1996. Entorhinal cortex modules of the human brain. J Comp Neurol 365:610-627.

Stephan H. 1983. Evolutionary trends in limbic structures. Neurosci Biobehav Rev 73:367-374.

Stensola H, Stensola T, Solstad T, Frøland K, Moser MB, Moser EI. 2012. The entorhinal grid map is discretized. Nature 492:72-78.

Sternberger LA, Sternberger NH. 1983. Monoclonal antibodies distinguish phosphorylated and nonphosphorylated forms of neurofilaments in situ. Proc Natl Acad Sciences USA 80:6126-6130.

Suárez J, Dávila JC, Real MÁ, Guirado S, Medina L. 2006. Calcium-binding proteins, neuronal nitric oxide synthase, and GABA help to distinguish different pallial areas in the developing and adult chicken. I. Hippocampal formation and hyperpallium. J Comp Neurol 497:751-771.

Suzuki WA, Porteros A. 2002. Distribution of calbindin D-28k in the entorhinal, perirhinal, and parahippocampal cortices of the macaque monkey. J Comp Neurol 451:392-412.

Tang Q, Burgalossi A, Ebbesen CL, Ray S, Naumann R, Schmidt H, Spicher D, Brecht M. 2014. Pyramidal and Stellate Cell Specificity of Grid and Border Representations in Layer 2 of Medial Entorhinal Cortex. Neuron. 84:1191-1197

Tsuji S. 1998. Electron microscopic localization of acetylcholinesterase activity in the central nervous system: chemical basis of a catalytic activity of Hatchett's brown cupric ferrocyanide precipitate revealed by 3, 3'-diaminobenzidine. Folia Histochem Cytobiol. 36:67-70.

van Groen T. 2001. Entorhinal cortex of the mouse: cytoarchitectonical organization. Hippocampus 11:397-407.

van Hoesen GW, Augustinack JC, Dierking J, Redman SJ, Thangavel R. 2000. The parahippocampal gyrus in Alzheimer's disease: clinical and preclinical neuroanatomical correlates. Ann N Y Acad Sci 911:254-274.

van Kleef ES, Gaspar P, Bonnin A. 2012. Insights into the complex influence of 5-HT signaling on thalamocortical axonal system development. Eur J Neurosci 35:1563-1572.

Varga C, Lee SY, Soltesz I. 2010. Target-selective GABAergic control of entorhinal cortex output. Nat Neurosci 13:822-824.

Velayudhan L, Proitsi P, Westman E, Muehlboeck JS, Mecocci P, Vellas B, Tsolaki M, Kłoszewska I, Soininen H, Spenger C, Hodges A, Powell J, Lovestone S, Simmons A; dNeuroMed Consortium. 2013. Entorhinal cortex thickness predicts cognitive decline in Alzheimer's disease. J Alzheimers Dis 33:755-66.

Waddell PJ, Kishino H, Ota R. 2001. A Phylogenetic Foundation for Comparative Mammalian Genomics. Genome Inform 12:141-154.

Wallace MN. 1986. Spatial relationship of NADPH-diaphorase and acetylcholinesterase lattices in the rat and mouse superior colliculus. Neuroscience 19:381-91.

Waters RS, McCandlish CA, Li CX. 1995. Organization and Development of the Forepaw Barrel Subfield in Somatosensory Cortex of Rat. In: The Barrel Cortex of Rodents. Jones E.G. and Diamond I.T. Eds. Plenum press, New York 77-122.

West MJ, Slomianka L. 1998. Total number of neurons in the layers of the human entorhinal cortex. Hippocampus 81:69–82.

Williams RW. 2000. Mapping genes that modulate brain development: a quantitative genetic approach. In: Mouse brain development Goffinet AF, Rakic P, eds. Springer Verlag, New York 21–49.

Wong-Riley M. 1979. Changes in the visual system of monocularly sutured or enucleated cats demonstrable with cytochrome oxidase histochemistry. Brain Res. 171:11-28.

Woolsey TA, Van der Loos H. 1970. The structural organization of layer IV in the somatosensory region SI of mouse cerebral cortex: the description of a cortical field composed of discrete cytoarchitectonic units. Brain Res 17:205-242.

Wree A, Lutz B, Thole U. 1992. Volumes of the cytoarchitectonic areas in the rat cerebral cortex. J Hirnforsch 33:545–548.

Yartsev MM, Witter MP, Ulanovsky N. 2011. Grid cells without theta oscillations in the entorhinal cortex of bats. Nature 479:103-107.

Figures

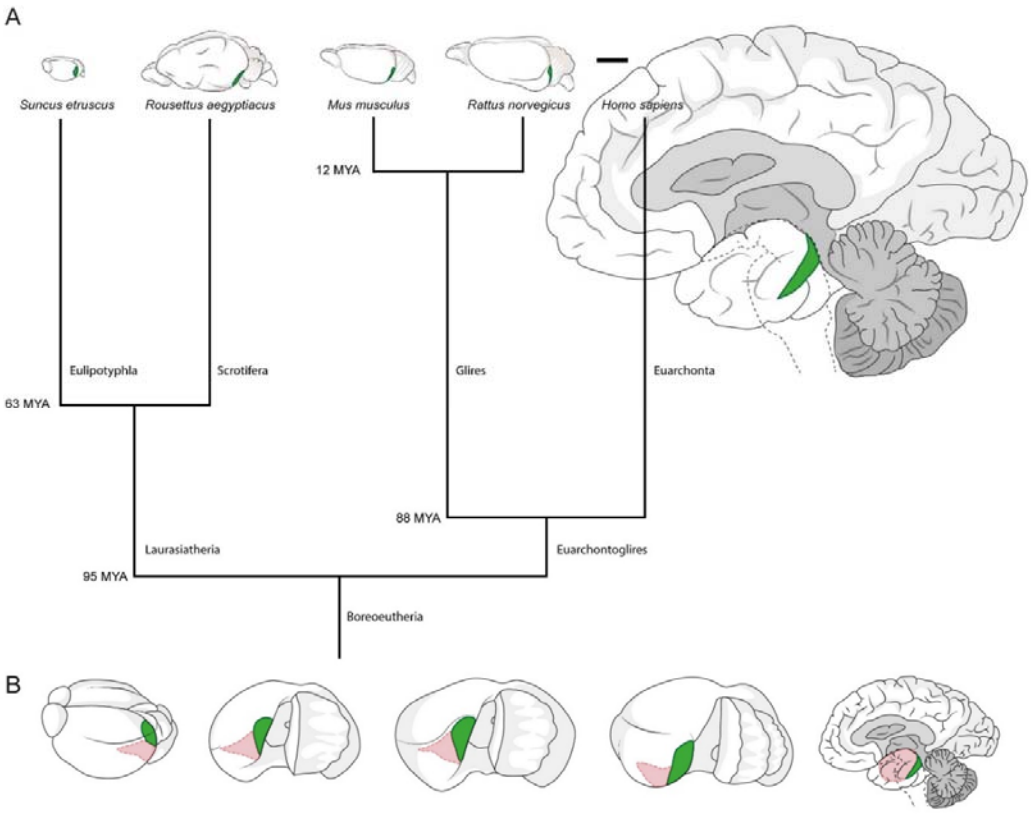

Figure 1: Position of medial and lateral entorhinal cortices and scaling of the brains under study

A, Position of medial/ caudal entorhinal cortices containing calbindin patches (highlighted in green) in the brain of the Etruscan shrew, the Egyptian fruit bat, the mouse, the rat and in the human brain (left to right, drawn to scale). Branch points of the tree show estimated divergence time according to (Janecka et al., 2007; Hallström et al., 2007; Jacobs and Downs, 1994; Jacobs and Flynn, 2005; Waddell et al., 2001).

B, Position of entorhinal cortices in the brain of the Etruscan shrew, the Egyptian fruit bat, the mouse, the rat and in the human brain (left to right, not to scale). The brains were rotated to show the surface of the medial/ caudal entorhinal cortex (highlighted in green). Remaining entorhinal areas marked in pink.

Scale bar: A, 5 mm.

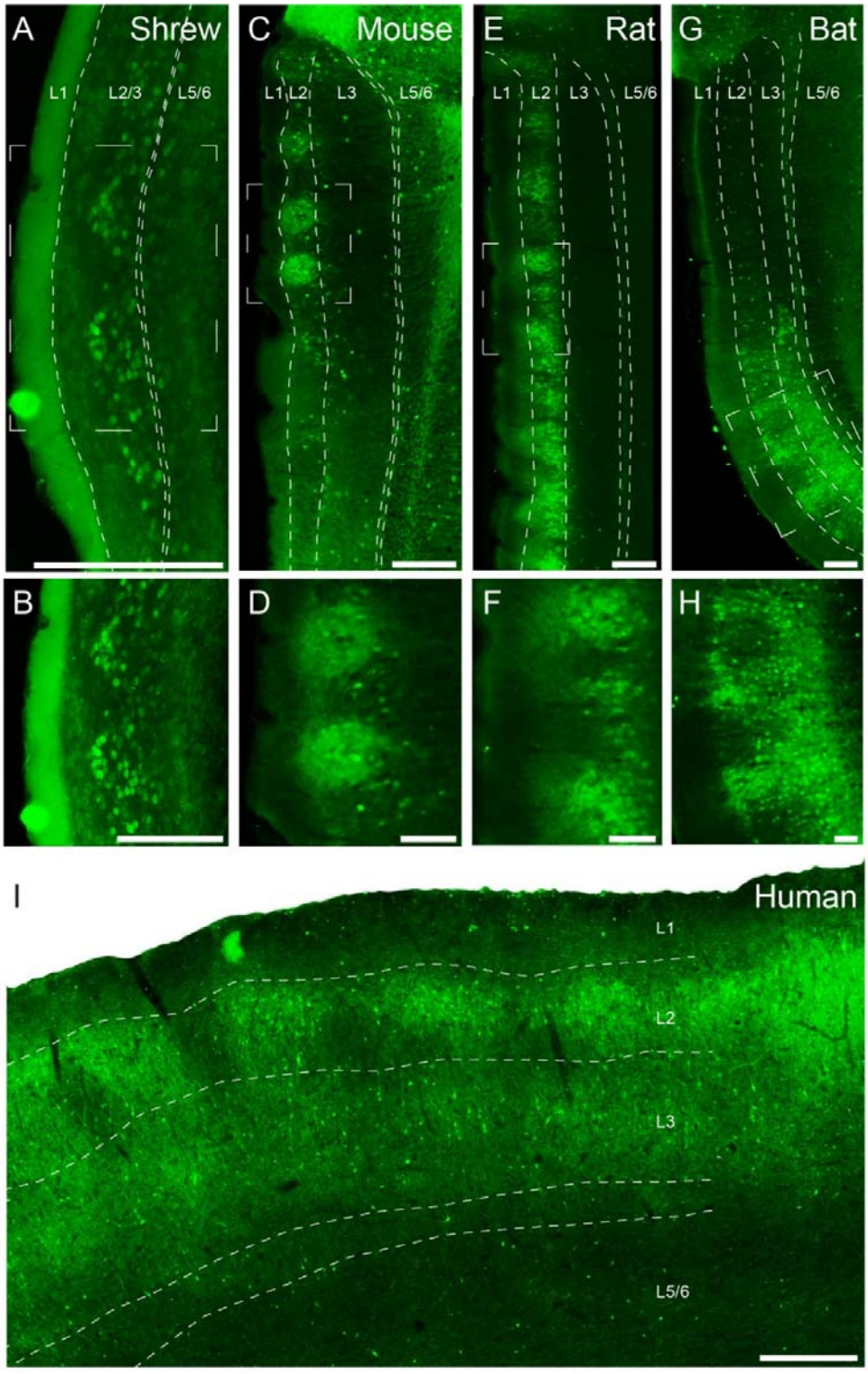

Figure 2: Sagittal and coronal sections through medial/caudal entorhinal cortex of Etruscan shrews, mice, rats, bats and humans stained for calbindin immunoreactivity revealing patches of pyramidal cells.

Calbindin-immunoreactivity in the entorhinal cortex reveals patches of calbindin-positive pyramidal cells, shown in a coronal section in the Etruscan shrew (**A**) and parasagittal sections in the mouse (**C**), rat (**E**), and Egyptian fruit bat (**G**).

B,D,F,H, Higher magnification views of the respective panels above.

I, Coronal section of a human caudal entorhinal cortex

Scale bars: **A**, 200 μm. **C, E, G**, 250 μm. **B, D, F, H**, 100 μm. **I**, 500 μm. White stippled lines indicate laminar borders. White stippled boxes in A, C, E, G indicate subregions used for higher magnification images in B, D, F, H. L1, L2, L3, L5/6 indicate entorhinal layers 1,2,3 and 5/6.

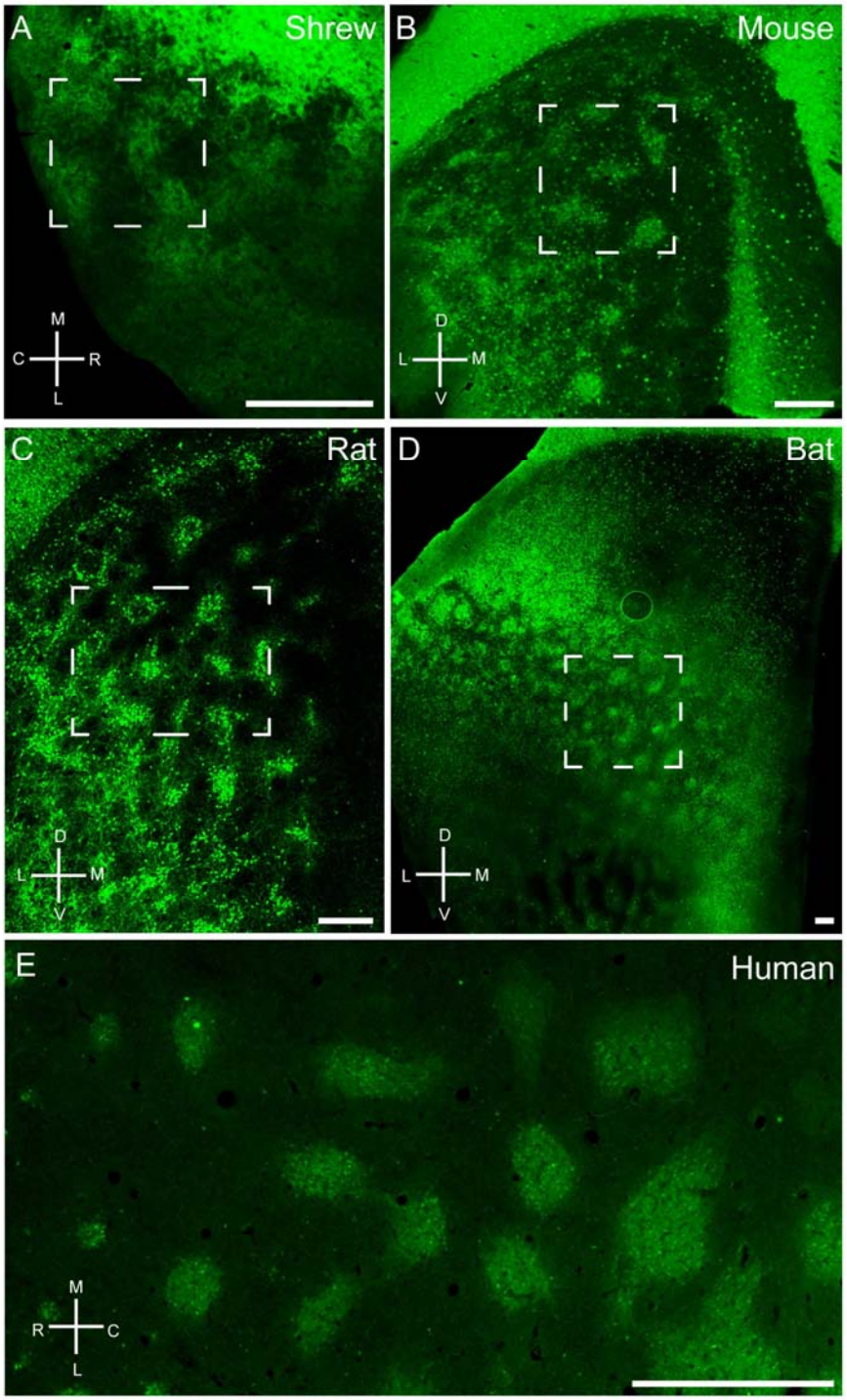

Figure 3: Tangential sections through medial entorhinal cortex of Etruscan shrews (A), mice (B), rats (C), bats (D) and humans (E) stained for calbindin immunoreactivity revealing grid-like patches of pyramidal cells.

Note that, especially in rodents, areas surrounding the entorhinal cortex such as postrhinal cortex and presubiculum contain a high density of calbindin positive cells in superficial layers.

Scale bars: **A-D**, 250 µm. **E**, 1 mm. Stippled boxes indicate the position of higher magnification images in Figure 4. C = caudal, D = dorsal, L = lateral, M = medial, R = rostral, V = ventral.

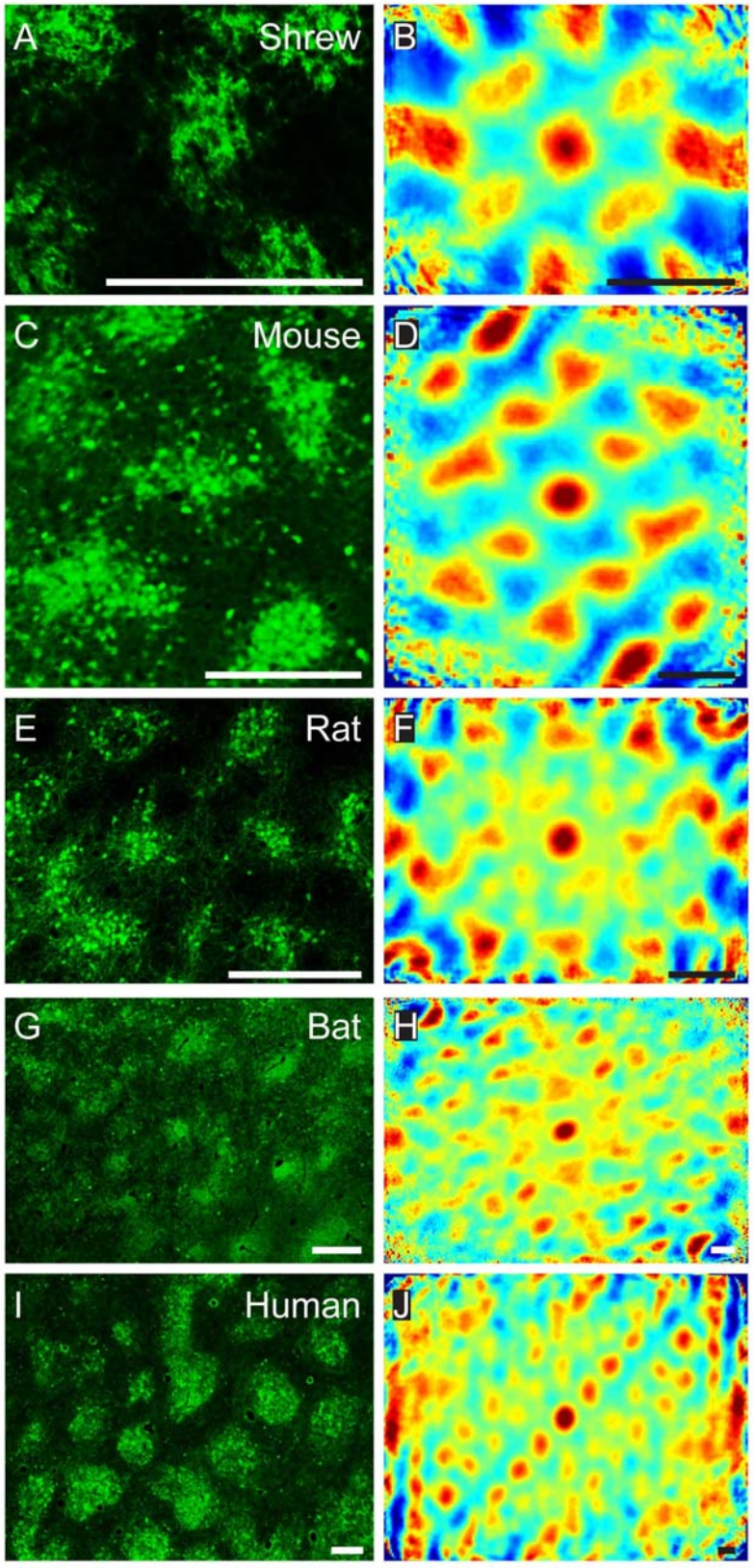
A
Shrew
B
C
Mouse
D
E
Rat
F
G
Bat
H
I
Human
J

Figure 4: Grid-like arrangement of calbindin-positive pyramidal cells in the medial entorhinal cortex

High magnification view of a tangential section of Etruscan shrew (**A**), mouse (**C**), rat (**E**), bat (**G**) and human entorhinal cortex (**I**).

B,D,F,H,J, Two-dimensional spatial autocorrelation of the respective panels to the left revealing a periodic spatial organization of calbindin-positive patches.

Color scale: -0.5 (blue) through 0 (green) to 0.5 (red), The mouse, rat and bat samples exhibit hexagonal spatial organization and their grid scores are 0.63 (**C,D**), 0.98 (**E,F**) and 0.82 (**G,H**) respectively. The Etruscan shrew and human exhibit rectangular spatial organization and their cartesian scores are 1.39 (**A,B**) and 0.46 (**I,J**) respectively

Scale bars: A-J, 250 μm. C = caudal, D = dorsal, L = lateral, M = medial, R = rostral, V = ventral.

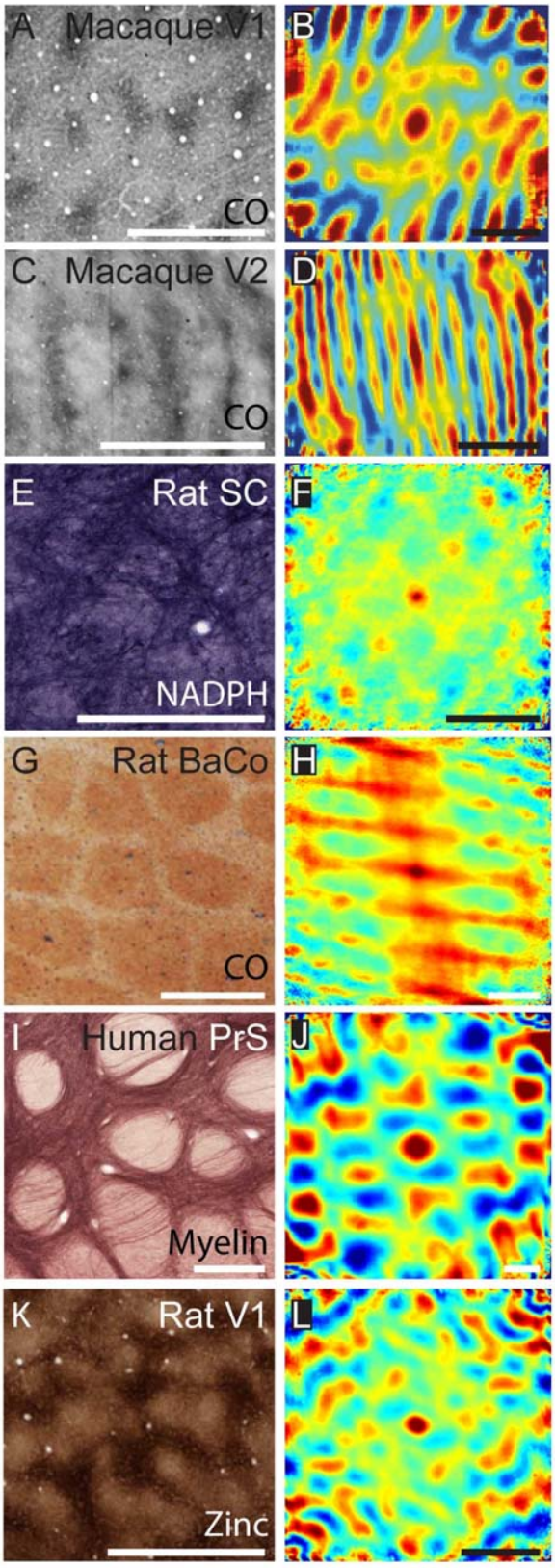

Figure 5: Structural analysis of different brain regions using spatial autocorrelation.

Macaque primary (**A**) and secondary (**C**) visual cortex stained for cytochrome oxidase. Adapted with permission from: Sincich LC and Horton JC. 2002. Pale cytochrome oxidase stripes in V2 receive the richest projection from macaque striate cortex. J Comp Neurol. 447:18–33. Copyright © 2002 Wiley-Liss, Inc.

E, Rat superior colliculus stained for NADPH diaphorase.

G, Rat barrel cortex stained for cytochrome oxidase.

I, Human presubiculum stained for myelin.

K, Rat visual cortex stained for presynaptic zinc ions.

B,D,F,H,J,**L**, Two-dimensional spatial autocorrelation of the respective panels to the left revealing different types of regular spatial organization.

Color scale: -0.5 (blue) through 0 (green) to 0.5 (red), (60 degree) grid scores are 0.24 (**A,B**), -0.04 (**C,D**), 0.31 (**E,F**), 0.29 (**G,H**), 0.74 (**I,J**), 0.3 (**K,L**) respectively. Cartesian (90 degree grid) scores are 0.24 (**A,B**), 0.09 (**C,D**), 0.56 (**E,F**), 0.91 (**G,H**), 0.08 (**I,J**) 0 (**K,L**) respectively.

Scale bars: **A,B**, 1 mm; **C,D**, 5 mm; **E,F**, 250 μm; **G-L**, 500 μm.CO = Cytochrome oxidase. V1 = primary visual cortex. V2 = secondary visual cortex. SC = superior colliculus. NADPH = NADPH diaphorase staining. BaCo = barrel cortex. PrS = presubiculum. Zinc = synaptic zinc staining.

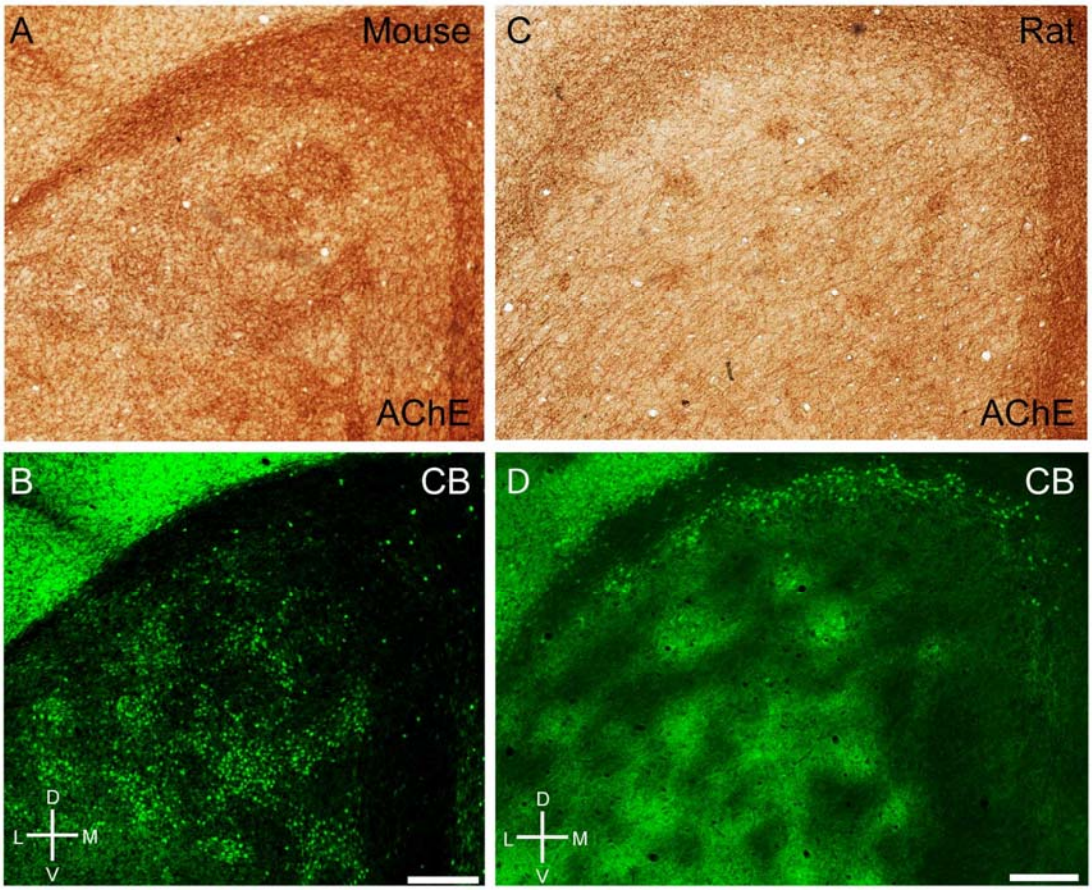

Figure 6: Cholinergic innervation targets calbindin patches in mice and rats

A, Tangential section through mouse entorhinal cortex stained for acetylcholinesterase activity, showing discrete clusters of staining.

B, The same section stained for calbindin.

C, Tangential section through rat entorhinal cortex stained for acetylcholinesterase activity, showing discrete clusters of staining.

D, The same section stained for calbindin.

Scale bars: **B**, 250 µm (also for **A**); **D**, 250 µm (also for **C**). D = dorsal, L = lateral, M = medial, V = ventral.

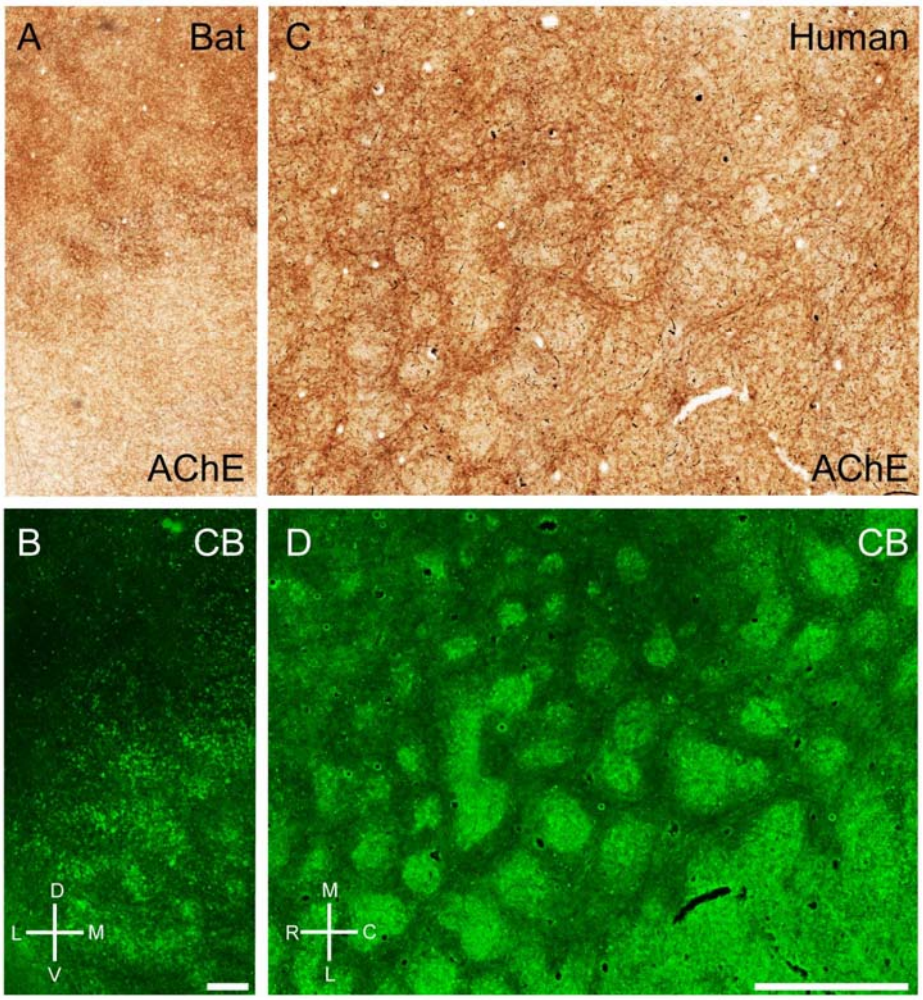

Figure 7: Cholinergic innervation avoids calbindin patches in bats and humans

A, Tangential section through Egyptian fruit bat entorhinal cortex stained for acetylcholinesterase activity, showing discrete clusters of staining.

B, The same section stained for calbindin.

C, Tangential section through human entorhinal cortex stained for acetylcholinesterase activity, showing discrete clusters of staining.

D, The same section stained for calbindin.

Scale bars: B, 250 μm (also for A); D, 250 μm (also for C). Stippled box in D indicates the position of higher magnification images in Figure 4. D = dorsal, L = lateral, M = medial, V = ventral.

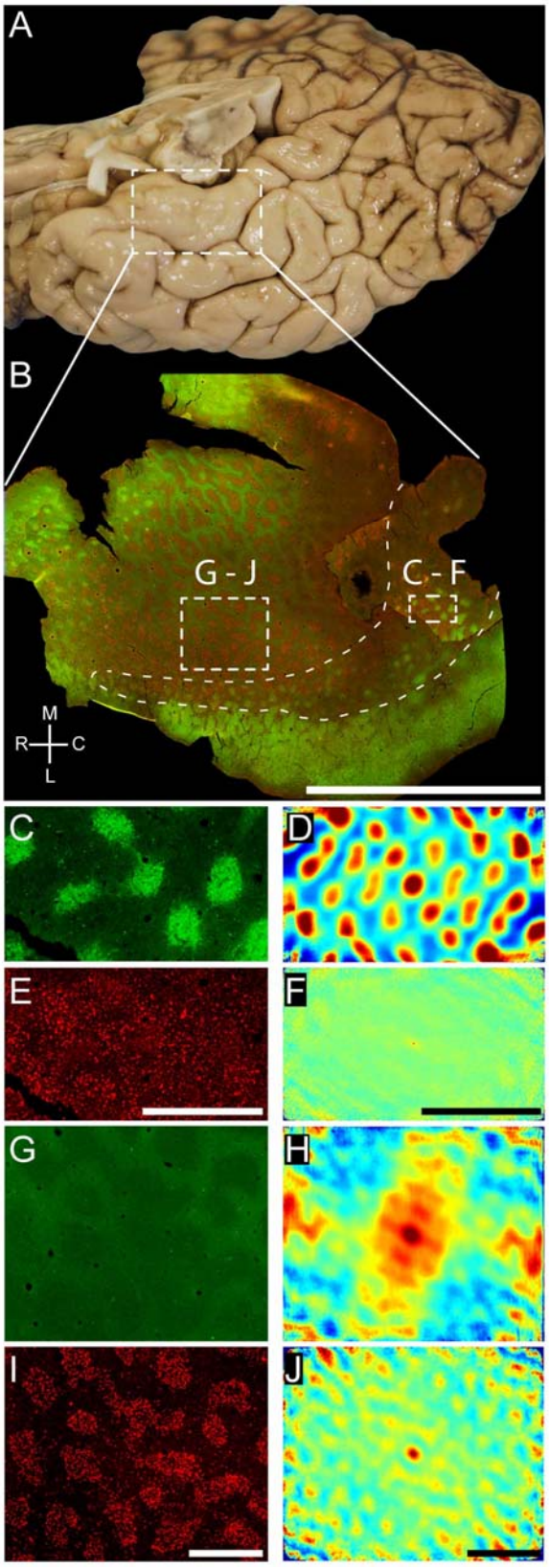
A
B
G - J
C - F
M
R
C
L
C
D
E
F
G
H
I
J

Figure 8: Grid-like arrangement of calbindin-positive pyramidal cells in the human entorhinal cortex

A, Overview of the human temporal lobe showing the entorhinal cortex close to the substantia nigra.

B, Tangential section through entorhinal cortex oriented as in **A** and stained for calbindin and neurofilament immunoreactivity (SMI-32). This figure was assembled from 2 different sections stained in the same way to show a larger number of calbindin positive patches. Stippled boxes indicate the location of panels C-F and G-J. Stippled line surrounds the caudal calbindin patch region and thus marks the caudal border of the entorhinal cortex.

C, High magnification view of calbindin-immunoreactivity in a tangential section of human caudal entorhinal cortex.

D, Two-dimensional spatial autocorrelation of the respective panel to the left revealing a hexagonal spatial organization of calbindin-positive patches. Grid score is 0.71.

E, High magnification view of SMI-32-immunoreactivity in a tangential section of human caudal entorhinal cortex.

F, Two-dimensional spatial autocorrelation of the respective panel to the left revealing a lack of spatial organization. Grid score is -0.03.

G, High magnification view of calbindin-immunoreactivity in a tangential section of human rostral entorhinal cortex.

H, Two-dimensional spatial autocorrelation of the respective panel **G** revealing a less regular spatial organization than in **D**. Grid score is -0.18.

I, High magnification view of SMI-32-immunoreactivity in a tangential section of human rostral entorhinal cortex.

J, Two-dimensional spatial autocorrelation of the respective panel to the left revealing a little regularity in spatial organization. Grid score is 0.19.

Scale bars: B, 1 cm; E, 1 mm (C); F, 2 mm (D); G, 1 mm; H, 2 mm. C = caudal, L = lateral, M = medial, R = rostral.

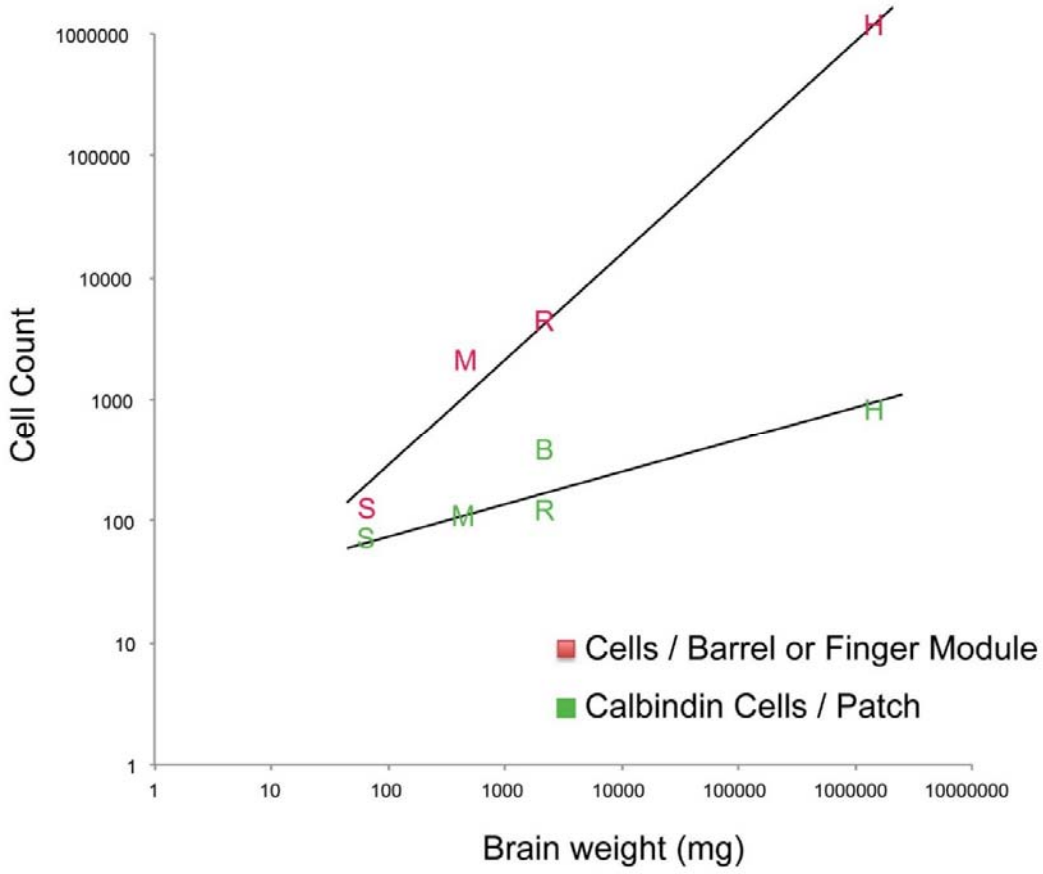

Figure 9: Neuron number in L2 entorhinal calbindin modules, L4 barrel / finger modules and brain size

Letters indicate barrel cell numbers in somatosensory barrels (red) and entorhinal calbindin patches (green) in S = Etruscan shrews, M = mice, R = rats, B = Egyptian fruit bats and H = humans (from left to right).

Tables

Table 1 Antibodies

Name	Immunogen	Supplier	Cat. No., RRID	Species	Dilution	Specificity
SMI-32	nonphosphorylated epitope of neurofilament H isolated from homogenized hypothalami from Fischer 344 rats	Chemicon (now part of Millipore, Billerica, MA)	NE1023, RRID:AB_2043449	mouse monoclonal	1:1,000	Sternberger and Sternberger,1983;
NeuN	N-Terminus of recombinant protein corresponding to mouse NeuN	Chemicon (now part of Millipore, Billerica, MA)	MAB377, AB_2298772	Mouse monoclonal	1:1,000	Lind et al., 2005
Calbindin D-28k	Calbindin D-28k purified from chicken gut	Swant (Bellinzona, Switzerland)	300, RRID:AB_10000347	mouse monoclonal	1:5,000	Celio M.R. et al., 1990
Calbindin D-28k	Calbindin D-28k purified from recombinant rat calbindin D-28k	Swant (Bellinzona, Switzerland)	CB38, RRID:AB_10000340	rabbit polyclonal	1:5,000	Airaksinen et al., 1997

Table 2 Neuron number / Calbindin patch

Species	Patches counted	Calbindin positive neurons / patch
Shrew	10 from 3 brains	79 ± 22
Mouse	11 from 4 brains	107 ± 22
Rat	19 from 4 brains	111 ± 42
Egyptian fruit bat	10 from 2 brains	381 ± 105
Human	8 from 2 brains	837 ± 84

Table 3 Brain Weight, Neuron Number in Somatosensory Barrels and Total Neuron Number in Entorhinal cortex

Species	Brain size (mg)	Reference	# of neurons in a layer 4 barrel / finger representation	Reference	EC # of neurons	Reference
Shrew	64	Naumann et al., 2012	~100	This study.	$1.3*10^5$	Naumann et al., 2012
Mouse	453	Williams, 2000	~2000 (1035-2624)	Lee & Woolsey, 1975	$4*10^5$	Irizzary et al., 1997
Rat	~2000	Donaldson & Hatai, 1931	4447±439	Meyer et al., 2010	$6.8*10^5$	Rapp et al., 2002
Egyptian fruit bat	2157 ± 100	This study				
Human	1320000	Blinkow & Glezer, 1968	~1150000	Estimate. This study (see text)	$7\text{-}8*10^6$	West & Slomianka, 1998

Table 4 Patch number, patch size & spacing

The number of neurons in a human finger representation was estimated as described in the method section. The total number of patches is difficult to estimate because it requires well-stained and completely analyzable specimen and also relies on accurate assessment of areal boundaries. Estimates of total of total patch number are based on 6 brains and 9 hemisphere in mice, 10 brains in rats, and 2 brains each for shrews, bats and humans.

Species	Total # of patches in a medial / caudal EC hemisphere	Patch diameter	Linear Patch density (Dorso-Ventral) (No. of patches per mm)	Patch density (No. of patches per square mm)
Shrew	14 ± 2	103 ± 23 µm	25	45
Mouse	22 ± 7	94 ± 37 µm	19	10
Rat	69 ± 17	145 ± 41 µm	17	14
Egyptian fruit bat	100 ± 1	250 ± 77 µm	20	6
Human	115 ± 16	532 ± 197 µm	8	1

Table 5 Modifiable Areal Unit Analysis

Number of regions having hexagonal periodicity/ rectangular periodicity/ no periodicity as illustrated by modifiable areal unit analysis of complete entorhinal micrographs of species having large entorhinal cortices.

Species	Scale 1 (hexagonal / rectangular / none)	Scale 2 (hexagonal / rectangular / none)
Rat	11 / 8 / 6	56 / 47 / 29
Egyptian fruit bat	16 / 13 / 6	64 / 68 / 33
Human	9 / 7 / 4	66 /37 / 29

Table 6 Grid scores, Elliptical grid scores and Cartesian scores

Average grid scores with and without elliptical modifications and Cartesian scores. Scores are represented as mean ± SD and are based on 9 samples in rats, 2 samples in shrews, and 3 samples each for mice, bats and humans.

Species	Grid Scores	Elliptical Grid scores	Cartesian Scores
Shrew	-0.02 ± 0.84	0.73 ± 0.21	0.58 ± 1.15
Mouse	0.35 ± 0.11	0.55 ± 0.09	0.14 ± 0.30
Rat	0.28 ± 0.43	0.84 ± 0.23	0.00 ± 0.15
Egyptian fruit bat	0.52 ± 0.35	0.81 ± 0.04	0.45 ± 0.42
Human	0.36 ± 0.39	1.18 ± 0.10	0.28 ± 0.39

Chapter 5

Structural development and dorsoventral maturation of the medial entorhinal cortex.

Published as:

Ray, S. & Brecht, M. (2016). Structural development and dorsoventral maturation of the medial entorhinal cortex. *eLife. 13343*

doi: 10.7554/eLife.13343

Structural Development and Dorsoventral Maturation of the Medial Entorhinal Cortex

Saikat Ray[1] & Michael Brecht[1]

[1]Bernstein Center for Computational Neuroscience
Humboldt University of Berlin
Philippstr. 13 Haus 6
10115 Berlin
Germany

Corresponding authors: S.R. (saikat.ray@bccn-berlin.de) & M.B. (michael.brecht@bccn-berlin.de)

Running Title: Development of MEC

Keywords: Grid layout, Pyramidal neurons, Calbindin patches, Cholinergic innervation, Reelin, Medial entorhinal cortex, Parasubiculum, Wfs1, doublecortin, immature neurons

Acknowledgements: We thank Juliane Steger and Undine Schneeweiß for outstanding technical support, Shimpei Ishiyama for excellent graphic design and Peter Bennett, Edith Chorev, Andreea Neukirchner, Juan Ignacio Sanguinetti, Jean Simonnet and Robert Naumann for comments.

Contributions: S.R. and M.B. designed the experiments and wrote the manuscript. S.R performed the experiments and analyzed the results. M.B. supervised the project.

Competing Financial Interest Statement: The authors declare that they have no competing financial interests.

Abstract

We investigated the structural development of superficial-layers of medial entorhinal cortex and parasubiculum in rats. The grid-layout and cholinergic-innervation of calbindin-positive pyramidal-cells in layer-2 emerged around birth while reelin-positive stellate-cells were scattered throughout development. Layer-3 and parasubiculum neurons had a transient calbindin-expression, which declined with age. Early postnatally, layer-2 pyramidal but not stellate-cells co-localized with doublecortin – a marker of immature neurons – suggesting delayed functional-maturation of pyramidal-cells. Three observations indicated a dorsal-to-ventral maturation of entorhinal cortex and parasubiculum: (i) calbindin-expression in layer-3 neurons decreased progressively from dorsal-to-ventral, (ii) doublecortin in layer-2 calbindin-positive-patches disappeared dorsally before ventrally, and (iii) wolframin-expression emerged earlier in dorsal than ventral parasubiculum. The early appearance of calbindin-pyramidal-grid-organization in layer-2 suggests that this pattern is instructed by genetic information rather than experience. Superficial-layer-microcircuits mature earlier in dorsal entorhinal cortex, where small spatial-scales are represented. Maturation of ventral-entorhinal-microcircuits – representing larger spatial-scales – follows later around the onset of exploratory behavior.

Introduction

The representation of space in the rodent brain has been investigated in detail. The functional development of spatial response properties has also been investigated in the cortico-hippocampal system[1-2], with studies suggesting the early emergence of head-directional selectivity[3-4], border representation[5] and place cell firing, but a delayed maturation of grid cell discharges[6-7].

Even though there is information on the emergence of functional spatial properties in the hippocampal formation, remarkably little is known about the structural development of the microcircuits which bring about these properties. To understand this, we investigated the development of the architecture of the medial entorhinal cortex (MEC) and parasubiculum (PaS), two key structures in the cortico-hippocampal system.

In adult animals, layer 2 of MEC contains two types of principal cells, stellate and pyramidal cells[8-9]. Stellate and pyramidal neurons are distinct in their intrinsic conductance[10-11], immunoreactivity[12], projections[13-14] and inhibitory inputs[12]. Pyramidal neurons in layer 2 of MEC can be identified by calbindin-immuno-reactivity[12] and are clustered in patches across various mammalian species[15-17], while stellate cells can be identified by reelin-immuno-reactivity[12] and a lack of structural periodicity[16]. In rodents, the grid-like arrangement of pyramidal cell patches is aligned to cholinergic inputs[16-17]. Functionally, about a third of all cells in layer 2 exhibit spatial tuning with grid, border, irregular and head-directional discharges being present[18].

Neurons in layer 3 of MEC are characterized by rather homogenous *in vitro* intrinsic and *in vivo* spatiotemporal properties[19]. A majority of cells exhibit a lack of spatial modulation, and the remaining are mainly dominated by irregular spatial responses[19] with a fraction also exhibiting grid, border and head-directional responses[20].

The parasubiculum is a long and narrow structure flanking the dorsal and medial extremities of MEC (Video 1). The superficial parasubiculum, corresponding to layer 1 of MEC is divided into large clusters, while the deeper part, corresponding to layers 2 and 3 of MEC, is rather homogenous[21]. In terms of functional tuning of cells, a majority of the cells of PaS show spatially tuned responses, and include grid, border, head-directional and irregular spatial cells[20-21].

Here we investigate the emergence of the periodic pyramidal-cell patch pattern in layer 2 of MEC, as well as the development of cellular markers that characterize the architecture of adult MEC and PaS. The results indicate an early emergence of pyramidal cell organization, a delayed maturation of pyramidal but not stellate cells and a dorsal-to-ventral maturation of MEC circuits.

Results

We first investigated development of brain size and thickness of layers of the MEC (Figure 1) by observing rats at E18, P0, P4, P8, P12, P16, P20, P24 and adults (>P42). The majority of the brain development takes place within the first few weeks postnatally (Figure 1a), with the brain size increasing 1000% from 0.12 ± 0.00 g at E18 (mean ± SD; n=3) to 1.23 ± 0.07 g at P12 (n=5). Subsequently, the growth plateaus to ~25% with the brain weighing 1.71 ± 0.08 g at P24 (n=6) and having a weight of 2.11 ± 0.14 g in adults (n=9) (Figure 1b). The superficial layers (layers 1-3) of the MEC (Figure 1c) double in thickness during this early postnatal period from 243 ± 35 μm at P0 (mean ± SD; n=21, 4 rats) to 652 ± 50 μm at P12 (n=24, 4 rats). A similar increase is also observed in the deeper layers (layers 4-6) from 167 ± 21 μm at P0 (n=21, 4 rats) to 329 ± 54 μm at P12 (n=24, 4 rats).The overall thickness plateaus around this point to 981 ± 81 μm at P12 (n=24, 4 rats) and remains at 882 ± 78 μm in adults (n=24, 4 rats) (Figure 1d). Proportionally, the thickness of the layers remains similar during development, with layer 2 accounting for ~20% and layers 3 and 5/6 each accounting for ~ 30% of the MEC. Layers 1 and 4 are the thinnest at about 10% and 5% of the total thickness respectively (Figure 1d).

We next investigated the microcircuit organization of superficial layers of MEC. Calbindin, a calcium binding protein, is selectively expressed in layer 2 pyramidal cells[12,15], which form a grid-like arrangement in adult animals[16]. Concurrently, reelin, an extracellular matrix protein, is selectively expressed in stellate cells in layer 2 of MEC, which are scattered throughout[16] layer 2. To visualize the development of entorhinal microcircuits we first prepared tangential sections (see our video animation on preparing tangential sections, Video 1) through layer 2 of medial entorhinal cortex and stained for calbindin-immunoreactivity. From the earliest postnatal stages, calbindin+ neurons in the MEC exhibited clustering, forming patches at P0 (Figure 2a). The calbindin+ patches at P0 exhibited a grid-like (Figure 2a,b) regular arrangement (Figure 2c), determined by spatial autocorrelation analysis and grid scores, similar to that observed in adults[16-17] (Figure 2d-f). Similar preparations for visualizing stellate cells by reelin-immunoreactivity (Figure 2 - Figure supplement 1), exhibited the presence of stellate cells in early postnatal stages (Figure 2 - Figure supplement 1a,b) and a lack of periodicity (Figure 2 - Figure supplement 1c), similar to observations made in adults[16] (Figure 2 - Figure supplement 1d-f). Calbindin+ pyramidal neurons in the MEC (Figure 2g) also received preferential cholinergic innervation early postnatally (Figure 2h-i), similar to adults[16-17] (Figure 2j-l).

In the parasubiculum, a transient presence of calbindin was observed with ~ 15 clusters of calbindin+ neurons at P0 (Figure 2a) and P4 (Figure 2g). This expression was curtailed in older animals, with only a calbindin+ stripe persisting in adults (Figure 2d).

To visualize the laminar development of MEC, we stained parasagittal sections for calbindin (Figure 3) and reelin (Figure 4) immunoreactivity. Indications of calbindin+ neuronal clusters were visible prenatally at E18 (Figure 3a). However, the calbindin+ patches in the MEC did not exhibit clustering of their dendrites, as previously described in adults[16] at E18 and P0 (Figure 3a,b). Some dendritic clustering could be observed at P4 (Figure 3c), while from P8 (Figure 3d-h) the dendritic clustering of calbindin+ pyramidal neurons was similar to that in adults. In layer 3 of the MEC, we observed a transient presence of calbindin expression. The number of calbindin+ neurons in layer 3 declined progressively from prenatal stages to P20 (Figure 3a-g), where it attained adult-like levels with rarely any calbindin+ neurons in layer 3 (Figure 3h). Quantitatively, calbindin+ neuronal density (calbindin+ neurons per mm^2) decreased from 955 ± 315 (mean ± SD; count refers to n=3776 neurons in 8 rats) in P4-P8 rats to 333 ± 99 (n=2104 neurons, 8 rats) in P12-P16 rats to 141 ± 56 (n=828 neurons, 7 rats) in adults (Figure 3i).

Reelin was present in layer 2 from early postnatal stages (Figure 4a; Figure 2- Figure supplement 1a, b), though the most prominent reelin-immunoreactive cells in the first two postnatal weeks were present in layer 1 (Figure 4 a-c). Reelin expression increased in layer 3 of the MEC from early postnatal stages to P20 (Figure 4 a-e), where it attained adult-like levels (Figure 4f). Quantitatively, reelin+ neuronal density in layer 3 increased from 729 ± 435 (n=1405 neurons, 4 rats) in P4-P8 rats to 1549 ± 115 (n=3309 neurons, 3 rats) in P12-P16 rats to 1996 ± 208 (n=5039 neurons, 3 rats) in adults.

Three observations indicated a dorsal-ventral developmental gradient in the superficial layers of medial entorhinal cortex and parasubiculum:

First, the transient calbindin expression in layer 3 disappeared from dorsal to ventral. Thus, most of layer 3 had calbindin+ neurons at P8 (Figure 5a), only the ventral half of layer 3 showed calbindin expression at P16 (Figure 5b), and in adults calbindin expression was largely absent from layer 3 of MEC (Figure 5c). This transient expression of calbindin in layer 3 followed a dorso-ventral developmental profile (Figure 5d). Early postnatally, in P4-P8 rats, we observed equitable densities of calbindin+ cells in dorsal, intermediate and ventral levels of MEC (n=3776 neurons, 8 rats). In contrast, around the end of the second postnatal week, in P12-P16 rats, we observed significantly lower densities (p=0.010, Mann-Whitney two tailed) in the dorsal (225 ± 96 cells / mm^2), as opposed to the ventral (449 ± 161 cells / mm^2) MEC (n=2104 neurons, 8 rats). In adults (n=828 neurons, 7 rats), calbindin+ neurons were largely absent in layer 3, but among the remaining population the density waxed from dorsal to intermediate and ventral MEC. The development of reelin expression in layer 3 neurons on the other hand (Figure 5 - Figure supplement 1a-c) occurred in equitable proportions in dorsal, intermediate and ventral levels of MEC (Figure 5 - Figure supplement 1d) with increasing age.

Second, layer 2 calbindin+ patches in the MEC also exhibited a dorsal-to-ventral maturation profile. The calbindin+ patches (Figure 6a) co-localized with doublecortin (Figure 6b), a well-established marker for immature neurons[22] throughout layer 2 at P8 (Figure 6c,d). At P16, the dorsal calbindin+ patches (Figure 6e,g) did not express doublecortin (Figure 6f,g), while ventral calbindin+ patches still co-localized with doublecortin (Figure 6h). In adults, calbindin+ patches (Figure 6i) did not exhibit doublecortin (Figure 6j) in either dorsal (Figure 6k) or ventral (Figure 6l) parts. A similar dorsal-to-ventral development gradient was evident in the PaS, with doublecortin being present throughout the PaS in P8 (Figure 6b), only in the ventral part in P16 (Figure 6f) and not present in adults (Figure 6j). To quantify the overlap between calbindin and doublecortin we performed spatial cross-correlations (Figure 6m). P8-P12 rats exhibited a high degree of overlap between calbindin and doublecortin in both dorsal (0.74 ± 0.05; mean ± SD, Pearson's cross-correlation coefficient) and ventral (0.61 ± 0.10) parts (n=9 regions, 5 rats). In P16-P20 rats (n=16 regions, 8 rats), the dorsal regions showed low correlations (0.14 ± 0.17), while the ventral regions still showed significantly higher overlap (0.60 ± 0.07; p=0.0008, Mann-Whitney two tailed). In adults (n=7 regions, 4 rats), both dorsal (0.19 ± 0.07) and ventral (0.20 ± 0.07) regions had low overlap. The difference in the Pearson's cross correlation coefficient between overlapping regions (dorsal and ventral in P8-P12; ventral in P16-P20) and non-overlapping regions (dorsal in P16-P20; dorsal and ventral in adults) was significant at p=0.000001 (Mann-Whitney two tailed).

A closer analysis of the co-localization of the immature neuronal marker doublecortin with calbindin+ pyramidal cells and reelin+ stellate cells (Figure 7a-c) revealed doublecortin to be mostly co-localized with calbindin+ rather than reelin+ neurons (Figure 7d). Spatial cross-correlations between doublecortin and either calbindin or reelin (Figure 7e; n=8 rats from ages P8 - P20) from triple-immunostained calbindin, reelin and doublecortin regions of layer 2 of the MEC revealed a greater overlap of doublecortin with calbindin (0.54 ± 0.10) than with

reelin (0.08 ± 0.13). This difference in the Pearson's cross correlation coefficient was significant at p=0.0009 (Mann-Whitney two tailed).

Third, wolframin expression, a marker which co-localizes with calbindin+ pyramidal neurons in layer 2 of MEC in adult rodents[23], develops from dorsal to ventral in layer 2 medial entorhinal cortex and parasubiculum (Figure 8). Specifically, wolframin expression starts to appear in the dorsal MEC and the dorsal PaS shortly after birth (Figure 8a) and is present only in the dorsal ~10% of the PaS. It extends progressively more ventrally (Figure 8b) and covers ~40% at P8 and ~75% at P12 of PaS. At P20 it is expressed throughout the full extent of medial entorhinal cortex and the parasubiculum (Figure 8c).

Discussion

Neurogenesis in the medial entorhinal cortex is completed prior to E18[24-25], and at this time the basic laminar organization of medial entorhinal cortex is already evident. While the basic structure of medial entorhinal cortex appears early, we observe massive developmental changes in the cortical structure, including a doubling of the thickness of the superficial layers during the first postnatal week.

The clustering of layer 2 MEC calbindin+ neurons into patches is also an early developmental event, and key aspects of the grid-layout of calbindin+ neurons are already present at birth. This observation indicates that the periodic structure of patches is a result of genetic signaling rather than spatial experience. Periodic patterns are ubiquitous in nature, and several chemical patterning systems have been explained on the basis of interaction between dynamical systems[26]. Since it has been suggested that the grid layout of calbindin+ neurons is functionally relevant for grid cell activity[27], it would be interesting to investigate, whether genetic manipulations would result in changes of layout periodicity and have functional effects. The dendritic clustering of calbindin+ pyramidal neurons is similar to dendritic development in the neocortex[28] and is established by the end of the first postnatal week. The cholinergic innervation of the calbindin+ patches was present by P4 in line with other long-range connectivity patterns in the MEC[29], which are also established early in development.

Reelin is an important protein in cortical layer development[30] and in the early stages of postnatal development we see the strongest reelin expression in layer 1, where reelin secreting Cajal-Retzius cells are involved in radial neuronal migration[31]. Stellate cells in layer 2 of MEC, which can be visualized by reelin-immunoreactivity[12], were scattered[16] throughout postnatal development.

Layer 3 of the MEC features a complementary transition of calbindin+ and reelin+ neurons during the first couple of postnatal weeks. While the density of reelin+ neurons increases, there is a concurrent decline in calbindin+ neuronal density in layer 3 of MEC, though part of the calbindin+ neuronal density decline can be attributed to the increasing brain size. Taken together with the presence of radial neuronal migration promoting Cajal-Retzius cells in layer 1 during this period, it would be interesting to investigate whether the transient calbindin+ neurons are migrating to layer 2 or changing their phenotype to reelin+ neurons, and what layer and cell-type specific functional differences are observed in this early postnatal development stage.

An interesting observation is the presence of clusters of neurons in the parasubiculum, which transiently express calbindin in early postnatal stages, and subsequently express wolframin. Transient expression of calbindin has been observed in early postnatal development in the neocortex[32] and midbrain regions[33], but its functional significance remains largely unknown. Our data show, however, that at early developmental stages the parasubiculum and medial entorhinal cortex share a similar organization in calbindin+ patches. Additionally, the expression of wolframin in the parasubiculum persists in adults, while calbindin+ neurons in MEC layer 2 also exhibit wolframin[23] from the end of the first postnatal week. Current studies generally focus on cell-type specific investigations using proteins expressed by these cells. However, investigations to study the specific roles of these proteins[34] might provide interesting insights towards understanding the finer differences in the functionalities exhibited by these cells. For instance, calbindin is a calcium buffer, and reduces the concentration of intracellular calcium[35], while wolframin is implicated in increasing intracellular calcium levels[36]. With the medial entorhinal cortex and parasubiculum having many similarities in their spatial discharge properties[18,20-21], a structure-function comparison of the wolframin+/transiently-calbindin+

neurons in the parasubiculum and the wolframin+/ permanently-calbindin+ neurons in the medial entorhinal cortex would be worthwhile.

A dorsal-to-ventral development profile was observed in the superficial layers of the MEC and parasubiculum. This conclusion was suggested by the progressive disappearance of the calbindin expression in layer 3 from dorsal to ventral; the progressive disappearance of doublecortin expression in layer 2 and parasubiculum from dorsal to ventral; and the progressive appearance of the wolframin expression in superficial layer 2 of MEC and parasubiculum from dorsal to ventral. Homing behavior in rats, as well as spontaneous exploratory behavior develops around the end of second postnatal week[2,37] while spontaneous exploration of larger environments outside the nest emerge towards the end of the third postnatal week[2]. This is coincident with the timeline of maturation of calbindin+ patches in the dorsal and ventral MEC respectively. Since the dorsal MEC represents smaller spatial scales and the ventral MEC progressively larger scales[38-39], these data may indicate that the rat's navigational system matures from small to large scales. Early eyelid opening experiments have indicated an accelerated development of spatial exploratory behaviour[40-41], and similar experiments might provide insights into whether early behavioral development is accompanied by an accelerated development of the microcircuit underlying spatial navigation.

The higher co-localization of doublecortin with calbindin+ pyramidal cells than reelin+ stellate cells, supports further the dichotomy of structure-function relationships exhibited by these two cell types[16,18]. Grid and border cells have been implicated to be largely specific to pyramidal and stellate cells respectively[18] and the delayed structural maturation of pyramidal cells might reflect the delayed functional maturation of grid cells[6-7], with the converse being applicable to stellate and border cells[5]. The divergent projection patterns of pyramidal and stellate cells, with the former projecting to CA1[23] and contralateral MEC[12] and the latter to dentate gyrus[12, 16] and deep layers of MEC[42], have differing theoretical interpretations in spatial information processing.

The same sets of neurons, which correspond to grid and border cells[18], have also been implicated to be differentially involved in temporal association memory[23] and contextual memory[43] respectively. An underlying differential structural maturation timeline of the microcircuit governing these processes may also translate into a differential functional maturation profile of these memories.

We conclude that the structural maturation of medial entorhinal cortex can be coarsely divided into an early appearance of the calbindin+ neuron patches and a progressive cell-type specific refinement of the cellular structure, which proceeds along the dorsal to ventral axis.

Materials and Methods

All experimental procedures were performed according to the German guidelines on animal welfare under the supervision of local ethics committees (LaGeSo) under the permit T0106-14.

Brain tissue preparation

Male and female Wistar rats (n=83) from E18 to P24 and adults (>P42) were used in the study. The ages were accurate to ± 1 day. Animals were anaesthetized by isoflurane, and then euthanized by an intraperitoneal injection of 20% urethane. They were then perfused transcardially with first 0.9% phosphate buffered saline solution, followed by 4% formaldehyde, from paraformaldehyde, in 0.1 M phosphate buffer (PFA). For prenatal animals, pregnant rats at E18 were perfused in the aforesaid manner and the E18 animals were then extracted from the uterus. Subsequently, brains were removed from the skull and postfixed in PFA overnight. Brains were then transferred to 10% sucrose solution for one night and subsequently immersed in 30% sucrose solution for at least one night for cryoprotection. The brains were embedded in Jung Tissue Freezing Medium (Leica Microsystems Nussloch, Germany), and subsequently mounted on the freezing microtome (Leica 2035 Biocut) to obtain 60 µm thick sagittal sections or tangential sections parallel to the pia.

Tangential sections of the medial entorhinal cortex were obtained by separating the entorhinal cortex from the remaining hemisphere by a cut parallel to the surface of the medial entorhinal cortex (Video 1). For subsequent sectioning the surface of the entorhinal cortex was attached to the block face of the microtome.

Histochemistry and immunohistochemistry

Acetylcholinesterase (AChE) activity was visualized according to previously published procedures [44-45]. After washing brain sections in a solution containing 1 ml of 0.1 M citrate buffer (pH 6.2) and 9 ml 0.9% NaCl saline solution (CS), sections were incubated with CS containing 3 mM $CuSO_4$, 0.5 m$MK_3Fe(CN)_6$, and 1.8 mM acetylthiocholine iodide for 30 min. After rinsing in PB, reaction products were visualized by incubating the sections in PB containing 0.05% 3,3'- Diaminobenzidine (DAB) and 0.03% nickel ammonium sulfate.

Immunohistochemical stainings were performed according to standard procedures. Briefly, brain sections were pre-incubated in a blocking solution containing 0.1 M PBS, 2% Bovine Serum Albumin (BSA) and 0.5% Triton X-100 (PBS-X) for an hour at room temperature (RT). Following this, primary antibodies were diluted in a solution containing PBS-X and 1% BSA. Primary antibodies against the calcium binding protein Calbindin (Swant: CB300, CB 38; 1:5000), the extracellular matrix protein Reelin (Millipore: MAB5364; 1:1000), the transmembrane protein Wolframin (Proteintech: 11558-1-AP; 1:200), the microtubule associated protein Doublecortin (Santa Cruz Biotechnology: sc-8086; 1:200) and the calmodulin binding protein Purkinje cell protein 4 (Sigma: HPA005792; 1:200) were used. Incubations with primary antibodies were allowed to proceed for at least 24 hours under mild shaking at 4°C in free-floating sections. Incubations with primary antibodies were followed by detection with secondary antibodies coupled to different fluorophores (Alexa 488, 546 and 633; Invitrogen). Secondary antibodies were diluted (1:500) in PBS-X and the reaction allowed to proceed for two hours in the dark at RT. For multiple antibody labeling, antibodies raised in different host species were used. For visualizing cell nuclei, sections were counterstained with DAPI (Molecular Probes: R37606). After the staining procedure, sections were mounted on gelatin coated glass slides with Vectashield mounting medium (Vectorlabs: H-1000).

Image acquisition

An Olympus BX51 microscope (Olympus, Shinjuku Tokyo, Japan) equipped with a motorized stage (LUDL Electronics, Hawthorne NY, USA) and a z-encoder (Heidenhain, Shaumburg IL, USA), was used for bright field microscopy. Images were captured using a MBF CX9000 (Optronics, Goleta CA, USA) camera using Neurolucida or StereoInvestigator (MBF Bioscience, Williston VT, USA). A Leica DM5500B epifluorescence microscope with a Leica DFC345 FX camera (Leica Microsystems, Mannheim, Germany) was used to image the immunofluorescent sections. Alexa fluorophores were excited using the appropriate filters (Alexa 350 – A4, Alexa 488 – L5, Alexa 546 – N3, Alexa 633 – Y5). Fluorescent images were acquired in monochrome, and color maps were applied to the images post acquisition. Post hoc linear brightness and contrast adjustment were applied uniformly to the image under analysis.

Analysis of Layer Width

To determine the width of different layers of the medial entorhinal cortex, we prepared parasagittal sections and stained them for calbindin-immunoreactivity, Purkinje cell protein-immunoreactivity and DAPI. Measurements were taken from dorsal, medial and ventral parts of each section analyzed using Leica Application Suite AF (Leica Microsystems, Mannheim, Germany).

Analysis of Spatial Periodicity

To determine the spatial periodicity of calbindin$^+$ patches, we determined spatial autocorrelations. The spatial autocorrelogram was based on Pearson's product moment correlation coefficient[46].

$$r(\tau_x, \tau_y) = \frac{\mathrm{n}\sum f(x,y) f(x-\tau_x, y-\tau_y) - \sum f(x,y) \sum f(x-\tau_x, y-\tau_y)}{\sqrt{n\sum f(x,y)^2 - (\sum f(x,y))^2}\sqrt{n\sum f(x-\tau_x, y-\tau_y)^2 - (\sum f(x-\tau_x, y-\tau_y))^2}}$$

where, $r(\tau_x, \tau_y)$ is the autocorrelation between pixels or bins with spatial offset τ_x and τ_y. f is the monochromatic image without smoothing, n is the number of overlapping pixels. Autocorrelations were not estimated for lags of τ_x and τ_y, where n<20. Grid scores were calculated, as previously described[16], and can vary from -2 to 2.

Analysis of Spatial Overlap

To determine the degree of overlap between doublecortin and calbindin or reelin, we determined spatial crosscorrelations. Spatial crosscorrelations were determined based on Pearson's product moment correlation coefficient.

$$r = \frac{\mathrm{n}\sum f1(x,y) f2(x,y) - \sum f1(x,y) \sum f2(x,y)}{\sqrt{n\sum f1(x,y)^2 - (\sum f1(x,y))^2}\sqrt{n\sum f2(x,y)^2 - (\sum f2(x,y))^2}}$$

where, r is the cross-correlation between the monochromatic images $f1$ and $f2$ without smoothing. n is the number of pixels in the image. The Pearson's cross-correlation coefficient can vary from -1 (anti-correlated) through 0 (un-correlated) to 1 (correlated).

For analysis of dorso-ventral variation in overlap between doublecortin with calbindin, two regions of the same size were selected from a section double-stained for calbindin and doublecortin. One region was selected from the dorsal half of the section and another from the ventral half and the regions were represented as pairs. Where, due to section damage, it was not possible to obtain regions from both dorsal and ventral parts, the data was presented as unpaired.

For analysis of variation in overlap between doublecortin and calbindin/reelin, comparisons were performed between the same regions from a section triple stained for calbindin, reelin and doublecortin.

References

1. Ainge, J.A. & Langston, R.F.. Ontogeny of neural circuits underlying spatial memory in the rat. *Frontiers in Neural Circuits* **6**, 8 (2012).
2. Wills, T.J., Muessig, L., Cacucci, F. The development of spatial behaviour and the hippocampal neural representation of space. *Phil. Trans. R. Soc. B* **369**, 20130409 (2014).
3. Tan, H.M., Bassett, J.P., O'Keefe, J., Cacucci, F., Wills, T.J. The development of the head direction system before eye-opening in the rat. *Curr. Biol.* **25**, 479–483 (2015).
4. Bjerknes, T.L., Langston, R.F., Kruge, I.U., Moser, E.I., Moser, M.B. Coherence among head direction cells before eye opening in rat pups. *Curr. Biol.* **25**, 103–108 (2015).
5. Bjerknes, T.L., Moser, E.I., Moser, M.B. Representation of geometric borders in the developing rat. *Neuron* **82**, 1–8 (2014).
6. Wills, T., Cacucci, F., Burgess, N., O'Keefe, J. Development of the hippocampal cognitive map in preweanling rats. *Science* **328**, 1573–1576 (2010).
7. Langston, R.F. *et al*. Development of the spatial representation system in the rat. *Science* **328**, 1576–1580 (2010).
8. Alonso, A. & Klink, R. Differential electroresponsiveness of stellate and pyramidal-like cells of medial entorhinal cortex layer II. *J. Neurophysiol.* **70**, 128–143 (1993).
9. Germroth, P., Schwerdtfeger, W. K., Buhl, E. H. Morphology of identified entorhinal neurons projecting to the hippocampus. A light microscopical study combining retrograde tracing and intracellular injection. *Neuroscience* **30**, 683–691 (1989).
10. Alonso, A. & Llinás, R. R. Subthreshold Na+-dependent theta-like rhythmicity in stellate cells of entorhinal cortex layer II. *Nature* **342**, 175–177 (1989).
11. Klink, R. & Alonso, A. Muscarinic modulation of the oscillatory and repetitive firing properties of entorhinal cortex layer II neurons. *J. Neurophysiol.* **77**, 1813–1828 (1997).
12. Varga, C., Lee, S. Y., Soltesz, I. Target-selective GABAergic control of entorhinal cortex output. *Nat. Neurosci.* **13,** 822–824 (2010).
13. Lingenhöhl, K. & Finch, D. M. Morphological characterization of rat entorhinal neurons in vivo: soma-dendritic structure and axonal domains. *Exp. Brain. Res.* **84**, 57–74 (1991).
14. Canto, C. B. & Witter, M. P. Cellular properties of principal neurons in the rat entorhinal cortex. II. The medial entorhinal cortex. *Hippocampus* **22**, 1277–1299 (2012).
15. Fujimaru Y. & Kosaka T. The distribution of two calcium binding proteins, calbindin D-28K and parvalbumin, in the entorhinal cortex of the adult mouse. *Neurosci Res.* **24**, 329-43 (1996).
16. Ray, S. *et al*. Grid-like arrangement and theta-modulation of a pyramidal cell microcircuit in layer 2 of medial entorhinal cortex. *Science* **343**, 891-896 (2014).
17. Naumann, R.K. *et al*. Conserved size and periodicity of pyramidal patches in layer 2 of medial/caudal entorhinal cortex. *J. Comp. Neurol.* **524**, 783-806(2016).
18. Tang, Q.*et al*. Pyramidal and stellate cell specificity of grid and border representations in layer 2 of medial entorhinal cortex. *Neuron* **84**, 1191–1197 (2014).
19. Tang Q. et al. Anatomical organization and spatiotemporal firing patterns of layer 3 neurons in rat medial entorhinal cortex. *J. Neurosci.* **35**, 12346-12354 (2015).
20. Boccara, C.N. *et al.* Grid cells in pre- and parasubiculum. *Nat. Neurosci.* **13**, 987–994 (2010).
21. Tang, Q. *et al*. Functional architecture of the rat parasubiculum. *J. Neurosci.* **36**, 2289-2301 (2016).

22. Brown, J.P. *et al*. Transient expression of doublecortin during adult neurogenesis. *J. Comp. Neurol.* **467**, 1–10 (2003).
23. Kitamura T. *et al*. Island Cells Control Temporal Association Memory. *Science* **343**, 896-901 (2014).
24. Bayer, S. A. Development of the hippocampal region in the rat I. Neurogenesis examined with 3H-thymidine autoradiography. *J. Comp. Neurol.* **190**, 87−114 (1980a).
25. Bayer, S.A. Development of the hippocampal region in the rat II. Morphogenesis during embryonic and early postnatal life. *J. Comp. Neurol.* **190**, 115–134 (1980b).
26. Turing, A.M. The chemical basis of morphogenesis. *Phil. Trans. R. Soc. Lond. B*, **237**, 37–72 (1952).
27. Brecht, M. *et al*. An isomorphic mapping hypothesis of the grid representation. *Phil. Trans. R. Soc. B* **369**, 20120521 (2014).
28. Petit, T. L., LeBoutillier, J. C., Gregorio, A., Libstug, H. The pattern of dendritic development in the cerebral cortex of the rat. *Brain Research* **469**, 209–19 (1988).
29. O'Reilly, K.C. *et al*. Identification of dorsal–ventral hippocampal differentiation in neonatal rats. *Brain Struct. Funct.* **220**, 2873–2893 (2015).
30. D'Arcangelo, G. et al. A protein related to extracellular matrix proteins deleted in the mouse mutant reeler. *Nature* **374**, 719-723 (1995).
31. Pesold, C. et al. Reelin Is Preferentially Expressed in Neurons Synthesizing Gamma Aminobutyric Acid in Cortex and Hippocampus of Adult Rats. *PNAS* **95**, 3221–3226 (1998).
32. Hogan, D. & Berman, N.E.J. Transient expression of calbindin-D28k immunoreactivity in layer V pyramidal neurons during postnatal development of kitten cortical areas. *Dev. Brain Res.* **74**, 177-192 (1993).
33. Liu, F.C. & Graybiel, A.M. Transient calbindin-D28k-positive systems in the telencephalon: Ganglionic eminence, developing striatum and cerebral cortex. *J. Neurosci.* **12**, 674-690 (1992).
34. Li, Z., Decavel, C., Hatton, G. I. Calbindin-D28k: role in determining intrinsically generated firing patterns in rat supraoptic neurones. *J. Physiol.* **488**, 601–608 (1995).
35. Mattson, M.P., Rychlik, B., Chu, C., Christakos, S. Evidence for calcium-reducing and excito-protective roles for the calcium-binding protein calbindin-D28k in cultured hippocampal neurons. *Neuron* **6**, 41-51 (1991).
36. Osman, A.A. et al. Wolframin expression induces novel ion channel activity in endoplasmic reticulum membranes and increases intracellular calcium. *J. Biol. Chem.* **278**, 52755-52762 (2003).
37. Bulut, F. & Altman, J. Spatial and tactile discrimination learning in infant rats motivated by homing. *Dev. Psychobiol.* **7**, 465–473 (1974).
38. Hafting, T., Fyhn, M., Molden, S., Moser, M.B., Moser, E.I. Microstructure of a spatial map in the entorhinal cortex. *Nature* **436**, 801–806 (2005).
39. Stensola, H.*et al*. The entorhinal grid map is discretized. *Nature* **492**, 72–78 (2012).
40. Kenny, P.A. & Turkewitz, G. Effects of unusually early visual stimulation on the development of homing behaviour in the rat pup. *Dev. Psychobiol.* **19**, 57-66 (1986).
41. Foreman, N. & Altaha, M. The development of exploration and spontaneous alternation in hooded rat pups: effects of unusually early eyelid opening. *Dev. Psychobiol.* **24**, 521-537 (1991).
42. Sürmeli, G. et al. Molecularly defined circuitry reveals input-output segregation in deep layers of the medial entorhinal cortex. *Neuron* **88** , 1040 – 1053 (2015).
43. Kitamura, T. *et al*. Entorhinal Cortical Ocean Cells Encode Specific Contexts and Drive Context-Specific Fear Memory. *Neuron* **87**, 1317-1331 (2015).

44. Ichinohe N. et al. Unusual patch-matrix organization in the retrosplenial cortex of the reeler mouse and shaking rat Kawasaki. *Cereb. Cortex* **18**, 1125–1138 (2008).
45. Tsuji S. Electron microscopic localization of acetylcholinesterase activity in the central nervous system: chemical basis of a catalytic activity of Hatchett's brown (cupric ferrocyanide) precipitate revealed by 3,3′-diaminobenzidine. *Folia Histochem. Cytobiol.* **36**, 67-70 (1998).
46. Sargolini, F. et al. Conjunctive representation of position, direction, and velocity in entorhinal cortex. *Science* **312**, 758–762 (2006).

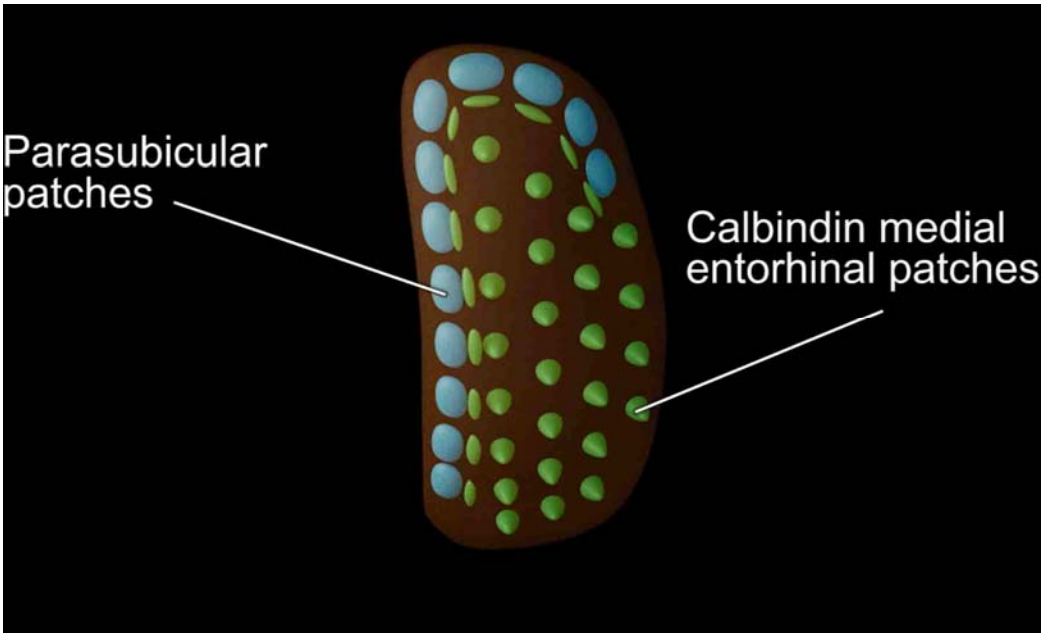

Video 1. Medial entorhinal cortex and parasubiculum in the rat brain.

The medial entorhinal cortex and parasubiculum are situated at the posterior extremity of the rat neocortex. This schematic video illustrates the location of the medial entorhinal cortex and parasubiculum *in situ*, the tangential sectioning process and the layout of parasubicular patches and calbindin-patches in the medial entorhinal cortex.

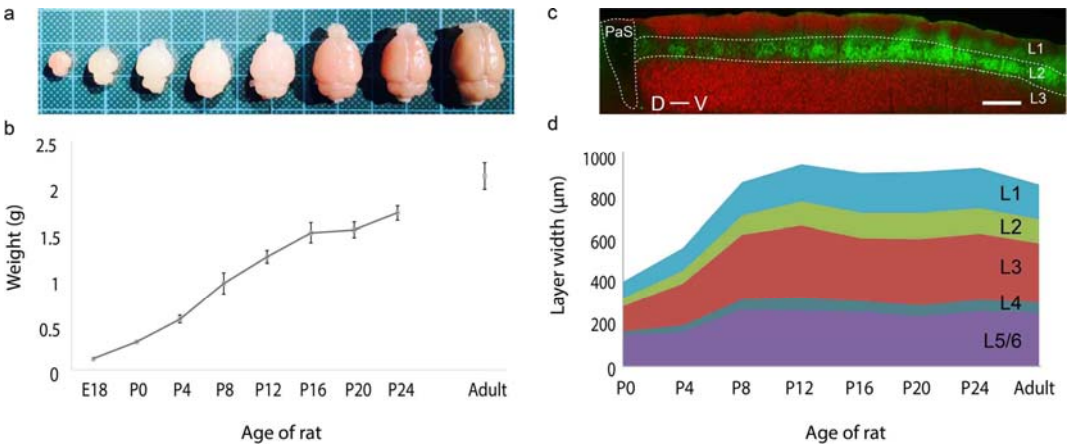

Figure 1. Rat brain and medial entorhinal cortex laminar development.

(a) Growth in rat brain size from E18, P0, P4, P8, P12, P16, P20 to adult. Brains are overlaid on a 1 cm x 1 cm grid.

(b) Mean weight (in grams) of E18 (n=3), P0 (n=6), P4 (n=5), P8 (n=5), P12 (n=5), P16 (n=5), P20 (n=5), P24 (n=6) and in adult (n=9) rat brains. Error bars indicate SD.

(c) Parasagittal section double stained for calbindin-immunoreactivity (green) and Purkinje cell protein 4 immunoreactivity (pcp4; red), illustrating the superficial layers of the medial entorhinal cortex and parasubiculum. Calbindin+ neurons (green) are in layer 2, pcp4+ neurons (red) are in layer 3 MEC.

(d) Development of mean layer width (in µm) of layer 1 (light-blue), layer 2 (green), layer 3 (red), layer 4 (gray-blue) and layer 5/6 (purple) from P0 to P24 and in adult rat medial entorhinal cortex.

Scale bars 250 µm. PaS- Parasubiculum; L1- Layer 1; L2- Layer 2; L3- Layer 3; D- Dorsal; V-Ventral.

Figure 1_Source data

Laminar widths (in µm) of the medial entorhinal cortex for P0, P4, P8, P12, P16, P20, P24 and adult rats.

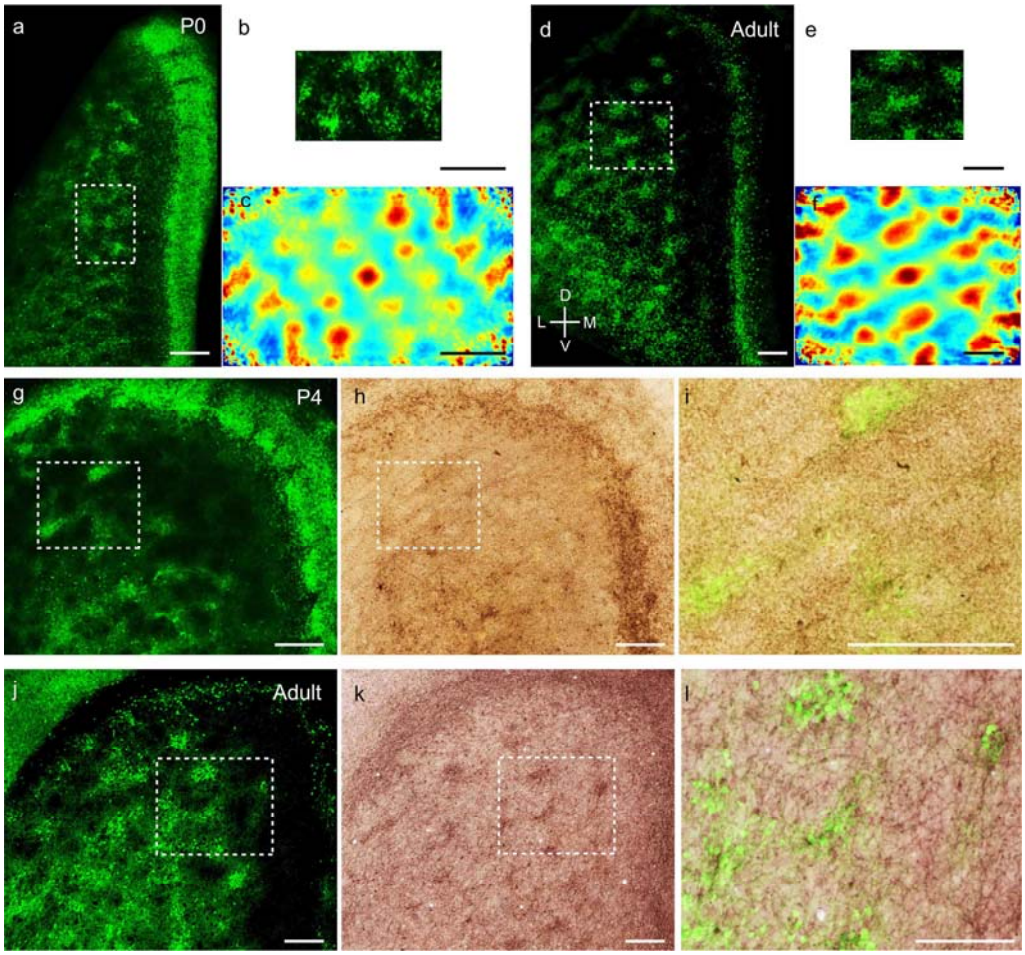

Figure 2: Adult-like grid layout and cholinergic innervation of calbindin+ pyramidal neurons in layer 2 of MEC at early postnatal stages

(a) Tangential sections of the MEC processed for calbindin-immunoreactivity (green). Patches of calbindin+ neurons are evident already in the MEC, while the parasubicular patches at the right extremity also show calbindin-immunoreactivity in P0 rats.

(b) Inset from (a), rotated 90 degrees clockwise, for presentation.

(c) Two-dimensional spatial autocorrelation of the MEC region shown in (b) showing a periodic spatial organization of calbindin+ patches. The grid score is 0.59

(d) as (a) for adult animals.

(e) Inset from (d)

(f) Two-dimensional spatial autocorrelation of the MEC region shown in (e) showing a periodic spatial organization of calbindin+ patches. The grid score is 1.18.

(g) Tangential section in a P4 animal processed for calbindin-immunoreactivity (green). Also note the calbindin-immunoreactive parasubicular patches present in a P4 rat.

(h) Section from (g) co-stained for acetylcholinesterase activity (brown).

(i) Overlay of inset regions from (g) and (h) shows overlap between calbindin and acetylcholinesterase in MEC in P4 rats.

(j-l) as (g-i) for adult animals.

(d-f, j-l) modified from Ray et al., 2014[16]. Colour scale of spatial autocorrelation, -0.5 (blue) through 0 (green) to 0.5 (red).

Scale bars 250 μm. D- Dorsal; V- Ventral; M- Medial; L- Lateral. Orientation in (d) applies to all sections apart from (b), where it's rotated 90 degrees clockwise.

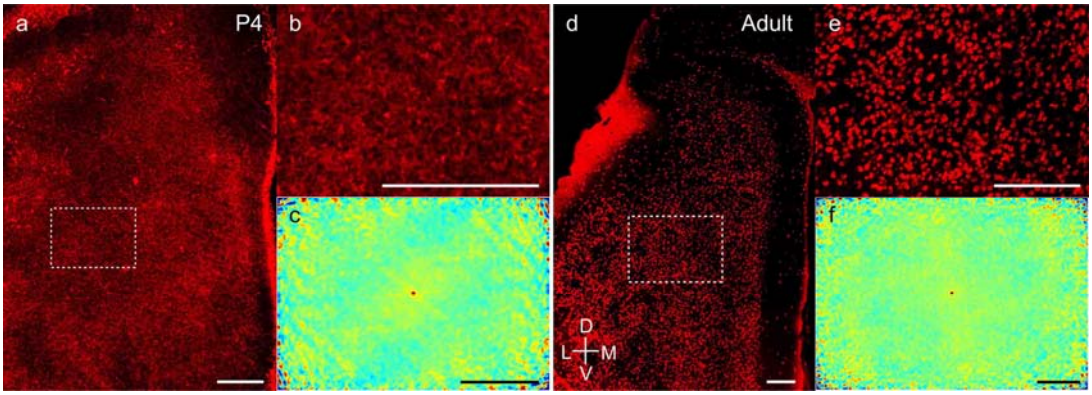

Figure 2 - Figure supplement 1: Adult-like scattered distribution of reelin+ stellate cells in early postnatal stages.

(a) Tangential sections of the MEC processed for reelin-immunoreactivity (red) in a P4 rat.

(b) Inset from (a).

(c) Two-dimensional spatial autocorrelation of the MEC region shown in (b) showing a lack of periodicity of reelin+ neurons. The grid score is -0.09.

(d-f) as (a-c) for adult animals. The grid score in (f) is 0.03.

Scale bars 250 µm. D- Dorsal; V- Ventral; M- Medial; L- Lateral. Orientation in (d) applies to all sections.

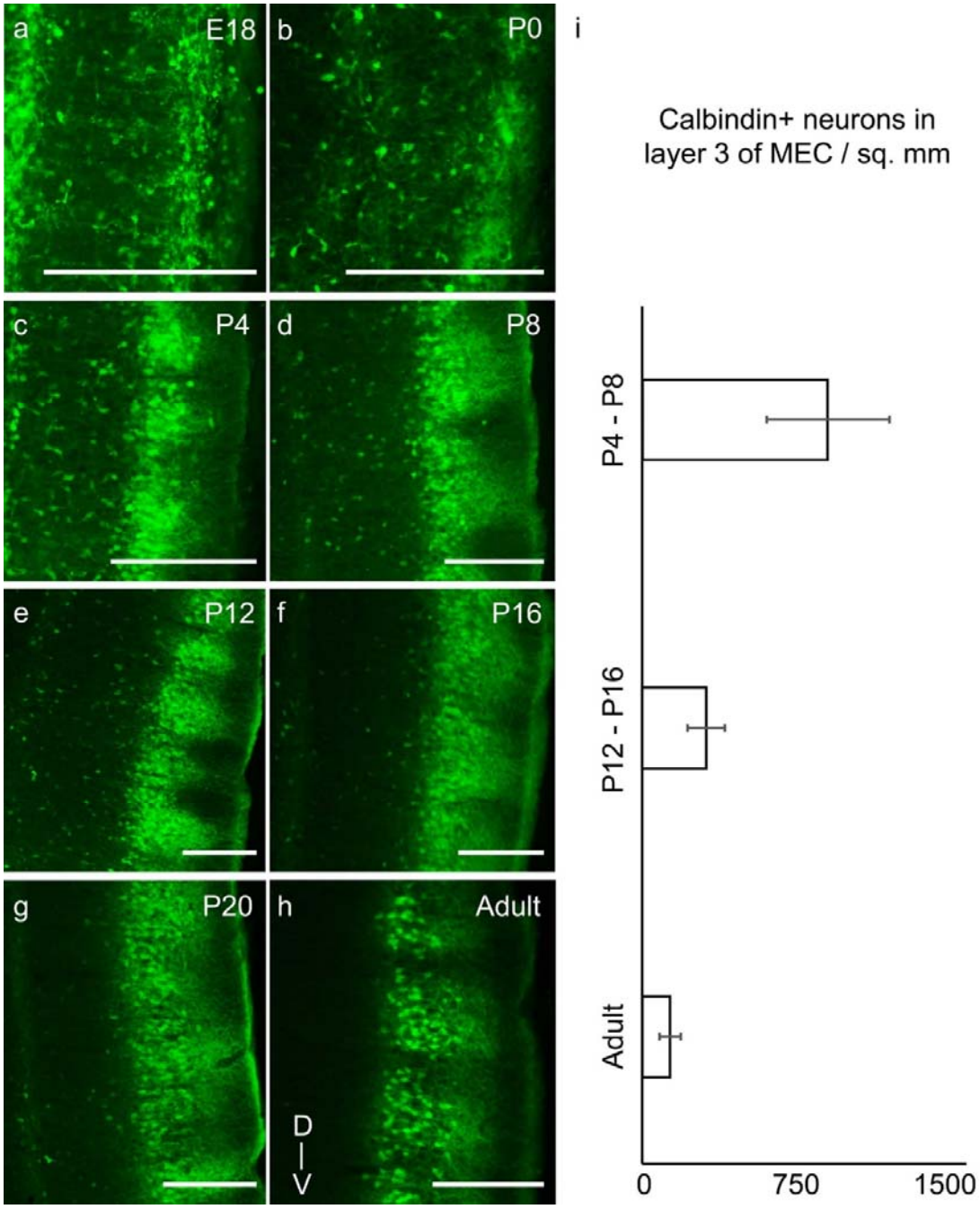

Figure 3: Transient presence of calbindin+ neurons in layer 3 of MEC in early postnatal stages reduces progressively to adult-like state by third postnatal week

Parasaggital sections of the MEC processed for calbindin-immunoreactivity (green). The sections show clustering of calbindin+ pyramidal cells in layer 2 and a transient presence of calbindin+ neurons in layer 3, which decrease with age in

(a) E18 rat.
(b) P0 rat.
(c) P4 rat.
(d) P8 rat.
(e) P12 rat.

(f) P16 rat.
(g) P20 rat.
(h) Adult rat.
(i) Decreasing density of calbindin+ neurons in layer 3 of MEC from P4-P8 (n=3776 neurons, 8 rats); to P12-P16 (n=2104 neurons, 8 rats) to adults (n=828 neurons, 7 rats). Error bars denote SD.

Scale bars 250 μm. D- Dorsal; V- Ventral. Orientation in (h) applies to all sections.

Figure 3_Source data

Calbindin+ neurons counted and areas (in μm2) in layer 3for determining calbindin+ neuronal density in layer 3 in P4-P8, P12-P16 and adult rats.

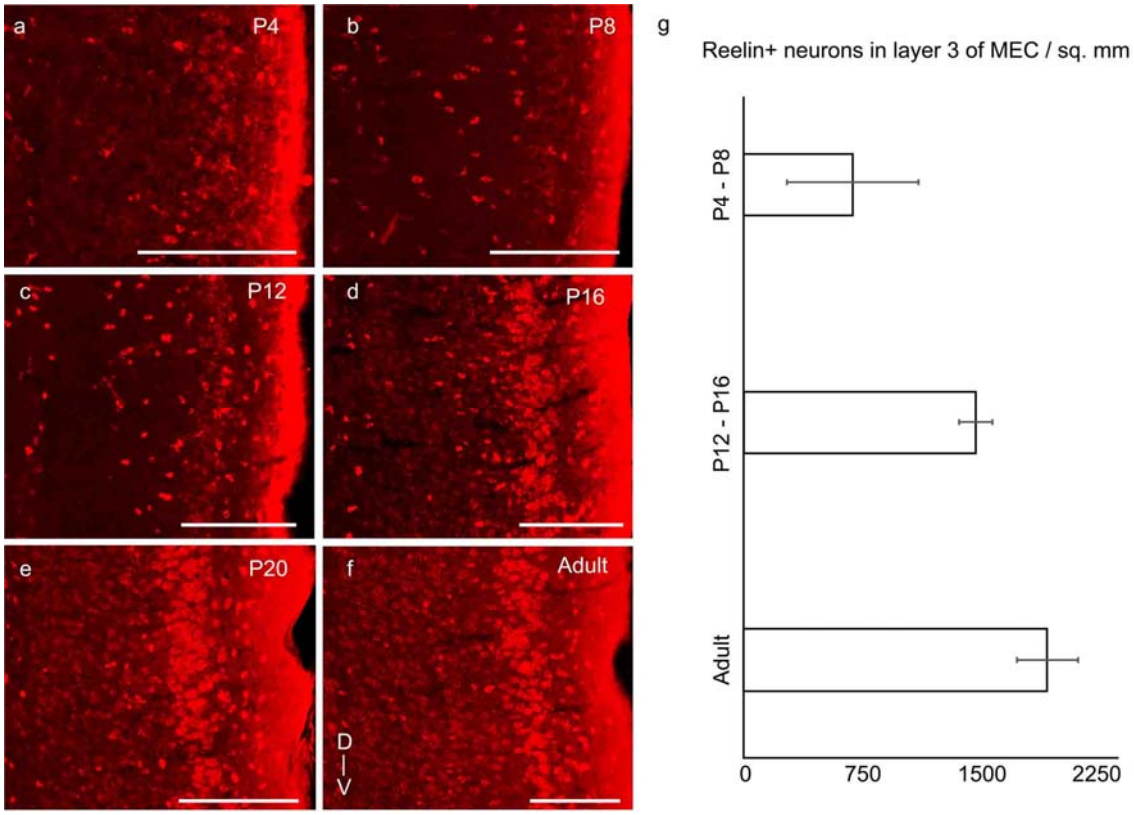

Figure 4: Increase of reelin expression in layer 3 neurons of MEC through development

Parasaggital sections of the MEC processed for reelin-immunoreactivity (red). The sections show reelin+ stellate cells in layer 2 and an increasing reelin expression in layer 3 neurons with development in

(a) P4 rat.
(b) P8 rat.
(c) P12 rat.
(d) P16 rat.
(e) P20 rat.
(f) Adult rat.
(g) Increasing density of reelin+ neurons in layer 3 of MEC from P4-P8 (n=1405 neurons, 4 rats); to P12-P16 (n=3309 neurons, 3 rats) to adults (n=5039 neurons, 3 rats). Error bars denote SD.

Scale bars 250 µm. D- Dorsal; V- Ventral. Orientation in (f) applies to all sections.

Figure 4_Source data

Reelin+ neurons counted and areas (in μm^2) in layer 3for determining reelin+ neuronal density in layer 3 in P4-P8, P12-P16 and adult rats.

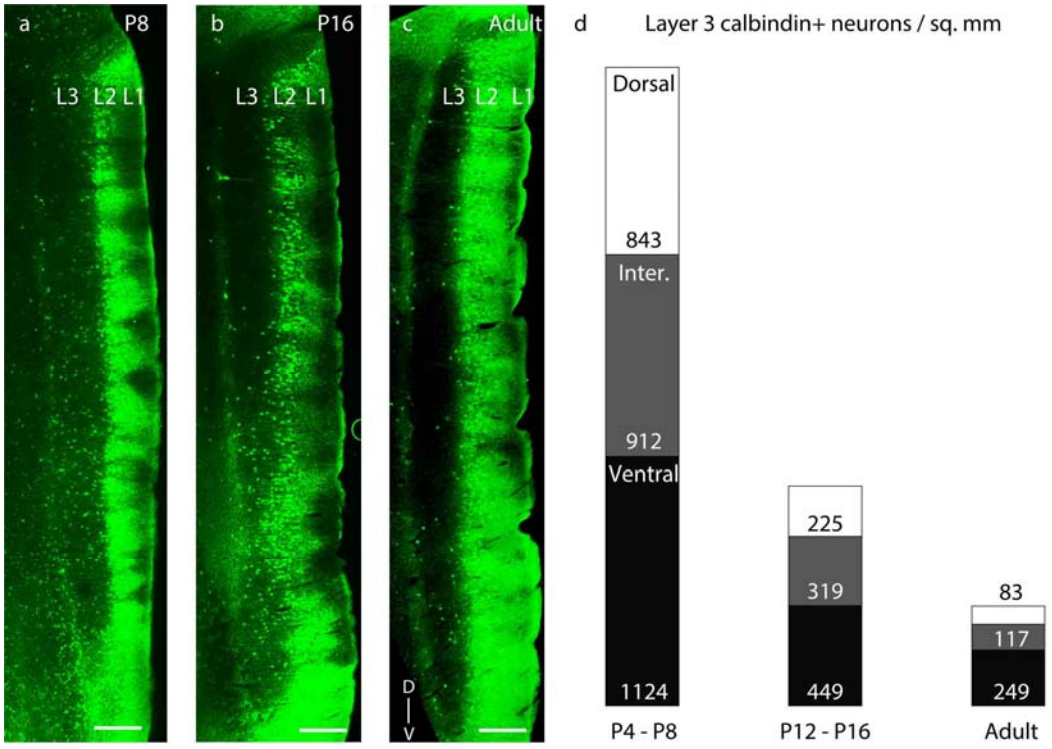

Figure 5: Dorsal-to-ventral disappearance of layer 3 calbindin expression

Parasaggital sections showing superficial layers of the MEC processed for calbindin-immunoreactivity (green).

(a) Calbindin expression is seen throughout layer 3 in P8 rats.

(b) Calbindin expression is seen only in ventral half of layer 3 in P16 rats.

(c) Calbindin expression is largely absent in layer 3 in adult rats.

(d) Proportion of layer 3 calbindin+ neurons in dorsal (white), intermediate (gray) and ventral (black) MEC in P4-P8 (n=3776 neurons, 8 rats); P12-P16 (n =2014 neurons, 8 rats); and adult (n=828 neurons, 7 rats) rats. The numbers represent layer 3 calbindin+ neuronal density and decay in a dorsal to ventral gradient with age as evident with the reduced proportions of the white (dorsal MEC) and gray (intermediate MEC) sections of the columns with increasing age.

Scale bars 250 µm. L1- Layer 1; L2- Layer 2; L3- Layer 3; D- Dorsal; V-Ventral. Orientation in (c) applies to all sections.

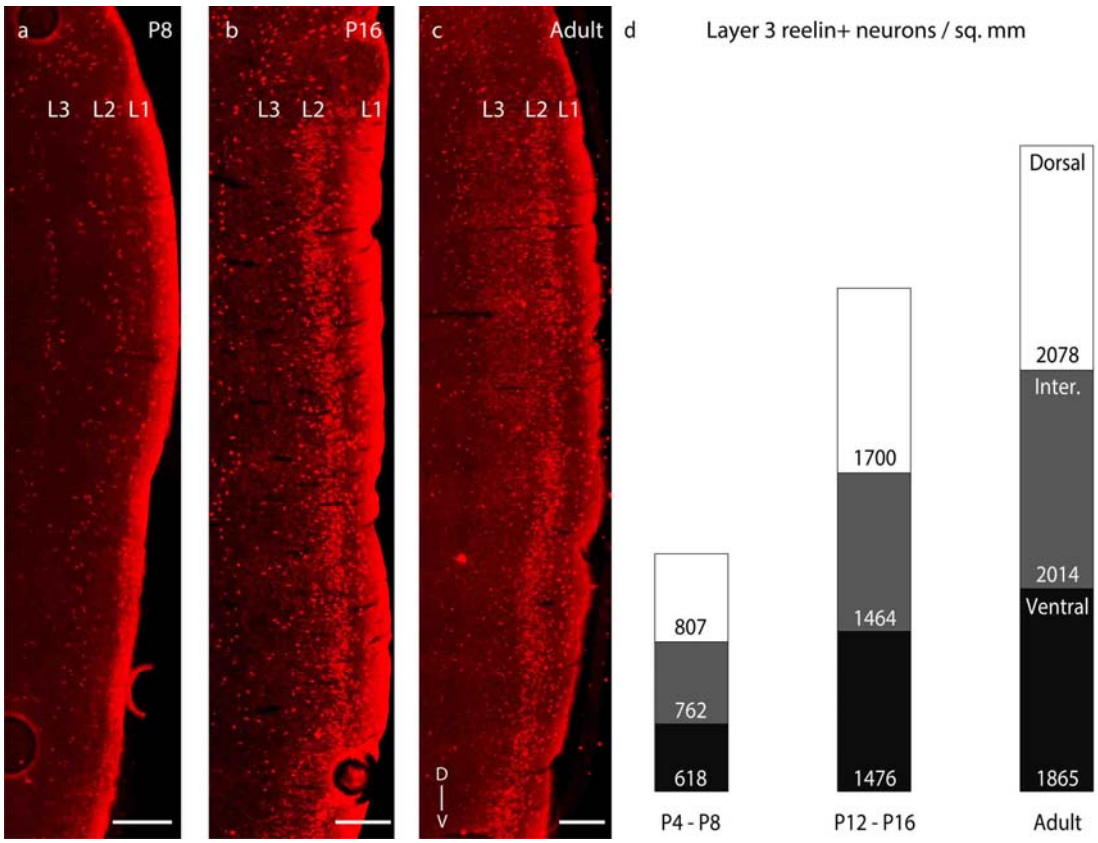

Figure 5 – Figure supplement 1: Dorsal- ventral distribution of layer 3 reelin expression

Parasaggital sections showing superficial layers of the MEC processed for reelin-immunoreactivity (red).

(a) Reelin expression is sporadic throughout layer 3 in P8 rats.

(b) Reelin expression equitably increases in layer 3 in P16 rats.

(c) Reelin expression is present throughout layer 3 in adult rats.

(d) Proportion of layer 3 reelin+ neurons in dorsal (white), intermediate (gray) and ventral (black) MEC in P4-P8 (n=1405 neurons, 4 rats); P12-P16 (n =3309 neurons, 3 rats); and adult (n=5039 neurons, 3 rats) rats. The numbers represent layer 3 reelin+ neuronal density and increase equitably with age as evident with the similar proportions of the white (dorsal MEC), gray (intermediate MEC) and black (ventral MEC) sections of the columns with increasing age.

Scale bars 250 µm. L1- Layer 1; L2- Layer 2; L3- Layer 3; D- Dorsal; V-Ventral. Orientation in (c) applies to all sections.

Figure 5 and Figure 5 - Figure supplement1_ Source data

Calbindin+ neurons (Figure 5) and reelin+ neurons (Figure 5_Figure supplement 1) counted and areas (in μm^2) in dorsal, intermediate and ventral parts of layer 3for determining calbindin+ and reelin+ neuronal densities respectively in P4-P8, P12-P16 and adult rats.

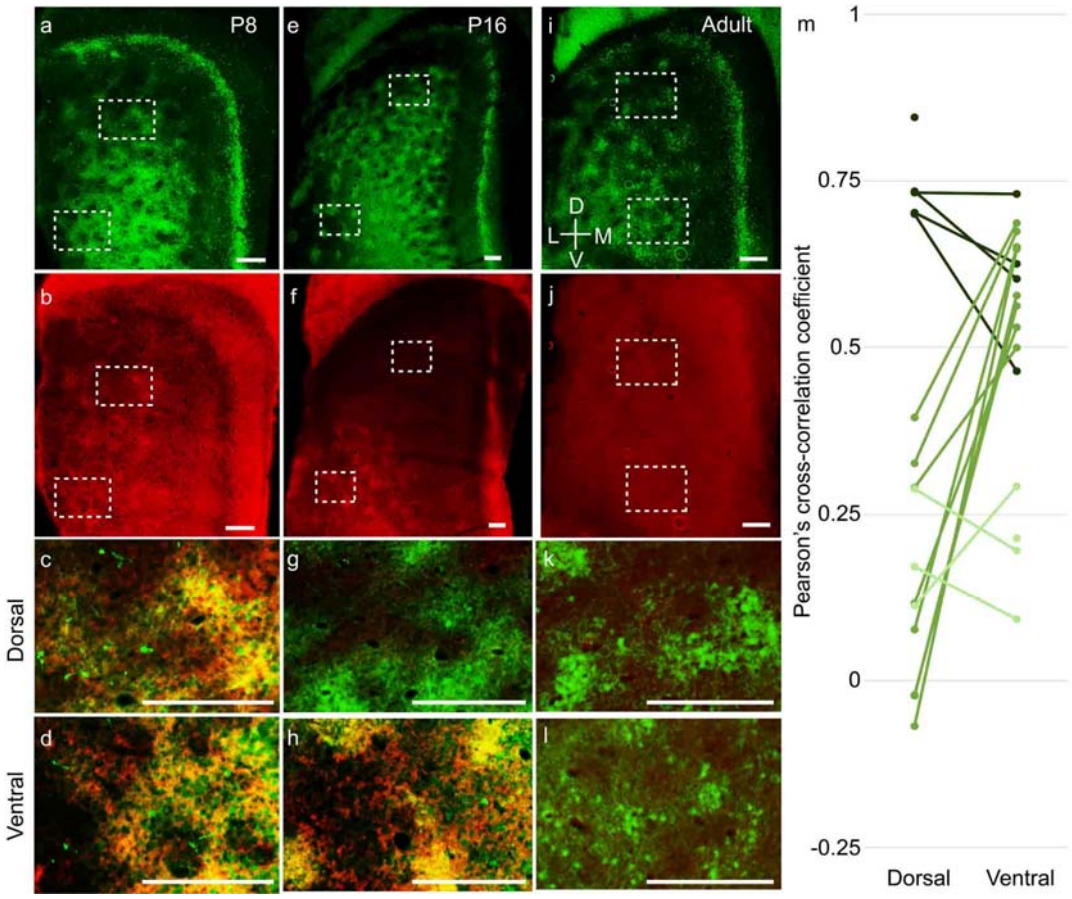

Figure 6: Dorsal-to-ventral maturation of layer 2 calbindin+ patches and parasubiculum.

Tangential sections of the MEC double-stained for calbindin immunoreactivity (green) and doublecortin immunoreactivity (red). Doublecortin is a marker for immature neurons and disappears in a dorsal-ventral gradient.

(a) Calbindin-expression (green) in P8 rats.

(b) Doublecortin-expression (red) in P8 rats. Note the presence of doublecortin throughout the dorso-ventral extent of MEC and parasubiculum.

(c) Overlay of the dorsal inset region (dashed) in (a) and (b), showing overlap of calbindin and doublecortin (hence the yellowish color).

(d) Overlay of the ventral inset region (dashed) in (a) and (b), showing overlap of calbindin and doublecortin.

(e-h) as (a-d) for P16 rats, respectively. However, note that dorsal inset region lacks doublecortin (g) while ventral inset region shows overlap of calbindin and doublecortin (h). Also, note the absence of doublecortin in the dorsal but not the ventral parasubiculum (f).

(i-k) as (a-d) for adult rats. No doublecortin is present in either dorsal (k) or ventral (l) regions.

(m) Spatial cross-correlations of calbindin and doublecortin in MEC showing high overlap in both dorsal and ventral regions in P8-P12 rats (dark green; n=9 regions, 5 rats); low

correlation in dorsal but high overlap in ventral in P16-P20 rats (green; n=16 regions, 8 rats) and low correlations in both dorsal and ventral in adult rats (light green; n=7 regions, 4 rats). The Pearson's cross-correlation coefficient can vary from -1 (anti-correlated) through 0 (un-correlated) to 1 (correlated).

Scale bars 250 μm. D- Dorsal; V- Ventral; M- Medial; L- Lateral. Orientation in (i) applies to all sections.

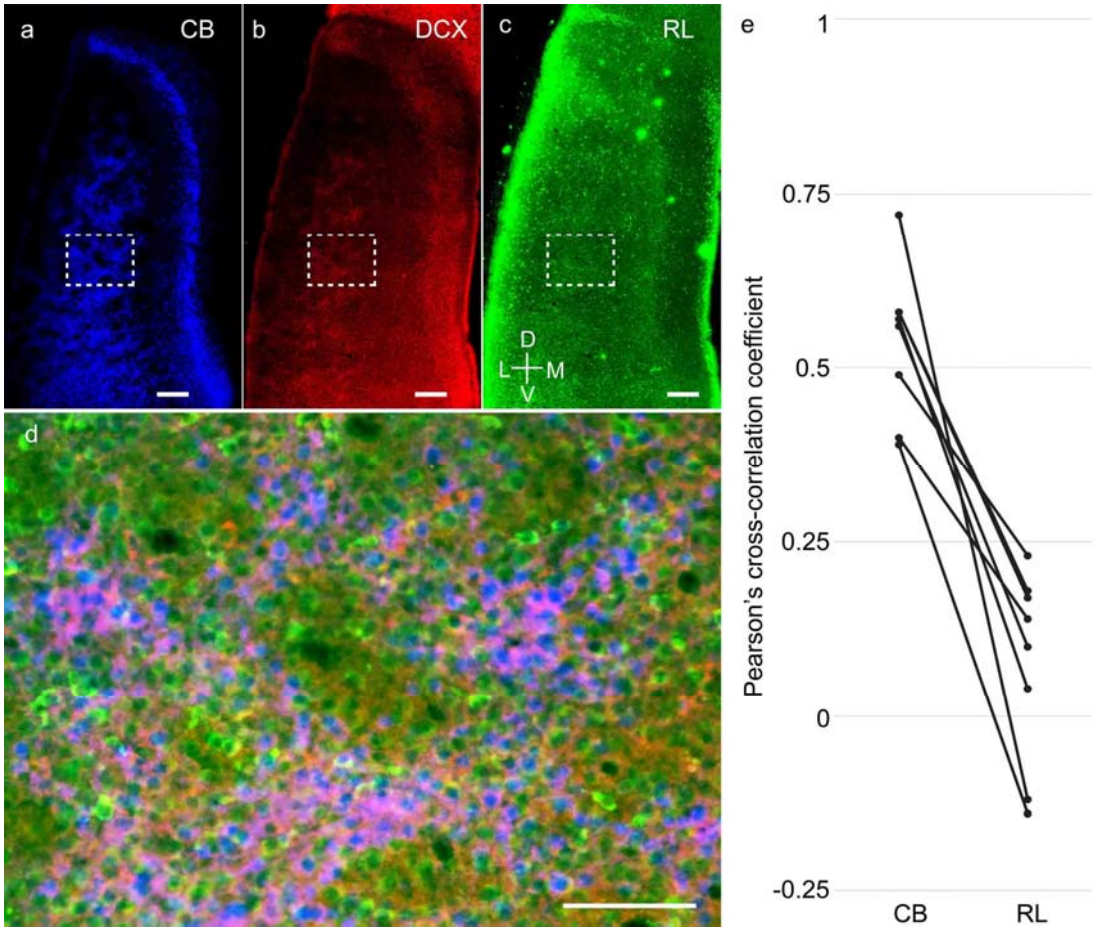

Figure 7: Higher co-localization of doublecortin with calbindin+ pyramidal than reelin+ stellate cells in the developing medial entorhinal cortex.

Tangential sections of the MEC layer 2 triple-stained for calbindin immunoreactivity (CB; blue), doublecortin immunoreactivity (DCX; red) and reelin immunoreactivity (RL; green). Pyramidal but not stellate cells are structurally immature during early postnatal stages.

(a) Calbindin-expression (blue) in layer 2 of MEC.

(b) Doublecortin-expression (red) in layer 2 of MEC.

(c) Reelin-expression (green) in layer 2 of MEC.

(d) Overlay of the inset region (dashed) in (a), (b) and (c), showing a higher co-localization of doublecortin (red) with calbindin (blue), than reelin (green).

(e) Spatial cross-correlations of doublecortin with calbindin and reelin showing high overlap of doublecortin with calbindin but not reelin (n=8 regions, 8 rats).

Scale bars (a-c) 250 µm; (d) 100 µm. D- Dorsal; V- Ventral; M- Medial; L- Lateral. Orientation in (c) applies to all sections.

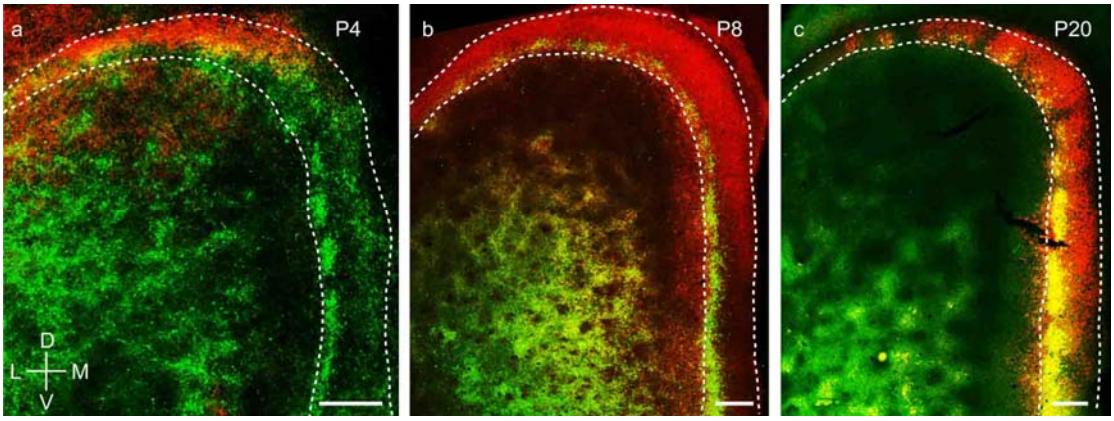

Figure 8: Dorsal-to-ventral maturation of wolframin expression in the medial entorhinal cortex and parasubiculum

(a) Tangential sections of the MEC and PaS (outlines dashed) double-stained for calbindin-immunoreactivity (green) and wolframin immunoreactivity (red) in a P4 rat. Shown is an overlay of red and green fluorescence.

(b) as (a) for a P8 rat.

(c) as (a) for a P20 rat.

Wolframin is present in the dorsal ~10% of the parasubiculum at P4, ~40% at P8 and 100% at P20.

Note that wolframin expression co-localizes with calbindin-expression in the MEC (hence the yellowish color) and increases from dorsal to ventral with age.

Scale bars 250 µm. D- Dorsal; V- Ventral; M- Medial; L- Lateral. Orientation in (a) applies to all sections.

Chapter 6

Anatomical organization and spatiotemporal firing patterns of layer 3 neurons in the rat medial entorhinal cortex.

Published as:

Tang, Q. et al. (2015). Anatomical organization and spatiotemporal firing patterns of layer 3 neurons in the rat medial entorhinal cortex. *J. Neurosci. 35:12346-12354*

doi: 10.1523/JNEUROSCI.0696-15.2015

Anatomical organization and spatiotemporal firing patterns of layer 3 neurons in the rat medial entorhinal cortex

Qiusong Tang[1], Christian Laut Ebbesen[1,2], Juan Ignacio Sanguinetti-Scheck[1], Patricia Preston-Ferrer[3], Anja Gundlfinger[4], Jochen Winterer[4], Prateep Beed[4], Saikat Ray[1], Robert Naumann[1,5], Dietmar Schmitz[4], Michael Brecht[1,‡] & Andrea Burgalossi[3,‡]

[1]Bernstein Center for Computational Neuroscience, Humboldt University of Berlin, Philippstr. 13, Haus 6, 10115 Berlin, Germany

[2]Berlin School of Mind and Brain, Humboldt University of Berlin, Philippstr. 13, Haus 6, 10115 Berlin, Germany

[3]Werner-Reichardt Centre for Integrative Neuroscience, Otfried-Müller-str. 25, 72076 Tübingen, Germany
[4]Charité Universitätsmedizin Berlin, Charité Crossover NWFZ Campus Mitte, Virchowweg 6 - Charitéplatz 1, 10117 Berlin, Germany
[5]Present address: Max Planck Institute for Brain Research, Max-von-Laue-Str. 4, 60438 Frankfurt am Main, Germany

‡To whom correspondence should be addressed: andrea.burgalossi@cin.uni-tuebingen.de or michael.brecht@bccn-berlin.de

Running Title: *Anatomy and Physiology of MEC L3*

Conflict of Interest: The authors declare no competing financial interests.

Acknowledgements: This work was supported by the Werner Reichardt Centre for Integrative Neuroscience (CIN) at the Eberhard Karls University of Tübingen (CIN is an Excellence Cluster funded by the Deutsche Forschungsgemeinschaft within the framework of the Excellence Initiative EXC 307), the Humboldt-Universität zu Berlin, BCCN Berlin (German Federal Ministry of Education and Research BMBF, Förderkennzeichen 01GQ1001A), NeuroCure, the Neuro-Behavior ERC grant and the Gottfried Wilhelm Leibniz Prize of the DFG. We thank Alexandra Eritja (Tübingen) for excellent assistance with anatomy experiments, Markus Frey (Tübingen) for data analysis, Moritz von Heimendahl for programming, Andreea Neukirchner, Juliane Steger and Undine Schneeweiß.

Abstract

Layer 3 of medial entorhinal cortex is a major gateway from the neocortex to the hippocampus. Here we addressed structure-function relationships in medial entorhinal cortex layer 3 by combining anatomical analysis with juxtacellular identification of single neurons in freely-behaving rats. Anatomically, layer 3 appears as a relatively homogeneous cell sheet. Dual-retrograde neuronal tracing experiments indicate a large overlap between layer 3 pyramidal populations, which project to ipsilateral hippocampus and contralateral medial entorhinal cortex. These cells were intermingled within layer 3, and had similar morphological and intrinsic electrophysiological properties. Dendritic trees of layer 3 neurons largely avoided the calbindin-positive patches in layer 2. Identification of layer 3 neurons during spatial exploration (n=17) and extracellular recordings (n=52) pointed to homogeneous spatial discharge patterns. Layer 3 neurons showed only weak spiking theta-rhythmicity and sparse head-direction selectivity. A majority of cells (50/69) showed no significant spatial modulation. All of the ~ 28% of neurons which carried significant amounts of spatial information (19/69), discharged in irregular spatial patterns. Thus, layer 3 spatiotemporal firing properties are remarkably different from those of layer 2, where theta-rhythmicity is prominent and spatially-modulated cells often discharge in grid or border patterns.

Significance Statement.

Neurons within the superficial layers of Medial Entorhinal Cortex (MEC) often discharge in border, head-direction and theta-modulated grid patterns. It is still largely unknown how defined discharge patterns relate to cellular diversity in the superficial layers of MEC. In the present study, we addressed this issue by combining anatomical analysis with juxtacellular identification of single layer 3 neurons in freely-behaving rats. We provide evidence that the anatomical organization and spatiotemporal firing properties of layer 3 neurons are remarkably different from those in layer 2. Specifically, most layer 3 neurons discharged in spatially-irregular firing patterns, with weak theta-modulation and head-directional selectivity. This work thus poses constraints on the spatio-temporal patterns reaching downstream targets, like the hippocampus.

Introduction

Layer 3 of medial entorhinal cortex (MEC) is a major component of the cortico-hippocampal memory loop. Within MEC, layer 3 is the main recipient of the ascending deep-to-superficial inputs (Caballero-Bleda and Witter, 1993, 1994; van Haeften et al., 2003; Abbasi and Kumar, 2013), which are then relayed to MEC layer 2 and the hippocampal subfields CA1 and subiculum (Gloveli et al., 1997; Behr et al., 1998). Although previous studies have provided evidence for morphological / electrophysiological heterogeneity within the layer 3 principal cell population (Germroth et al., 1989; Dickson et al., 1997; Gloveli et al., 1997; Behr et al., 1998; Canto and Witter, 2012), their relationship to in-vivo firing patterns and behavior has remained unexplored. Layer 3 pyramidal neurons differ from the layer 2 pyramidal cells morphologically and electrophysiologically (Germroth et al., 1989; van der Linden and Lopes da Silva, 1998; Erchova et al., 2004). Interlaminar connectivity and microcircuit structures are also remarkably different between layer 2 and layer 3 of MEC (Kloosterman et al., 2003; Beed et al., 2010; Varga et al., 2010; Ray et al. 2014; Couey et al., 2013; Pastoll et al., 2013), thus pointing towards possible functional dissociations between the two entorhinal layers (Kitamura et al., 2014).

The discovery of spatially-modulated neurons in parahippocampal circuits has been a major milestone in systems neuroscience (Moser et al., 2008; Moser and Moser, 2013). Extracellular recordings revealed a rich repertoire of functionally-specialized cell-types in MEC including grid cells, border cells, head-direction cells and cells with conjunctive responses (Hafting et al., 2005; Sargolini et al., 2006; Solstad et al., 2008; Savelli et al., 2008; Lever et al., 2009). Classically layer 2 was seen as the home of "pure" grid cells, where head-direction responses are virtually absent (but see Tang et al., 2014b; Zhang et al., 2013). Initial studies also reported large fractions of grid cells in layer 3, phase-locked to the local field potential theta oscillations (4-12 Hz), and the large majority of them displayed conjunctive tuning to head-direction (Sargolini et al., 2006; Hafting et al., 2008). Accordingly layer 3 might be a source of theta-modulated, directional and grid signals to both MEC layer 2 and the hippocampus. Other studies have however provided divergent views, and suggested that theta-rhythmicity and theta-phase locking might be weaker among layer 3 neurons (Mizuseki et al., 2009; Burgalossi et al., 2011).

Layer 3 neurons provide a massive excitatory input to the hippocampus (Germroth et al., 1989), where most place cells are found and play a crucial role in hippocampal dependent memory formation (Suh et al., 2011). Thus resolving the functional and temporal properties of layer 3 neurons is crucial for understanding how place-memory is implemented at the cellular level.

Here we addressed this issue with a combined anatomical and functional approach (Burgalossi et al., 2011; Tang et al., 2014a). We show that layer 3 principal neurons, albeit differentiable in respect to long-range projection targets, constitute a largely homogeneous neuronal population, both physiologically and morphologically. By recording from identified layer 3 neurons in animals exploring 2-dimensional (2D) environments, we provide evidence that head-direction, grid and theta-rhythmic responses might be very sparse among layer 3 neurons.

Materials & Methods

All experimental procedures were performed according to the German guidelines on animal welfare under the supervision of local ethics committees.

Anatomy methods

Brain tissue preparation, histochemical and immunohystochemical experiments, neurobiotin detection were performed as described in Ray et al., 2014 and Tang et al., 2014b. Briefly, Wistar rats (150-400 g) were euthanized by an intraperitoneal injection of 20% urethane. Brains were cut on freezing microtome to obtain 20-60 μm thick para-sagittal sections or tangential sections (parallel to the pial surface). Immunohistochemical stainings for Calbindin and the DNA binding neuron specific protein NeuN and Purkinje Cell Protein 4 (PCP4) were performed as previously described on free-floating sections (Ray et al., 2014).

Retrograde Neuronal Labeling

Retrograde tracer solutions containing Cholera Toxin Subunit B, Alexa Fluor 488 or 546 Conjugate (CTB) (0.8 % in PB) were injected in juvenile rats (~150 gr) or in p23 rats (for in-vitro electrophysiology, see below) under ketamine/xylazine anesthesia. Briefly, 2 small craniotomies were opened both above the contralateral medial entorhinal cortex and ipsilateral hippocampus. Animals were placed in a stereotaxic apparatus, and prior to injection, the layer 3 of MEC was localized by electrophysiological mapping with low-resistance electrodes (1-3 M□), based on characteristic signatures of the local field potential and neuronal spiking activity in MEC layer 2 and layer 1 (Quilichini et al., 2010). Hippocampal injections were aimed at the pyramidal layer, which was localized by the characteristic sharp-wave / ripple activity patters. Glass electrodes with a tip diameter of 10-20 μm, filled with CTB solution, were then lowered into the target region. Tracer solutions (~0.3-0.8 □l) were slowly injected using positive pressure. After the injections, the pipettes were left in place for several minutes and slowly retracted. The craniotomies were closed by application of silicone and dental cement. The animals survived for 3-7 days before being transcardially perfused or sacrificed for in-vitro electrophysiology (below).

Analysis of anatomy data

For neuron counting, regions of interest (ROIs) were selected from tangential sections through layer 3 of MEC from double-retrograde tracing experiments (as described above, n=3). Neurons were counted manually with NeuroLucida on z-stacks or single-confocal planes acquired with a confocal microscope Zeiss LSM 710 (Tübingen) or Leica TCS SP5 (Leica Microsystems) (Berlin). Only ROIs with the highest regional overlap between back-labeled somata were selected for counting.

Reconstructions of dendritic morphologies were performed manually with NeuroLucida and displayed as 2D projections on the tangential plane (i.e. parallel to the MEC pial surface). For quantitative analysis of the relationship between apical dendritic morphologies of layer 3 neurons and layer 2 calbindin patches, the patches were manually outlined from calbindin

stainings on tangential MEC sections; then, the fraction of apical dendrites contained within the patch-area was calculated with the NeuroLucida software.

Slice preparation for in vitro electrophysiology

4-7 days after retrograde neuronal labeling (see above), rats (P26-29, n=4) were decapitated following isoflurane anesthesia. Brains were removed and transferred to ice-cold, sucrose-based artificial cerebrospinal fluid (sACSF) containing (in mM) 87 NaCl, 75 sucrose, 26 $NaHCO_3$, 2.5 KCl, 1.25 NaH_2PO_4, 0.5 $CaCl_2$, 7 $MgCl_2$, 25 glucose, saturated with 95% O_2, 5% CO_2, pH 7.4. Slices (400μm) were cut in a horizontal plane, tilted to the perpendicular axis of the pial surface of the entorhinal cortex on a vibratome (VT1200S; Leica). Slices were stored in an interface chamber (32-34°C), continuously oxygenized with carbogen, and perfused with artificial cerebrospinal fluid (ACSF) containing (in mM): 119 NaCl, 26 $NaHCO_3$, 10 glucose, 2.5 KCl, 2.5 $CaCl_2$, 1.3 $MgCl_2$, 1 NaH_2PO_4, at a rate of ~1ml/min. Slices were allowed to recover for at least 1h after preparation before they were transferred into the recording chamber.

In vitro electrophysiology and immunohistochemistry.

Whole-cell patch-clamp recordings (pipette resistance 2.5-4MΩ) were performed in ACSF near physiological temperature in a submerged-type recording chamber. Fluorescently labeled cells in layer 3 of the MEC were identified using fluorescence microscopy (XM10, Olympus) and infrared differential contrast microscopy (BX51WI, Olympus). For characterization, increasing steps of negative and positive current were injected (1s duration). The intracellular solution contained (in mM): 135 K-gluconate, 6 KCl, 2 $MgCl_2$, 0.2 EGTA, 5 Na_2-phosphocreatine, 2 Na_2-ATP, 0.5 Na_2-GTP, 10 HEPES buffer and 0.2% biocytin. The pH was adjusted to 7.2 with KOH. Recordings were performed using Multiclamp 700A/B amplifiers (Molecular Devices). Signals were filtered at 6kHz, sampled at 20kHz and digitized using the Digidata 1550 and pClamp 10 (Molecular Devices) or custom-written procedures in Igor Pro.

After recording, slices were transferred into a fixative solution containing 4% paraformaldehyde in 0.1M phosphate buffer. Biocytin-filled cells were visualized by streptavidin conjugated to Alexa 647 (diluted 1:500 in PBS containing 1% Triton). The slices were then mounted in Fluoroshield (Sigma-Aldrich) and analyzed. Image stacks of specimens were imaged on a Leica TCS SP5 confocal microscope (Leica Microsystems).

Juxtacellular and tetrode recordings

Juxtacellular recordings in urethane/ketamine anesthetized animals were obtained in male Wistar rats and were performed essentially as previously described (Klausberger et al., 2003; Ray et al., 2014). Before juxtacellular recordings, mapping experiments with low-resistance electrodes (0.5 – 1 M□) were performed to estimate the recording depth of the entorhinal layers, based on known electrophysiological features of the of the entorhinal laminar structure (Quilichini et al., 2010). Morphological identification of a subset of the recorded neurons confirmed the expected laminar location (7 out of 7 neurons in layer 3).

Juxtacellular recordings in freely-moving animals were obtained in male Wistar rats. Experimental procedures, signal acquisition and processing and animal tracking were performed as recently described (Tang et al., 2014a; Tang et al., 2014b). 27 juxtacellular recordings were identified, i.e. at least a soma and/or dendrite(s) could be recovered in layer 3.

2 juxtacellular recordings, where cell identification failed but recording sites were localized to MEC layer 3, were included as "non-identified" recordings. 50 units were recorded with tetrodes, according to described procedures (Tang et al., 2014b) in Wistar and Long-Evans rats. All tetrode recording experiments were performed in 1x1m arena; 10 juxtacellular recordings were performed in 1x1m arena, the rest in 70x70cm. MEC layer 2 data, shown here for direct comparison, have been published in previous papers (Ray et al., 2014; Tang et al., 2014b).

Theta-rhythmicity and theta-phase analysis

Theta-rhythmicity of spiking discharge was determined in the following way: First, we calculated the autocorrelation of the spike train, binned in 10 ms bins. Then we calculated the power spectrum of the autocorrelation using the welch estimate ("pwelch" in Matlab). To measure spiking rhythmicity in the theta band, a 'theta rhythmicity' index was computed, defined as the average power within 1 Hz of the maximum of the autocorrelation function in the theta range (4-12 Hz).

For spiking theta-phase analysis, we calculated the locking to theta phase based on spiking discharge in relation to theta rhythm in the local field potential. The local field potential was zero-phase band-pass filtered (4-12 Hz) and a Hilbert transform was used to determine the instantaneous phase of the theta wave. The strength of locking to theta phase, S, and the preferred phase angle, φ, was defined as the modulus and argument of the Rayleigh average vector of the theta phase at all spike times. Only spikes during running (speed cutoff = 1 cm/s for juxtacellular signals, 5 cm/s for tetrode recordings) were included in the analysis.

Only cells with firing rate > 0.5 Hz were included in the theta-rhythmicity and theta-phase analysis. Three juxtacellular recordings were not included in the theta-phase analysis (since LFP signals were not recorded) but only theta-rhythmicity was computed. For direct comparability of MEC layer 2 and layer 3 data, both the analysis procedures and the juxtacellular data set largely correspond to our recent work (Ray et al., 2014; Tang et al., 2014b).

Analysis of Spatial Modulation and head-directionality.

Rate maps, spatial autocorrelations, spatial information (Skaggs et al., 1993), grid scores, border scores and head-directionality were computed as previously described (Tang et al., 2014b), to remain consistent with the criteria of our previous report on the MEC layer 2 (Tang et al., 2014b), thus allowing direct comparison to those results (as in Figures 5 and 7).

Briefly, grid scores were calculated as previously described (Barry et al., 2012a; Tang et al., 2014b) by taking a circular sample of the autocorrelogram, centered on, but excluding the central peak. The Pearson correlation of this circle with its rotation for 60 degrees and 120 degrees was obtained (on peak rotations) and also for rotations of 30 degrees, 90 degrees and 150 degrees (off peak rotations). Gridness was defined as the minimum difference between the on-peak rotations and off-peak rotations (see also Tang et al., 2014b).

Briefly, head-direction tuning was measured as the eccentricity of the circular distribution of firing rates. A cell was defined as head-direction, if the length of the average vector exceeded the 95th percentile of a distribution of average vector lengths calculated from shuffled data and had a Rayleigh vector length > 0.3. For head-direction analysis, a firing rate inclusion criteria (> 0.5 Hz) was applied. For spatial analysis, both a spatial (> 50% spatial coverage) and a firing

rate inclusion criterion (> 0.5 Hz) were applied. Spatial coverage was defined as the fraction of visited pixels (bins) in the arena to the total pixels. Of the 79 recordings (juxtacellular + tetrode), 69 recordings (17 identified + 52 non-identified recordings) satisfied these criteria, and were included in the spatial and head-direction analysis.

None of the layer 3 neurons met our previous grid cell criteria (Tang et al., 2014b; grid score > 0.3 and significant spatial information). Two juxtacellularly recorded and identified L3 neurons showed hexagonally-arranged firing fields in the spatial autocorrelation (one cell shown in Tang et al., 2014a); the short duration of the recordings however prevented statistical assessment of spatial modulation in these two neurons. Only one neuron (marked with asterisk in Fig. 6) met the inclusion criteria for border activity (border score > 0.5 & significant spatial information; Tang et al., 2014b). This neuron was classified as a border cell, although the small border score (border score 0.52, spatially significant with $p = 0.03$) and visual assessment of the rate map indicated that it might be a false positive border cell.

Results

To assess the cytoarchitectonic organization of MEC layer 3, we stained tangential and parasaggital section through MEC for the neuronal marker NeuN, cytochrome oxidase activity and cholinergic markers. Unlike MEC layer 2 (Burgalossi et al., 2011; Ray et al., 2014) in all these preparations layer 3 had a relatively homogeneous appearance (Figure 1A,B and not shown). Next, we sought to determine how the projection patterns of layer 3 neurons were spatially arranged. To this end, we performed double-injections of the retrograde tracer Cholera-Toxin B subunit (CTB) in both ipsilateral hippocampus and contralateral MEC. Consistent with previous findings (Germroth et al., 1989; Brun et al., 2008; Suh et al., 2011), layer 3 neurons were readily labeled following hippocampal injections. We found however that a large fraction of layer 3 neurons also project densely to contralateral MEC (Figure 1C). This contralateral projection, which originates in layer 3, targeted mostly superficial layers on the contralateral side (not shown). Tangential sections of the layer 3 cortical sheet stained for both hippocampal-projecting (red) and contralateral MEC-projecting cells (green) provide a particularly clear overview of the distribution of these two cell populations (Figure 1C). While hippocampal-projecting neurons were arranged in a transverse band (Honda et al., 2012), neurons labeled following contralateral injections were predominantly restricted to a single location, consistent with a point-to-point contralateral connectivity (Figure 1C). We observed that a large fraction of contralateral-projecting neurons (~40%, 162/397 cells; n=3 rats) were also double-labeled by the ipsilateral hippocampal injection (Figure 1D). These data indicate that hippocampally and contralaterally projecting neurons might not form discrete neuronal populations.

To assess morphological characteristics and intrinsic properties, we conducted whole-cell patch clamp recordings of layer 3 pyramidal cells in slices of the medial entorhinal cortex. The majority of recorded neurons (n=17 of a total of 23 cells) were labeled post-hoc with streptavidin-A647 and could morphologically be identified as pyramidal cells (Figure 2A). In addition to the morphological description of the recorded neurons, we also tested their intrinsic properties and spiking behavior by applying a series of hyper- and depolarizing current steps (Figure 2B). All intrinsic properties (input resistance, spike duration, tau of the sag potential, sag amplitude, rebound depolarization and adaptation ratio) were homogeneously distributed among the population of recorded neurons (Figure 2C,D). In a subset of recorded cells, the projection targets were identified by retrograde tracers from the ipsilateral hippocampus and contralateral MEC (see Methods and Figure 1). We did not observe a correlation between projection targets and intrinsic parameters of the neurons (not shown). Our i*n vitro* electrophysiology analysis thus consolidates the picture of a largely homogenous population of neurons in MEC layer 3.

We next investigated the relationship between layer 3 neurons and the modular architecture of MEC layer 2 pyramidal cells (Ray et al., 2014). PCP4 labels neurons in layer 3 and deep layers of the entorhinal cortex (Lein et al., 2007). Here we show using antibodies against calbindin and PCP4 that the layer 3 apical dendrites tend to form clusters in-between the calbindin patches in layer 2 (Fig. 3A). To further explore this issue, we analyzed the relationship between the neuropil of retrogradely-labeled layer 3 neurons and the layer 2 pyramidal cell patches, identified by calbindin immunoreactivity (Ray et al., 2014). Interestingly, both hippocampal and contralateral-projecting layer 3 cell populations largely avoided the calbindin patches

(Figure 3B). To clarify this relationship at the single-cell level, we reconstructed the apical dendritic morphology of single layer 3 neurons, labeled juxtacellularly in-vivo (Figure 3C). The majority of dendritic branches from layer 3 cells avoided the calbindin patches (total dendritic length inside- versus outside-of-patches, 900 ± 101 versus 7193 ± 588 □m, n=5; Figure 3C), in line with the retrograde-tracing data. Moreover, labeling small "clusters" of layer 3 neurons by neurobiotin spillover led to similar results, i.e. dendritic trees of layer 3 neurons largely avoiding the calbindin-patch territories in superficial layer 2/1 (Figure 3D). These data suggest that the dendrites from layer 3 pyramidal cells do not sample inputs, which are selective for the calbindin-patches (i.e. cholinergic and parasubicular inputs; Ray et al., 2014; Tang et al., in prep.).

What are the firing properties of layer 3 neurons during spatial navigation? An example of a cell identified in layer 3 is shown in Figure 4. The cell is a pyramidal neuron with wide-spreading basal dendrites and a single, bifurcating apical dendrite (Figure 4A). Spiking activity carried a significant amount of spatial information, Skaggs et al., 1993), but no clear spatial firing pattern was revealed by 2D spatial autocorrelation (Figure 4B). The cell's firing was not modulated by head-direction (Figure 4C), it lacked theta-rhythmicity (Figure 4D) but displayed a clear phase-preference near the theta-peak (Figure 4D,E). Similarly to this representative neuron, in most recordings from identified layer 3 neurons, we did not observe spike-rhythmicity or regular spatial firing patterns (see below). In only two neurons - one of which was located at the layer 2/3 border and showed strongest theta-rhythmicity - we observed hexagonal "grid-like" firing (not shown). The short duration of the recordings however prevented statistical assessment of spatial modulation in these two neurons (see Methods). The discharge properties of the neuron shown in Figure 4 are in many regards prototypic for layer 3 as will be pointed out in the population data shown in the next two Figures.

To clarify the temporal spiking properties of layer 3 neurons relative to local field potential theta-oscillations, we combined data from juxtacellular recordings with single units from tetrode recordings. Spatial and temporal analysis of this extended data set (n = 79) confirmed the observations from the identified dataset. First, most layer 3 cells showed weak theta-rhythmicity and theta-phase locking strength (see example in Fig. 5A). As a population, layer 3 neurons did not show a significant theta-phase preference ($p = 0.47$), even when only neurons with significant theta-phase locking (n = 64 with Rayleigh test, $p < 0.01$; Mizuseki et al., 2009) were included ($p = 0.27$) (Figure 5B). Compared to identified layer 2 pyramidal and stellate cells (Ray et al. 2014), they showed significantly weaker theta-rhythmicity ($p = 0.0001$ and $p = 0.0212$, respectively, Mann-Whitney U-test, Bonferroni-Holm corrected for multiple comparisons; Figure 5C) and significantly weaker theta-phase locking strength ($p = 0.0006$ and $p = 0.0365$, respectively, Mann-Whitney U-test, Bonferroni-Holm corrected for multiple comparisons; Figure 5D). Notably, similar results were obtained under urethane/ketamine anesthesia (Klausberger et al., 2003), where unlike layer 2 neurons (Ray et al., 2014) layer 3 neurons (n=13) lacked theta-rhythmicity (average theta rhythmicity = $0.8 \pm 0.2 \times 10^{-3}$) and were weakly locked to ongoing theta oscillations (average locking strength = 0.32 ± 0.15) (not shown). Altogether, these data show that layer 3 neurons are distinct from layer 2 cells with respect to their weak theta-rhythmicity and their average weak entrainment by theta-oscillations.

When we assessed spatial discharge properties of layer 3 cells we found that a fraction of the layer 3 neurons included in the spatial analysis (19/69; ~28%, see Methods) carried significant spatial modulation, confirming previous reports (Sargolini et al., 2006; Hafting et al., 2008; Burgalossi et al., 2011; Domnisoru et al., 2013; Schmidt-Hieber and Häusser, 2013). However, in none of the neurons, which were located well within layer 3, we observed clear grid or border firing patterns (Figure 6). Rather, spatially irregular firing patterns dominated among spatially-modulated neurons (Figure 6). Surprisingly, only a small fraction of the layer 3 neurons (5/69) met the head-directionality criteria (Figure 7A,B). Although the proportion of head-direction cells did not differ statistically between layer 3 and layer 2 ($p = 0.069$, χ^2-*test*), average head-direction Rayleigh vector lengths of layer 3 neurons was smaller than in layer 2 cells ($p = 0.0317$ and $p = 0.0326$ vs. putative pyramidal cells and stellate cells, respectively, Mann-Whitney U-test, Bonferroni-Holm corrected for multiple comparisons, Figure 7C). The layer 2 cell sample shown here for comparison comes from our earlier work and contains identified cells and layer 2 recordings, which were putatively assigned to cell types based on temporal discharge characteristics (Tang et al., 2014b). In summary, these data indicate that theta-rhythmic discharges and head-direction modulated responses are sparse in MEC layer 3, where on the other hand non-theta-rhythmic, spatially-irregular response patterns dominate.

Discussion

Here we confirm that layer 3 is a major source of the contralateral MEC projection. Thus layer 3 is a major hub not only for entorhinal-hippocampal communication, but also for inter-hemispheric coordination. We found that unlike layer 2 principal neurons (Ray et al., 2014) layer 3 neurons displayed homogeneous *in vitro* intrinsic and *in vivo* spatiotemporal properties, without clear indications of bimodality. The unique arrangement of layer 3 dendrites in respect to the calbindin-positive layer 2 patches (Figure 3) puts anatomical constraints on the inputs that these neurons might receive. Since cholinergic (Ray et al., 2014) and parasubicular inputs (Burgalossi et al., 2011; Tang et al., in prep.) are strongly selective for the calbindin-patch territories in layer 2 and 1 of MEC, the fact that layer 3 dendrites largely avoid these territories makes them unlikely recipients of such inputs. Notably, cholinergic transmission has been linked to grid activity in MEC (Koenig et al., 2011; Brandon et al., 2011; Newmann et al., 2014); the fact that we observed a very low abundance of grid cells (0/69; however 2/69, ~ 3%, showed non-significant hexagonality) in our (albeit limited) layer 3 dataset might be suggestive of a causal relationship. Parasubicular neurons show the strongest theta-rhythmicity of spiking among parahippocampal neurons (Burgalossi et al., 2011; Tang et al., in prep.); layer 2 pyramidal neurons are likely recipients of such theta-modulated inputs (Ray et al., 2014), while our anatomical observations indicate that layer 3 neurons might not (but see Canto et al., 2012). The weak theta-modulation of layer 3 neurons observed here is in line with previous work (Mizuseki et al., 2009) and might be the result of the arrangement of layer 3 dendrites and their relationship to layer 2 patches.

The apparent sparseness of head-directionality among layer 3 neurons is puzzling, because there is a dense presubicular projection into layer 3 (Caballero-Bleda and Witter, 1993, 1994). Thus, further work will be required for resolving the functional nature of presubicular inputs to MEC layer 3, and how directional information is integrated within the local neuronal network and/or at single-cell level. Our results diverge from earlier findings on layer 3, which described dominant conjunctive responses and head-directionality in this layer (Sargolini et al., 2006, Boccara et al., 2010). Part of the discrepancy might be accounted for by different sampling methods (juxtacellular versus tetrode) between the current and previous studies, and more inclusive criteria for head-directional tuning (Sargolini et al., 2006). We note also that sharp head-direction signals are typically observed at the dorsalmost border of MEC (e.g. Fyhn et al., 2008; Wills et al., 2010; Giocomo et al., 2014), a region where the parasubiculum extends in a long and narrow stripe above the MEC (Burgalossi et al., 2011; Tang et al., in prep). Considering the limited spatial resolution achievable with tetrode recordings, this is compatible with a parasubicular origin of sharp head-direction signals. Assessment of directionality from more ventral layer 3 locations, where tuning has been shown to be much weaker (Giocomo et al., 2014) agrees well with our current data. The strength of our dataset stems from histological confirmation of the cellular/laminar origin of our recordings; we acknowledge, however, that our conclusions rest on a relatively limited sample.

Resolving the functional properties of layer 3 neurons is of significance for our understanding of spatial coding in entorhinal cortex and its downstream targets (e.g. hippocampus). Indeed a recent study has reported a majority of non-spatially modulated inputs to the hippocampus (Zhang et al., 2013), which is consistent with our average picture of layer 3 responses. We are intrigued by the very different spatial discharge patterns that we observed in the directly adjacent layers 2 and 3. Almost all layer 3 cells discharged in irregular spatial patterns and showed weak head-directionality. In contrast, spatially-modulated layer 2 neurons often discharged in grid or border patterns. Despite the lack of strict geometry, layer 3 discharges

could however provide sufficient information for decoding the animal's position in space, provided that the cells' responses are reliable and stable across time (Zhang and Sejnowski, 1998; Zhang et al., 1999). It remains to be established if and how these irregular spatial firing patterns contribute to place-cell activity in the downstream hippocampus.

References

Abbasi S, Kumar SS (2013) Electrophysiological and morphological characterization of cells in superficial layers of rat presubiculum. J Comp Neurol 521:3116–3132.

Beed P, Bendels MHK, Wiegand HF, Leibold C, Johenning FW, Schmitz D (2010) Analysis of excitatory microcircuitry in the medial entorhinal cortex reveals cell-type-specific differences. Neuron 68:1059–1066.

Behr J, Gloveli T, Heinemann U (1998) The perforant path projection from the medial entorhinal cortex layer III to the subiculum in the rat combined hippocampal-entorhinal cortex slice. Eur J Neurosci 10:1011–1018.

Boccara CN, Sargolini F, Thoresen VH, Solstad T, Witter MP, Moser EI, Moser M-B (2010) Grid cells in pre- and parasubiculum. Nat Neurosci 13:987–994.

Brandon MP, Bogaard AR, Libby CP, Connerney MA, Gupta K, Hasselmo ME (2011) Reduction of theta rhythm dissociates grid cell spatial periodicity from directional tuning. Science 332, 595–599.

Brun VH, Leutgeb S, Wu HQ, Schwarcz R, Witter MP, Moser EI, Moser MB (2008) Impaired spatial representation in CA1 after lesion of direct input from entorhinal cortex. Neuron 57:290-302.

Burgalossi A, Herfst L, von Heimendahl M, Förste H, Haskic K, Schmidt M, Brecht M (2011) Microcircuits of functionally identified neurons in the rat medial entorhinal cortex. Neuron 70:773–786.

Caballero-Bleda M, Witter MP (1993) Regional and laminar organization of projections from the presubiculum and parasubiculum to the entorhinal cortex: An anterograde tracing study in the rat. J Comp Neurol 328:115–129.

Caballero-Bleda M, Witter MP (1994) Projections from the presubiculum and the parasubiculum to morphologically characterized entorhinal-hippocampal projection neurons in the rat. Exp Brain Res 101:93–108.

Canto CB, Koganezawa N, Beed P, Moser EI, Witter MP (2012) All layers of medial entorhinal cortex receive presubicular and parasubicular inputs. J Neurosci. 32:17620-31.

Canto CB, Witter MP (2012) Cellular properties of principal neurons in the rat entorhinal cortex. II. The medial entorhinal cortex. Hippocampus 22:1277–1299.

Couey JJ, Witoelar A, Zhang S-J, Zheng K, Ye J, Dunn B, Czajkowski R, Moser M-B, Moser EI, Roudi Y, Witter MP (2013) Recurrent inhibitory circuitry as a mechanism for grid formation. Nat Neurosci 16:318–324.

Dickson CT, Mena AR, Alonso A (1997) Electroresponsiveness of medial entorhinal cortex layer III neurons in vitro. Neuroscience 81:937–950.

Erchova I, Kreck G, Heinemann U, Herz AVM (2004) Dynamics of rat entorhinal cortex layer II and III cells: characteristics of membrane potential resonance at rest predict oscillation properties near threshold. J Physiol 560:89–110.

Fyhn M, Hafting T, Witter MP, Moser EI, Moser MB (2008) Grid cells in mice. Hippocampus 18:1230-8.

Germroth P, Schwerdtfeger WK, Buhl EH (1989) Morphology of identified entorhinal neurons projecting to the hippocampus. A light microscopical study combining retrograde tracing and intracellular injection. Neuroscience 30:683–691.

Giocomo LM, Stensola T, Bonnevie T, Van Cauter T, Moser M-B, Moser EI (2014) Topography of head direction cells in medial entorhinal cortex. Current Biology 24:252-62.

Gloveli T, Schmitz D, Empson RM, Dugladze T, Heinemann U (1997) Morphological and electrophysiological characterization of layer III cells of the medial entorhinal cortex of the rat. Neuroscience 77:629–648.

Hafting T, Fyhn M, Bonnevie T, Moser M-B, Moser EI (2008) Hippocampus-independent phase precession in entorhinal grid cells. Nature 453:1248–1252.

Hafting T, Fyhn M, Molden S, Moser M-B, Moser EI (2005) Microstructure of a spatial map in the entorhinal cortex. Nature 436:801–806.

Honda Y, Sasaki H, Umitsu Y, Ishizuka N (2012) Zonal distribution of perforant path cells in layer III of the entorhinal area projecting to CA1 and subiculum in the rat. Neuroscience Research 74: 200-209.

Kitamura T, Pignatelli M, Suh J, Kohara K, Yoshiki A, Abe K, Tonegawa S (2014) Island cells control temporal association memory. Science 343:896–901.

Klausberger T, Magill PJ, Márton LF, Roberts JD, Cobden PM, Buzsáki G, Somogyi P (2003) Brain-state- and cell-type-specific firing of hippocampal interneurons in vivo. Nature 421:844-8.

Kloosterman F, Van Haeften T, Witter MP, Lopes Da Silva FH (2003) Electrophysiological characterization of interlaminar entorhinal connections: An essential link for re-entrance in the hippocampal-entorhinal system. Eur J Neurosci 18:3037–3052.

Koenig J, Linder AN, Leutgeb JK, Leutgeb S (2011) The spatial periodicity of grid cells is not sustained during reduced theta oscillations. Science 332, 592–595.

Lein ES et al. (2007) Genome-wide atlas of gene expression in the adult mouse brain, Nature 445: 168-176.

Lever C, Burton S, Jeewajee A, O'Keefe J, Burgess N (2009) Boundary vector cells in the subiculum of the hippocampal formation. J Neurosci 29, 9771-7.

Mizuseki K, Sirota A, Pastalkova E, Buzsáki G (2009) Theta oscillations provide temporal windows for local circuit computation in the entorhinal-hippocampal loop. Neuron 64:267–280.

Moser EI, Kropff E, Moser M-B (2008) Place cells, grid cells, and the brain's spatial representation system. Annu Rev Neurosci 31:69–89.

Moser EI, Moser M-B (2013) Grid cells and neural coding in high-end cortices. Neuron 80:765–774.

Newman EL, Climer JR, Hasselmo ME (2014) Grid cell spatial tuning reduced following systemic muscarinic receptor blockade. Hippocampus 24, 643-655.

Pastoll H, Solanka L, van Rossum MCW, Nolan MF (2013) Feedback inhibition enables theta-nested gamma oscillations and grid firing fields. Neuron 77:141–154.

Quilichini P, Sirota A, Buzsáki G (2010) Intrinsic circuit organization and theta-gamma oscillation dynamics in the entorhinal cortex of the rat. J Neurosci 18, 11128-11142.

Ray S, Naumann R, Burgalossi A, Tang Q, Schmidt H, Brecht M (2014) Grid-layout and theta-modulation of layer 2 pyramidal neurons in medial entorhinal cortex. Science 343:891–896.

Sargolini F, Fyhn M, Hafting T, McNaughton BL, Witter MP, Moser M-B, Moser EI (2006) Conjunctive representation of position, direction, and velocity in entorhinal cortex. Science 312:758–762.

Savelli F, Yoganarasimha D, Knierim JJ (2008) Influence of boundary removal on the spatial representations of the medial entorhinal cortex. Hippocampus 18, 1270-82.

Solstad T, Boccara CN, Kropff E, Moser M-B, Moser EI (2008) Representation of geometric borders in the entorhinal cortex. Science 322:1865–1868.

Suh J, Rivest AJ, Nakashiba T, Tominaga T, Tonegawa S (2011) Entorhinal cortex layer III input to the hippocampus is crucial for temporal association memory. Science 334:1415–1420.

Tang Q, Brecht M, Burgalossi A (2014a) Juxtacellular recording and morphological identification of single neurons in freely moving rats. Nat Protoc 9:2369–2381.

Tang Q, Burgalossi A, Ebbesen CL, Ray S, Naumann R, Schmidt H, Spicher D, Brecht M (2014b) Pyramidal and stellate cell specificity of grid and border representations in layer 2 of medial entorhinal cortex. Neuron 84, 1191–1197.

Van der Linden S, Lopes da Silva FH (1998) Comparison of the electrophysiology and morphology of layers III and II neurons of the rat medial entorhinal cortex in vitro. Eur J Neurosci 10:1479–89.

Van Haeften T, Baks-te-Bulte L, Goede PH, Wouterlood FG, Witter MP (2003) Morphological and numerical analysis of synaptic interactions between neurons in deep and superficial layers of the entorhinal cortex of the rat. Hippocampus 13:943–952.

Wills TJ, Cacucci F, Burgess N, O'Keefe J (2010) Development of the hippocampal cognitive map in preweanling rats. Science 328:1573-6.

Zhang K, Ginzburg I, McNaughton BL, Sejnowski TJ (1998) Interpreting neuronal population activity by reconstruction: unified framework with application to hippocampal place cells. Journal of Neurophysiology 79: 1017-1044.

Zhang K, Sejnowski TJ (1999) Neuronal tuning: To sharpen or broaden? Neural Computation 11: 75-84.

Zhang S-J, Ye J, Miao C, Tsao A, Cerniauskas I, Ledergerber D, Moser M-B, Moser EI (2013) Optogenetic dissection of entorhinal-hippocampal functional connectivity. Science 340:1232627.

Figures

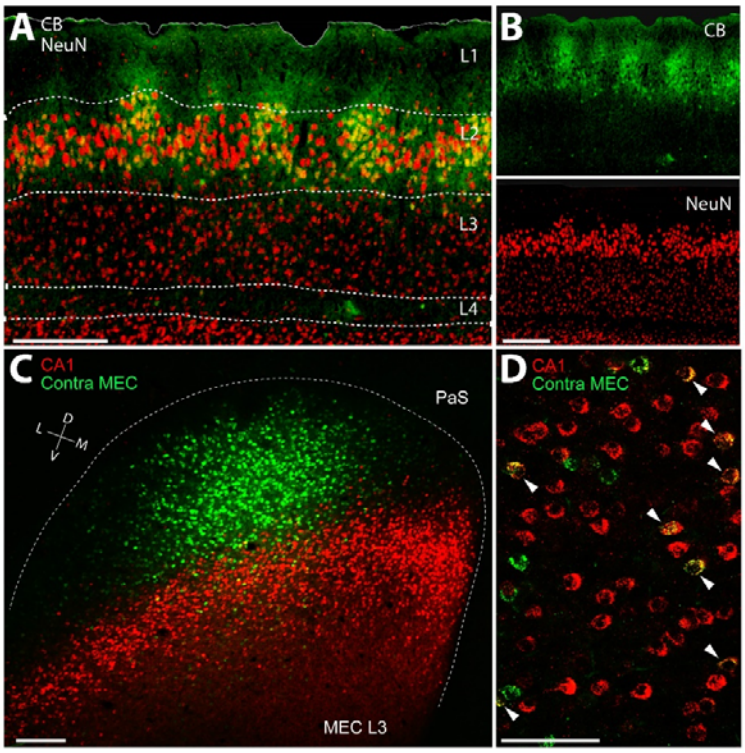

Figure 1. Layer 3 of medial entorhinal cortex: homogeneous layout and organization of long-range projections.

(A) Superimposed staining for calbindin (green) and NeuN (red) showing the homogeneous and uniform distribution of neuronal somata in layer 3 of MEC. Note in comparison the modular organization of the adjacent layer 2. Scale bar, 250 □m.

(B) Parasaggital section through MEC stained for calbindin (top, green) and NeuN (bottom, red) from (A). Scale bar = 250 □m.

(C) Tangential section trough MEC layer 3 showing retrogradely-labeled neuronal somata following injection of CTB-Alexa 488 (green) and CTB-Alexa 546 (red) in ipsilateral hippocampus ("CA1") and contralateral MEC ("contra MEC"), respectively. The border of the MEC is outlined (dotted line). PaS = Parasubiculum. Scale bar, 250 □m.

(D) High-magnification of a parasagittal section from a dual-retrograde neuronal tracing experiment as in (C). Arrowheads indicate double-labeled neurons. Labels as in (C). Scale bar, 100 μm.

D = dorsal, L = lateral, M = medial, V = ventral.

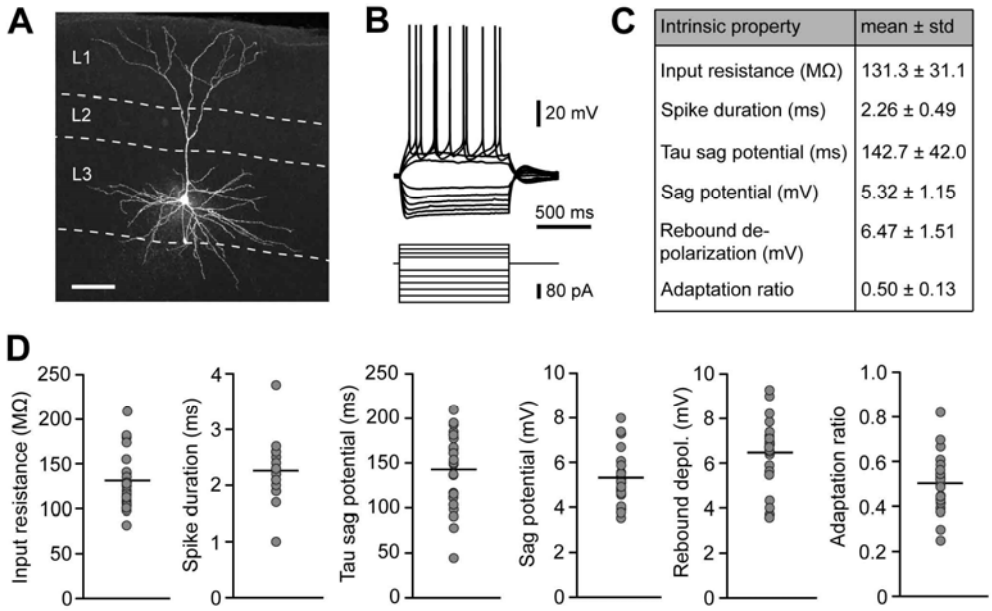

Intrinsic property	mean ± std
Input resistance (MΩ)	131.3 ± 31.1
Spike duration (ms)	2.26 ± 0.49
Tau sag potential (ms)	142.7 ± 42.0
Sag potential (mV)	5.32 ± 1.15
Rebound de-polarization (mV)	6.47 ± 1.51
Adaptation ratio	0.50 ± 0.13

Figure 2: **Morphology and intrinsic properties of layer 3 principal neurons in the medial entorhinal cortex.**

(**A**) Maximal intensity projection of a confocal image stack of an exemplary layer 3 pyramidal cell in MEC. The shown cell was filled with biocytin during electrophysiological recording and counterstained with streptavidin A647 after fixation. Scale bar, 100 □m.

(**B**) Representative electrophysiological characterization of a layer 3 pyramidal cell. Hyper- and depolarizing current steps were applied to determine passive properties and action potential pattern.

(**C**) Summary table of intrinsic membrane properties of layer 3 pyramidal cells.

(**D**) Distribution of intrinsic parameters for all recorded cells. Grey circles represent mean values of individual neurons, black lines are mean values of all neurons (n=23).

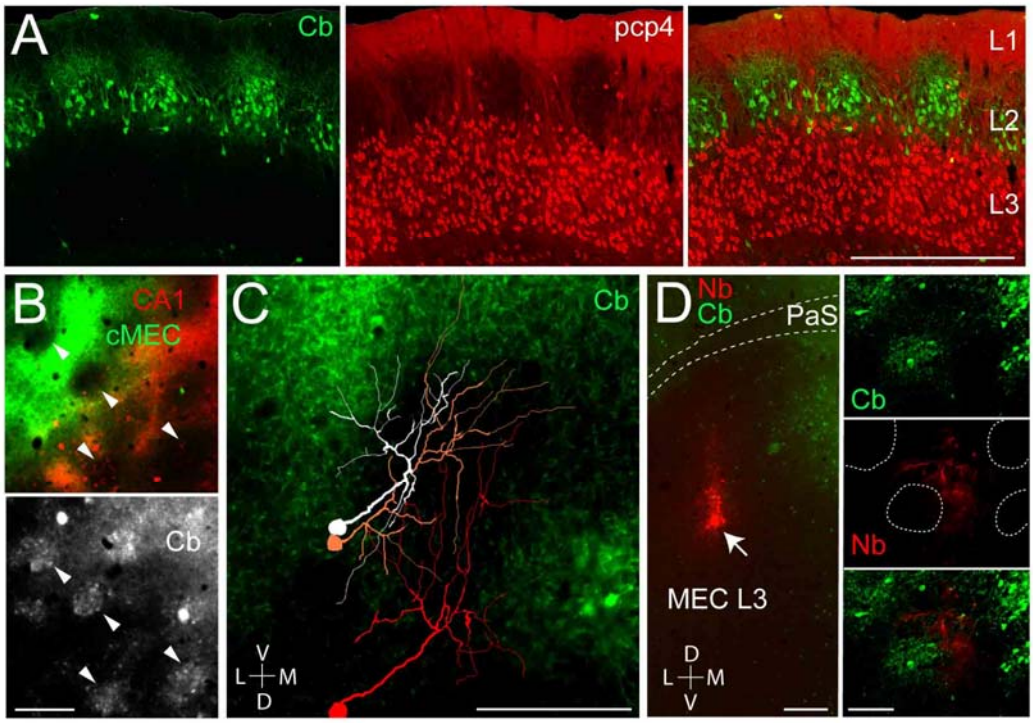

Figure 3. Layer 3 dendrites avoid calbindin-positive pyramidal cell patches in layer 2.

(A) Sagittal lection through MEC stained for calbindin (green, left) and PCP4 (red, middle). Right panel, overlay. Note the clustering of apical layer 3 dendrites around the calbindin patches in layer 2. Scale bar = 500 □m

(B) Close-up views from a tangential section through superficial MEC layer 2, showing neuropil signal of retrogradely-labeled layer 3 neurons, following injections of CTB-Alexa 488 (green) and CTB-Alexa 546 (red) as in Fig. 1C, stained for calbindin (grey). Arrowheads indicate calbindin patches.

(C) Reconstructions of the apical dendritic morphologies of three representative layer 3 pyramidal neurons, superimposed on the calbindin staining in MEC layer 2 (tangential view). Note that the dendrites largely avoid the calbindin territories. Scale bar = 200 □m.

(D) Left panel, tangential section trough layer 3 of MEC stained for neurobiotin (red) and calbindin (green) showing the site of neurobiotin "spillover" in MEC layer 3, where a cluster of layer 3 neurons is labeled (arrow). A close-up magnification on the apical dendrites is shown in the right panel: calbindin patches (green, top), neurobiotin (Nb) labeled dendrites (middle, red) and overlay (bottom). Dotted lines represent patches outline. Note that the labeled dendrites (red) largely avoid the patch territories (green). Scale bars = 200 □m (left) and 100 □m (right).

D = dorsal, L = lateral, M = medial, V = ventral.

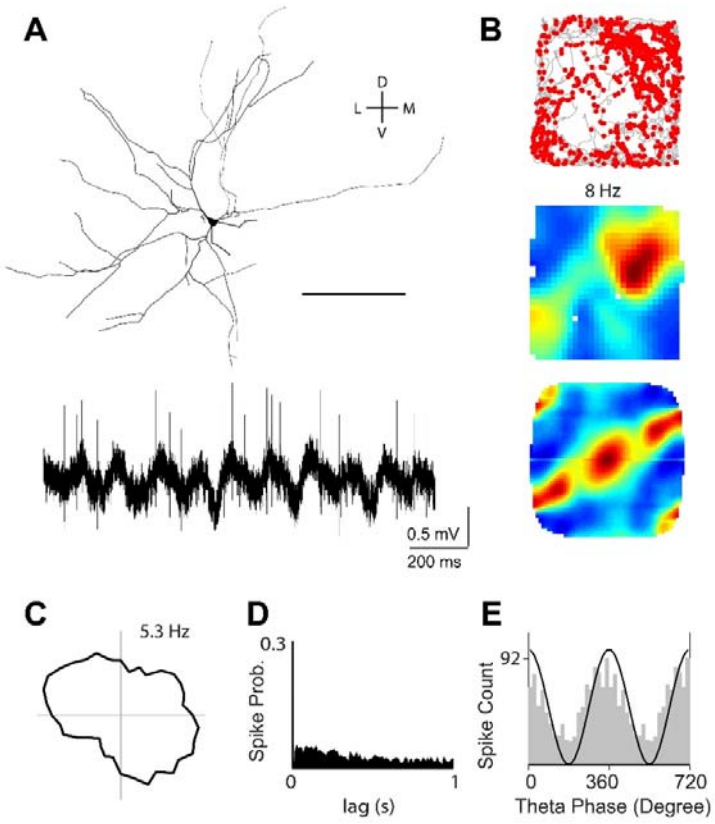

Figure 4. Irregular spatial firing pattern of an identified pyramidal layer 3 neuron.

(A) Top, tangential view showing the reconstruction of the layer 3 pyramidal neuron recorded and identified in a rat exploring a 2D environment (70 x 70 cm). Scale bar, 100 µm. Bottom, representative raw spike-trace, recorded during freely-moving behavior.

(B) Spike-trajectory plot (top), rate map (middle) and two-dimensional spatial autocorrelation of the rate map (bottom) for the neuron shown in (A). Spike-trajectory plot: red dots indicate spike locations; grey lines indicate the rat trajectory. Rate map: red indicates maximal firing rate, value noted above. Spatial autocorrelation: color scale -1 (blue) through 0 (green) to 1 (red). This cell was classified as irregular, spatially-modulated (se Methods).

(C) Polar plot of the cell's head-direction tuning. Value indicates maximum firing rate. Note the absence of head-directional firing.

(D) Spike-autocorrelogram for the cell shown in (A). Note the absence of theta-rhythmicity of spiking.

(E) Theta-phase histogram of spikes for the cell shown in (A). For convenience, two repeated cycles are shown. The black sinusoid is a schematic local field potential theta wave for reference. Note the spiking phase-preference near the theta-peak for this neuron.

D = dorsal, L = lateral, M = medial, V = ventral.

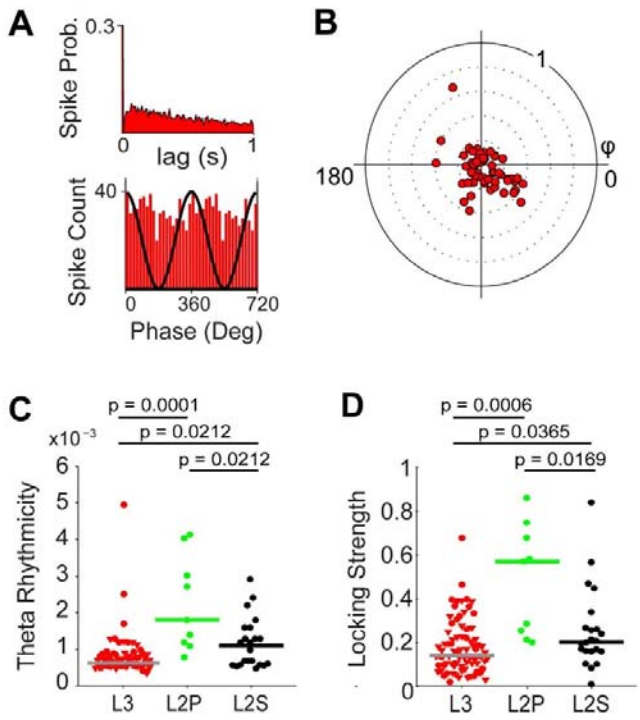

Figure 5. Theta modulation of layer 3 and layer 2 neurons in medial entorhinal cortex.

(A) Representative spike-autocorrelogram (top) and theta-phase histogram of spikes (bottom) of a juxtacellularly-recorded and identified MEC layer 3 neuron. Note the absence of theta-rhythmicity (top), as in the representative neuron in Fig. 4. In the bottom panel, two repeated cycles are shown; the black sinusoid is a schematic local field potential theta wave for reference.

(B) Polar plot of preferred theta phase (theta-peak = 0°) and theta-phase locking strength (0-1) for layer 3 neurons (n = 79). Red dots = cells and single units, grey line = (circular average, median strength). Note the non-significant theta-phase preference in our dataset (p=0.47).

(C-D) Theta-rhythmicity (C) and theta-phase locking strength (D) in MEC L3 (red), identified L2 pyramidal (green) and stellate (black) neurons. Triangles indicate non-identified layer 3 recordings (juxtacellular + tetrode). Circles indicate cells recorded and identified juxtacellularly. Horizontal lines indicate medians, p-values indicate result of Mann-Whitney U-test (in D-E). All p-values are Bonferroni-Holm corrected for multiple comparisons. Data from MEC L2 are from Tang et al. 2014b and are shown for comparison.

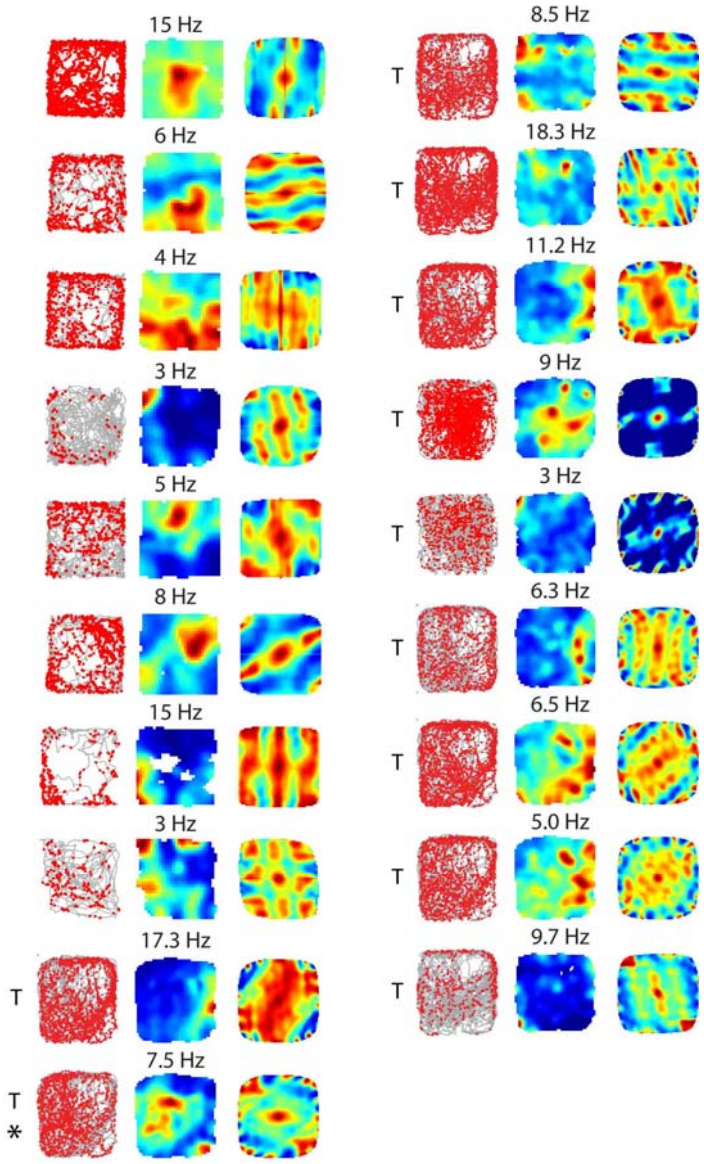

Figure 6. Spatially-irregular firing patterns of layer 3 neurons, which carry significant spatial information.

Spike-trajectory plot, rate map and two-dimensional spatial autocorrelation of MEC layer 3 recordings, which carry significant spatial information (see Methods). Numbers above the rate map indicate maximum firing rate. (T) indicates cells recorded with tetrodes (1x1m arena); all other cells are from juxtacellular recordings (70x70cm arena). The neuron indicated with the asterisk (*) met the border criteria (border score = 0.52) and was thus included in this category (see Fig. 7A and Methods).

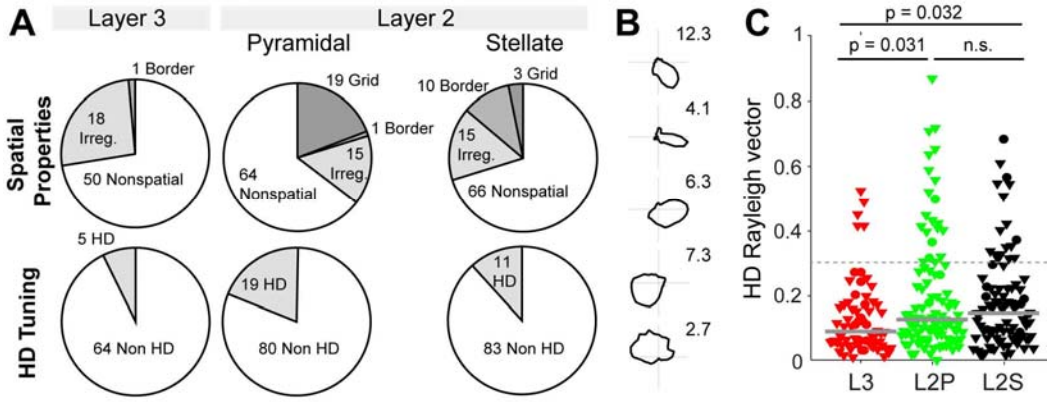

Figure 7. Spatial firing properties and head-directionality of layer 2 and layer 3 neurons in medial entorhinal cortex.

(A) Distribution of spatial and directional firing patterns observed in MEC L3 (left) and L2 neurons (identified + classified in "putative" pyramid (middle) and "putative" stellate (right); data from Tang et al. 2014b shown for comparison).

(B) Layer 3 head-direction cells, which met the inclusion criteria (see Methods) arranged top-to-bottom according to the head-direction vector length. Peak firing rate in Hz is indicated next to the plots.

(C) Comparison of the head-direction Rayleigh vector lengths in MEC layer 3 (red) and layer 2 neurons (identified + classified in "putative" pyramid (green) and "putative" stellate (black)). Horizontal lines indicate medians, *p*-values indicate result of Mann-Whitney U-test (Bonferroni-Holm corrected for multiple comparisons). Data from MEC layer 2 are from Tang et al. 2014b and are shown for comparison.

Chapter 7

Functional architecture of the rat parasubiculum.

Published as:

Tang, Q. et al. (2016). Functional architecture of the rat parasubiculum. *J. Neurosci. 36:2289-2301*

doi: 10.1523/JNEUROSCI.3749-15.2016

Functional architecture of the rat parasubiculum

Qiusong Tang[1,*], Andrea Burgalossi[2,*,‡], Christian Laut Ebbesen[1,3,*], Juan Ignacio Sanguinetti-Scheck[1,*], Helene Schmidt[1], John J. Tukker[1,4], Robert Naumann[1,5], Saikat Ray[1], Patricia Preston-Ferrer[2], Dietmar Schmitz[4] & Michael Brecht[1,‡]

[1]Bernstein Center for Computational Neuroscience, Humboldt Universität zu Berlin, Philippstr. 13, Haus 6, 10115 Berlin, Germany

[2]Werner Reichardt Centre for Integrative Neuroscience, Otfried-Müller-Str. 25, 72076 Tübingen, Germany
[3]Berlin School of Mind and Brain, Humboldt University of Berlin, 10115 Berlin, Germany

[4]Charité Universitätsmedizin Berlin, Charité Crossover NWFZ Campus Mitte, Virchowweg 6, Charitéplatz 1, 10117 Berlin, Germany
[5]Current Address: Max-Planck-Institute for Brain Research, Max-von-Laue-Str. 4, 60438 Frankfurt am Main, Germany

* These authors contributed equally

‡To whom correspondence should be addressed: andrea.burgalossi@cin.uni-tuebingen.de or michael.brecht@bccn-berlin.de

Acknowledgements

This work was supported by Humboldt-Universität zu Berlin, BCCN Berlin (German Federal Ministry of Education and Research BMBF, Förderkennzeichen 01GQ1001A), NeuroCure, the Neuro-Behavior ERC grant, the Gottfried Wilhelm Leibniz Prize of the DFG, and by the Werner Reichardt Centre for Integrative Neuroscience (CIN) at the Eberhard Karls University of Tübingen. The CIN is an Excellence Cluster funded by the Deutsche Forschungsgemeinschaft (DFG) within the framework of the Excellence Initiative (EXC 307). We thank Moritz von Heimendahl for programming, Falko Fuhrmann and Stefan Remy for generous donations of PV-Cre mice and help with the AAV-injections, Susanne Schoch (University of Bonn) for providing the virus, and Andreea Neukirchner, Juliane Steger, Alexandra Eritja, Susanne Rieckmann and Undine Schneeweiß for outstanding technical assistance.

Abstract

The parasubiculum is a major input structure of layer 2 of medial entorhinal cortex, where most grid cells are found. Here we investigated parasubicular circuits of the rat by anatomical analysis combined with juxtacellular recording/labeling and tetrode recordings during spatial exploration. In tangential sections, the parasubiculum appears as a linear structure flanking the medial entorhinal cortex medio-dorsally. With a length of ~ 5.2 mm and a width of only ~ 0.3 mm (approximately one dendritic tree diameter) the parasubiculum is both one of the longest and narrowest cortical structures. Parasubicular neurons span the height of cortical layers 2 and 3 and we observed no obvious association of deep layers to this structure. The "superficial parasubiculum" (layers 2 and 1) divides into ~ 15 patches, whereas deeper parasubicular sections (layer 3) form a continuous band of neurons. Anterograde tracing experiments show that parasubicular neurons extend long 'circumcurrent' axons establishing a 'global' internal connectivity. The parasubiculum is a prime target of GABAergic and cholinergic medial septal inputs. Other input structures include the subiculum, the presubiculum and anterior thalamus. Functional analysis of identified and unidentified parasubicular neurons shows strong theta-rhythmicity of spiking, a large fraction of head-direction selectivity (50%, 34/68) and spatial responses (grid, border and irregular spatial cells, 57%, 39/68). Parasubicular output preferentially targets patches of calbindin-positive pyramidal neurons in layer 2 of medial entorhinal cortex, which might be relevant for grid cell function. These findings suggest the parasubiculum might shape entorhinal theta-rhythmicity and the (dorsoventral) integration of information across grid scales.

Significance Statement

Grid cells in medial entorhinal cortex (MEC) are crucial components of an internal navigation system of the mammalian brain. The parasubiculum is a major input structure of layer 2 of MEC, where most grid cells are found. Here we provide a functional and anatomical characterization of the parasubiculum, and show that parasubicular neurons display unique features, i.e. strong theta rhythmicity of firing, prominent head-direction selectivity, and output selectively targeted to layer 2 pyramidal cell patches of MEC. These features could contribute to shaping the temporal and spatial code of downstream grid cells in entorhinal cortex.

Introduction

The analysis of spatial discharge patterns in hippocampal and parahippocampal brain regions is a remarkable success story (Moser et al., 2008; Moser and Moser, 2013, Burgess, 2014). Extracellular recordings revealed an astonishing degree of complexity, abstractness, but also identified clear behavioral correlates of discharge patterns, such as place, head-direction, border and grid cells. Along with the exploration of discharge properties, anatomists delineated in great detail the basic circuitry of the hippocampal formation (Amaral and Witter, 1989; van Strien et al., 2009).

The detailed data available about certain parts of the hippocampal formation – such as dorsal CA1 in the rodent – should not blind us for gaps in our knowledge about less 'classic' hippocampal processing nodes. The parasubiculum is one such structure that lies beyond the classic tri-synaptic hippocampal loop (Andersen et al., 1971) and has been investigated relatively little. This parahippocampal region provides massive input to layer 2 of medial entorhinal cortex (van Groen and Wyss, 1990; Caballero-Bleda and Witter, 1993, 1994) and shows prominent expression of markers for cholinergic activity (Slomianka and Geneser, 1991). Early physiological analysis described a small fraction of place-responsive cells in the parasubiculum (Taube, 1995) and subsequent extracellular recordings have also identified head-direction, border and grid responses among parasubicular neurons (Cacucci et al., 2004; Boccara et al., 2010).

Both from a physiological and an anatomical perspective, the parasubiculum is somewhat difficult to study. First, the small size of the parasubiculum complicates recordings and tracer injections. Second, the parasubicular position (on the caudal edge of the parahippocampal lobe wrapping around entorhinal cortex, which goes along with a strong bending of the cortical sheet) greatly complicates the delineation of the parasubiculum. Here we aimed for a comprehensive description of parasubicular circuits by a combined anatomical and functional approach (Burgalossi et al., 2011; Tang et al., 2014a). Specifically, we were interested in how parasubicular circuits relate to pyramidal and stellate neuron microcircuits in layer 2 of medial entorhinal cortex (MEC, Ray et al., 2014; Tang et al., 2014b).

In our current analysis we investigate four issues: First, we delineate the location, shape, laminar organization and internal structure of parasubiculum. Second, we investigate the sources of parasubicular inputs, as well as the targets of parasubicular outputs. Third, we assess spatial discharge patterns of parasubicular neurons by juxtacellular recording/labeling and tetrode recordings in freely moving rats. Fourth, we assess the temporal discharge patterns of identified and unidentified parasubicular neurons, and how this might relate to anatomical connectivity.

Materials and methods

All experimental procedures were performed according to the German guidelines on animal welfare under the supervision of local ethics committees.

Brain tissue preparation

For anatomy experiments, male and female Wistar rats (150-400 g) were anesthetized by isoflurane, and then euthanized by an intraperitoneal injection of 20% urethane or sodium-pentobarbital. They were then perfused transcardially with 0.9% phosphate buffered saline solution, followed by 4% paraformaldehyde (PFA) in 0.1 M phosphate buffer (PB). After perfusion, brains were removed from the skull and postfixed in PFA overnight. They were then transferred into a 10% sucrose solution in PB and left overnight, and subsequently immersed in 30% sucrose solution for at least 24 hours for cryoprotection. The brains were embedded in Jung Tissue Freezing Medium, and subsequently mounted on the freezing microtome to obtain 20-60 μm thick sagittal sections or tangential sections (parallel to the pial surface of the medial entorhinal cortex (MEC)). Tangential sections were obtained by removing the cerebellum, visually identifying the pial surface of the MEC (Figure 1A in Ray et al., 2014) and making a cut 3mm anterior and parallel to the pial surface of the medial entorhinal cortex. The tissue was then frozen and positioned with the pial side to the block face of the microtome.

Tissue from PV-Cre mice, expressing Cre recombinase under the parvalbumin promoter (B6;129P2-Pvalbtm1(cre)Arbr/J mice, stock no 008069, Jackson, Bar Harbor, ME, USA), was prepared using similar methods, except that the sections were cut on a standard microtome (nominal thickness 100 μm, horizontal) right after overnight fixation in PFA.

Histochemistry and immunohistochemistry

Acetylcholinesterase (AChE) activity was visualized according to previously published procedures (Ray et al., 2014). After washing brain sections in a solution containing 1 ml of 0.1 M citrate buffer (pH 6.2) and 9 ml 0.9% NaCl saline solution (CS), sections were incubated with CS containing 3 mM $CuSO_4$, 0.5 m$MK_3Fe(CN)_6$, and 1.8 mM acetylthiocholine iodide for 30 min. After rinsing in PB, reaction products were visualized by incubating the sections in PB containing 0.05% 3,3'- Diaminobenzidine (DAB) and 0.03% nickel ammonium sulfate. Immunohistochemical stainings were performed according to standard procedures. Briefly, brain sections were pre-incubated in a blocking solution containing 0.1 M PBS, 2% Bovine Serum Albumin (BSA) and 0.5% Triton X-100 (PBS-X) for an hour at room temperature (RT). Following this, primary antibodies were diluted in a solution containing PBS-X and 1% BSA. We used primary antibodies against the calcium binding protein Calbindin (1:5000), the DNA binding neuron specific protein NeuN (1:1000) and, for the mice, against green fluorescent protein (GFP). Incubations with primary antibodies were allowed to proceed for at least 24 hours under mild shaking at 4°C in free-floating sections. Incubations with primary antibodies were followed by detection with secondary antibodies coupled to different fluorophores (Alexa 488 and 546). Secondary antibodies were diluted (1:500) in PBS-X and the reaction was allowed to proceed for two hours in the dark at RT. For multiple antibody labeling, antibodies

raised in different host species were used. After the staining procedure, sections were mounted on gelatin coated glass slides with Mowiol or Vectashield mounting medium. In a subset of experiments, primary antibodies were visualized by DAB staining. For this purpose, endogenous peroxidases were first blocked by incubating brain tissue sections in methanol containing 0.3% hydrogen peroxide in the dark at RT for 30 min. The subsequent immunohistochemical procedures were performed as described above, with the exception that detection of primary antibodies was performed by biotinylated secondary antibodies and the ABC detection kit. Immunoreactivity was visualized using DAB staining.

The relative density of putative parvalbuminergic fibres in PV-Cre mice in hippocampus CA1-3, presubiculum, parasubiculum, and medial entorhinal cortex was estimated by manually outlining these four areas (Paxinos & Franklin, 2012) in epifluorescence images (2.5x) from horizontal sections (estimated depth 3mm relative to Bregma) and then measuring mean fluorescence signals in each area with the ImageJ software. For comparison between brains, these values were then normalized to the mean hippocampal value in each brain (n = 3).

Anterograde and Retrograde Neuronal Labeling

Anterograde or retrograde tracer solutions containing Biotinylated Dextrane Amine (BDA) (10% w/v; 3.000 MW or 10.000 MW) were injected in juvenile rats (~150 gr) under ketamine/xylazine anesthesia. Briefly, a small craniotomy was opened above the parasubiculum/medial entorhinal cortex. Prior to injection, the parasubiculum was localized by electrophysiological recordings, based on cortical depth, characteristic signatures of the local field potential theta oscillations and neuronal spiking activity. Glass electrodes with a tip diameter of 10-20 µm, filled with BDA solution, were then lowered into the target region. Tracers were either pressure-injected (10 injections using positive pressure of 20 p.s.i., 10-15 s injection duration) or iontophoretically-injected (7s on/off current pulses of 1-5 mA for 15 min). After the injections, the pipettes were left in place for several minutes and slowly retracted. The craniotomies were closed by application of silicone and dental cement. The animals survived for 3-7 days before being transcardially perfused.

Viral injections and quantification of anterorgradely-traced axons

PV-Cre mice, expressing Cre recombinase under the parvalbumin promoter (B6;129P2-Pvalbtm1(cre)Arbr/J mice, stock no 008069, Jackson, Bar Harbor, ME, USA) were injected with AAV-Ef1a-dbf-hChR2(H134R)-EYFP-WPRE (serotype 1/2) roughly 6 weeks prior to perfusion. The medial septum was targeted under stereotaxic guidance: starting from the pial surface at 1 mm anterior, 0.7 mm right lateral to Bregma, a 34-gauge NanoFil™ needle (WPI, Berlin, Germany) was advanced at an angle of 10° in the coronal plane for 4200 and 4600 µm, where we injected 1 µl each (100 nl/s), waiting 5 minutes after each injection before moving the needle. The AAV virus was generously provided to us by Susanne Schoch (University of Bonn).

Fluorescence signals were normalized to dentate gyrus intensity levels and quantified. Briefly, regions of interests from horizontal sections (at a depth of ~ 3.5 mm ventral to Bregma (Paxinos

& Franklin, 2012) were manually outlined and the mean fluorescence intensity for each area quantified using the ImageJ software (n = 3 mice).

Juxtacellular recordings

Juxtacellular recordings and tetrode recordings in freely moving animals were obtained in male Wistar and Long-Evans rats (150-250 g). Experimental procedures were performed, as recently described (Tang et al., 2014a; Tang et al., 2014b, Tang et al., 2015). Briefly, rats are maintained in a 12-h light/dark phase and were recorded in the dark phase. Glass pipettes with resistance 4-6 MΩ were filled with extracellular (Ringer) solution containing (in mM) NaCl 135, KCl 5.4, HEPES 5, $CaCl_2$ 1.8, and $MgCl_2$ 1 (pH = 7.2) and Neurobiotin (1-2%). Animal implantations were performed, as previously described (Tang et al., 2014a). In order to target the parasubiculum, a plastic ring was placed 0.2-0.5 mm anterior to the transverse sinus and 4.0-4.5 mm lateral to the midline. After implantation, rats were allowed to recover from the surgery and were habituated to head fixation for 3-5 days. Rats were trained in the experimental arena (70 x 70 cm or 1 x 1 m square black box, with a white cue card on the wall) for 3-7 days Juxtacellular recordings and labeling were essentially performed as previously described (Tang et al, 2014a; Pinault, 1996). Unidentified recordings in parasubiculum were either lost before the labeling could be attempted, or the recorded neurons could not be unequivocally identified; but either pipette tracks or dendritic processes were found in the parasubiculum. After the experiment, the animals were euthanized with an overdose of ketamine, urethane or sodium-pentobarbital, and perfused transcardially with 0.1 M PB followed by 4% paraformaldehyde solution, shortly after the labeling protocol. The juxtacellular signals were amplified by the ELC-03XS amplifier (NPI Electronics) and sampled at 20 kHz by a data-acquisition interface under the control of PatchMaster 2.20 software (HEKA). The animal's location and head-direction was automatically tracked at 25 Hz by the Neuralynx video-tracking system and two head-mounted LEDs. MEC data for comparison have been published in previous papers (Ray et al., 2014; Tang et al., 2014b; Tang et al., 2015). One head-direction cell recorded and identified in the parasubiculum has been shown in a previous paper (Tang et al., 2014a).

Tetrode recordings

Tetrode recordings from parasubiculum were essentially performed as recently described (Tang et al., 2014b; Tang et al., 2015). Tetrodes were turned from 12.5 μm diameter nichrome wire (California Fine Wire Company) and gold plated to ~250 kΩ impedance. Spiking activity and local field potential were recorded at 32 kHz (Neuralynx; Digital Lynx). The local field potential was recorded from the same tetrode as single units, and referenced to a superficial silent neocortical tetrode or to the rat ground. All recordings were performed following behavioral training, as specified above for juxtacellular procedures. The animal's location and head direction was automatically tracked at 25 Hz by video tracking and head-mounted LEDs, as described above. After recordings, tetrodes were retracted from the parahippocampal areas, and multiple lesions were performed at distinct sites along the individual tetrode tracks, thereby allowing unequivocal assignment of the different tetrode tracks. Following perfusion, brains were sectioned tangentially and recording sites assigned by histology. Spikes were pre-clustered using KlustaKwik (K.D. Harris, Rutgers University) and manually using MClust

(A.D. Redish, University of Minnesota). Cluster quality was assessed by spike shape, ISI-histogram, L-ratio and isolation distance.

Neurobiotin labeling and calbindin immunohistochemistry

For histological analysis of juxtacellularly-labeled neurons, Neurobiotin was visualized with streptavidin conjugated to Alexa 546 (1:1000). Subsequently, immunohistochemistry for Calbindin was performed, as previously described (Ray et al., 2014), and visualized with Alexa Fluor 488. After fluorescence images were acquired, the Neurobiotin staining was converted into a dark DAB reaction product. Neuronal morphologies were reconstructed by computer-assisted manual reconstructions (Neurolucida).

Analysis of theta rhythmicity

Theta rhythmicity of spiking discharge was determined from the Fast Fourier Transform–based power spectrum of the spike-train autocorrelation functions of the neurons, binned at 10 ms. To measure modulation strength in the theta band (4-12 Hz), a theta power was computed, defined as the average power within 1 Hz of the maximum of the autocorrelation function in the theta rhythm (4-12 Hz). This is referred to in the paper as theta rhythmicity. Only neurons with mean firing rate > 0.5 Hz were included in the theta analysis. Statistical significance between groups was assessed by two-tailed Mann-Whitney non-parametric test with 95th confidence intervals.

Analysis of theta locking

For all neurons, we calculated the locking to theta-phase based on spiking discharge in relation to theta rhythm in the local field potential. The local field potential was zero-phase band-pass filtered (4-12 Hz) and a Hilbert transform was used to determine the instantaneous phase of the theta wave. In line with previous studies (Mizuseki et al., 2009), the theta-phase locking strength, S, and the preferred phase angle, φ, were defined as the modulus and argument of the Rayleigh average vector of the theta phase for all spikes. The Theta-phase locking strength value can vary between 0 (uniform distribution of spikes over the theta cycle) and 1 (all spikes have the same theta-phase). Only spikes during running (speed cutoff = 1 cm/s for juxtacellular signals, 5 cm/s for tetrode recordings) were included in the analysis. Only neurons with mean firing rate ≥ 0.5 Hz were included in the analysis. For comparison to MEC L2 data, both the analysis procedures and the juxtacellular data set correspond to our recent publications (Ray et al., 2014; Tang et al., 2014b; Tang et al., 2015).

Analysis of Spatial Modulation

The position of the rat was defined as the midpoint between two head-mounted LEDs. A running speed threshold (see above) was applied for isolating periods of rest from active movement. Color-coded firing maps were plotted. For these, space was discretized into pixels of 2.5 cm x 2.5 cm, for which the occupancy z of a given pixel x was calculated as

$$z(x) = \sum_t w(|x - x_t|)\Delta t$$

where x_t is the position of the rat at time t, Δt the inter-frame interval, and w a Gaussian smoothing kernel with σ = 5cm.
Then, the firing rate r was calculated as

$$r(x) = \frac{\sum_i w(|x - x_i|)}{z}$$

where x_i is the position of the rat when spike i was fired. The firing rate of pixels, whose occupancy z was less than 20 ms, was considered unreliable and not shown.
To determine the spatial periodicity of juxtacellularly recorded neurons, we determined spatial autocorrelations. The spatial autocorrelogram was based on Pearson's product moment correlation coefficient:

$$r(\tau_x, \tau_y) = \frac{n\sum f(x,y) f(x-\tau_x, y-\tau_y) - \sum f(x,y) \sum f(x-\tau_x, y-\tau_y)}{\sqrt{n\sum f(x,y)^2 - (\sum f(x,y))^2}\sqrt{n\sum f(x-\tau_x, y-\tau_y)^2 - (\sum f(x-\tau_x, y-\tau_y))^2}}$$

where, $r(\tau_x, \tau_y)$the autocorrelation between pixels or bins with spatial offset τ_x and τ_y. f is the image without smoothing or the firing rate map after smoothing, n is the number of overlapping pixels or bins. Autocorrelations were not estimated for lags of τ_x and τ_y, where n < 20. For spatial and head-directional analysis, both a spatial (> 50% spatial coverage) and a firing rate inclusion criterion (> 0.5 Hz) were applied. Spatial coverage was defined as the fraction of visited pixels (bins) in the arena to the total pixels.

Analysis of Spatial Information

For all neurons, we calculated the spatial information rate, I, from the spike train and rat trajectory:

$$l = \frac{1}{T}\int r(x) \log_2 \frac{r(x)}{\bar{r}} o(x) dx$$

where $r(x)$ and $o(x)$ are the firing rate and occupancy as a function of a given pixel x in the rate map. $\bar{r}$ is the overall mean firing rate of the cell and T is the total duration of a recording session (Skaggs et al., 1993). A cell was determined to have a significant amount of spatial information, if the observed spatial information rate exceeded the 95th percentile of a distribution of values of I obtained by circular shuffling. Shuffling was performed by a circular time-shift of the

recorded spike train relative to the rat trajectory by a random time $t' \in]0, T[$ for 1000 permutations (von Heimendahl et al., 2012; Bjerknes et al., 2014).

Analysis of Border Cells

To determine the modulation of a cell firing along a border, we determined border scores (Solstad et al., 2008). Border fields were identified from a collection of neighboring pixels having a firing rate higher than 0.3 times the maximum firing rate and covering an area of at least 100 cm (Sargolini et al., 2006). The coverage (Cm) along a wall was defined as the maximum length of a putative border field parallel to a boundary, divided by the length of the boundary. The mean firing distance (Dm) of a field was defined as the sum of the square of its distance from the boundary, weighted by the firing rate (Solstad et al., 2008). The distance from a boundary was defined as the exponential of the square of the distance in pixels from the closest boundary, normalized by half the length of the boundary. Border scores were defined as the maximum difference between Cm and Dm, divided by their sum, and ranged from -1 to +1.

Analysis of Grid Cells

Analysis of Gridness. Grid scores were calculated, as previously described (Barry et al., 2012), by taking a circular sample of the autocorrelogram, centered on, but excluding the central peak. The Pearson correlation of this circle with its rotation for 60 degrees and 120 degrees was obtained (on peak rotations) and also for rotations of 30 degrees, 90 degrees and 150 degrees (off peak rotations). Gridness was defined as the minimum difference between the on-peak rotations and off-peak rotations. To determine the grid scores, gridness was evaluated for multiple circular samples surrounding the center of the autocorrelogram with circle radii increasing in unitary steps from a minimum of 10 pixels more than the width of the radius of the central peak to the shortest edge of the autocorrelogram. The radius of the central peak was defined as the distance from the central peak to its nearest local minima in the spatial autocorrelogram. The radius of the inner circle was increased in unitary steps from the radius of the central peak to 10 pixels less than the optimal outer radius. The grid score was defined as the best score from these successive samples. Grid scores reflect both the hexagonality in a spatial field and also the regularity of the hexagon. To disentangle the effect of regularity from this index, and consider only hexagonality, we transformed the elliptically distorted hexagon into a regular hexagon and computed the grid scores (Barry et al., 2012). A linear affine transformation was applied to the elliptically distorted hexagon, to stretch it along its minor axis, until it lay on a circle, with the diameter equal to the major axis of the elliptical hexagon. The grid scores were computed on this transformed regular hexagon (Barry et al., 2012).

Analysis of head directionality

Head-direction tuning was measured as the eccentricity of the circular distribution of firing rates. For this, firing rate was binned as a function of head-direction (n = 36 bins). A cell was said to have a significant head-direction tuning, if the length of the average vector exceeded the 95th percentile of a distribution of average vector lengths calculated from shuffled data and

had a Rayleigh vector length > 0.3. Data was shuffled by applying a random circular time-shift to the recorded spike train for 1000 permutations.

Classification of cells into functional categories

Cells were classified as head-direction cells, grid cells, conjunctive cells, border cells, spatially irregular cells and non-spatially modulated cells, based on their grid score, border score, spatial information and significance of head directionality according to the following criteria:

-Head-direction cells: Rayleigh vector length > 0.3 & significant head-direction tuning (Boccara et al., 2010)
-Grid cells: Grid score > 0.3 & significant spatial information.
-Border cells: Border score > 0.5 & significant spatial information (Solstad et al., 2008), or those who passed border test (Lever et al., 2009).
-Spatially irregular cells: significant spatial information (Bjerknes et al., 2014), while not passing Grid score or Border score criteria.
-Non-spatially modulated cell: no significant spatial information.

Results

Geometry of the parasubiculum

In our initial analysis we sought to determine the general organization of the parasubiculum. Tangential sections (parallel to the pial surface of the MEC, see Methods) of the cortical sheet stained for acetylcholine esterase activity (Figure 1A, left) or calbindin immunoreactivity (Figure 1A, right) provide a particularly clear overview of the spatial extent of the parasubiculum. Consistent with findings from previous stud–ies (Geneser, 1986; Slomianka and Geneser, 1991), we find that the parasubiculum shows prominent acetylcholine esterase activity (Figure 1A, left). The parasubiculum can also be identified by an absence of calbindin immunoreactivity (Figure 1A, left; Fujise et al., 1995; Boccara et al., 2010). Further subdivisions of the parasubiculum have been suggested (Blackstad, 1956). Our data refer to the calbindin free area surrounding the MEC outlined in Figure 1A left and highlighted in light-blue in Figure 1B (possibly related to 'parasubiculum b' in the terminology of Blackstad, 1956). Laterally contiguous to the parasubiculum one observes a thin strip of cortex containing numerous calbindin-positive neurons (Figure 1A right, Figure 1B red 'calbindin stripe').

As shown in Figure 1A-B, and quantified in Figure 1C, the parasubiculum forms a fairly narrow (310 ± 83 μm width, N = 10), but very elongated (5.190 ± 0.485 mm length, N = 10) continuous curved stripe, which flanks the medial entorhinal cortex from its medial to dorso-lateral side. The lateral part of the parasubiculum, dorsal to the medial entorhinal cortex, is narrower than the medial part. This may explain why this part of the parasubiculum has not been classified as such in most previous studies (Boccara et al., 2010; Ding, 2013). Other histological markers, such as cytochrome-oxidase activity, or soma morphologies, as visualized from Nissl stains (Burgalossi et al., 2011) also delineated the parasubiculum in the same way as shown in Figure 1 (not shown). Similarly, parasagittal sectioning angles delineate the same outlines of the parasubiculum. We conclude that the parasubiculum has a linear structure with a narrow width.

We also investigated the laminar structure of the parasubiculum. Consistent with our previous conclusions (Burgalossi et al., 2011), we did not find direct evidence for a clear association of deep layers with the parasubiculum. For example, following tracer injections in the superficial parasubicular layers, we did not observe back-labeled neurons in the adjacent deep layers, even when we observed back-labeled neurons as distant as the subiculum (data not shown). Hence, we speculate that deep layers close to the parasubiculum might not be part of this structure but could rather be associated to the neighboring medial entorhinal cortex or the presubiculum (Mulders et al., 1997).

Internal structure of the parasubiculum

Consistent with our previous observations (Burgalossi et al., 2011), we found the superficial parts of the parasubiculum (corresponding to layers 1 and 2) can be divided into ~15 large patches with a diameter around 500 μm each. These patches can be revealed in superficial tangential sections (Figure 1D, left) by parvalbumin (PV)-immunoreactivity and by cell density

visualized by NeuN immunoreactivity (Figure 1D, right). However, the deeper parts of the parasubiculum (corresponding to layer 3) were not obviously divided into patches (Figure 1D).

Injections of the anterograde tracer Biotinylated Dextrane Amine (BDA, 3000 MW) showed that parasubicular neurons extend long axons throughout the full length of the parasubiculum (Figure 1E), consistent with previous evidence from single-cell microcircuits (Burgalossi et al., 2011). In the latter work, these axons were termed "circumcurrent", as they appeared to inter-connect parasubicular patches. As a consequence of this internal connectivity, a single tracer injection could label the full extent of the parasubiculum (Figure 1F). This is a remarkable feature of the parasubiculum not seen in the medial entorhinal cortex. Thus, analysis of the internal structure of parasubiculum indicates both modularity and global connectivity.

Inputs to the parasubiculum

Of particular interest for hippocampal function are the inputs from the medial septum, which are of critical importance to grid cell activity (Brandon et al., 2011; Koenig et al., 2011). We first sought to determine the patterns of GABAergic inputs from the medial septum, which are thought to play a critical role in theta-rhythm generation (Mitchell et al., 1982; Buzsáki, 2002; Hangya et al., 2009; Brandon et al., 2011; Koenig et al., 2011). To this end, we performed viral injections in the medial septum in PV-Cre mice (see Methods), and expressed GFP selectively in GABAergic septal neurons (Figure 2A,B). As shown in Figure 2A, the parasubiculum is an area within the hippocampal formation, which receives a comparatively dense innervation from GABAergic medial septal neurons (as quantified by normalized fluorescence levels, Mean values (n=3), PaS = 1.5 ± 0.23, MEC = 1.0 ± 0.05, CA1-3 = 1.2 ± 0.06, PreS = 1.0 ± 0.04. Figure 2C). As we already noted earlier, there is also a prominent expression of cholinergic activity markers (Figure 1A and Figure 2D) in line with in vitro work showing robust response of parasubicular neurons to muscarinic activation (Glasgow and Chapman, 2013). Taken together, these data point towards a strong medial septal drive to parasubicular neurons, likely contributing to strong theta rhythmicity in the parasubiculum (Burgalossi et al., 2011; see below).

By retrograde-tracer injections, we also identified parasubiculum-projecting neurons in the anterior thalamus, subiculum and presubiculum. The findings are consistent with the earlier conclusions of previous authors (Köhler, 1985; van Groen and Wyss, 1992; Honda and Ishizuka, 2004) and are therefore not shown.

Outputs from the parasubiculum

Previous work showed that the parasubicular axons innervate layer 2 of the medial entorhinal cortex (van Groen and Wyss, 1990; Caballero-Bleda and Witter, 1993, 1994; but see Canto et al., 2012). Recent work showed that principal neurons in layer 2 of medial entorhinal cortex segregate into stellate and pyramidal cell subnetworks, which can be differentiated by the calbindin immunoreactivity of the pyramidal neurons (Varga et al., 2010). Layer 2 pyramidal

neurons are arranged in a hexagonal grid, show strong theta-rhythmic discharges (Ray et al., 2014) and might preferentially contribute to the grid cell population (Tang et al. 2014b; but see Sun et al., 2015). To determine if parasubicular inputs target a specific subpopulation of neurons in layer 2 of medial entorhinal cortex, we performed fine scale injections of anterograde tracers in the dorsal parasubiculum, combined with visualization of calbindin patterns (Figure 3). As shown in Figure 3, tangential sections through layer 2 with calbindin immuno-staining revealed a regular organization of patches of pyramidal neurons (Ray et al., 2014). Surprisingly, these patches were selectively innervated by parasubicular afferents (Figure 3A-B), which targeted the center of patches (Figure 3C). This indicates that parasubicular axons may preferentially target layer 2 pyramidal neurons of medial entorhinal cortex, which may in turn contribute to the strong theta rhythmicity in these neurons (Ray et al., 2014.)

Identification of functional cell types in the parasubiculum

In comparison to its major target structure - the entorhinal cortex - limited information is currently available about the spatial discharge properties in the parasubiculum (Taube, 1995; Cacucci et al., 2004; Boccara et al., 2010). To address this issue, we juxtacellularly recorded and labeled neurons (n = 16) in the parasubiculum of freely moving rats trained to explore 2D environments (Tang et al., 2014a) A representative recording from an identified parasubicular neuron is shown in Figure 4A. This neuron had divergent sideward-directed dendrites (seen from the top), was situated in the dorsal part of the parasubiculum (Figure 4A, right) and discharged in spike bursts strongly entrained by the theta rhythm (Figure 4B). Theta rhythmicity of spiking was revealed by the spiking autocorrelogram (Figure 4C, left) and the spikes were also strongly locked to local theta oscillations (Figure 4C, right). The neuron discharged along the border of the enclosure (Figure 4D, left), a defining feature of border activity (Solstad et al., 2008) and showed head-direction selectivity (Figure 4D, right).

In line with previous observations in linear mazes (Burgalossi et al., 2011), many juxtacellularly-recorded neurons showed head-direction selectivity. A representative neuron is shown in Figure 4E. This neuron was situated in the medial part of the parasubiculum (Figure 4E, right) and also discharged in bursts with strong theta rhythmicity (Figure 4F, right). The spiking autocorrelogram also revealed a strong theta rhythmicity (Figure 4G, left), and the spikes were strongly locked to local theta oscillations (Figure 4G, right). Spikes were fired throughout the enclosure without obvious spatial modulation (Figure 4H, left), but showed a clear head-direction preference (Figure 4H, right).

Spatial firing properties of parasubicular neurons

By combining juxtacellularly-recorded and identified parasubicular neurons with verified recording sites of single-cell and tetrode recordings (see Methods), we could provide a more comprehensive characterization of functional cell types in parasubiculum. In line with previous work (Boccara et al., 2010), we observed border discharges (9%, 6/68, Figure 4D & 5A), grid discharges (9%, 6/68, Figure 5B), strong head-direction selectivity (50%, 34/68, Figure 4H &

5C) and a substantial proportion of irregular spatial discharges (40%, 27/68) (cells not shown). This last group contains cells with significant spatial information content (Skaggs et al., 1993; see Methods) but that do not meet grid or border inclusion criteria (see Methods).

Next, we compared the spatial discharge properties of the parasubiculum to those of identified and putative MEC Layer 2 pyramidal and stellate neurons (Tang et al., 2014b) as well as neurons recorded in MEC Layer 3 (Tang et al. 2015). We found significantly more spatial responses in the parasubicular neurons than in the other cell types (Figure 6A, all $p < 0.01$, χ^2-test with Bonferroni-Holm correction: 39/68 PaS, $\chi^2 = 7.91$ vs. 35/99 Pyr, $\chi^2 = 12.4$ vs. 28/94 Stel, $\chi^2 = 11.1$ vs. 19/66 L3). We also observed a strong head directionality of parasubicular neurons, in line with previous observations from linear track recordings (Burgalossi et al., 2011). At the population level, the median head-direction vector of all parasubicular neurons was 0.31, much larger than in MEC Layer 2 (0.12 in Pyramidals; 0.14 in Stellates) and Layer 3 (0.09 in Layer 3 cells; Figure 6B, all $p < 0.001$, Mann-Whitney U-tests with Bonferroni-Holm correction: z(Pyr) = 5.54, z(Stel) = 5.79, z(L3) = 7.01). Similarly, the proportion of neurons classified as head-direction cells was also considerably larger than in MEC Layer 2 and Layer 3 (Figure 6C, all $p < 0.001$, χ^2-test with Bonferroni-Holm correction: χ^2(Pyr)= 17.7, χ^2(Stel) = 28.8, χ^2(L3) = 30.7)

Theta modulation of parasubicular neurons

As shown in representative neurons (Figures 4 and 5), the large majority of parasubicular neurons showed strong theta-rythmicity, as revealed by autocorrelation of spike trains (Figure 7A, see also Tang et al., 2014b and Tang et al., 2015). Parasubicular neurons were also strongly locked to local field potential theta oscillations, which is known to be in phase with MEC theta (Glasgow and Chapman, 2007; Figure 7B). On average, theta rhythmicity was stronger in parasubicular neurons than in identified layer 2 stellates and layer 3 neurons (Both $p < 0.01$, Mann-Whitney U-test, z(Stel) = 3.19, z(L3) = 8.39, Figure 7C; MEC cells from Tang et al., 2014b and Tang et al., 2015). Identified parasubicular neurons tended to have a higher theta rhythmicity than identified layer 2 neurons (juxtacellularly recorded cells, $p = 0.0116$, Mann-Whitney U-test), but this difference did not reach statistical significance when tetrode-units were included in the sample of parasubicular neurons. Theta-phase locking strength (mean (circular) vector length, see Methods) of parasubicular neurons was similar to that of MEC layer 2 pyramidal neurons ($p > 0.05$, Mann-Whitney U-test: $z = -0.89$, Figure 7D), and significantly stronger than that of layer 2 stellates and layer 3 neurons (Both $p<0.001$, Mann-Whitney U-test: z(Stel) = 3.73, z(L3) = 7.83, Figure 7D; MEC cells from Tang et al., 2014b and Tang et al., 2015).

Notably, at the population level parasubicular and MEC layer 2 pyramidal and stellate neurons showed distinct preferred theta phases (all $p < 0.05$, Rayleigh test for non-uniformity: z(PaS) = 29.5, z(Pyr) = 4.07, z(Stel) = 3.36, Figure 7E; MEC cells from Tang et al., 2014b and Tang et al., 2015). When we compared the preferred phase of identified MEC Layer 2 pyramids and identified parasubicular neurons, we found that the parasubicular neurons preferred an earlier theta phase (slightly before the trough, Figure 7F left, $p = 0.048$, Watson-Williams test for equal circular means: $F = 4.34$). When we included all non-identified juxta and tetrode

recordings of parasubicular and putative MEC Layer 2 pyramidal neurons, this difference remained statistically significant (Figure 7F right, 155° vs. 174° p = 0.0000085, Watson-Williams test for equal circular means: F = 22.7). Since tetrode recordings of MEC Layer 2 were assigned their putative cell identity based on their temporal spiking properties, we wondered whether this might have biased the comparison of preferred theta phase. However, two indications suggest that this was not the case: *(i)* in the identified dataset, we had not excluded any MEC Layer 2 neurons which locked before the trough (see Tang et al. 2014b). *(ii)* Even when we applied the same classifier to all parasubicular neurons and only compared MEC Layer 2 putative pyramids to parasubicular neurons, which would have been classified as putative pyramids, the difference in preferred phase was still trending towards significance (p = 0.076, Watson-Williams test for equal circular means: F = 3.21).

The strong theta-phase locking strength and theta rhythmicity of both parasubicular neurons and layer 2 pyramidal (but not stellate) neurons, as well as the preference of parasubicular neurons to fire at a slightly earlier theta phase (~19° phase angle, i.e. ~7 ms, assuming an 8 Hz theta rhythm) than layer 2 pyramidal neurons, is consistent with the idea that parasubicular neurons might impose a feed-forward theta-modulated drive onto layer 2 pyramidal neurons.

Discussion

Unique features of the parasubiculum

The parasubiculum is distinct from other parahippocampal structures. The elongated shape of the parasubiculum and an almost linear arrangement of neurons differs from other (para-) hippocampal structures such as dentate gyrus, CA3, CA2, CA1, subiculum, presubiculum and medial or lateral entorhinal cortex (Amaral and Witter, 1989; Cenquizca and Swanson, 2007). Further, absence of directly-associated deep layers distinguishes the parasubiculum from the surrounding entorhinal, retrosplenial and presubicular cortices. The 'circumcurrent' axons (as defined by Burgalossi et al., 2011; Figure 1E-F) that traverse the parasubiculum and could thus establish a 'global' connectivity are also a unique feature of parasubicular anatomy. Furthermore, the parasubiculum is a preferred target of medial septal inputs and provides the major input to pyramidal neuron patches in layer 2 of medial entorhinal cortex. We observed a larger fraction of spatial and head-directional responses in the parasubiculum than in the adjacent medial entorhinal cortex (Solstad et al., 2008; Tang et al., 2014b).

Comparison to previous work

Our anatomical analysis agrees with earlier descriptions that large parts of the parasubiculum are situated between the medial entorhinal cortex and the presubiculum (Amaral and Witter, 1989; Cenquizca and Swanson, 2007). We provide evidence that the parasubiculum extends further laterally than previously thought (Van Strien et al., 2009, Boccara et al., 2010) and that this structure might lack direct association with deep layers. The idea that the parasubiculum extends dorso-laterally from the medial entorhinal cortex is based on three observations: *(i)* staining of cholinergic markers, calbindin immunoreactivity or cytochrome oxidase activity all delineate a continuous band, which extends dorso-laterally; similarly, both *(ii)* the modular structure of the 'large patches' and *(iii)* 'circumcurrent' axons extend as a continuous dorso-lateral band (Figure 1; see Burgalossi et al., 2011). Our conclusion that the parasubiculum extends dorso-laterally is strongly supported by recent high resolution mapping of gene expression in parahippocampal cortices (Ramsden et al., 2015). The authors not only observed that this dorsolateral part is different from medial entorhinal cortex, but also showed that it shares patterns of gene expression with the 'classical' medial parasubiculum (Ramsden et al., 2015). The extent to which deep layers were assigned to the parasubiculum varies in the literature. While some studies assigned deep layers to the parasubiculum (Funahashi and Stewart, 1997; Glasgow and Chapman, 2007; Boccara et al., 2010), other work found it difficult to assign adjacent deep layers to either the presubiculum or the parasubiculum based solely on cytoarchitectonic criteria (Mulders et al., 1997). Our assessment that these deep layer neurons should not be viewed as part of the parasubiculum is based on three observations: *(i)* the shape of dorsal part of the parasubiculum, as revealed by cholinergic markers, calbindin immunoreactivity or cytochrome oxidase activity, delineates only a "superficial-layer structure" encompassing layer 1-3 (Burgalossi et al., 2011); *(ii)* we did not observe axons from the superficial parasubiculum into adjacent deep cortical layers; *(iii)* we did not observe axons from the adjacent deep cortical layers into the superficial parasubiculum. The idea that large

parts of the parasubiculum lack deep layers is again supported by the gene expression analysis of Ramsden et al., 2015.

Our results agree with previous extracellular recording data that also revealed the presence of spatially-modulated neurons in the parasubiculum (Taube, 1995; Cacucci et al., 2004; Boccara et al., 2010; Burgalossi et al., 2011; Cacucci et al., 2004). The present data are also consistent with the study of Boccara et al., 2010, where the authors described grid, border and head-direction responses in the parasubiculum. Notably, the strong head-direction tuning in the parasubiculum is also consistent with previous (Fyhn et al., 2008; Wills et al., 2010) and more recent work (Giocomo et al., 2014), where sharply-tuned head-direction neurons were recorded "near" the dorsalmost border medial entorhinal cortex – hence compatible with a parasubicular origin of these signals (Figure 1; Burgalossi et al., 2011). Extracellular recordings have also identified both theta-rhythmic and non-theta-rhythmic border cells in this dorsalmost region of MEC (Solstad et al., 2008), where the parasubiculum extends in a narrow stripe above MEC (Figure 1A). We found that parasubicular border cells lock strongly to the theta rhythm, while border cells in MEC layer 2 show only weak entrainment by theta oscillations (Tang et al., 2014b). Our results show a substantial proportion of spatially irregular cells, in line with previous work (Krupic et al., 2012), which also showed a larger percentage of non-grid, spatially modulated cells in the parasubiculum compared to adjacent MEC. Spatially irregular cells could provide sufficient spatial information for coding the animal's position in space (Zhang et al., 1998; Zhang and Sejnowski, 1999).

Parasubicular discharge properties mirror those of its input structures

Parasubicular response properties match well with the properties of its inputs. Parasubicular head-direction selectivity is in line with its inputs from anterior thalamus and presubiculum (Taube, 2007). The border responses observed here are in line with subicular inputs, as numerous boundary-vector cells have been observed there (Lever et al., 2009). A prominent aspect of parasubicular activity is the strong theta-phase locking and theta rhythmicity of spike discharges. Large membrane-potential theta oscillations have also been recorded from parasubicular neurons in awake animals (Domnisoru et al., 2013). Such strong entrainment may result from the massive septal GABAergic innervation (Figure 3A,B), since GABAergic neurons in the medial septum are known to be a key theta pacemaker (Buzsáki, 2002; Hangya et al., 2009; Brandon et al., 2011; Koenig et al., 2011). Cholinergic innervation may also drive parasubicular neurons to depolarized states promoting theta oscillations (Glasgow and Chapman 2007; Glasgow and Chapman, 2013).

Does the parasubiculum provide input to the grid system?

Our data suggest a relationship between the parasubiculum and layer 2 of medial entorhinal cortex grid cells (Sargolini et al., 2006; Boccara et al., 2010). Grid cells in the medial entorhinal cortex show strong theta rhythmicity of spiking (Boccara et al., 2010). It is therefore most interesting that the strongly theta-rhythmic parasubicular neurons project selectively into layer 2 pyramidal cell patches, where neurons show strong entrainment by the theta rhythm (Ray et

al., 2014) and where most grid cells might be located (Tang et al., 2014b). The discharge timing is consistent with an activation/entrainment of layer 2 pyramidal neurons by parasubicular inputs. Parasubicular neurons discharge on average at an earlier theta phase (~19° phase angle, i.e. ~7 ms) than layer 2 pyramidal neurons (Figure 7E,F). The parasubicular input to layer 2 pyramidal neurons is also remarkable, in light of the sparse excitatory connectivity within layer 2 of medial entorhinal cortex (Couey et al., 2013; Pastoll et al., 2013). Parasubicular inputs could be important for three aspects: *(i)* for imposing theta rhythmicity on grid responses, and possibly also contributing to their temporal spiking dynamics (Hafting et al., 2008, Mizuseki et al., 2009, Ray et al., 2014, Tang et al., 2014b); *(ii)* parasubicular head-directional responses could be causally related to downstream grid activity in layer 2 of MEC. Indeed, grid cells have been shown to receive head-directional inputs and disruptions of head-direction signals also impaired grid cell firing (Bonnevie et al., 2013; Winter et al., 2015). The parasubiculum might be the source of this input, given the large-fraction of head-direction cells and the selective output to MEC layer 2 (Figure 3); (*iii*) parasubicular border activity could be needed for anchoring entorhinal layer 2 grids to environmental boundaries (Hardcastle et al., 2015). Interestingly, direct projections from border to grid cells have been recently postulated, which might be responsible for determining grid orientation, ellipticity and stability (Krupic et al., 2015; Stensola et al., 2015; Hardcastle et al., 2015; Kruge et al., 2014). The parasubiculum might be one source of border signals into the entorhinal grid system.

Functional considerations

What does the parasubiculum do? It seems likely that the parasubiculum plays a role in determining spike-timing of downstream neurons relative to theta oscillations. The massive internal connectivity of the parasubiculum by circumcurrent axons is rather unique. These axons connect along the dorso-ventral axis of the parahippocampal cortex. As different spatial scales are mapped onto the dorsoventral axis of the medial entorhinal cortex (Brun et al., 2008), we wonder whether these axons ensure that those parasubicular neurons along the dorsoventral axis signaling the same positions (at different spatial scales) fire at the same time relative to the theta cycle. Another peculiar aspect of parasubicular anatomy is the lack of strong direct hippocampal connections (van Strien et al., 2009). Together with the absence of deep layers (the recipient of CA1/subicular back-projections in the medial entorhinal cortex) and a thinner layer 1, it seems that the parasubiculum is only poorly connected to the 'trisynaptic memory loop' (reciprocal connections between the parasubiculum and postrhinal cortex could however provide an indirect pathway; Agster and Burwell, 2013). We envision the parasubiculum may function more for providing online spatial information like a pointer ('where am I?') rather than for long-term storage of information ('where was I?'). This pointer hypothesis is consistent with disruption of place cell activity (Liu et al., 2004) and working memory deficits after parasubicular lesions (Kesner and Giles, 1998).

References:

Agster KL, Burwell RD (2013) Hippocampal and subicular efferents and afferents of the perirhinal, postrhinal, and entorhinal cortices of the rat. Behav Brain Res. 254:50-64.

Amaral DG, Witter MP (1989) The three-dimensional organization of the hippocampal formation: a review of anatomical data. Neuroscience 31:571–591.

Andersen P, Bliss TVP, Skrede KK, Lomo T, Olsen LI (1971) Lamellar organization of hippocampal excitatory pathways. Exp Brain Res 13:222–238.

Barry C, Ginzberg LL, O'Keefe J, Burgess N (2012) Grid cell firing patterns signal environmental novelty by expansion. Proc. Natl. Acad. Sci. USA 109: 17687-17692.

Bjerknes TL, Moser EI, Moser MB (2014) Representation of geometric borders in the developing rat. Neuron 82: 71-78.

Blackstad TW (1956) Commissural connections of the hippocampal region in the rat, with special reference to their mode of termination. J Comp Neurol 105:417–537

Boccara CN, Sargolini F, Thoresen VH, Solstad T, Witter MP, Moser EI, Moser M-B (2010) Grid cells in pre- and parasubiculum. Nat Neurosci 13:987–994.

Bonnevie T, Dunn B, Fyhn M, Hafting T, Derdikman D, Kubie JL, Roudi Y, Moser EI, Moser M-B (2013) Grid cells require excitatory drive from the hippocampus. Nat Neurosci 16:309–317.

Brandon MP, Bogaard AR, Libby CP, Connerney MA, Gupta K, Hasselmo ME (2011) Reduction of theta rhythm dissociates grid cell spatial periodicity from directional tuning. Science 332:595–599.

Brun VH, Solstad T, Kjelstrup KB, Fyhn M, Witter MP, Moser EI, Moser MB (2008) Progressive increase in grid scale from dorsal to ventral medial entorhinal cortex. Hippocampus 18:1200–1212.

Burgalossi A, Herfst L, von Heimendahl M, Förste H, Haskic K, Schmidt M, Brecht M (2011) Microcircuits of Functionally Identified Neurons in the Rat Medial Entorhinal Cortex. Neuron 70:773–786.

Burgess, N. (2014). The 2014 Nobel Prize in Physiology or Medicine: A Spatial Model for Cognitive Neuroscience. Neuron, 84(6), 1120–1125. doi:10.1016/j.neuron.2014.12.009

Buzsáki G (2002) Theta oscillations in the hippocampus. Neuron 33:325–340.

Caballero-Bleda M, Witter MP (1993) Regional and laminar organization of projections from the presubiculum and parasubiculum to the entorhinal cortex: An anterograde tracing study in the rat. J Comp Neurol 328:115–129.

Caballero-Bleda M, Witter MP (1994) Projections from the presubiculum and the parasubiculum to morphologically characterized entorhinal-hippocampal projection neurons in the rat. Exp Brain Res 101:93–108.

Cacucci F, Lever C, Wills TJ, Burgess N, O'Keefe J (2004) Theta-modulated place-by-direction cells in the hippocampal formation in the rat. J Neurosci 24:8265–8277.

Canto CB, Koganezawa N, Beed P, Moser EI, Witter MP (2012) All layers of medial entorhinal cortex receive presubicular and parasubicular inputs. J Neurosci 32:17620–17631.

Cenquizca LA, Swanson LW (2007) Spatial organization of direct hippocampal field CA1 axonal projections to the rest of the cerebral cortex. Brain Res Rev 56:1–26.

Couey JJ, Witoelar A, Zhang S-J, Zheng K, Ye J, Dunn B, Czajkowski R, Moser M-B, Moser EI, Roudi Y, Witter MP (2013) Recurrent inhibitory circuitry as a mechanism for grid formation. Nat Neurosci 16:318–324.

Ding SL (2013) Comparative anatomy of the prosubiculum, subiculum, presubiculum, postsubiculum, and parasubiculum in human, monkey, and rodent. J Comp Neurol 521:4145-62.

Domnisoru C, Kinkhabwala AA, Tank DW (2013) Membrane potential dynamics of grid cells. Nature 495, 199–204.

Fujise N, Hunziker W, Heizmann CW, Kosaka T (1995) Distribution of the calcium binding proteins, calbindin D-28K and parvalbumin, in the subicular complex of the adult mouse. Neurosci Res 22:89–107.

Funahashi M, Stewart M (1997) Presubicular and parasubicular cortical neurons of the rat: Functional separation of deep and superficial neurons in vitro. J Physiol 501:387–403.

Fyhn M, Hafting T, Witter MP, Moser EI, Moser MB (2008) Grid cells in mice. Hippocampus 18:1230-8.

Geneser FA (1986) Distribution of acetylcholinesterase in the hippocampal region of the rabbit: I. Entorhinal area, parasubiculum, and presubiculum. J Comp Neurol 254:352–368.

Giocomo LM, Stensola T, Bonnevie T, Van Cauter T, Moser MB, Moser EI (2014) Topography of head direction cells in medial entorhinal cortex. Curr Biol 24:252–262.

Glasgow SD, Chapman CA (2007) Local generation of theta-frequency EEG activity in the parasubiculum. J Neurophysiol 97:3868–3879.

Glasgow SD, Chapman CA (2013) Muscarinic depolarization of layer II neurons of the parasubiculum. PLoS One 8(3):e58901

Hafting T, Fyhn M, Bonnevie T, Moser MB, Moser EI (2008) Hippocampus-independent phase precession in entorhinal grid cells. Nature 453:1248-52.

Hangya B, Borhegyi Z, Szilágyi N, Freund TF, Varga V (2009) GABAergic neurons of the medial septum lead the hippocampal network during theta activity. J Neurosci 29:8094–8102.

Hardcastle, K., Ganguli, S., & Giocomo, L. M. (2015). Environmental Boundaries as an Error Correction Mechanism for Grid Cells. *Neuron*, *86*(3), 827–839. doi:10.1016/j.neuron.2015.03.039

Honda Y, Ishizuka N (2004) Organization of Connectivity of the Rat Presubiculum: I. Efferent Projections to the Medial Entorhinal Cortex. J Comp Neurol 473:463–484.

Kesner RP, Giles R (1998) Neural circuit analysis of spatial working memory: role of pre- and parasubiculum, medial and lateral entorhinal cortex. Hippocampus 8:416–423.

Koenig J, Linder AN, Leutgeb JK, Leutgeb S (2011) The spatial periodicity of grid cells is not sustained during reduced theta oscillations. Science 332:592–595.

Köhler C (1985) Intrinsic projections of the retrohippocampal region in the rat brain. I. The subicular complex. J Comp Neurol 236:504–522.

Kruge IU, Waaga T, Wernle T, Moser EI, Moser MB (2014) Grid Cells requiere experience with local boundaries during development. 2014 Neuroscience Meeting Planner. Washington, DC : Society for Neuroscience, 2014. Online. 94.01/SS21

Krupic J, Burgess N, O'keefe J (2012) Neural representations of location composed of spatially periodic bands. Science. 337:853-857.

Krupic J, Bauza M, Burton S, Barry C, O'Keefe J (2015) Grid cell symmetry is shaped by environmental geometry. Nature 518:232-5.

Lever C, Burton S, Jeewajee A, O'Keefe J, Burgess N (2009) Boundary vector cells in the subiculum of the hippocampal formation. J Neurosci 29:9771–9777.

Liu P, Jarrard LE, Bilkey DK (2004) Excitotoxiclesions of the pre- and parasubiculum disrupt the place fields of hyppocampal pyramidal cells. Hippocampus, 14:107-116.

Mitchell SJ, Rawlins JN, Steward O, Olton DS (1982) Medial septal area lesions disrupt theta rhythm and cholinergic staining in medial entorhinal cortex and produce impaired radial arm maze behavior in rats. J Neurosci 2:292–302.

Mizuseki K, Sirota A, Pastalkova E, Buzsáki G (2009) Theta oscillations provide temporal windows for local circuit computation in the entorhinal-hippocampal loop. Neuron 64: 267-280.

Moser EI, Kropff E, Moser M-B (2008) Place cells, grid cells, and the brain's spatial representation system. Annu Rev Neurosci 31:69–89.

Moser EI, Moser M-B (2013) Grid cells and neural coding in high-end cortices. Neuron 80:765–774.

Mulders WHAM, West MJ, Slomianka L (1997) Neuron numbers in the presubiculum, parasubiculum, and entorhinal area of the rat. J Comp Neurol 385:83–94.

Pastoll H, Solanka L, van Rossum MCW, Nolan MF (2013) Feedback Inhibition Enables Theta-Nested Gamma Oscillations and Grid Firing Fields. Neuron 77:141–154.

Paxinos G and Franklin KBJ (2012) Paxinos and Franklin's the mouse brain in stereotaxic coordinates. Academic Press.

Pinault D (1996) A novel single-cell staining procedure performed in vivo under electrophysiological control: Morpho-functional features of juxtacellularly labeled thalamic cells and other central neurons with biocytin or Neurobiotin. J Neurosci Methods 65:113–136.

Ramsden HL, Sürmeli G, McDonagh SG, Nolan MF (2015) Laminar and dorsoventral molecular organization of the medial entorhinal cortex revealed by large-scale anatomical analysis of gene expression. PLoS Computational Biology 11: e1004032.

Ray S, Naumann R, Burgalossi A, Tang Q, Schmidt H, Brecht M (2014) Grid-layout and theta-modulation of layer 2 pyramidal neurons in medial entorhinal cortex. Science 343:891–896.

Sargolini F, Fyhn M, Hafting T, McNaughton BL, Witter MP, Moser M-B, Moser EI (2006) Conjunctive representation of position, direction, and velocity in entorhinal cortex. Science 312:758–762.

Skaggs WE, McNaughton BL, Gothard KM, Markus EJ (1993) An information-theoretic approach to deciphering the hippocampal code. In: Advances in neural processing systems, vol. 5 (Hanson SJ, Cowan JD, Giles CL, eds). San Mateo: Morgan Kaufmann.

Slomianka L, Geneser FA (1991) Distribution of acetylcholinesterase in the hippocampal region of the mouse: I. Entorhinal area, parasubiculum, retrosplenial area, and presubiculum. J Comp Neurol 303:339–354.

Solstad T, Boccara CN, Kropff E, Moser M-B, Moser EI (2008) Representation of geometric borders in the entorhinal cortex. Science 322:1865–1868.

Stensola T, Stensola H, Moser M-B, Moser EI (2015) Shearing-induced asymmetry in entorhinal grid cells. Nature 518:207-212.

Sun C, Kitamura T, Yamamoto J, Martin J, Pignatelli M, Kitch LJ, Schnitzer MJ, Tonegawa S (2015) Distinct speed dependence of entorhinal island and ocean cells, including respective grid cells. Proc Natl Acad Sci U S A. 112 (30): 9466-9471.

Tang Q, Brecht M, Burgalossi A (2014a) Juxtacellular recording and morphological identification of single neurons in freely moving rats. Nat Protoc 9:2369–2381.

Tang Q, Burgalossi A, Ebbesen CL, Ray S, Naumann R, Schmidt H, Spicher D, Brecht M (2014b) Pyramidal and Stellate Cell Specificity of Grid and Border Representations in Layer 2 of Medial Entorhinal Cortex. Neuron 84:1191-1197.

Tang Q, Ebbesen CL, Sanguinetti-Scheck JI , Preston-Ferrer P , Gundlfinger A, Winterer J, Beed P, Ray S, Naumann R, Schmitz D, Brecht M, Burgalossi A (2015) Anatomical Organization and Spatiotemporal Firing Patterns of Layer 3 Neurons in the Rat Medial Entorhinal Cortex. Journal of Neuroscience, *35*(36), 12346–12354.

Taube JS (1995) Place cells recorded in the parasubiculum of freely moving rats. Hippocampus 5:569–583.

Taube JS (2007) The head direction signal: origins and sensory-motor integration. Annu Rev Neurosci 30:181–207.

Wills TJ, Cacucci F, Burgess N, O'Keefe J (2010) Development of the hippocampal cognitive map in preweanling rats. Science 328:1573-6.

Winter SS, Clark BJ, Taube JS (2015) Disruption of the head direction cell network impairs the parahippocampal grid cell signal. Science 347:870-4.

Van Groen T, Wyss JM (1990) The connections of presubiculum and parasubiculum in the rat. Brain Res 518:227–243.

Van Groen T, Wyss JM (1992) Projections from the laterodorsal nucleus of the thalamus to the limbic and visual cortices in the rat. J Comp Neurol 324:427–448.

Van Strien NM, Cappaert NLM, Witter MP (2009) The anatomy of memory: an interactive overview of the parahippocampal-hippocampal network. Nat Rev Neurosci 10:272–282.

Varga C, Lee SY, Soltesz I (2010) Target-selective GABAergic control of entorhinal cortex output. Nat Neurosci 13:822–824.

von Heimendahl M, Rao RP, Brecht M (2012) Weak and nondiscriminative responses to conspecifics in the rat hippocampus. J Neurosci 32:2129-2141.

Zhang K, Ginzburg I, McNaughton BL, Sejnowski TJ (1998) Interpreting neuronal population activity by reconstruction: unified framework with application to hippocampal place cells. J Neurophysiol 79:1017-1044.

Zhang K, Sejnowski TJ (1999) Neuronal tuning: to sharpen or broaden? Neural Comput 11:75-84.

Figures:

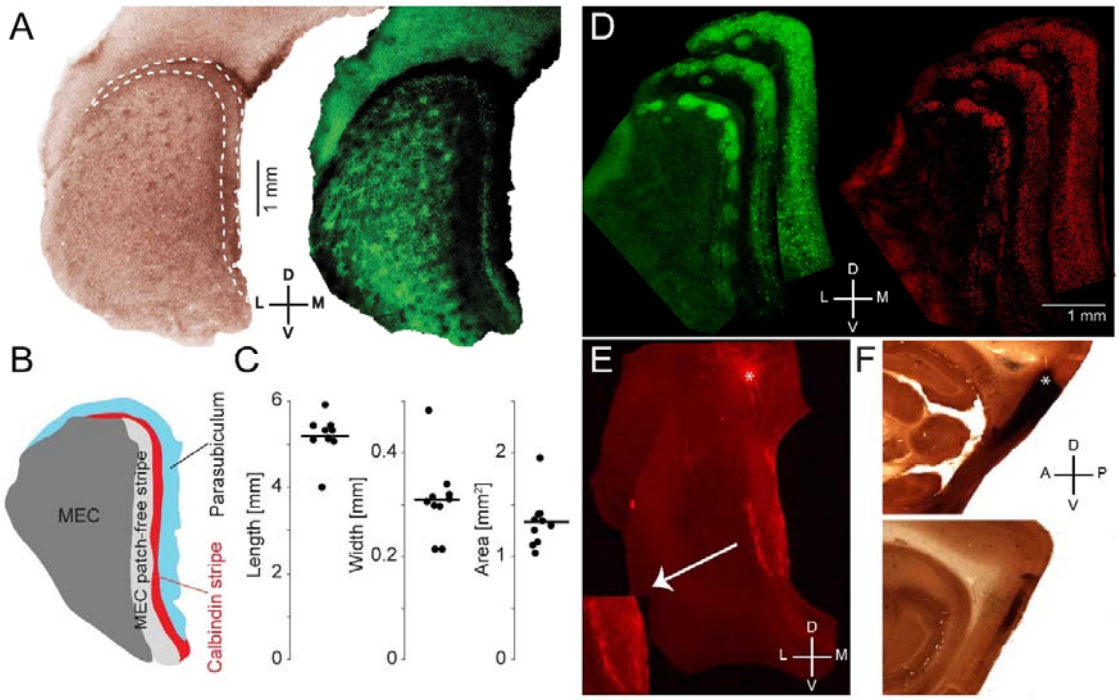

Figure 1. Shape and internal structure of the parasubiculum.

(A) Left: Tangential section stained for acetylcholinesterase activity (dark precipitate). The shape of the parasubiculum is outlined (white dashed line) coinciding with high acetylcholinesterase activity. Right: Tangential section (same section as in Figure 1A left) processed for calbindin immunoreactivity (green), the shape of the parasubiculum is negatively outlined by an absence of calbindin immunoreactivity.

(B) Schematic of the parasubiculum (light blue) and adjacent medial entorhinal cortex (MEC) subdivisions.

(C) Quantification of parasubiculum size in 10 hemispheres: Length, width and area.

(D) Tangential sections stained for parvalbumin (PV) immunoreactivity (green, left) and NeuN immunoreactivity (red, right). The parasubiculum stands out by its intense staining. Three sections are shown, the left one is most superficial (closest to the pia), middle and right are progressively deeper. Note how the patchy structure of the superficial parasubiculum is replaced by continuous cell band in deeper sections.

(E)Tangential sections of the parasubiculum showing the injection site of BDA tracer (red fluorescence) and anterogradely-traced circumcurrent axons (according to the terminology of Burgalossi et al., 2011) extending throughout the parasubiculum (see also magnified inset on the left). Injection site is marked with a white asterisk.

(F) Parasagittal sections of the parasubiculum (top), parasubiculum and MEC (bottom) after the injection of larger amounts of BDA (tracer, dark color). The tracer completely fills the parasubiculum and stains layer 2 of the MEC. Injection site is marked with a white asterisk.

(A) and (B) were modified from (Ray et al., 2014).

D = dorsal, L = lateral, M = medial, V = ventral

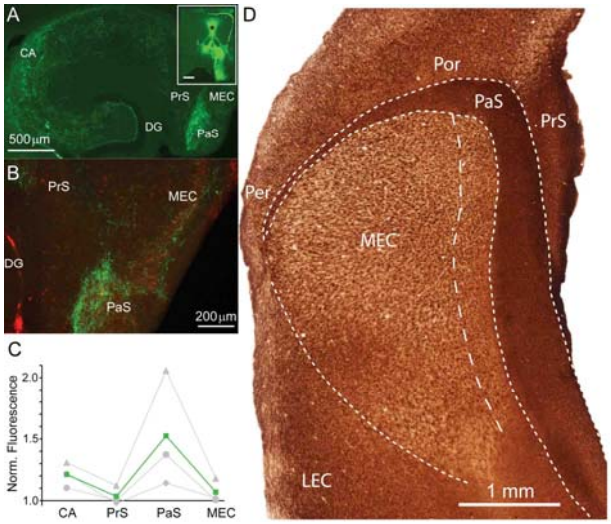

Figure 2. Parasubiculum receives GABAergic and cholinergic inputs.

(A) Horizontal sections showing that the parasubiculum contains the densest projection in the hippocampal formation of GFP-positive, putative parvalbuminergic fibers. Deriving from injection of AAV into the medial septum (inset, asterisk) of mice expressing Cre recombinase under the parvalbumin promoter. This dense projection pattern was seen in 3/3 injected mice. Note in this brain also olfactory and accessory olfactory areas were labelled unilaterally.

(B) PV immunostaining (red) marks the extent of the parasubiculum (as shown in Figure 1D Left). Note the higher density of GABAergic medial septal fibers (green) within the parasubiculum.

(C) Normalized fluorescence intensity levels relative to dentate gyrus (n = 3 mice, different grey symbols represent the different mice). Mean normalized fluorescence shown as green squares.

(D) Tangential section showing high levels of Acetylcholinesterase (AChE) in the parasubiculum.

MEC= medial entorhinal cortex, PrS= presubiculum, DG= dentate gyrus, LEC= lateral entorhinal cortex, PaS= parasubiculum, Por= postrhinal cortex, Per= perirhinal cortex, CA= cornus ammonis.

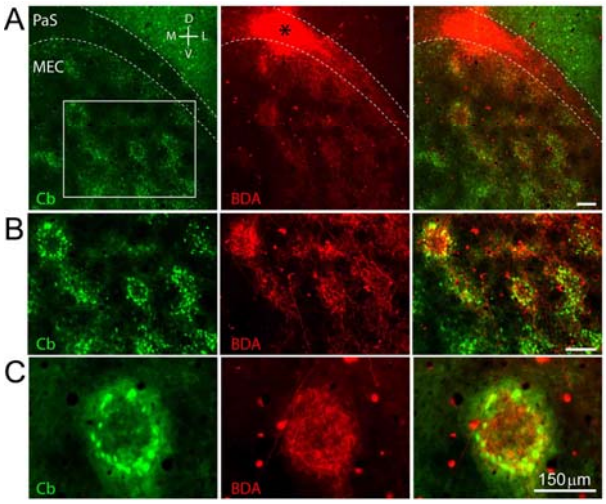

Figure 3. Parasubicular axons target layer 2 pyramidal cell patches in medial entorhinal cortex.

(A) Left, tangential section stained for calbindin (green) revealing patches of calbindin-positive pyramidal neurons. Middle, same section as left processed to reveal the tracer BDA (red). The location of the parasubicular injection site is marked with a black star. Right, overlay. Scale bar, 150 microns

(B) Same as (A) but higher magnification. Scale bar, 150 microns

(C) High magnification view of a single patch. D = dorsal, L = lateral, M = medial, V = ventral.

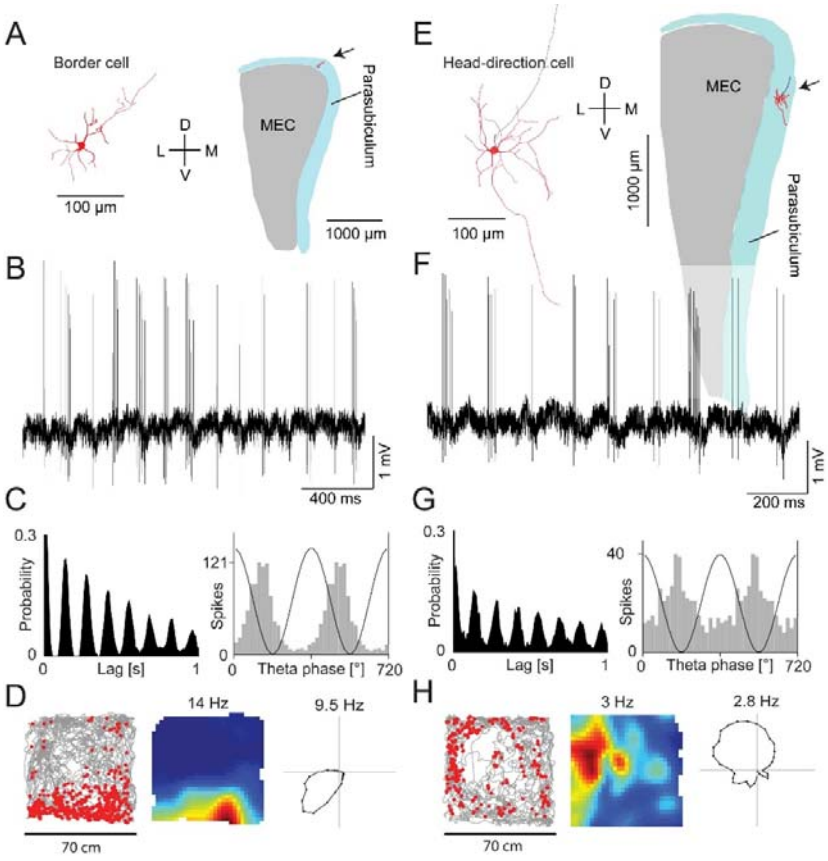

Figure 4. Physiology of identified parasubicular neurons.

(A) Left: Reconstruction of a border cell juxtacellularly-recorded and identified in a rat exploring a 2D environment (70 x 70 cm). Reconstructed dendrites and axon shown in red and blue, respectively. Scale bar, 100 µm. Right: Schematic of the location the cell in the parasubiculum (arrow). The cell is located in the dorsal band of parasubiculum (blue), close to medial entorhinal cortex (grey). Scale bar, 1000 µm.

(B) Representative raw traces of the recorded cell shown in (A). Note the prominent theta rhythm in LFP and theta-modulated firing of the recorded cell.

(C) Left: Autocorrelogram of spike discharges for the cell shown in (A). Right: Theta-phase histogram of spikes for the cell shown in (A). For convenience, two repeated cycles are shown. The black sinusoid is a schematic local field potential theta wave for reference.

(D) Spike-trajectory plot (left), rate map (middle) revealing the border firing. Spike-trajectory plot: red dots indicate spike locations; grey lines indicate the rat trajectory. Rate map: red indicates maximal firing rate, value noted above. For this cell, the border score is 0.86. Right: Polar plot of the cell's head-direction tuning. Value indicates maximum firing rate to the preferred direction.

(E-H) Same as (A-D) for an identified head-direction cell.

D = dorsal, L = lateral, M = medial, V = ventral.

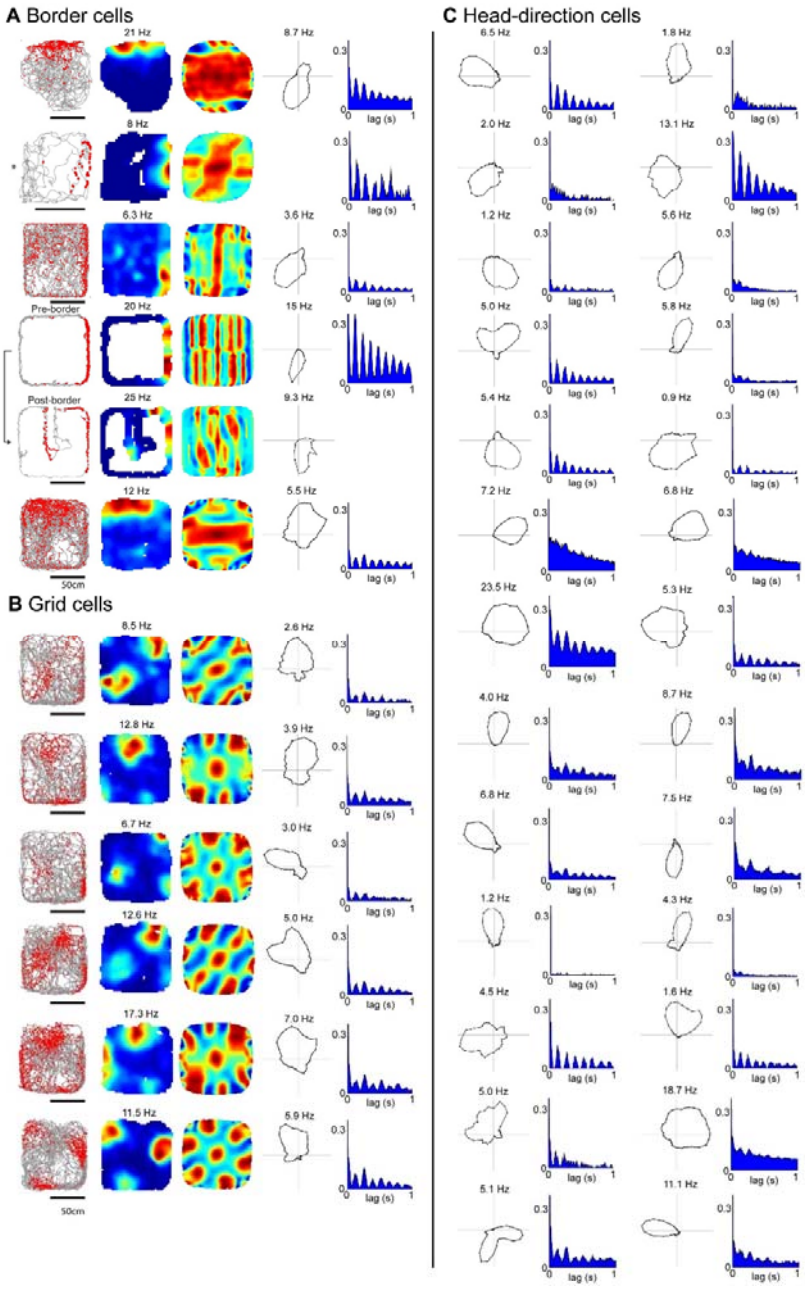

Figure 5. Border, grid and head-direction firing properties of parasubicular neurons.

(A) Parasubicular neurons classified as border cells. From left to right: Spike-trajectory plot, rate map, two-dimensional spatial autocorrelation, angular tuning (shown only for head-direction selective cells) and spike autocorrelogram. Numbers above the rate map indicate maximum firing rate. Numbers above the angular tuning map indicate maximum firing rate at the preferred direction. Scale bar below the Spike-trajectory plot corresponds to 50cm. An asterisk marks a border cell recorded in a 70x70 cm arena. Pre-border and Post-border refer to the border test (recording of the same cell before and after the introduction of an additional wall into the arena).

(B) Parasubicular neurons classified as grid cells (same panels as in A)

(C) Parasubicular neurons classified as Head Direction cells (see Methods). Left: angular tuning. Right: spike autocorrelogram. Conventions as in (A).

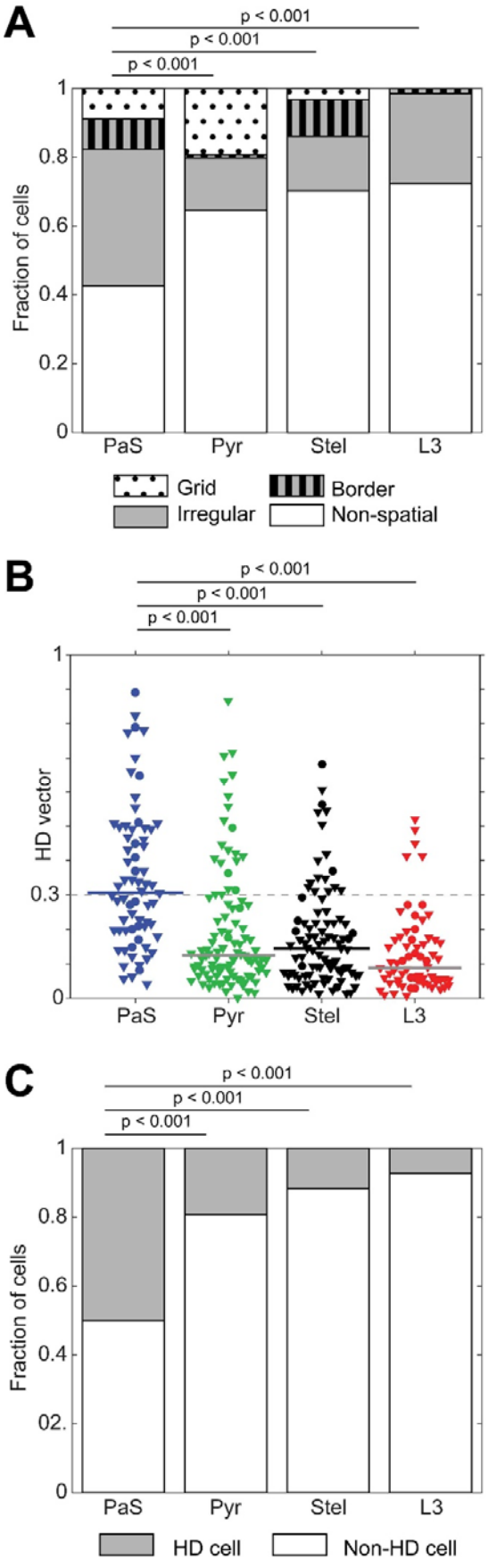
A
p < 0.001
p < 0.001
p < 0.001
Fraction of cells
1
0.8
0.6
0.4
0.2
0
PaS
Pyr
Stel
L3
Grid
Border
Irregular
Non-spatial
B
p < 0.001
p < 0.001
p < 0.001
HD vector
1
0.3
0
PaS
Pyr
Stel
L3
C
p < 0.001
p < 0.001
p < 0.001
Fraction of cells
1
0.8
0.6
0.4
02.
0
PaS
Pyr
Stel
L3
HD cell
Non-HD cell

Figure 6. Border and head-direction firing properties of parasubicular neurons.

Data from layer 2 and layer 3 of medial entorhinal cortex (MEC) come from the work of (Tang et al., 2014b) and (Tang et al., 2015) and are shown for comparison.

(A) Comparison of fractions of spatial discharges for parasubiculum, MEC L2 pyramidal, MEC L2 stellate and MEC L3 neurons. Parasubicular neurons show large fraction of significantly spatially modulated cells: grid cells, border cells and spatially irregular cells. (χ^2 test with Bonferroni-Holm correction).

(B) Comparison of head-direction (HD) vector lengths for parasubiculum (blue), MEC L2 pyramidal (green), MEC L2 stellate (black) and MEC L3 (red) neurons. Parasubicular neurons show significantly higher average HD vector length than all others (Mann-Whitney U-tests with Bonferroni-Holm correction). Lines indicate medians. Horizontal dotted line at 0.3 marks the threshold for HD classification.

(C) Comparison of fractions of head-direction cells (HD cells) for parasubiculum, MEC L2 pyramidal, MEC L2 stellate and MEC L3 neurons. Parasubicular neurons show significantly higher percentage of HD cells (χ^2 test with Bonferroni-Holm correction).

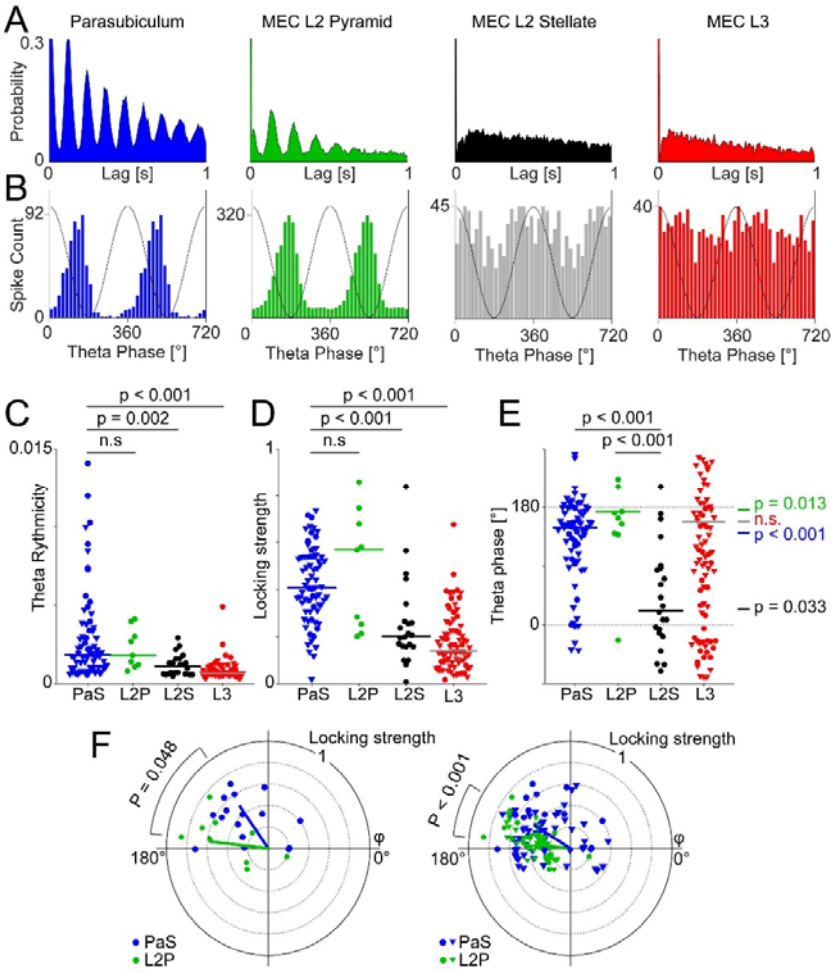

Figure 7. Theta modulation of parasubicular neurons compared to superficial medial entorhinal cortex.

Data from layer 2 and layer 3 of medial entorhinal cortex (MEC) come from the work of (Tang et al., 2014b) and (Tang et al., 2015) and are shown here for comparison.

(A) Representative autocorrelograms of spike discharges of identified neurons recorded from parasubiculum (blue), MEC L2 pyramidal (L2P, green), MEC L2 stellate (L2S, black) and MEC L3 (red) neurons.

(B) Theta-phase histogram of spikes for the neurons shown in (A). For convenience, two theta-cycles are shown. The black sinusoid is a schematic local field potential theta wave for reference.

(C) Comparison of the power of theta rhythmicity in parasubiculum (blue), MEC L2 pyramid (L2P, green), MEC L2 stellate (L2S, black) and MEC L3 (L3, red) neurons. Parasubiculum neurons show significantly stronger theta rhythmicity than MEC L2 stellate and MEC L3 neurons (Kruskal-Wallis test with Bonferroni correction). Lines indicate medians.

(D) Comparison of the theta-phase locking strength (abbreviated in the Figure as Locking Strength) for the neurons shown in in (C). Parasubicular and MEC L2 pyramidal neurons show significantly higher theta-phase locking than MEC L2 stellate and MEC L3 neurons

(Kruskal-Wallis test with Bonferroni-Holm correction; significant differences between L2P and L2S has been shown in Ray et al., 2014). Lines indicate medians.

(E) Comparison of the preferred theta phase for the neurons shown in (C). Parasubicular and MEC L2 neurons show significant preferred theta phases, while MEC L3 neurons do not (Rayleigh test for non-uniformity with Bonferroni-Holm correction: colored p-values on the right side; Watson-Williams test for equal means with Bonferroni-Holm correction: black lined p-values top). Colored lines indicate circular means.

(F) Polar plots of preferred theta phase (theta peak = 0°) and theta-phase locking strength ((Locking Strength; Rayleigh vector, 0-1) for parasubiculum (blue), MEC L2 pyramidal (green). Left: only identified neurons. Right: Identified neurons and tetrode recordings. dots = identified neurons, triangles = tetrode units, line = (mean direction, median strength of locking).

Chapter 8

Discussion

Neurons are the fundamental building blocks of our brain (Cajal, 1894). They are components which respond rather simplistically individually, but together with other neurons, form microcircuits and circuits to perform significantly complex functions like perception or action.

An unequivocally significant function of the brain is memory. The ability to remember is central to our effective functioning as living organisms. An aspect of memory which we can both understand, and effectively interrogate is spatial memory, or the memory of a place. The discovery of place cells (O'Keefe & Dostrovsky, 1971), neurons which fire in only one location of the environment heralded the era which recognized that even a basic component of the brain, a single neuron, could represent an idea as complex as a place. Decades later, the discovery of neurons which had a hexagonal discharge pattern, much like the grid-nodes on a map (and hence termed grid cells), rekindled the excitement in uncovering the mechanism which leads to the formation of these complex, cognitive maps. The grid cells were located in the major input structure of the hippocampus, the medial entorhinal cortex (MEC). The medial entorhinal cortex also contained other cells having interesting spatial properties, like border cells (Solstad et al., 2008), which fire when the animal is in the borders of an environment; head direction cells (Sargolini et al., 2006), which fire only when the animal is looking towards a specific direction and band cells (Krupic et al., 2012), which fire in parallel bands in the environment.

This thesis works towards discovering the structural identity of functionally spatial cells like grid cells and border cells, the functional architecture of the microcircuit they are found in and how their structural development might be correlated to their functional readout.

Grid cells are primarily located in layer 2 of the medial entorhinal cortex (Hafting et al., 2005; Boccara et al., 2010) which has two major types of principal cells– pyramidal cells and stellate cells. On the basis of their projections to the hippocampus and intrinsic properties (Lingenhöhl & Finch, 1991; Alonso & Llinás, 1989), stellate cells had been considered the prime candidates for grid cells (Pastoll et al., 2012).

Stellate and pyramidal cells are distinct in their intrinsic conductance, immunoreactivity, projections and inhibitory inputs (Varga et al., 2010). Stellate cells in layer 2 of the medial entorhinal cortex could be identified by their immunoreactivity to reelin, while pyramidal cells were immunoreactive to calbindin. In chapter 2 (Ray et al., 2014) we found that calbindin+ pyramidal cells in the MEC of rats were clustered in patches while the reelin+ stellate cells were scattered throughout layer 2 of the MEC. These calbindin+ patches were physically arranged in a hexagonal layout in the brain, much like how grid-cell discharges occur in the environment. This inspired an isomorphism hypothesis (Brecht et al., 2013) where we suggested that external space was topographically mapped to the entorhinal cortex, similar to how the body is somatotopically represented in the somatosensory cortex (Woolsey & van der Loos, 1970; Catania et al., 1993). Further, the calbindin+ pyramidal cells received preferential cholinergic input, and exhibited higher theta-rhythmicity, characteristics which are considered integral for grid cell activity (Koenig et al., 2011; Brandon et al., 2011).

In chapter 3 (Tang et al., 2014), we performed a large number of single-cell recordings from pyramidal and stellate cells, in freely behaving animals, to definitively establish a link between the structural phenotype of the cell and its functional spatial characteristics. We further developed a method to classify unidentified recordings, on the basis of results obtained in the previous chapter. These results indicated that grid cells primarily arise from the calbindin+ pyramidal cell population, and border cells are mostly found in the calbindin- stellate cell population.

In chapter 4 (Naumann et al., 2016), we undertook a comparative investigation into the architecture of medial entorhinal cortex across five mammalian species, which spanned ~100

million years of evolutionary diversity and ~20,000 fold difference in brain size. The species investigated included the smallest mammal in the world– Etruscan shrews (Jurgens et al., 1996), the only flying mammals– bats, reportedly the smartest mammals– mice (Adams, 1979) and probably the most successful mammal in the world, humans. We found that even in this diverse group of mammals, the architecture of the medial entorhinal cortex was remarkably conserved and exhibited clusters of calbindin+ pyramidal neurons, with a stark periodicity. Further, the size of these modules was also relatively conserved, and increased only 10 fold in terms of the number of calbindin+ neurons/patch, across ~20,000 fold differing brain sizes. An intriguing observation was that in rodents, where grid cells are theta modulated, the calbindin+ patches received preferential cholinergic input, while in bats and humans, where grid cells do not exhibit a clear theta-rhythmicity, these cells were not targeted by cholinergic inputs. This pointed towards an integral role of cholinergic inputs in driving grid cells at theta rhythmicity in rodents (Hafting et al., 2005) but not in bats (Yartsev et al, 2011).

To understand the development of the architecture of the medial entorhinal area, we investigated the structural development of the medial entorhinal cortex and parasubiculum in chapter 5 (Ray & Brecht, 2016). In layer 2 of MEC, the grid-layout of calbindin+ patches and scattered presence of reelin+ stellate cells was present around birth, indicating that genetic signaling, rather than experience, dictated the nature of this periodic layout. In terms of structural maturation of specific cell types, we observed that pyramidal and not stellate cells displayed a delayed postnatal development, on the basis of their co-localization with doublecortin, a marker for immature neurons. This further pointed to the structure-function dichotomy between pyramidal grid cells and stellate border cells, as functionally, grid cells (Wills et al., 2010; Langston et al., 2010), but not border cells (Bjerknes et al., 2014) exhibit a delayed developmental profile. Grid cells in the dorsal extent of the entorhinal cortex exhibit smaller grid spacing, thus probably representing nearby areas (Hafting et al., 2005; Stensola et al., 2012), while those in ventral parts have progressively larger spacing thus representing larger areas (Hafting et al., 2005; Stensola et al., 2012). We observed a dorsal to ventral developmental profile of layers 2 and 3 of the medial entorhinal cortex and parasubiculum indicating that the microcircuits underlying representation of smaller and larger spaces might display a graded development, which manifests behaviorally with younger animals exploring areas nearby their home (Wills et al., 2014; Bulut & Altman, 1974) before engaging in extended exploration at a later age (Wills et al., 2014).

In chapters 6 (Tang et al., 2015) and 7 (Tang et al., 2016) we investigated the functional architecture of layer 3 of the medial entorhinal cortex and the parasubiculum respectively. Layer 3 of the MEC exhibited a homogenous cell sheet and a rather homogenous distribution of functional properties. Cell populations had distinctive projections to either the ipsilateral hippocampus or the contralateral medial entorhinal cortex but had largely similar intrinsic electrophysiological, *in vivo* spatio-temporal and morphological properties. In chapter 7, we investigated the parasubiculum, a long and narrow structure which flanks the dorsal and medial extremities of the MEC in rats. The parasubiculum can be divided into ~ 15 large clusters and its medial part is aligned to an axis of the calbindin-grid described in chapter 2. Further, the parasubicular neurons also preferentially target the calbindin+ pyramidal patches in layer 2 of MEC, while receiving GABAergic and cholinergic medial septal inputs. This would point towards the parasubiculum providing dominant inputs to the MEC which could be instrumental in generating grid cell activity.

In summary, this thesis delves into the architecture of the medial entorhinal cortex across mammals and illustrates a structure-function dichotomy in layer 2 of MEC. The anatomical identification of the components corresponding to divergent functional cell types,

provides an essential link in resolving entorhinal microcircuits. The segregation of these cells on the basis of their protein expression provides a handle to utilize an array of genetic tools to study their inputs and outputs (Lo & Anderson, 2011; Rothermel et al., 2013) or switch them on and off (Boyden et al., 2005; Zhang et al., 2007) and effectively interrogate their position and exact roles in these microcircuits. The similarity in architecture of the medial entorhinal cortex across mammals points towards a conserved microcircuit across evolution, and that discoveries made in animal models like rodents might also be applicable to a large extent in humans. The development of different components of this microcircuit at varying rates might indicate that some aspects of memory might develop faster than others and understanding these would provide a more comprehensive view of the neuronal microcircuits underlying spatial representation in particular and memory processes in general.

References

Adams, D. The hitchhiker's guide to the galaxy. *Pan Books* (1979).

Alonso, A. & Llinás, R. R. Subthreshold Na+-dependent theta-like rhythmicity in stellate cells of entorhinal cortex layer II. *Nature* **342**, 175–177 (1989).

Bjerknes, T.L., Moser, E.I., Moser, M.B. Representation of geometric borders in the developing rat. *Neuron* **82**, 1–8 (2014).

Boccara, C.N. et al. Grid cells in pre- and parasubiculum. Nat. Neurosci. 13, 987–994 (2010).

Boyden, E.S., Zhang, F., Bamberg, E., Nagel., G., Diesseroth, K. Millisecond-timescale, genetically targeted optical control of neural activity. *Nat. Neurosci.* **8**, 1263-1268 (2005).

Brandon, M.P. et al. Reduction of theta rhythm dissociates grid cell spatial periodicity from directional tuning. *Science* **332**, 595-599 (2011).

Brecht, M. et al. An isomorphic mapping hypothesis of the grid representation. *Phil. Trans. R. Soc. B* **369**, 20120521 (2014).

Bulut, F. & Altman, J. Spatial and tactile discrimination learning in infant rats motivated by homing. *Dev. Psychobiol.* **7**, 465–473 (1974).

Cajal, S.R. The Croonian lecture: la fine structure des centres nerveux. *Proc. R. Soc.* **55**, 444-468 (1894).

Catania, K. C., Northcutt, R. G., Kaas, J. H., & Beck, P. D. Nose stars and brain stripes. *Nature* **364**, 493 (1993).

Hafting, T., Fyhn, M., Molden, S., Moser, M.B., Moser, E.I. Microstructure of a spatial map in the entorhinal cortex. *Nature* **436**, 801–806 (2005).

Jurgens, K.D., Fons, R., Peters, T., Sender, S. Heart and respiratory rates and their significance for convective oxygen transport rates in the smallest mammal, the Etruscan shrew Suncus etruscus. *J. Exp. Biol.* **199**, 2579–2584 (1996).

Koenig, J., Linder, A.N., Leutgeb, J.K., Leutgeb, S. The spatial periodicity of grid cells is not sustained during reduced theta oscillations. *Science* **332**, 592-595 (2011).

Krupic, J., Burgess, N., O'Keefe, J. Neural representations of location composed of spatially periodic bands. *Science* **337**, 853-857 (2012).

Langston, R.F. et al. Development of the spatial representation system in the rat. *Science* **328**, 1576–1580 (2010).

Lingenhöhl, K. & Finch, D. M. Morphological characterization of rat entorhinal neurons in vivo: soma-dendritic structure and axonal domains. *Exp. Brain. Res.* **84**, 57–74 (1991).

Lo, L. & Anderson, D.J.A. Cre-dependent, anterograde transsynaptic viral tracer for mapping output pathways of genetically marked neurons. *Neuron* **72**, 938–950 (2011).

Naumann, R.K. et al. Conserved size and periodicity of pyramidal patches in layer 2 of medial/caudal entorhinal cortex. *J. Comp. Neurol.* **524**, 783-806 (2016).

O'Keefe, J. & Dostrovsky, J. The hippocampus as a spatial map. Preliminary evidence from unit activity in the freely-moving rat. *Brain Res.* **34**, 171-175 (1971).

Pastoll, H., Ramsden, H.L., Nolan, M.F. Intrinsic electrophysiological properties of entorhinal cortex stellate cells and their contribution to grid cell firing fields. *Front. Neural Circuits* **6**, 17 (2012).

Ray, S. & Brecht, M. Structural development and dorsoventral maturation of the medial entorhinal cortex. *eLife* 13343 (2016).

Ray, S. et al. Grid-like arrangement and theta-modulation of a pyramidal cell microcircuit in layer 2 of medial entorhinal cortex. *Science* **343**, 891-896 (2014).

Rothermel, M., Brunert, D., Zabawa, C., Díaz-Quesada, M., Wachowiak, M. Transgene expression in target-defined neuron populations mediated by retrograde infection with adeno-associated viral vectors. *J. Neurosci.* **33**, 15195–15206 (2013).

Sargolini, F. et al. Conjunctive representation of position, direction, and velocity in entorhinal cortex. *Science* **312**, 758–762 (2006).

Solstad, T., Boccara, C.N., Kropff, E., Moser, M.B., Moser, E.I. Representation of geometric borders in the entorhinal cortex. *Science* **322**, 1865–1868 (2008).

Stensola, H.et al. The entorhinal grid map is discretized. *Nature* **492**, 72–78 (2012).

Tang Q. et al. Anatomical organization and spatiotemporal firing patterns of layer 3 neurons in rat medial entorhinal cortex. *J. Neurosci.* **35**, 12346-12354 (2015).

Tang, Q. et al. Functional architecture of the rat parasubiculum. *J. Neurosci.* **36**, 2289-2301 (2016).

Tang, Q.et al. Pyramidal and stellate cell specificity of grid and border representations in layer 2 of medial entorhinal cortex. *Neuron* **84**, 1191–1197 (2014).

Varga, C., Lee, S. Y., Soltesz, I. Target-selective GABAergic control of entorhinal cortex output. *Nat. Neurosci.* **13**, 822–824 (2010).

Wills, T., Cacucci, F., Burgess, N., O'Keefe, J. Development of the hippocampal cognitive map in preweanling rats. *Science* **328**, 1573–1576 (2010).

Wills, T.J., Muessig, L., Cacucci, F. The development of spatial behaviour and the hippocampal neural representation of space. *Phil. Trans. R. Soc. B* **369**, 20130409 (2014).

Woolsey, T. A., & Van der Loos, H. The structural organization of layer IV in the somatosensory region (SI) of mouse cerebral cortex: the description of a cortical field composed of discrete cytoarchitectonic units. *Brain Res.* **17**, 205-242 (1970).

Yartsev, M.M., Witter, M.P., Ulanovsky, N. Grid cells without theta oscillations in the entorhinal cortex of bats. *Nature* **479**, 103–107 (2011).

Zhang, F. et al. Multimodal fast optical interrogation of neural circuitry. *Nature* **446**, 633-639 (2007).

Acknowledgements

To Michael, for being a great supervisor and a fellow scientist who ensured that doing science was a creative and fun process.

To Robert, for being a great colleague who taught me the ropes and was a sounding board for my usually insane ideas.

To Qiusong, for some crazy ups and downs and for all those days which ended with some schnapps.

To Undine, for being one of the constants in the lab, on whom I could count on for anything.

To Andreea and Margret for ensuring that the exactness of the german administration mostly remained a myth to me.

To Eddy and Konstantin, for translating the abstract of this thesis into german.

To Shimpei, for some insane animations and karaoke nights.

To Susanne, Denise and Ramona, for all the weekends they put in for our sake.

To Lena and Tizi, for a hell of a ride through the last half a decade.

To Rajnish, for a lot of things, some scientific and some not.

To Nacho, for coming up with ideas even crazier than mine.

To Constanze, Jean and Ann for tacos and margaritas.

To Johanna, Peter, Edith, Moritz and John for the lunches, the coffees and the beers.
To Claudia.

To Simon, Andrea, Christian, Guy, Evgney, Brigette and Jule for being amazing lab mates.

To my folks, for pretty much everything.

To Shadan, for the amazing time we've had and to much more ahead.

To Sergey Brin and Larry Page for making the world a smaller place.

To all those people who are always there!

Publications

Ray, S. et al. (2014) Grid-layout and theta-modulation of layer 2 pyramidal neurons in medial entorhinal cortex. Science 343:891-896

Tang, Q. et al. (2014) Pyramidal and stellate cell specificity of grid and border representations in layer 2 of medial entorhinal cortex. Neuron 84:1191-1197

Naumann, R., et al. (2016) Conserved size and periodicity of layer 2 pyramidal patches in medial/caudal entorhinal cortex. J. Comp. Neurol. 524:783-806

Ray, S. & Brecht, M. (2016) Structural development and dorsoventral maturation of the medial entorhinal cortex. eLife. 13343

Tang, Q. et al. (2015) Anatomical organization and spatiotemporal firing patterns of layer 3 neurons in the rat medial entorhinal cortex. J. Neurosci. 35:12346-12354

Tang, Q. et al. (2016) Functional architecture of the rat parasubiculum. J. Neurosci. 36:2289-2301

Declaration of Contribution

Anlage zu § 6, Abs. 2 der Promotionsordnung der Lebenswissenschaftlichen Fakultät vom 05.03.2015, veröffentlicht in: Amtliches Mitteilungsblatt HU 12/2015
Annex to § 6, para. 2 of the Doctoral Degree Regulations of the Faculty of Life Sciences, amended on 05.03.2015, published in: University Gazette of Humboldt-Universität zu Berlin 12/2015

Erklärung über den Eigenanteil an den veröffentlichten bzw. zur Veröffentlichung angenommenen wissenschaftlichen Schriften innerhalb meiner Dissertationsschrift gemäß § 6, Abs. 2 der Promotionsordnung
Declaration regarding my own contribution to the published academic papers, or academic papers which have been accepted for publishing, within my doctoral thesis, under the provisions of § 6, para. 2 of the Doctoral Degree Regulations

Von der Antragstellerin/Vom Antragsteller einzutragen: | *To be completed by the applicant:*

1. Name, Vorname | *Ray, Saikat*
Institut (ggf. externe Einrichtung) | *Life Sciences*
Promotionsfach | *Biology*
Thema der Dissertation | *Functional Architecture of the Medial Entorhinal Cortex*

2. Nummerierte Aufstellung der eingereichten Schriften (Titel, Autor/innen, wo und wann veröffentlicht bzw. eingereicht):
Numbered breakdown of the submitted papers (title, authors, where and when published or submitted):

(i) *Ray, S.* et al. (2014)* Grid-layout and theta-modulation of layer 2 pyramidal neurons in medial entorhinal cortex. *Science 343:891-896*
(Equal contribution)*

(ii) Tang, Q. et al. (2014) Pyramidal and stellate cell specificity of grid and border representations in layer 2 of medial entorhinal cortex. *Neuron 84:1191-1197*

(iii) *Naumann, R.*, Ray, S.* et al. (2016)* Conserved size and periodicity of layer 2 pyramidal patches in medial/caudal entorhinal cortex. *J. Comp. Neurol. 524:783-806*
(Equal contribution)*

(iv) Ray, S. & Brecht, M. (2016) Structural development and dorsoventral maturation of the medial entorhinal cortex. *eLife. 13343*

(v) Tang, Q. et al. (2015) Anatomical organization and spatiotemporal firing patterns of layer 3 neurons in the rat medial entorhinal cortex. *J. Neurosci. 35:12346-12354*

(vi) Tang, Q. et al. (2016) Functional architecture of the rat parasubiculum. *J. Neurosci. 36:2289-2301*

3. Darlegung des eigenen Anteils an diesen Schriften:
Statement regarding my own contribution to these papers:

Erläuterung: Legen Sie dar, welche von Ihnen geleisteten Arbeiten diese Schriften enthalten (**z. B**. Entwicklung der Konzeption, Literaturrecherche, Methodenentwicklung, Versuchsdesign, Datenerhebung, Datenauswertung, Ergebnisdiskussion, Erstellen des Manuskripts, Programmierung, Beweisführung) und wie groß Ihr Anteil (**z. B.** vollständig, überwiegend, mehrheitlich, in Teilen) an den jeweiligen Leistungen war.
*Explanation: State which of the works which you rendered comprise these papers (**e. g**. development of the conception, literature research, development of methods, test design, data collection, data analysis, results discussion, compiling the manuscript, programming, reasoning), and how large your contribution (**e. g.** entire, large, predominant, partial) was the respective works.*
(scale of 0-5, with 0 for no contribution and 5 for 100% contribution)

(i)	Design of Experiments	3
	Acquisition of Data	3
	Analysis of Data	3
	Writing of Manuscript	3
(ii)	Design of Experiments	3
	Acquisition of Data	2
	Analysis of Data	2
	Writing of Manuscript	2
(iii)	Design of Experiments	3
	Acquisition of Data	4
	Analysis of Data	4
	Writing of Manuscript	3
(iv)	Design of Experiments	4
	Acquisition of Data	5
	Analysis of Data	5
	Writing of Manuscript	4
(v)	Design of Experiments	0
	Acquisition of Data	1
	Analysis of Data	1
	Writing of Manuscript	1
(vi)	Design of Experiments	1
	Acquisition of Data	2
	Analysis of Data	1
	Writing of Manuscript	1

Datum, Unterschrift der Antragstellerin/des Antragstellers:
Date, signature of the applicant: 2.4.2016, Saikat Ray

Die Angaben zu Punkt 3 müssen von den Mitautor/innen schriftlich bestätigt werden.
The information submitted in point 3 must be confirmed in writing by the co-authors.

Ich bestätige die von Herrn Saikat Ray unter Punkt 3 abgegebene Erklärung:
I confirm the declaration submitted by Mr. Saikat Ray in point 3:

1. Beed, Prateep
2. Brecht, Michael
3. Burgalossi, Andrea
4. Ebbesen, Christian Laut
5. Gundlfinger, Anja
6. Heppner, Frank L.
7. Las, Liora
8. Naumann, Robert
9. Preston-Ferrer, Patricia
10. Prokop, Stefan
11. Sanguinetti-Scheck, Juan Ignacio
12. Schmidt, Helene
13. Schmitz, Dietmar
14. Spicher, Dominik
15. Tang, Qiusong
16. Tukker, John J.
17. Winterer, Jochen